

Orbit-space sensitivity of fast-ion diagnostics

Henrik Järleblad

Department of Physics
Technical University of Denmark

Dissertation submitted for the degree of
Doctor of Philosophy



Kongens Lyngby, November 2022

Orbit-space Sensitivity of Fast-ion Diagnostics

Ph.D. dissertation

Henrik Järleblad

November 30th, 2022

Copyright: Reproduction of this dissertation in whole or in part must include the customary bibliographic citation, including author attribution, dissertation title, etc.

Cover: An example of all six possible standard fast-ion orbit types for a 3.5 MeV α -particle in ITER, computed using a magnetic equilibrium with a B-field on-axis of 5 Teslas. Figure is original and not reproduced; this type of figure has previously not been published for ITER. Colors are kept consistent with previous publications solely for pedagogical purposes.

Technical University of Denmark

DTU Physics

Department of Physics

Section for Plasma Physics and Fusion Energy

Fysikvej

2800 Kongens Lyngby, Denmark

Tlf. +45 4525 3344

info@fysik.dtu.dk

www.fysik.dtu.dk

Orbit-space sensitivity of fast-ion diagnostics

Supervisor: Dr. Techn. Mirko Salewski
Technical University of Denmark

Co-supervisor: Dr. Luke Stagner
*General Atomics,
California, United States of America*

Examiners: Dr. Antti T. O. Snicker
Aalto University, Finland

Dr. Philipp Lauber
*Max Planck Institute for Plasma Physics
Garching, Germany*

Chairman: Dr. Søren Bang Korsholm
Technical University of Denmark

Submitted to the Technical University of Denmark
on November 30th 2022.

Abstract

The sensitivity of fast-ion diagnostics in magnetic confinement fusion can be quantified in the form of weight functions. They can be used to relate the fast-ion distribution function in phase space to a measurement in a diagnostic measurement bin. Via tomographic inversion, weight functions can be used to reconstruct the fast-ion distribution function from diagnostic measurements. Due to the magnetic field, the fast ions must follow fixed trajectories known as orbits. This work continues to build upon orbit weight functions, which can be utilized to reconstruct the full gyro-averaged fast-ion distribution in tokamaks. Orbit weight functions for neutron emission spectroscopy and gamma-ray spectroscopy for one-step fusion reactions were developed and analyzed in this project. Gained insights include: a high sensitivity to trapped orbits whose tips are inside the line-of-sight of the diagnostic, and an increased understanding of the optimal positioning and orientation of diagnostic sightlines. In addition, this project also birthed new ways of using fast-ion orbits to analyze diagnostics. These include: 1) The decomposition of diagnostic signals, fast-ion distributions and weight functions, in terms of their fast-ion orbit-type origin. 2) Interactive analysis of which fast-ion orbit types pass through certain (R, z) points. 3) The mapping of poloidal and toroidal transit times for all of orbit space, which could provide further insight into the interaction between fast ions and e.g. Alfvén eigenmodes. A code framework was created to enable future use of the new tools developed in this work. This is envisioned to increase the vital understanding of the behaviour of fast ions in tokamak fusion plasmas.

Dansk Resume

Sensitiviteten af hurtig-ion diagnostik i fusionsplasma indesluttet af magnetfelter kan kvantificeres i form af vægtfunktioner. De kan bruges til at relatere hurtig-ion fordelingsfunktionen i fasrummet til en måling i et målingsinterval. Ved hjælp af tomografisk inversion kan vægtfunktioner bruges til at rekonstruere hurtig-ionfordelingsfunktionen fra målinger. Takket være magnetfeltet følger hurtige ioner faste baner, som kaldes orbits. Dette projekt fortsætter arbejdet med at udvikle orbit vægtfunktioner, der kan bruges til at rekonstruere den fulde gyro-midlet hurtig-ionfordelingen i tokamaks. Orbit vægtfunktioner for neutronudlednings- og gamma-strålingsspektroskopi for fusionsreaktioner med kun ét trin er blevet udviklet og analyseret i dette projekt. Eksempler på indsigter er: en høj sensitivitet for trapped orbits med deres 'banana tips' indenfor målingsdiagnostikkens line-of-sight, og en øget forståelse for den optimale positionering og orientering af målingsdiagnostikkens lines-of-sight. Dette projekt resulterede også i nye måder at bruge hurtig-ion orbits på for at analysere målingsdiagnostik. Disse inkluderer: 1) Opsplitning af målingssignaler, hurtig-ionfordelinger og vægtfunktioner, i deres hurtig-ion orbit-kilder. 2) Værktøj for interaktiv analyse af hvilke hurtig-ion orbit-typer der rammer gennem hver (R, z) punkt. 3) Kortlægningen af poloidale og toroidale transittider for hele orbitrummet, der kan resultere i yderligere indsigt i interaktionen mellem hurtige ioner og f.eks. Alfvén eigenmodes. Et kodepakke er blevet skabt for at muliggøre nemt brug af disse nye værktøjer. Dette vil øge den nødvendige forståelse for, hvordan hurtige ioner bevæger sig i tokamakfusionsplasmaer.

Included papers

This thesis is based on the following papers attached as appendices. In the text, the papers are cited together with their Roman numerals, as defined below.

- I Fast-ion orbit sensitivity of neutron emission spectroscopy diagnostics**
H. Järleblad, L. Stagner, M. Salewski, J. Eriksson, S. Benjamin, B. Madsen, M. Nocente, J. Rasmussen, and B.S. Schmidt
Review of Scientific Instruments **92** 043526 (2021)
Reproduced from [1], with the permission of AIP Publishing
- II Fast-ion orbit sensitivity of neutron and gamma-ray diagnostics for one-step fusion reactions**
H. Järleblad, L. Stagner, M. Salewski, J. Eriksson, M. Nocente, J. Rasmussen, Z. Stancar, Ye.O. Kazakov, B. Simmendefeldt and JET contributors
Nuclear Fusion **62** 112005 (2022)
Reproduced from [2], with the permission of IOP Publishing
- III A Framework for Synthetic Diagnostics using Energetic-particle Orbits in Tokamaks**
H. Järleblad, L. Stagner, M. Salewski, J. Eriksson, M. Nocente, B.S. Schmidt, and M. Rud Larsen
Submitted to *Computer Physics Communications*
- IV Fast-ion Orbit Origin of Neutron Measurements in the JET DT Campaign**
H. Järleblad, L. Stagner, M. Salewski, J. Eriksson, M. Nocente, K. Kirov, M. Rud Larsen, B.S. Schmidt, M. Maslov, D. Kinga, D. Keeling, C. Maggi, J. Garcia, E.A. Lerche, P. Mantica, and JET contributors
In preparation, To be submitted to *Nuclear Fusion*

Additional co-authored papers not attached to this thesis include the following:

S. Mazzi *et al* (incl. **H. Järleblad**). *Enhanced performance in fusion plasmas through turbulence suppression by megaelectronvolt ions*. Nature Physics, **18**, 776-782 (2022)

J. Vega *et al* (incl. **H. Järleblad**). *Disruption prediction with artificial intelligence techniques in tokamak plasmas*. Nature Physics, **18**, 741-750 (2022)

R. Gerrú, M. Wiesenberger, M. Held, A.H. Nielsen, V. Naulin, J. Juul Rasmussen and **H. Järleblad**. *Conservation of currents in reduced full-F electromagnetic kinetic and fluid models*. Plasma Physics and Controlled Fusion, **64**, 054005 (2022)

J. Mailloux *et al* (incl. **H. Järleblad**). *Overview of JET results for optimising ITER operation*. Nuclear Fusion, **62**, 042026 (2022)

M. Fenstermacher *et al* (incl. **H. Järleblad**). *DIII-D research advancing the physics basis for optimising the tokamak approach to fusion energy*. Nuclear Fusion, **62**, 042024 (2022)

B.S. Schmidt, M. Salewski, B. Reman, R.O. Dendy, D. Moseev, R. Ouchoukov, A. Fasoli, M. Baquero-Ruiz and **H. Järleblad**. *Determining 1D fast-ion velocity distribution functions from ion cyclotron emission data using deep neural networks*. Review of Scientific Instruments, **92**, 053528 (2021)

B. Madsen, J. Huang, M. Salewski, **H. Järleblad**, P.C. Hansen, L. Stagner, J. Su, J.F. Chang, J. Fu, J.F. Wang, L.Z. Liang, G.Q. Zhong, Y.Y. Li, B. Lyu, H.Q. Lui, Q. Zhang, Z.P. Luo, M. Nocente, D. Moseev, T.S. Fan, Y.M. Zhang, D. Yang, J.Q. Sun, L.Y. Liao and the EAST team. *Fast-ion velocity-space tomography using slowing-down regularisation in EAST plasmas with co- and counter-current neutral beam injection*. Plasma Physics and Controlled Fusion, **62**, 115019 (2020)

Acknowledgements

I have had the pleasure of working with truly bright and talented individuals during my PhD studies. In fact, I consider everyone who works in the field of plasma physics and fusion energy nothing short of exceptional. Nevertheless, I would like to take the opportunity to thank the people who have helped me get through these three years, and whose collaborations were invaluable to the project.

First and foremost, I would like to thank my main supervisor Mirko Salewski for his great support. He has helped me get back on track when I was stuck and provided more insightful discussions than I can count. His work on velocity-space tomography is the foundation upon which the field of fast-ion tomography stands.

I would also like to thank my co-supervisor Luke Stagner. His code is the most brilliant I have ever seen in my life, and his razor-sharp insights and quick thinking has helped me push my limits. Being both the father of orbit tomography and slowing-down regularization, his contributions to the field of fast-ion tomography and orbit analysis are truly great. His work is the backbone of the OWCF, which would not have seen the light of day without his ingenious code.

Continuing, many thanks to Stuart Benjamin whom I had the great pleasure of part-time supervising remotely. It has been a great experience to support his contributions to the complex Julia codes developed by Luke and me. MIT should be glad to have acquired such a bright PhD student.

A big thank you to the current, and former, PhD students of the fast-ion tomography group at PPFE: Asger, Birgitte, Bo, Mads and Andrea. You have all helped me learn everything I know, make progress in the field and optimize the OWCF as well as review this dissertation.

I am also grateful to my collaborators in Sweden and Italy: Jacob Eriksson and Massimo Nocente. Thank you kindly for the fruitful discussions and for the projects we realized together. This work has also received support from the ITPA energetic particles group, and financial support from the Royal Danish Academy of Sciences through the Niels Bohr Foundation.

Furthermore, I feel I have to thank a particular person who taught me manners and everything I know about good practice regarding code documentation, already prior to my PhD studies. Pablo Vallejos, your lessons continue to haunt me everytime I forget them. Honestly, I am very grateful for that.

Thanks also to Thomas Jonsson (KTH), Sander and everyone at the FuseNet European Teacher's Day team. I am glad to have helped to educate high school teachers all over Europe on fusion together with you.

While on external research stay at General Atomics and DIII-D, I had the pleasure of meeting some truly awesome people. A special thanks to Severin, Jasper, Sabine and Bill (sorry for indirectly calling you an old man! You are a living legend). On a fun sidenote, thanks to Dirtcheap Car Rentals San Diego for letting me rent a Mustang Cabriolet for a week almost for free. I drove to Hollywood, as you recommended.

Thanks a lot to my office mates for making my time at DTU and PPFE a fun and enjoyable experience! In particular: thank you Birgitte, Nishta, Mads and Andrea (godspeed at General Fusion!).

Continuing with the rest of PPFE, past and present, thanks to everyone for being a hard-working yet welcoming group! Thank you Jesper (for being the best manuscript draft feedback giver), Anders (the journal club guru), Jens (the Gandalf of PPFE), Stefan, Thomas, Martin, Eric, Agata, Pernille, Marianne (for providing me with my own quiet office for writing this dissertation), Galina, Axel, Heidi, Théo (times 3. You know who you are!), Matthias (that German noodle recipe is the best), Alexander (for being the board game master and including me in the Lyngby public science outreach day), Søren (my favorite DANfusion director), Riccardo (the man, the myth, the legend), Volker, Mads (the senior and, plausibly, wiser), Aslak, and Raúl (the Iron man himself).

In terms of supportive friends, against all odds, I managed to both make and keep some during my PhD studies. They have given me the energy to finish this PhD project and write this dissertation. A big thanks to Fabian, Johann, Olga, Matthew, Mark and Rasmus for all the adventures during these three years, which has helped me to take my mind of work and relax. It's amazing what an annoying Linde Allé fire alarm back in 2019 can lead to!

Now, for some acknowledgements in Swedish: Först ut, varmt tack till alla Malmöbor och Skåningar! Tack till Alexander Le Backis, Diego, Johan och Archi, och Kevin. Hur skulle jag tagit mig igenom de här tre åren utan my Maine man, alla morgondopp vid Scaniabadet, VR-spelbygge, hundpassning, brädspel och min favorit-statsvetare? Och SEALS (Jack, get in here)! Om det här arbetet hjälper till att realisera fusion så har ni nu officiellt varit med och bidragit! Tack också till Micha och Luna för alla äventyr, filmkvällar, och hundpassningar! Tack till Matias för alla fina stunder! Tack till Elin för all energi och för att du är bästa grannen! Och tack till Jennifer, Merrit och alla på MBA för den grymma energin som gått från kickboxningen rakt in i denna avhandling!

Längre norrut i Sverige har jag också hämtat energi till det här arbetet, och då syftar jag inte bara på elen som laddar min dator och mobil. Andreas, jag hade inte tagit mig igenom början av mina doktorand-studier utan dig, det vet du. Tack för att du fångade upp mig när jag inte själv kunde! Halo-marathon snart igen? Maciej, alltså om det är någon som borde få en privat fusionsreaktor av mig i julklapp i framtiden, så är det du. See you back in Lumbridge for Christmas, old sport! Malte, att få komma upp och besöka dig i Umeå är en av mina favorit-tider på året. Varmt tack för all vänskap!

Tack också till Gunnar, August, Christopher, Lucas, Oskar, Pontus, Betti, Hassan, John, Pablo, och Sebastian! Energin från alla våra möten och vår vänskap är det som gjort att jag klarat mig igenom det här. Jag är tacksam för alla år tillsammans, och ser fram emot ännu fler!

Sist men inte minst så vill jag självklart tacka min familj och släkt. Louise, mamma och pappa, betydelsen av ert stöd och er fasta punkt i mitt liv går knappt att sätta ord på. Varmt tack för all uppmuntran och förståelse, både innan och under mina doktorand-studier! Tack också till farmor Gun, Christian, Lisbeth, Daniel, Alexandra, Isabella, Katya och Mereta. Energin från alla gånger vi sågs under de senaste tre åren har hjälpt mig att skriva klart den här doktorsavhandlingen.

Coming back to English, I would also like to thank the examiners Dr. Antti T.O. Snicker and Dr. Philipp Lauber, and the chairman Dr. Søren Bang Korsolm. Finally, I would like express my deepest gratitude to the ITER organization, Martin Kocan and Michael Walsh for giving me the opportunity of a lifetime, starting right after these PhD studies.

Preface

At the end of the day, I believe I ultimately decided to pursue a PhD in plasma physics and fusion energy because of, and thanks to, how I seem to never stop marvelling when I explore the wonders of nature and our universe. Of course the allure of nuclear fusion as a virtually limitless source of sustainable energy played a prominent part as well. But the last mile, the final straw, came from the amazement I always feel when I discover something new about the universe. The universe is filled with mysteries, and when I learn of yet another one, and I understand how it works and why it works, the awe I feel is borderline indescribable. I mean, how elegant is it, that everything works because of the laws of nature that we humans are starting to get the hang of? How awesome it is, that no matter how complex a machine we manage to build, no matter how advanced our technology becomes, it will still have been made possible by the scientific method. Even if it may seem like magic, sometime way ahead in the distant future, it will still be based on the same basic building blocks of nature that we are exploring today. It will always be subject to the same fundamental physical laws of nature. It is the realisation that Mother nature is bigger than all of us, and that her game is the only game in town.

The universe is a chessboard. We are finally starting to understand what the allowed moves are, and what the best moves are. And we are getting better and better at that game all the time. Hopefully, my work on fast-ion orbits can serve as a springboard for further research in the area. There is so much left to do, and so much yet to discover. Let's explore the universe together.

A handwritten signature in black ink, reading "Henrik Järleblad". The signature is written in a cursive style with a horizontal line underneath.

Henrik Järleblad, November 30th, 2022

*We do not have to worry about nothing
Because we have got the fire
And we are burning one hell of a something
They are going to see us from outer space*

*Light it up
Like we are the stars of the human race*

*When the light started out, they don't know what they heard
Strike the match, play it loud, giving love to the world
We will be raising our hands, shining up to the sky
Because we have got the fire*

*Yes, we have got the fire
And we are going to let it burn*

*We start the fire, and we burn it up
It is over now, we have got the love
There is no sleeping now
We can light it up, so they can put it out*

*Light it up
Like we are the stars of the human race
Because we have got the fire*

*Yes, we have got the fire
And we are going to let it burn*

"T.S. was able to build this in a cave! ...With a box of scraps!!"

Contents

Abstract	i
Dansk Resume	iii
Included papers	v
Acknowledgements	vii
Preface	xi
1 Introduction	1
1.1 Fusion energy	1
1.2 Plasma confinement	4
1.3 Fast-ion distribution function	5
1.4 Weight functions and fast-ion tomography	7
1.5 This work	9
2 Fast-ion orbits	11
2.1 Charged particle motion in tokamaks	11
2.2 Orbit coordinates	13
2.3 Orbit space	16
2.4 Computing orbits in this work	18
2.5 Transforming to (E, p, R, z)	21
2.5.1 Dual numbers	22
2.5.2 Computing \mathcal{J}	22
2.5.3 Transforming using orbit covariance	26
2.5.4 Transforming using grid-mapping	27
3 Fast-ion Diagnostics	29
3.1 TOFOR	29
3.2 NE213-scintillator	31
3.3 GRS diagnostics	31
3.4 KN3 Neutron Camera System	34

3.5	MPRu	34
4	Orbit sensitivity of fast-ion diagnostics	37
4.1	TOFOR	39
4.1.1	$E_d < E_{n,nominal}$	40
4.1.2	$E_d \approx E_{n,nominal}$	43
4.1.3	$E_d > E_{n,nominal}$	44
4.2	NE213-scintillator	45
4.2.1	$E_d < E_{n,nominal}$	45
4.2.2	$E_d \approx E_{n,nominal}$	49
4.2.3	$E_d > E_{n,nominal}$	50
4.3	GRS	52
4.3.1	$E_d < E_{g,nominal}$	52
4.3.2	$E_d \approx E_{g,nominal}$	52
4.3.3	$E_d > E_{g,nominal}$	55
4.4	KN3 orbit weight functions	55
4.5	MPRu	57
5	Orbit-space origin of diagnostic signals	59
5.1	Weight function signals split into orbit types	59
5.2	Orbit sensitivity split into orbit types	62
5.3	Fast-ion distribution split into orbit types	66
5.4	Orbit weight function signal density detailed analysis	68
6	Discussion on orbit tomography	73
6.1	Attempts at reconstructing from synthetic measurements	73
6.2	Null measurements (null orbits)	77
6.3	Importance of varying sightlines	81
6.4	Magnetic flux surfaces in (E, p_m, R_m) coordinates	85
7	The Orbit Weight Computational Framework (OWCF)	91
7.1	Background	91
7.2	Compatibility with computational clusters	92
7.3	Orbit web app	93
7.4	Constants-of-motion web app	93
7.5	Future work	95
8	Conclusion and outlook	99

CONTENTS

Bibliography	102
Appendices	109
Paper I	111
Paper II	118
Paper III	135
Paper IV	170

CHAPTER 1

Introduction

Energy is the fundamental currency of our universe. As the first law of thermodynamics states, it cannot be destroyed, nor created, but simply converted between different forms. Our ancestors might have started to realise this fundamental principle, as they learned how to convert the chemical energy stored in wood to thermal energy and light via the process known as fire. As living beings, we humans have always been dependent on a regular input of energy to stay alive, not only via the heating that fire provides but first and foremost via the intake of food and the rays of our sun. It can be estimated that humans require about 2.4 kWh per person per day to stay alive (see Appendix A and [3, 4]). However, when fire was invented (or, maybe more accurately, discovered), human society started its ever-increasing journey upwards to higher and higher levels of energy dependence.

Today, the average person in Denmark demands roughly 30-40 times as much energy per day (~ 90 kWh per person per day [5]) and globally the average energy demand is expected to increase even further in the future [6]. It is evident that to meet the levels of energy consumption to come, human society needs to find new solutions to the problem of satisfying its energy demand, if a decrease in the levels of greenhouse gas emissions is also to be achieved [6].

One such solution is to replicate the process by which the stars of our universe convert mass into energy, as described by Einstein's famous equation $E = mc^2$: the process of nuclear fusion.

1.1 Fusion energy

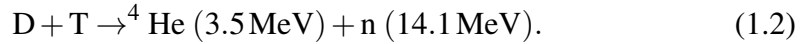
Nuclear fusion is the process by which lighter atomic nuclei fuse into heavier atomic nuclei. Together with a heavier atomic nucleus, there will often also be an emitted particle (proton, neutron, gamma-ray etc). Nuclear fusion can be distilled

into the expression

$$a(b,c)d \quad (1.1)$$

where 'a' and 'b' are the reacting nuclei (by convention, we will let 'b' denote the more energetic of the two reactants), 'c' is the emitted particle and 'd' is the product nucleus. There are also more uncommon fusion reactions with three product particles ('c', 'd1' and 'd2') and even three reacting particles ('a1', 'a2', 'b'). However, in practice all fusion reactions suitable for energy production are of the form (1.1). Two especially important fusion reactions include $D(D,n)^3\text{He}$ and $D(T,n)^4\text{He}$, where 'D' stands for the hydrogen isotope deuterium, 'n' stands for neutron, ^3He is helium-3, 'T' is the hydrogen isotope tritium and ^4He is helium-4 (also known as an alpha particle, α). The $D(D,n)^3\text{He}$ has been used extensively in fusion research and the $D(T,n)^4\text{He}$ reaction is envisioned to be the power-generating fusion reaction in the first generation of future fusion power plants [7]. The $D(T,n)^4\text{He}$ reaction has been illustrated in Figure 1.1.

In every fusion reaction, a small amount of mass is converted into a large amount of energy. For example, this can be illustrated for the $D(T,n)^4\text{He}$ reaction as [8]



The sum of the masses of the fusion products is slightly smaller than the sum of the masses of the fusion reactants. This small mass difference is converted into a large amount of energy via $E = mc^2$, and is distributed among the two fusion products. $1\text{MeV} = 10^6\text{eV}$ is equivalent to $10^6 \times 1.6 \times 10^{-19} = 1.6 \times 10^{-13}$ Joule. That might not sound like much, but when scaled up to e.g. 60 kg of DT-fuel (instead of just a single DT-reaction as in equation 1.2) one can start to appreciate the enormous energy prospect of fusion energy. By noting that the total energy release from a DT-reaction is $3.5 + 14.1 = 17.6\text{MeV}$, we can write

$$N \times E_{fus} = \frac{60\text{kg}}{(m_D + m_T)} \times 17.6\text{MeV}, \quad (1.3)$$

where N is the number of fusion reactions each releasing E_{fus} amount of energy. Using the mass of a deuterium ion $m_D \approx 3.34 \times 10^{-27}\text{kg}$ and a tritium ion $m_T \approx 5.01 \times 10^{-27}\text{kg}$, we can get an estimation for the amount of energy that can be released by fusing the atomic nuclei in a 50/50 mixture of 60 kg deuterium/tritium:

$$\frac{60\text{kg}}{(3.34 \times 10^{-27} + 5.01 \times 10^{-27})\text{kg}} \times 17.6\text{MeV} \approx 2.0 \times 10^{16}\text{Joule}. \quad (1.4)$$

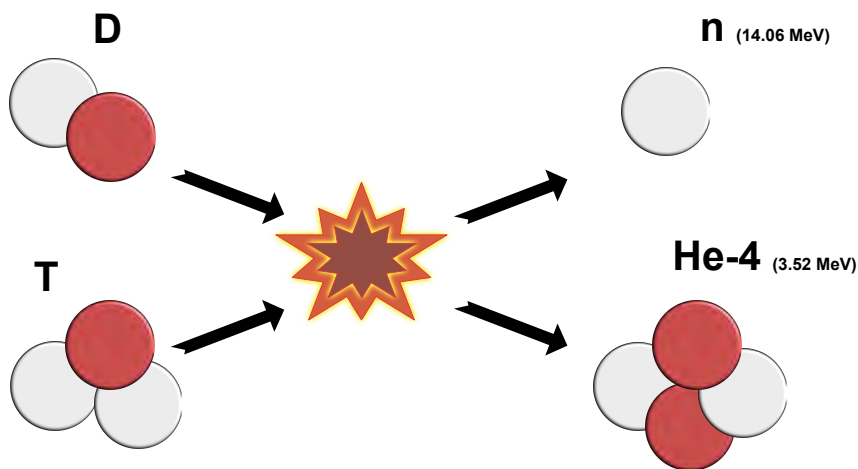


Figure 1.1: A graphical illustration of the $D(T,n)^4\text{He}$ fusion reaction. The output energy $E_{fus} = 17.6$ MeV is shared among the neutron n and the alpha particle (He-4). $E_{fus,n} = 14.1$ MeV $= E_{fus} \times \frac{m_{\text{He-4}}}{m_{\text{He-4}} + m_n}$ and $E_{fus,\text{He-4}} = 3.5$ MeV $= E_{fus} \times \frac{m_n}{m_{\text{He-4}} + m_n}$. There is a small mass difference between the products and the reactants. This is converted to energy via $E = mc^2$, resulting in the output energy. The energies can be obtained from solving the energy and momentum equations together.

This is equivalent to 5.6 TWh. How much coal would we need to burn to be able to release the same amount of energy? The energy density of (burning) coal is roughly 24 MJ/kg (or 6.7 kWh/kg) [9, 10]. Basic arithmetic thus yields

$$\frac{5.6 \text{ TWh}}{6.7 \text{ kWh/kg}} = \frac{5.6 \times 10^9}{6.7} \text{ kg} \approx 8.0 \times 10^8 \text{ kg}. \quad (1.5)$$

In short, without taking power plant efficiencies into account, the energy released from burning 800 000 000 kg of coal is equivalent to the extractable fusion energy in just 60 kg of a 50/50 mixture of deuterium-tritium fuel.

It may then come as no surprise that fusion energy is what powers the sun and all the stars in our universe. What can we do to replicate this process here on Earth? As in the core of the sun, we need to heat matter to extremely high temperatures, namely millions of degrees Celsius. In fact, due to the impossible task of replicating the immense scale of the sun, we need to utilize even higher temperatures in the tens and hundreds of millions of degrees. In such conditions, the electrons and atomic nuclei no longer constitute atoms, but rather float around in a 'soup' of mixed positive and negative charges. This so called fourth state of matter is known as a plasma. How can we confine a plasma here on Earth and utilize it for energy production? Since the particles have non-zero charge, we can use magnetic fields to confine the plasma in a vacuum vessel, preventing direct contact with material walls.

1.2 Plasma confinement

Since the middle of the 20th century, several magnetic confinement configurations for fusion plasma have been explored. These include tokamaks [7], stellarators [11], reversed field pinches [12] and many other configurations [13–15]. First and foremost, it is important to mention that the confinement of a fusion plasma using magnetic fields is but one of several potential ways to achieve future commercial fusion energy production. Other potential ways include inertial confinement fusion [16], magneto-inertial fusion [17] and, possibly even, sonofusion [18]. However, this work and the methods developed herein are relevant first and foremost for tokamaks.

A tokamak is a magnetic confinement configuration for high-temperature plasmas [7]. It was originally developed in Russia in the 1950s and is short for тороидальная камера с магнитными катушками (English translation: toroidal chamber with magnetic coils). As Figure 1.2 illustrates, the plasma

confinement is a result of mainly two magnetic field components: the toroidal magnetic field \mathbf{B}_ϕ and the poloidal magnetic field \mathbf{B}_θ . The ratio of the two is usually $B_\phi/B_\theta \approx 10$. The tokamak configuration ensures that the charged particles follow the magnetic field lines, but that charged particle drifts are cancelled due to the total magnetic field being helical. An example of a tokamak is the Joint European Torus (JET) [19] in Culham, Oxfordshire, United Kingdom. This project has been heavily focused on analysis of JET.

Before thermonuclear reactions can take place, the plasma needs to be heated to many million degrees Celcius. One of the most common ways to achieve this is to first drive a current through the plasma, which results in an increase in temperature via ohmic heating [20]. However, this becomes ineffective as the temperature increases [21] and heating schemes such as neutral beam injection (NBI) and ion-cyclotron resonance heating (ICRH) often follows [7, 22] to heat the plasma up to the required temperatures. NBI constitutes neutral particles that are shot into the plasma at high energies, thus transferring their energy to the plasma [23]. ICRH uses antennas to propagate an electromagnetic wave into the plasma and achieve heating via particle resonance [24].

Depending on the tokamak, these heating schemes result in highly energetic particles with energies up into the MeV-range (~ 10 billion degrees Celcius), also known as fast ions [25]. The MeV-range is also the energy range in which fusion products are usually born [8]. These fast ions can interact with the plasma in various ways, resulting in the growth of instabilities and the loss of fast ions from the plasma, possibly damaging vessel walls and components [26, 27]. It is therefore vital to understand the behaviour of fast ions and their interaction with the plasma. One way of achieving this is by examining the fast-ion distribution function.

1.3 Fast-ion distribution function

The fast-ion (FI) distribution is essentially a function of three spatial coordinates \mathbf{x} , three velocity coordinates \mathbf{v} and time t . This means that at every point in three-dimensional space, we have a certain number of fast ions moving with a certain velocity at a certain point in time. In a tokamak, we have toroidal symmetry which means that we reduce the number of spatial coordinates from three to two. As we shall see in chapter 2, we can also reduce the number of velocity coordinates down to two if the relative variation of the magnetic field is small and slow enough. For

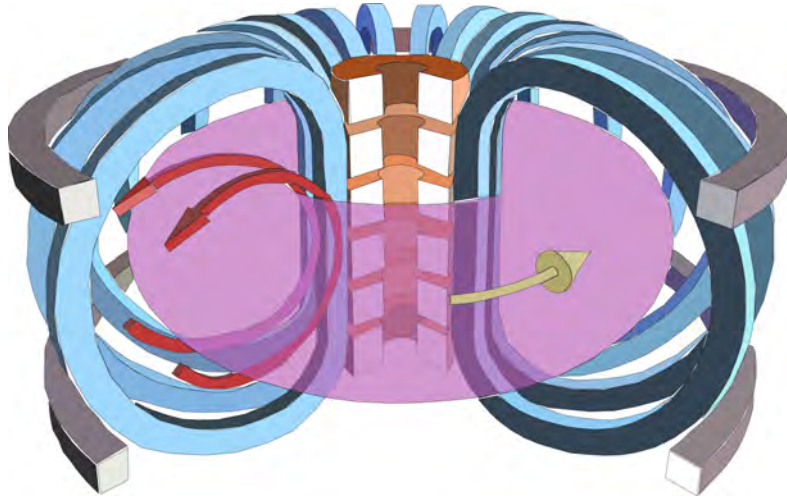


Figure 1.2: A graphical illustration of a tokamak magnetic confinement device. The toroidal and poloidal magnetic fields have been illustrated with a yellow and red arrows, respectively. The components of the central solenoid have been depicted in brown. The toroidal and vertical field coils are shown in blue and gray, respectively. The fusion plasma can be seen in indigo.

any point in time t , we can then describe the full distribution of fast ions using two spatial coordinates and two velocity coordinates. As for what coordinates to use, there are several choices available [28–31].

One common choice is to use the energy E of the fast ion, the pitch $p = v_{\parallel}/v$ (where v_{\parallel} is the speed parallel to the magnetic field and $v = \sqrt{\mathbf{v} \cdot \mathbf{v}}$), the major radius position R and the vertical position z of the fast ion. An example of a FI distribution in (E, p, R, z) coordinates has been visualized in Figure 1.3.

We can observe how the fast-ion distribution is well-peaked close to the center of the plasma, commonly referred to as the magnetic axis. One can then imagine that if we have a plasma diagnostic with a sightline that crosses the magnetic axis, it will be in a good position to detect signals originating from fast ions, such as neutrons or gamma-rays. But how can we quantify how good a diagnostic is at measuring fast ions in general, and fast ions with specific E -, p -, R - and z -values in particular? And, more importantly, how can we determine or estimate the fast-ion distribution given a (possibly noisy) signal of diagnostic measurements? To answer both questions, we introduce weight functions.

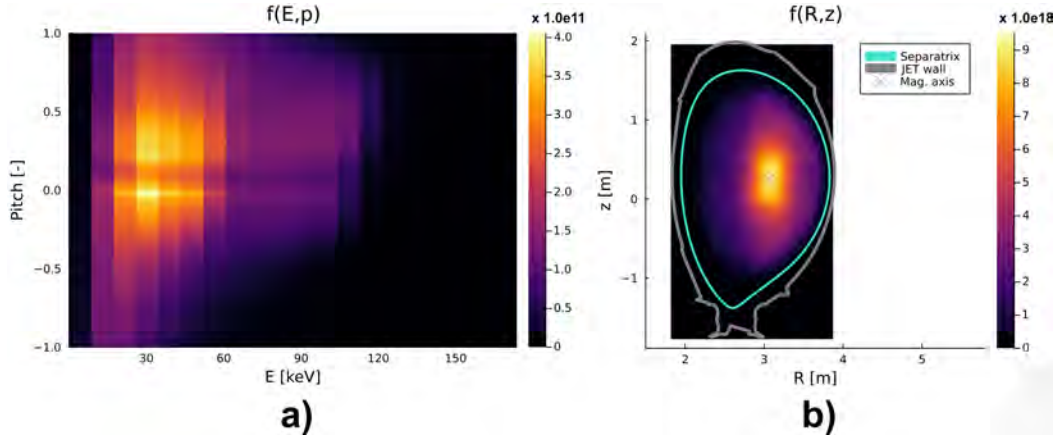


Figure 1.3: An example of a FI distribution in (E, p, R, z) coordinates. In a), the FI distribution has been integrated over all (R, z) points to illustrate its dependence on (E, p) . In b), the opposite has been performed. The separatrix (turquoise) marks the boundary between closed and open magnetic field lines. The JET wall is illustrated in gray. Fast-ion distribution data is obtained from the K71 TRANSP [32] run for JET shot No. 99965 (at 48.4 seconds), computed with the NUBEAM [33] module.

1.4 Weight functions and fast-ion tomography

As stated in H. Järleblad *et al*, Nucl. Fusion, 2022 (Paper II), and developed by M. Salewski [34–37], L. Stagner [38, 39], B. Heidbrink [40], B. Geiger [41], B. Madsen [30], A. Jacobsen [42, 43], J. Eriksson [44], M. Nocente [45] and B. Simmendefeldt [46], a diagnostic signal s can be related to the fast-ion distribution f via the weight function w as

$$s(E_{d,1}, E_{d,2}) = \int w(E_{d,1}, E_{d,2}, \mathbf{x}, \mathbf{v}) f(\mathbf{x}, \mathbf{v}) d\mathbf{x} d\mathbf{v}, \quad (1.6)$$

where $E_{d,1}$ and $E_{d,2}$ are the lower and upper boundaries of a diagnostic energy bin and (\mathbf{x}, \mathbf{v}) are general position \mathbf{x} and velocity \mathbf{v} coordinates. Equation (1.6) assumes a linear relationship between the signal s and the fast-ion distribution f . Although non-linear effects are neglected, equation (1.6) is a valid approximation in many situations, for example in so called beam-target situations where the signal originates from highly energetic NBI-ions being shot into the bulk plasma.

From equation (1.6), we can see that if $w = 0$ for some (\mathbf{x}, \mathbf{v}) then no signal will originate from (\mathbf{x}, \mathbf{v}) for that particular diagnostic energy bin $(E_{d,1}, E_{d,2})$. At the

same time, if $w \gg w_{\text{ref}}$, where w_{ref} is some reference value, then the diagnostic is relatively sensitive towards signal originating from that particular (\mathbf{x}, \mathbf{v}) phase-space point (if we also have that $f(\mathbf{x}, \mathbf{v}) \gg f_{\text{ref}}$ where f_{ref} is some reference value, we can expect a lot of diagnostic signal to originate from (\mathbf{x}, \mathbf{v})). In this way, the sensitivity for all of phase-space can be mapped, forming a weight function $w(\mathbf{x}, \mathbf{v})$ for a particular diagnostic energy bin $(E_{d,1}, E_{d,2})$.

From equation 1.6, we can see that, if we know s and w , the problem of computing f constitutes an inverse problem. This type of problem is solved in many different areas of science using tomographic inversion. It essentially involves discretizing equation 1.6 into

$$s = \sum_{i=1}^N \sum_{j=1}^M w(x_i, v_j) f(x_i, v_j) \Delta x \Delta v, \quad (1.7)$$

where $E_{d,1}, E_{d,2}$ has been omitted for brevity and, without loss of generality, we have assumed an equidistant phase-space grid. For fast ions, the full charged-particle motion in magnetic confinement devices is described using three position coordinates and three velocity coordinates (ignoring time). Does that mean that, given a measurement signal s , we have to use tomography to reconstruct the fast-ion distribution function f in six-dimensional phase space? No, fortunately there are ways to reduce the dimensionality.

Velocity-space tomography [29, 34, 36, 47–52] uses two-dimensional weight functions to reconstruct the fast-ion distribution in just energy $E = mv^2/2$ and pitch $p = v_{\parallel}/v$ (where v_{\parallel} is the ion speed parallel to the magnetic field \mathbf{B}) or equivalently in v_{\parallel} and v_{\perp} (with v_{\perp} being the ion speed perpendicular to \mathbf{B}). This is possible by restricting the tomographic reconstruction to a single point \mathbf{x} in position space and assuming we can approximate the ion motion using only two velocity coordinates (since the variation of \mathbf{B} is usually negligible on the scale of the gyro-motion, as we shall discuss in the next chapter). Velocity-space weight functions have been developed to be able to reconstruct $f(E, p)$ (equiv. $f(v_{\parallel}, v_{\perp})$) using measurements from several fast-ion diagnostics, including fast-ion D- α [35, 53], collective Thomson scattering [36, 47], gamma-ray spectroscopy [36, 37], fast-ion loss detectors [54], neutral particle analyzers [55], neutron emission spectroscopy [42, 43] and 1D weight functions for ion cyclotron emission diagnostics [46]. But what if we would like to use the very same measurements to reconstruct the fast-distribution for all points \mathbf{x} in position space? Apart from needing more data to keep the number of unknowns and the number of equations

roughly the same, we also need to relate the points in position space to each other. In a tokamak, one way to do this is by using the physics embedded in the periodic motion of the fast ions, known as orbits.

1.5 This work

In this PhD project, we have developed three-dimensional weight functions for neutron emission spectroscopy (NES) and (one-step) gamma-ray spectroscopy (GRS) using the fast-ion orbits as basis, which allows us to relate the points in position space to each other. These so-called orbit weight functions have then been used to reconstruct the fast-ion distribution from measurements in three-dimensional orbit space. This 3D distribution can then be transformed into (E, p, R, z) phase space, to investigate the fast-ion distribution in energy and pitch for all major radius and vertical positions R and z , respectively. The method of using the fast-ion orbits as a basis for weight functions and tomography was initially developed by L. Stagner [38, 39, 56].

This work builds upon that approach. Furthermore, this work has also developed novel methods of visualizing quantities in 3D orbit space, by identifying the topological regions for different orbit types and superimposing their topological boundaries onto 2D slices where the fast-ion energy has been held constant. In addition, this work has also identified new areas of application for orbit weight functions, such as the possibility of splitting a synthetic diagnostic signal into its orbit-type constituents. Finally, an extensive code library for computing, visualizing and working with orbit weight functions was developed. This toolkit will facilitate continued analysis of the fast-ion distribution in terms of orbits and pave the way for an improved understanding of how fast ions interact with tokamak fusion plasmas. This is thought to be vital for the success of next generation fusion experiments such as ITER [57], as well as for future fusion power plants.

CHAPTER 2

Fast-ion orbits

This chapter will give an overview of the periodic large-scale motion of fast ions in tokamaks, known as orbits. We will examine how the fundamental Lorentz force gives rise to particle drifts as the ion moves around the tokamak and how this six-dimensional motion can be reduced under relevant assumptions. We will then discuss how this reduced motion can be categorized and how the categories give rise to topological regions in our reduced coordinate-motion phase space, known as orbit space. Some specific discussion about how orbits are computed in this PhD project follows and then, finally, the chapter finishes with some discussion on how to transform orbit-space quantities into energy and pitch for all major radius and vertical positions.

2.1 Charged particle motion in tokamaks

The charged particle motion is always governed by the Lorentz force law. Assuming non-relativistic speeds, we have that

$$\mathbf{F} = q(\mathbf{E} + \mathbf{v} \times \mathbf{B}) \quad (2.1)$$

where \mathbf{F} is the force acting upon the particle, q is the particle charge, \mathbf{E} is the electric field, \mathbf{v} is the particle velocity and \mathbf{B} is the magnetic field. Without going into detail as to why, the Lorentz force law results in particle motion where the particle gyrates around the magnetic field lines as depicted in Figure 2.1.

In a tokamak, where we have magnetic field lines that twist around a torus, the particle tries to follow the field lines while maintaining the gyro-motion around them, as has been depicted in Figure 2.2a. Even though the full 3D trajectory might look complicated, its projection onto a poloidal cross-section (i.e a 'slice') of the tokamak is much simpler, as Figure 2.2b shows. At low energies, the particles will approximately keep to the contours of constant poloidal magnetic flux, known as *magnetic flux surfaces* since they map out surfaces in the full 3D space.

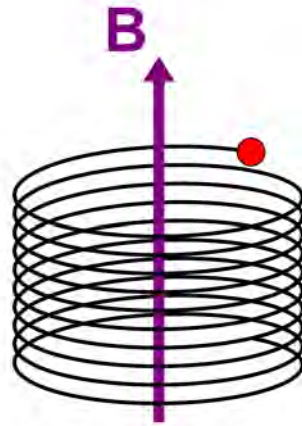


Figure 2.1: An example of a charged particle (red) that gyrates around a magnetic field line (purple) due to the equations of motion dictated by the Lorentz force, eq. (2.1).

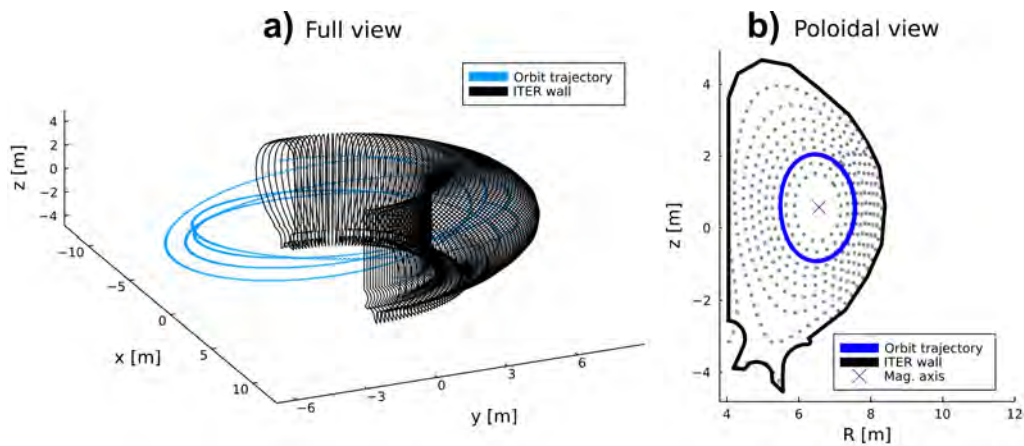


Figure 2.2: An example of a 3.5 MeV α -particle (He^4) trajectory in a future potential ITER [57] magnetic equilibrium. The full 3D trajectory a) is quite complicated while the 2D projection b) of the same trajectory onto a poloidal cross-section ('slice') of the tokamak is much simpler. The magnetic flux surfaces have been included in b) as dotted lines for reference, and the magnetic axis (plasma center) as a purple cross.

For high-energy particles, such as fast ions, the motion can start to deviate substantially from the magnetic flux surfaces lines however. This deviation is due to particle drift. In general, the particle drift can be computed as [58, 59]

$$\mathbf{v}_{\text{drift}} = \frac{1}{q} \frac{\mathbf{F} \times \mathbf{B}}{B^2} \quad (2.2)$$

where $\mathbf{v}_{\text{drift}}$ is the particle drift velocity, \mathbf{F} is a specific force (e.g. gravitational force) and $B = |\mathbf{B}|$. The specific force \mathbf{F} can be whatever force is relevant for the situation. In a tokamak, there are mainly two specific forces of interest: the centrifugal force and the force on a charged particle in a B-field with a spatial gradient. The two resulting particle drifts are

$$\mathbf{v}_R = \frac{mv_{\parallel}^2}{qB^2} \frac{\mathbf{R}_c \times \mathbf{B}}{R_c^2} \quad (2.3)$$

and

$$\mathbf{v}_{\nabla B} = -\frac{1}{2} \frac{mv_{\perp}^2}{qB} \frac{\nabla B \times \mathbf{B}}{B^2} \quad (2.4)$$

where m is the particle mass, q is the charge, v_{\parallel} is the particle speed parallel to the magnetic field, \mathbf{R}_c is the major radius vector to the particle position, $R_c = |\mathbf{R}_c|$ and v_{\perp} is the particle speed perpendicular to the magnetic field. These particle drifts will result in charged particle motion that causes the particles to drift perpendicular to the magnetic field, as Figure 2.3a shows. Depending on the particle energy, starting position (R, z) and pitch, the trajectories can differ completely, as Figure 2.3b shows.

The trajectories can differ substantially because of (2.3) and (2.4). When the energy, position and angle w.r.t. the magnetic field (pitch) changes, the resulting drifts perpendicular to the magnetic field lines change as well. In turn, the drifts add up and result in different particle trajectories.

How do we categorize all of these different trajectories? And how do we label them? This can be accomplished in several different ways, via the utilization of so-called orbit coordinates.

2.2 Orbit coordinates

The full motion of charged particles in a magnetic field can be described using a six-dimensional phase-space with three position coordinates \mathbf{x} and three velocity

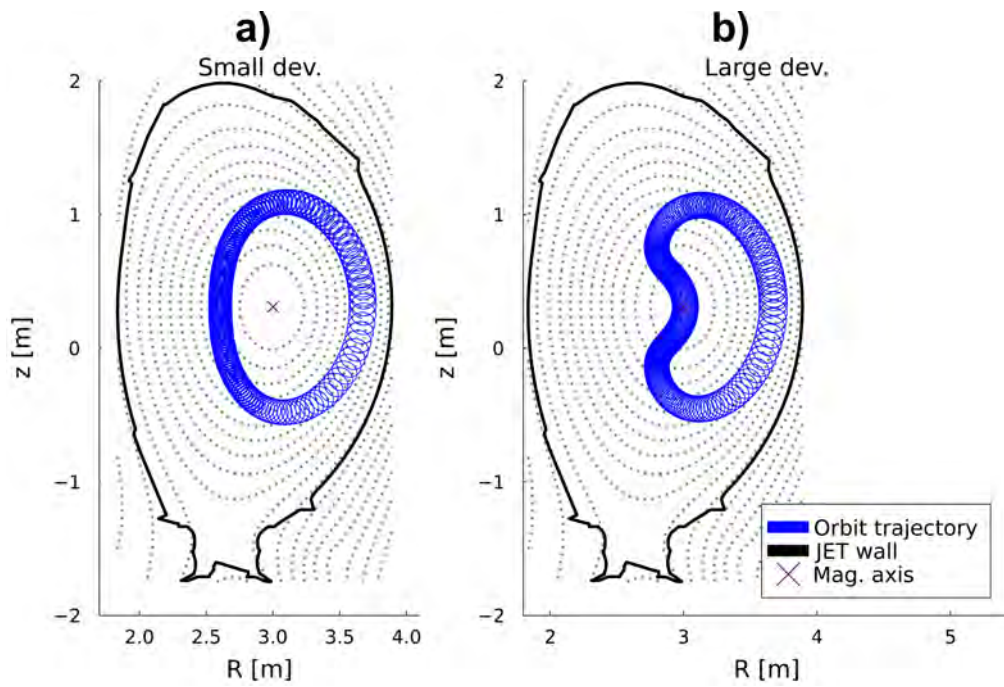


Figure 2.3: An illustration of 3.5 MeV α -particle trajectories deviating from magnetic flux surfaces. In a), the starting position (R, z) and pitch differ slightly from those in b). This results in a substantially different trajectory. The magnetic flux surfaces are depicted as dotted lines for reference, and the magnetic axis (plasma center) as a purple cross. JET shot No. 96100 at 13 s.

coordinates \mathbf{v} . As discussed in Paper I (H. Järleblad *et al*, Rev. Sci. Instrum., 2021, [1]) and Paper II (H. Järleblad *et al*, Nucl. Fusion, 2022, [2]), if we simply want to identify and label the motion, the description can be dimensionally reduced under certain assumptions. If we assume one redundant spatial dimension (such as in the toroidal symmetry of a tokamak), we can reduce the number of spatial coordinates by one. If we assume the variation of the magnetic field to be negligible on the scale of the gyro-motion of the ion (or electron) (so that the perpendicular motion is approximately a circle), then we can reduce the number of velocity coordinates by one. Finally, if we assume the ion motion to have been unperturbed as the ion revisits the same (R, z) coordinate, we can further reduce the number of spatial dimensions by one. Together, these assumptions allow us to uniquely label all charged particle motion in a tokamak using just three coordinates (one spatial, two velocity).

The two velocity and one spatial coordinates can be combined in many different ways to form sets of coordinates suitable for various needs and problems. There are thus several different triplets of coordinates to choose from. For example, the most popular set of so-called orbit coordinates are the constants-of-motion (COM)

$$(E, \mu, P_\phi; \sigma) \quad (2.5)$$

where E is the energy, $\mu = mv_\perp^2/2B$ is the magnetic moment and $P_\phi = q\psi + mv_\parallel RB_\phi/B$ is the toroidal canonical angular momentum with q being the particle charge (Coulomb) and ψ being the magnetic flux function (meter²xTesla)(also, note that v_\parallel is signed $v_\parallel \propto \mathbf{v} \cdot \mathbf{B}$). σ is a binary coordinate to keep track of certain orbits that unfortunately have the same (E, μ, P_ϕ) triplet (this differentiation could also be achieved via the usage of superficial negative energies for example). The COM space is partially bounded ($E > 0$ keV, $0 < \mu < E/B$) and mixes position- and velocity-space ($P_\phi \propto v_\parallel R$). However, it does have the advantage of being the only 'true' orbit space in the sense that E , μ and P_ϕ all correspond to a symmetry of the system of equations used to compute charged particle motion (due to a differentiable symmetry of the action, as can be understood from Noether's theorem [60]).

But what if we would like to work with a more clearly bounded set of coordinates, that do not mix position and velocity-space? One intuitive set of coordinates we could then choose to work with, would be the so-called orbit-space coordinates

$$(E, p_m, R_m) \tag{2.6}$$

as promoted by Rome [61], Järleblad [1], Stagner [38] and others [62]. E is again the energy of the fast-ion, and p_m is the pitch (v_{\parallel}/v) at the maximum major radius position R_m of the orbit. For a given fast-ion energy, p_m is bounded by $[-1.0, 1.0]$ and R_m is bounded by $[R_{\text{HFS}}, R_{\text{LFS}}]$ where R_{HFS} and R_{LFS} are the major radius position of the high-field and low-field side wall, respectively. However, most populatable orbits with $R_m < R_{\text{axis}}$ (where R_{axis} is the major radius position of the magnetic axis) satisfy $R_m \approx R_{\text{axis}}$. Therefore, in practice, $[R_{\text{axis}} - \delta R, R_{\text{LFS}}]$ are used as the R_m boundaries for (E, p_m, R_m) orbit space. $\delta R = 1/5(R_{\text{axis}} - R_{\text{HFS}})$ is usually enough to include all possible populatable orbits. Examples of every possible orbit type in a regular tokamak magnetic equilibrium can be found in Figure 2.4.

Together, the E, p_m, R_m coordinates span a three-dimensional space, henceforth referred to as orbit space, in which every point corresponds to an orbit of a specific tokamak magnetic equilibrium.

2.3 Orbit space

As Figure 2.5 shows, we can identify topological regions in orbit space by looking at slices of constant fast-ion energy. For a given slice, there are six valid orbit regions: co-passing, trapped, counter-passing, stagnation, potato and counter-stagnation. The valid orbits are orbits that can be populated, given the magnetic equilibrium. Conversely, the invalid (E, p_m, R_m) coordinates correspond to unrealizable orbits. The lost regions correspond to orbits that intersect the tokamak wall in some way. The six valid orbit types are distinguished as follows:

- **Co-passing:** A particle trajectory that encircles the magnetic axis and has $p = v_{\parallel}/v > 0$ for all points along the orbit.
- **Counter-passing:** A particle trajectory that encircles the magnetic axis and has $p < 0$ for all points along the orbit.
- **Trapped:** A particle trajectory that does not encircle the magnetic axis and changes sign of p along the orbit.
- **Potato:** A particle that encircles the magnetic axis and changes sign of p along the orbit.
- **Stagnation:** A particle trajectory that does not encircle the magnetic axis and has $p = v_{\parallel}/v > 0$ for all points along the orbit.

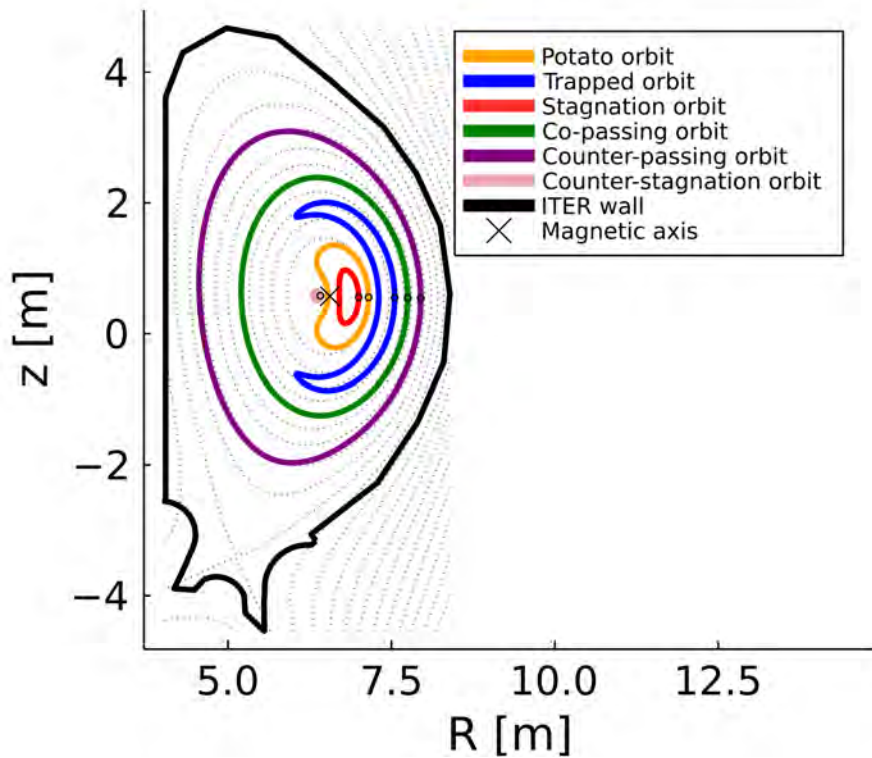


Figure 2.4: An example of all six valid fast-ion orbit types in a regular tokamak magnetic equilibrium. All orbits correspond to 3.5 MeV α -particle trajectories, but the initial pitch (v_{\parallel}/v) and (R, z) starting position have been varied, which results in different orbits. The magnetic flux surfaces are depicted as dotted lines for reference, and the magnetic axis (plasma center) as a black cross. ITER [57] planned magnetic test equilibrium with $B_0 = 5$ T. Figure is original and not reproduced from [1] and [2]; this type of figure has never been done for ITER before, and colors are kept consistent solely for pedagogical purposes.

- **Counter-stagnation:** A particle trajectory that does not encircle the magnetic axis and has $p = v_{\parallel}/v < 0$ for all points along the orbit.

In terms of lost orbits, there are usually two separate regions at low fast-ion energies. Both are located at R_m values close to the LFS tokamak wall but one is at p_m values close to 1.0 and the other at p_m values close to -1.0 . The one located at p_m values close to 1.0 corresponds to ions not having enough energy to drift past the divertor region or avoid hitting the HFS wall. This lost region thus shrinks as we examine higher and higher fast-ion energies. The lost region in the $p_m < 0.0$ half-plane corresponds to counter-passing orbits that drift into the divertor region or hit the LFS wall, due to having too much energy. This lost region thus grows as we examine higher and higher fast-ion energies.

We can see in Figure 2.5a how we have almost exclusively co-passing, trapped and counter-passing orbits at low energies. As we move to higher and higher energies (Figure 2.5b and c), the stagnation, potato and counter-stagnation regions grow to significant size. At the same time, the trapped, co-passing and counter-passing regions shrink. Thus, at progressively higher energies an increasing fraction of the populatable orbits will be stagnation, potato and counter-stagnation orbits. This is relevant for fusion-born ions as well as ions accelerated to great energies via for example ion-cyclotron resonance heating (ICRF).

2.4 Computing orbits in this work

To compute guiding-center orbits in this work, the equations discussed in [63] are used. In short, they are derived as follows. Define the order parameter $\varepsilon \equiv \rho_0/L_0 \ll 1$ where ρ_0 is the typical gyroradius and L_0 is the length scale of background fields. The particle phase-space Lagrangian one-form can then be written in terms of extended (position, momentum; time, energy) phase-space coordinates $\mathbf{z} = (\mathbf{x}, \mathbf{p}; t, W_p)$ as

$$\Gamma_p = \left[\frac{1}{\varepsilon} \frac{q}{c} \mathbf{A}(\mathbf{x}, t_1) + \mathbf{p} \right] \cdot d\mathbf{x} - W_p dt - \mathcal{H}_p d\sigma \quad (2.7)$$

where subscript 'p' denotes particle species and $\mathcal{H}_p = H_p - W_p$ is the extended particle Hamiltonian, with $H_p = \gamma mc^2 + q\Phi(\mathbf{x}, t_1)$ the Hamiltonian in regular phase space. γ is the relativistic factor $\gamma = \sqrt{1 + |\mathbf{p}/mc|^2}$, m is the particle mass, c is the speed of light, q is the particle charge, $\Phi(\mathbf{x}, t_1)$ is the electric potential, $\mathbf{A}(\mathbf{x}, t_1)$ is the magnetic vector potential, $t_1 = \varepsilon t$ and σ is an orbit parameter.

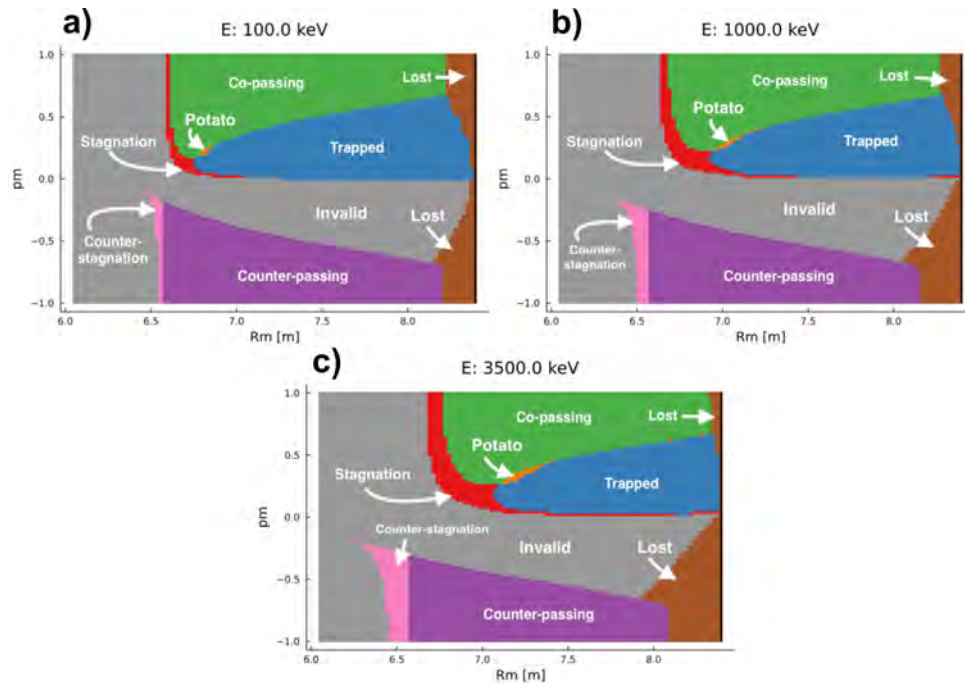


Figure 2.5: An example of orbit-space topology, split into three slices of constant fast-ion energy. The six regions corresponding to the different orbit types have been given individual colors for easy identification. The example is computed for α -particles in an ITER [57] planned magnetic test equilibrium with $B_0 = 5$ T. The major radius position of the ITER low-field side wall is depicted as a black line. Figure is original and not reproduced from [1] and [2]; this type of figure has never been done for ITER before, and colors are kept consistent solely for pedagogical purposes.

By performing a Lie transform of (2.7), we obtain the guiding-center Lagrangian in extended guiding-center phase-space coordinates $\mathbf{Z} = (\mathbf{X}, p_{\parallel}, \mu, \theta; t, W_g)$ as

$$\Gamma_g = \left[\frac{1}{\varepsilon} \frac{q}{c} \mathbf{A}(\mathbf{X}, t_1) + p_{\parallel} \hat{\mathbf{B}}(\mathbf{X}, t_1) + \mathcal{O}(\varepsilon) \right] \cdot d\mathbf{X} + \varepsilon \frac{mc}{q} \mu d\theta - W_g dt - \mathcal{H}_p d\sigma \quad (2.8)$$

where subscript 'g' denotes guiding-center variables and p_{\parallel} is the component of the relativistic momentum parallel to \mathbf{B} . $\hat{\mathbf{B}} = \mathbf{B}/|\mathbf{B}|$ with the magnetic field \mathbf{B} , $\mathcal{O}(\varepsilon)$ denotes terms of order ε , μ is the magnetic moment and $d\theta$ is the differential of the gyro angle.

For a Lagrangian \mathcal{L}_g which is related to Γ_g by $\Gamma_g \equiv \mathcal{L}_g d\sigma$, written in extended guiding-center phase-space coordinates Z^V , the Euler-Lagrange equations are

$$\frac{d}{d\sigma} \left(\frac{\partial \mathcal{L}_g}{\partial \dot{Z}^V} \right) - \frac{\partial \mathcal{L}_g}{\partial Z^V} = 0 \quad (2.9)$$

where $\dot{Z}^V = dZ/d\sigma$. Leaving out details from [63], we can apply the Euler-Lagrange equations (2.9) to the extended guiding-center phase-space coordinates $(\mathbf{X}, p_{\parallel}, \mu, \theta; t, W_g)$ to obtain the equations of motion for the system as

$$\dot{\mathbf{X}} = \frac{p_{\parallel} \mathbf{B}^*}{\gamma m B_{\parallel}^*} + \varepsilon \mathbf{E}^* \times \frac{c \hat{\mathbf{B}}}{B_{\parallel}^*} \quad (2.10)$$

$$\dot{p}_{\parallel} = q \mathbf{E}^* \cdot \frac{\mathbf{B}^*}{B_{\parallel}^*} \quad (2.11)$$

where the effective fields $(\mathbf{E}^*, \mathbf{B}^*)$ are defined as

$$\mathbf{B}^* \equiv \mathbf{B} + \varepsilon \frac{c p_{\parallel}}{q} \nabla \times \hat{\mathbf{B}} \quad (2.12)$$

and

$$\mathbf{E}^* \equiv \mathbf{E} - \frac{\varepsilon}{q} \left(p_{\parallel} \frac{\partial \hat{\mathbf{B}}}{\partial t_1} + mc^2 \nabla \gamma \right) \quad (2.13)$$

where

$$B_{\parallel}^* = \mathbf{B}^* \cdot \hat{\mathbf{B}} \quad (2.14)$$

and $\nabla\gamma = (\mu/\gamma mc^2)\nabla B$. Note also that the derived equations of motion are relativistic, which enables the methods developed in this PhD project to be used for particles with velocities close to the speed of light without loss of fidelity, e.g. for runaway electrons. Equations (2.10) and (2.11) are implemented in the guiding-center codes developed by L. Stagner [56], which have been built upon and utilized in this work. The codes are written in the scientific-computing programming language of Julia [64], which allows ultra-fast integration times of guiding-center orbits. For example, all types of guiding-center orbits in JET can be integrated in ~ 1 millisecond using Julia's adaptive integration libraries. Practically all computations in this project have been performed in the Julia programming language.

2.5 Transforming to (E, p, R, z)

The (E, p_m, R_m) orbit space is a compact three-dimensional space in which every point corresponds to a valid guiding-center fast-ion orbit. The quantities in this space, such as fast-ion distributions, can be transformed to four-dimensional (E, p, R, z) so-called particle space. This allows an examination of the energy-pitch dependence of the fast-ion distribution for every (R, z) point. However, to be able to transform from orbit space to particle space, a Jacobian (the determinant of a Jacobi matrix) is required to be able to relate the $dEdp_m dR_m$ three-dimensional volume elements to their $dEdpdRdz$ four-dimensional counterparts. A guiding-center orbit corresponds to a line in (E, p, R, z) space, and we need an additional coordinate to identify where the particle is at a given point in time, since the (E, p_m, R_m) coordinate does not contain this information. In addition, since a Jacobi matrix requires equal number of dimensions between spaces, for the sake of transformation we introduce a redundant fractional orbit transit time coordinate $\tau_m = t/\tau_p$ where $\tau_m \in [0, 1]$ and τ_p is the orbit poloidal transit time. The Jacobi matrix we seek is therefore

$$\mathcal{J}_t = \begin{bmatrix} \frac{\partial E}{\partial E} & \frac{\partial p}{\partial E} & \frac{\partial R}{\partial E} & \frac{\partial z}{\partial E} \\ \frac{\partial E}{\partial p_m} & \frac{\partial p}{\partial p_m} & \frac{\partial R}{\partial p_m} & \frac{\partial z}{\partial p_m} \\ \frac{\partial E}{\partial R_m} & \frac{\partial p}{\partial R_m} & \frac{\partial R}{\partial R_m} & \frac{\partial z}{\partial R_m} \\ \frac{\partial E}{\partial \tau_p} & \frac{\partial p}{\partial \tau_p} & \frac{\partial R}{\partial \tau_p} & \frac{\partial z}{\partial \tau_p} \end{bmatrix} \quad (2.15)$$

where the subscript t denotes that it is the Jacobi matrix for time t . Now, let's say we have discretized a fast-ion orbit into N points. Compute

$|\det \mathcal{J}_1|, |\det \mathcal{J}_2|, \dots, |\det \mathcal{J}_N|$. We will thus get a vector of length N , relating the volume of the orbit space voxel at (E, p_m, R_m) to the volume of the particle space hyper-voxels at $(E, p_1, R_1, z_1), (E, p_2, R_2, z_2), \dots, (E, p_N, R_N, z_N)$. Suitable choices of how to discretize orbit space and particle space must be made to ensure a good transform. But how do we compute the Jacobi matrix \mathcal{J}_i ? As we shall see in the following sections, this can be achieved by using dual numbers.

2.5.1 Dual numbers

Dual numbers $(a + b\epsilon)$ are just like complex numbers $(a + bi)$ but instead of the imaginary part bi we have the dual part $b\epsilon$. Like the imaginary number i has the property $i * i = -1$, the dual number ϵ has the property $\epsilon * \epsilon = 0$. This has several interesting results for functions. For example (proof can be derived using Taylor expansion) the functional value of a dual number becomes

$$f(a + b\epsilon) = f(a) + bf'(a)\epsilon \quad (2.16)$$

where $f'(a)$ is the derivative of the function $f(x)$ at $x = a$. It is important to note that $f(x)$ can be **any** function, even a function that is a whole computer program. By setting $b = 1$, one can obtain the derivative of a program at $x = a$ automatically by feeding the program the dual number

$$a + 1\epsilon \quad (2.17)$$

and simply taking the dual part of the program output, since

$$f(a + 1\epsilon) = f(a) + f'(a)\epsilon. \quad (2.18)$$

This way of obtaining functional/program derivatives is called *automatic differentiation* and is a whole field of computational techniques in itself. For the interested reader, please see e.g. [65].

2.5.2 Computing \mathcal{J}

Assume that we have computed our guiding-center orbit and resolved the trajectory in four-dimensional (E, p, R, z) -space using N points. Our goal is to acquire a vector of length N where each element is the determinant of the Jacobi matrix (the Jacobian) from the (E_i, p_i, R_i, z_i) quadruplet at time t_i to the (E, p_m, R_m) triplet of the orbit. $i = 1, 2, \dots, N$.

To compute Jacobians and the gradients of multi-variate functions, one simply uses vectors for the dual part instead of a scalar. The vectors should be thought of as orthogonal ε components. By making the vectors orthogonal, and associating one vector with a particular variable, one isolates the derivatives from that particular variable. First, we write

$$\mathbf{x}_i = \begin{bmatrix} E_i \\ p_i \\ R_i \\ z_i \\ dt_i \end{bmatrix} \quad (2.19)$$

where dt_i is the incremental time between \mathbf{x}_i and \mathbf{x}_{i+1} . Let's start by examining how to compute the Jacobian for (E_1, p_1, R_1, z_1) . That is, the first of our N orbit points. As we shall see, we will need an initial starting vector \mathbf{x}_0 , defined as

$$\mathbf{x}_0 = \begin{bmatrix} E_1 \\ p_1 \\ R_1 \\ z_1 \\ 10^{-30} \end{bmatrix} = \begin{bmatrix} E \\ p_m \\ R_m \\ z_1 \\ 10^{-30} \end{bmatrix} \quad (2.20)$$

where the reason for the 10^{-30} element will become clear in a moment. The energy E is constant, so we can ignore the subscript i for E . The first point $i = 1$ on the orbit is assumed to correspond to the (E, p_m, R_m) -triplet with added z -coordinate. Now, convert \mathbf{x}_0 to its dual counterpart $\mathbf{x}_{0,\varepsilon}$ by adding dual components as

$$\mathbf{x}_{0,\varepsilon} = \begin{bmatrix} E + \varepsilon_{E,0} \\ p_m + \varepsilon_{p_m,0} \\ R_m + \varepsilon_{R_m,0} \\ z_1 + \varepsilon_{z,0} \\ 10^{-30} + \varepsilon_{\tau_p,0} \end{bmatrix} \quad (2.21)$$

where $\varepsilon_{E,0}$, $\varepsilon_{p_m,0}$, $\varepsilon_{R_m,0}$, $\varepsilon_{\tau_p,0}$ are

$$\begin{bmatrix} 1.0 \\ 0.0 \\ 0.0 \\ 0.0 \end{bmatrix} \boldsymbol{\varepsilon} = \boldsymbol{\varepsilon}_{E,0} \quad \begin{bmatrix} 0.0 \\ 1.0 \\ 0.0 \\ 0.0 \end{bmatrix} \boldsymbol{\varepsilon} = \boldsymbol{\varepsilon}_{p_m,0} \quad \begin{bmatrix} 0.0 \\ 0.0 \\ 1.0 \\ 0.0 \end{bmatrix} \boldsymbol{\varepsilon} = \boldsymbol{\varepsilon}_{R_m,0} \quad \begin{bmatrix} 0.0 \\ 0.0 \\ 0.0 \\ 1.0 \end{bmatrix} \boldsymbol{\varepsilon} = \boldsymbol{\varepsilon}_{\tau_p,0} \quad (2.22)$$

and with $\boldsymbol{\varepsilon}_{z,0}$ as

$$\begin{bmatrix} 0.0 \\ 0.0 \\ 0.0 \\ 0.0 \end{bmatrix} \boldsymbol{\varepsilon} = \boldsymbol{\varepsilon}_{z,0}. \quad (2.23)$$

The subscripts '0' denote that it is a special case before the first of the N points. The dual vector components of $\boldsymbol{\varepsilon}_{z,0}$ are identically zero because z is not one of the derivatives of interest for our Jacobian (2.15). Now, let f be the function that takes one (E, p, R, z) -point along the orbit and computes the next one. That is, $f(\mathbf{x}_i) = \mathbf{x}_{i+1}$. Analogous to [65], we can thus write

$$f(\mathbf{x}_{0,\boldsymbol{\varepsilon}}) = f(\mathbf{x}_0) + \frac{\partial f(\mathbf{x}_0)}{\partial E} \boldsymbol{\varepsilon}_{E,0} + \frac{\partial f(\mathbf{x}_0)}{\partial p_m} \boldsymbol{\varepsilon}_{p_m,0} + \frac{\partial f(\mathbf{x}_0)}{\partial R_m} \boldsymbol{\varepsilon}_{R_m,0} + \frac{\partial f(\mathbf{x}_0)}{\partial \tau_p} \boldsymbol{\varepsilon}_{\tau_p,0} \quad (2.24)$$

where we have omitted the $\boldsymbol{\varepsilon}_{z,0}$ part because all of its components are identically zero. The reason why we get derivatives taken with respect to E , p_m and R_m is because we have arranged so that the first orbit point $i = 1$ corresponds to the quantities of interest, namely $E_1 = E$, $p_1 = p_m$ and $R_1 = R_m$. We get a derivative taken with respect to τ_p because we used the fourth orthogonal (non-zero) $\boldsymbol{\varepsilon}$ -vector for the time step dt ¹.

For the sake of example, let's examine how we acquire the derivatives in the last column of the Jacobi matrix 2.15 for $i = 1$. Let $[f]_z$ denote the subprocess of computing the next z -coordinate along our orbit, given one (E, p, R, z) -point. That is, $[f(\mathbf{x}_i)]_z = z_{i+1}$. We can then write

¹Strictly speaking, we should write $d\tau_p$ instead of dt because it's a small fraction of the poloidal transit time.

$$[f(\mathbf{x}_{0,\varepsilon})]_z = [f(\mathbf{x}_0)]_z + \left[\frac{\partial f(\mathbf{x}_0)}{\partial E} \varepsilon_{E,0} \right]_z + \left[\frac{\partial f(\mathbf{x}_0)}{\partial p_m} \varepsilon_{p_m,0} \right]_z + \left[\frac{\partial f(\mathbf{x}_0)}{\partial R_m} \varepsilon_{R_m,0} \right]_z + \left[\frac{\partial f(\mathbf{x}_0)}{\partial \tau_p} \varepsilon_{\tau_p,0} \right]_z \quad (2.25)$$

$$\approx z_1 + \frac{\partial z_1}{\partial E} \varepsilon_{E,0} + \frac{\partial z_1}{\partial p_m} \varepsilon_{p_m,0} + \frac{\partial z_1}{\partial R_m} \varepsilon_{R_m,0} + \frac{\partial z_1}{\partial \tau_p} \varepsilon_{\tau_p,0}. \quad (2.26)$$

The subprocesses for E, p and R are analogous. Now, since \mathbf{x}_0 is a special case and contains (E_1, p_1, R_1, z_1) , equation 2.26 only works for \mathbf{x}_0 because $dt = 10^{-30}$ (hence the \approx symbol in the second row of (2.26)). Using the method in (2.26), we can acquire the Jacobi matrix \mathcal{J}_1 for the first point (E, p_1, R_1, z_1) of our orbit by **examining all the different subprocesses, extracting the dual parts and putting together the elements in the correct structure**. We write compactly

$$\boxed{f(\mathbf{x}_{0,\varepsilon}) \Rightarrow \mathcal{J}_1 \Rightarrow |\det \mathcal{J}_1|} \quad (2.27)$$

There is yet one obstacle to overcome however. Or rather $N - 1$ obstacles. As stated in the beginning of this section *Our goal is to acquire a vector of length N where each element is the determinant of the Jacobi matrix from the (E_i, p_i, R_i, z_i) quadruplet at time t_i to the (E, p_m, R_m) triplet of the orbit. $i = 1, 2, \dots, N$. So far, we have only acquired the very first element. How do we acquire the Jacobian for the second point on our orbit? And the third? And so on.*

To solve all the obstacles at the same time, we can use the multi-variate chain rule. It states that

$$\mathcal{J}_{f \circ g}(\mathbf{x}) = \mathcal{J}_f(g(\mathbf{x})) \mathcal{J}_g(\mathbf{x}). \quad (2.28)$$

Namely, the Jacobi matrix for a composite multi-variable function is the product of the Jacobi matrix of the outer function and the Jacobi matrix of the inner function. We can utilise this in our quest for the orbit Jacobians. As an example, for the second point on our orbit, we get

$$\mathcal{J}_2 = \mathcal{J}(f(\mathbf{x}_1)) \mathcal{J}_1 \quad (2.29)$$

where \mathcal{J} is the Jacobi matrix obtained by repeating the same process as we did for our first orbit point, but using an actual time step instead of 10^{-30} for dt . And \mathcal{J}_1 is the Jacobi matrix we have already computed. In terms of concretely working with dual numbers, we achieve (2.29) by setting

$$\frac{\partial f(\mathbf{x}_{i-1}, \varepsilon)}{\partial E_{i-1}} \varepsilon = \varepsilon_{E,i} \quad \frac{\partial f(\mathbf{x}_{i-1}, \varepsilon)}{\partial p_{m,i-1}} \varepsilon = \varepsilon_{p_m,i} \quad \frac{\partial f(\mathbf{x}_{i-1}, \varepsilon)}{\partial R_{m,i-1}} \varepsilon = \varepsilon_{R_m,i} \quad \frac{\partial f(\mathbf{x}_{i-1}, \varepsilon)}{\partial \tau_{p,i-1}} \varepsilon = \varepsilon_{\tau_p,i} \quad (2.30)$$

and

$$\frac{\partial f(\mathbf{x}_{i-1}, \varepsilon)}{\partial z_{i-1}} \varepsilon = \varepsilon_{z,i} \quad (2.31)$$

with the special case of $\varepsilon_{E,0}, \varepsilon_{p_m,0}, \varepsilon_{R_m,0}, \varepsilon_{\tau_p,0}$ and $\varepsilon_{z,0}$ having been addressed above. In short, we compute the Jacobians for all N orbit points as summarized below.

$$\boxed{f(\mathbf{x}_{i-1}, \varepsilon) \Rightarrow \mathcal{J}_t \Rightarrow |\det \mathcal{J}_t|} \quad (2.32)$$

with f being the process of taking one (E, p, R, z) point and computing the next one along the orbit, given a time-step.

2.5.3 Transforming using orbit covariance

Using the determinants of the Jacobi matrices for our N orbit points from section 2.5.2, we can now transform quantities such as fast-ion distributions from (E, p_m, R_m) -space to (E, p, R, z) -space. One way of achieving this, is by first computing the covariance between fast-ion orbits of interest. As was first formulated by L. Stagner [39], the orbit covariance K between an orbit with coordinate $\mathbf{o}_i = (E_i, p_{m,i}, R_{m,i})$ and another orbit with coordinate $\mathbf{o}_j = (E_j, p_{m,j}, R_{m,j})$ can be written as

$$K(\mathbf{o}_i, \mathbf{o}_j) = \int_0^1 \int_0^1 C(\mathbf{x}_i(\mathbf{o}_i, \tau_i), \mathbf{x}_j(\mathbf{o}_j, \tau_j)) \mathcal{J}(\mathbf{o}_i, \tau_i) \mathcal{J}(\mathbf{o}_j, \tau_j) d\tau_i d\tau_j \quad (2.33)$$

where $\tau_i, \tau_j \in [0, 1)$ are the normalized poloidal transit times for the orbits, and $\mathbf{x}_i, \mathbf{x}_j$ are the (E, p, R, z) -coordinates of $\mathbf{o}_i, \mathbf{o}_j$ at τ_i, τ_j , respectively. C is the inner

covariance function that reflects the smoothing effect of collisions and can be expressed using the standard Gaussian process squared exponential covariance function

$$C(\mathbf{x}_i, \mathbf{x}_j) = \exp\left(-\frac{1}{2}(\mathbf{x}_i - \mathbf{x}_j)^T \Sigma_\sigma^{-1}(\mathbf{x}_i - \mathbf{x}_j)\right) \quad (2.34)$$

where Σ_σ is a diagonal matrix containing correlation lengths for each dimension. Now, let \mathbf{K} denote the $N \times M$ covariance matrix where every element $K_{i,j}$ is a case of 2.33, with $i = 1, \dots, N$ and $j = 1, \dots, M$. Without loss of generality, let our (E, p_m, R_m) -space be spanned by a grid containing M number of valid orbits. Then, for every (R, z) -point of interest, let our (E, p) -space be spanned by a grid containing a total of N points. We can then write the transformation from (E, p_m, R_m) to (E, p, R, z) as

$$f(E, p) = (1/|\det \mathcal{J}(\mathbf{o}_i, 0)|) \circ \mathbf{K} \Sigma_{ff}^{-1} f(E, p_m, R_m) \text{ for } \forall (R, z) \text{ of interest} \quad (2.35)$$

where $\mathcal{J}(\mathbf{o}_i, 0)$ is a case of (2.15) at $\tau_p = 0$ s, computed using (2.27). Σ_{ff} is a special case of \mathbf{K} where $N = M$ and the orbits are the valid orbits of our (E, p_m, R_m) -grid. $f(E, p_m, R_m)$ is a vector of length M in which every element corresponds to the fast-ion distribution of a valid orbit. $1/|\det \mathcal{J}(\mathbf{o}_i, 0)|$ will be of size $N \times 1$ and $\mathbf{K} \Sigma_{ff}^{-1} f(E, p_m, R_m)$ will also be of size $N \times 1$. They are then multiplied element-wise, hence the ' \circ ' symbol in (2.35). $f(E, p)$ will then be a vector of size $N \times 1$ that is reshaped to our (E, p) -grid. Naturally, if some of the M orbits of the (E, p) gridpoints at (R, z) correspond to lost orbits, they will need to be filtered out from the transformation, as well as orbits for which $|\det \mathcal{J}(\mathbf{o}_i, 0)| = 0$. This can be achieved by setting $f(E, p) = 0$ for those (E, p) gridpoints.

2.5.4 Transforming using grid-mapping

An arguably more straightforward approach to transform fast-ion distributions from (E, p_m, R_m) -space to (E, p, R, z) -space, and back, is the grid-mapping transform developed by S. Benjamin [66]. It is based on the simple relations

$$f(E, p, R, z) = f(E, p_m, R_m, \tau_p) \left| \frac{dE dp_m dR_m d\tau_p}{dE dp dR dz} \right| \quad (2.36)$$

and

$$f(E, p_m, R_m, \tau_p) = f(E, p, R, z) \left| \frac{dEdpdRdz}{dEdp_m dR_m d\tau_p} \right| \quad (2.37)$$

where the fast-ion distribution in orbit space has been extended with the redundant poloidal transit time τ_p . The two Jacobians in (2.36) and (2.37) are reciprocals of one another if the transform from (E, p_m, R_m, τ_p) to (E, p, R, z) is a diffeomorphism, i.e. a differentiable bijection, where the inverse transform is also differentiable. This implies that the function that maps an (E, p, R, z) coordinate to its (E, p_m, R_m, τ_p) coordinate, and the inverse of the function, should be well-behaved. Because our guiding-center equations of motion (section 2.4) are well-behaved, we can conclude that it is indeed the case. The Jacobi matrix determinants of the forwards and reverse transform are therefore reciprocals of one another.

Using automatic differentiation built on the algebraic properties of dual numbers, we can however easily compute the necessary Jacobians in (2.36) and (2.37). As discussed in section 2.5.2, this is done by converting the inputs of

$$f(E, p, R, z) \rightarrow (E, p_m, R_m) \quad (2.38)$$

and

$$g(E, p_m, R_m) \rightarrow \{E, p, R, z\} \quad (2.39)$$

where f is the computational process of determining the orbit coordinate (E, p_m, R_m) given the guiding-center coordinate (E, p, R, z) , and g is the computational process of determining the set of all guiding-center coordinates $\{E, p, R, z\}$ given the orbit coordinate (E, p_m, R_m) . The choice governing a successful transform, is then the choice of temporal (τ_p) and grid-related resolutions (in (E, p_m, R_m) and (E, p, R, z)).

CHAPTER 3

Fast-ion Diagnostics

To be able to reconstruct the fast-ion distribution, experimental measurements from so-called fast-ion diagnostics are needed. Even though the fast-ion distribution cannot be measured directly, we can use measurements of e.g. neutrons, gamma-rays, fast-ion D-alpha light, ion cyclotron emissions and fast-ion losses to reconstruct the most-likely distribution given the often noisy data [67].

Fast-ion diagnostics can be divided into *active* and *passive* systems. Active systems obtain information about the fast-ion distribution by perturbing the plasma somehow. For example via injection of radiation or neutrals into the plasma. This is the process of e.g. collective Thomson scattering (CTS, [68]) and fast-ion D-alpha (FIDA, [69]) diagnostics. Passive systems acquire information by simply measuring relevant quantities emitted from the fusion plasma during plasma operation. Examples include neutron emission spectroscopy (NES, [70]) and gamma-ray spectroscopy (GRS, [71]).

In this project, the diagnostics of interest have been exclusively passive diagnostics; more specifically NES and GRS. In this chapter, we will therefore provide a short discussion on the specific fast-ion diagnostics that have been investigated.

3.1 TOFOR

TOFOR is a time-of-flight (TOF) spectrometer optimized for high rates (TOFOR) and measurements of 2.5 MeV neutron emission from fusion plasmas. [72] It was built and tested at Uppsala University, and transported as well as put into use at JET in 2008. TOFOR improved the count rate capability for NES diagnostics of D plasmas by more than an order of magnitude. The method is based on the measurements of neutrons in two detector parts, S1 and S2, as can be viewed in Figure 3.1. S1 measures the 'start' time for the neutron that enters TOFOR. S2 then measures the 'stop' time. Since the distance between S1 and S2 ($L = 1221$

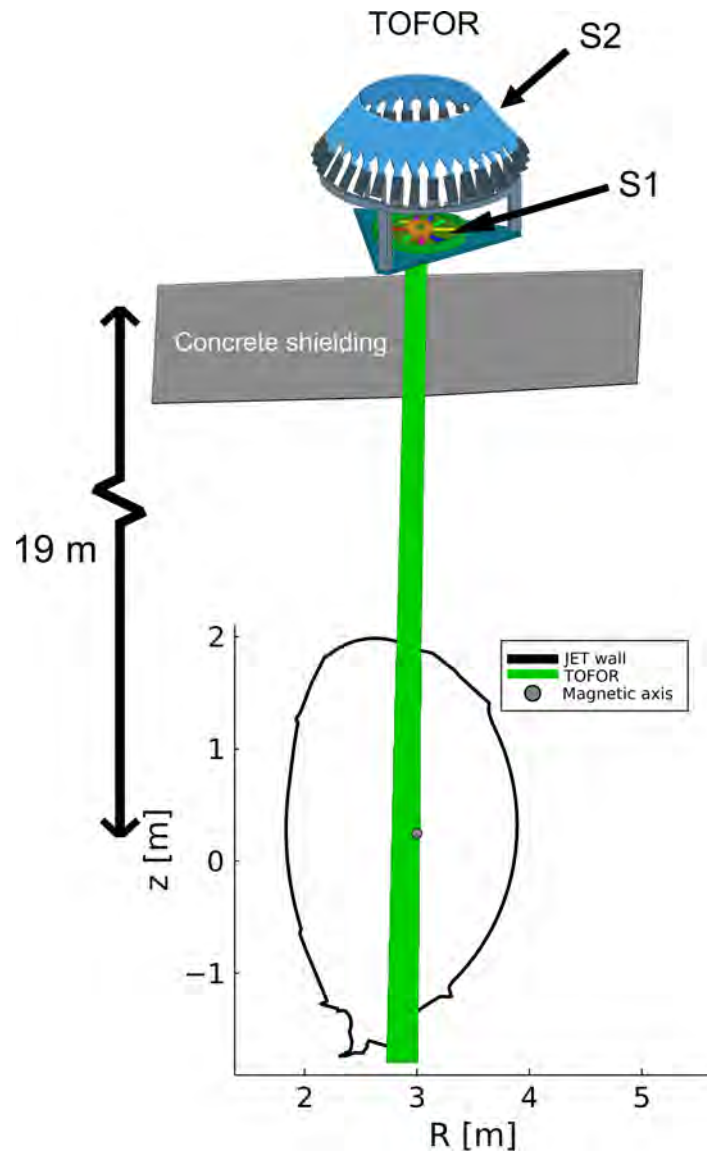


Figure 3.1: The TOFOR diagnostic is a neutron time-of-flight diagnostic with a detector installed approximately 19 meters above the (usual) magnetic axis of JET discharges. The sightline is (almost) completely vertical. The neutrons are first detected by the S1 plastic scintillator, marking the 'start time' of the time-of-flight measurement. They are then scattered onto a S2 plastic scintillator, marking the 'stop time' of the time-of-flight measurement. A measure of the neutron energy can then be computed from the time difference.

mm) is known, the velocity, and thus energy, of the neutron can be deduced. 2.5 MeV ($\approx 2 \times 10^7$ m/s) neutrons will have a TOF of $t_{\text{TOF}} \approx 65$ ns, for example. Both S1 and S2 are plastic scintillators and detect neutrons via proton recoil.

The line-of-sight (LOS) of TOFOR has been illustrated in Figure 3.1. As can be observed, the LOS is in practice completely vertical, i.e. perpendicular with respect to the magnetic field. For tomographic purposes, this means that the data from TOFOR can be used to obtain well-resolved information about the energy distribution of fast ions, but not as much information about the pitch (v_{\parallel}/v) distribution. Since, for a completely perpendicular LOS a positive pitch is indistinguishable from a negative pitch. This will be discussed further in Chapter 6.

3.2 NE213-scintillator

The NE213 diagnostic [73, 74] used in this work is a liquid scintillator NES diagnostic consisting of an active cylindrical cell of about 1 cm^3 connected to a Photomultiplier Tube, which is covered with a thin layer of mu-metal for magnetic shielding.

The LOS of the NE213-scintillator has been illustrated in Figure 3.2. As can be observed, it has an oblique LOS w.r.t. the magnetic field. This is advantageous for phase-space tomography, since positive pitches can be easily distinguished from negative pitches. If a fast ion travels towards the detector and partakes in a DD fusion reaction, it will produce a neutron with a slightly upshifted birth energy, compared to the nominal case. Similarly, fast ions travelling away from the detector will produce neutrons with a downshifted birth energy.

3.3 GRS diagnostics

The LOS of TOFOR, Figure 3.1, is shared with several GRS diagnostics. In H. Järleblad *et al*, Nucl. Fusion, 2022 (Paper II), results relevant for a lanthanum bromide (Brilliance) detector [76] sharing this LOS were presented. It uses a $\text{LaBr}_3(\text{Ce})$ crystal as scintillating material to detect γ -rays. It allows operation at event rates of up to 2 MHz and it is insensitive to neutrons. The $\text{LaBr}_3(\text{Ce})$ crystal is coupled to a Photomultiplier Tube, which produces a signal that is fed into a fast preamplifier with five times gain before being digitized.

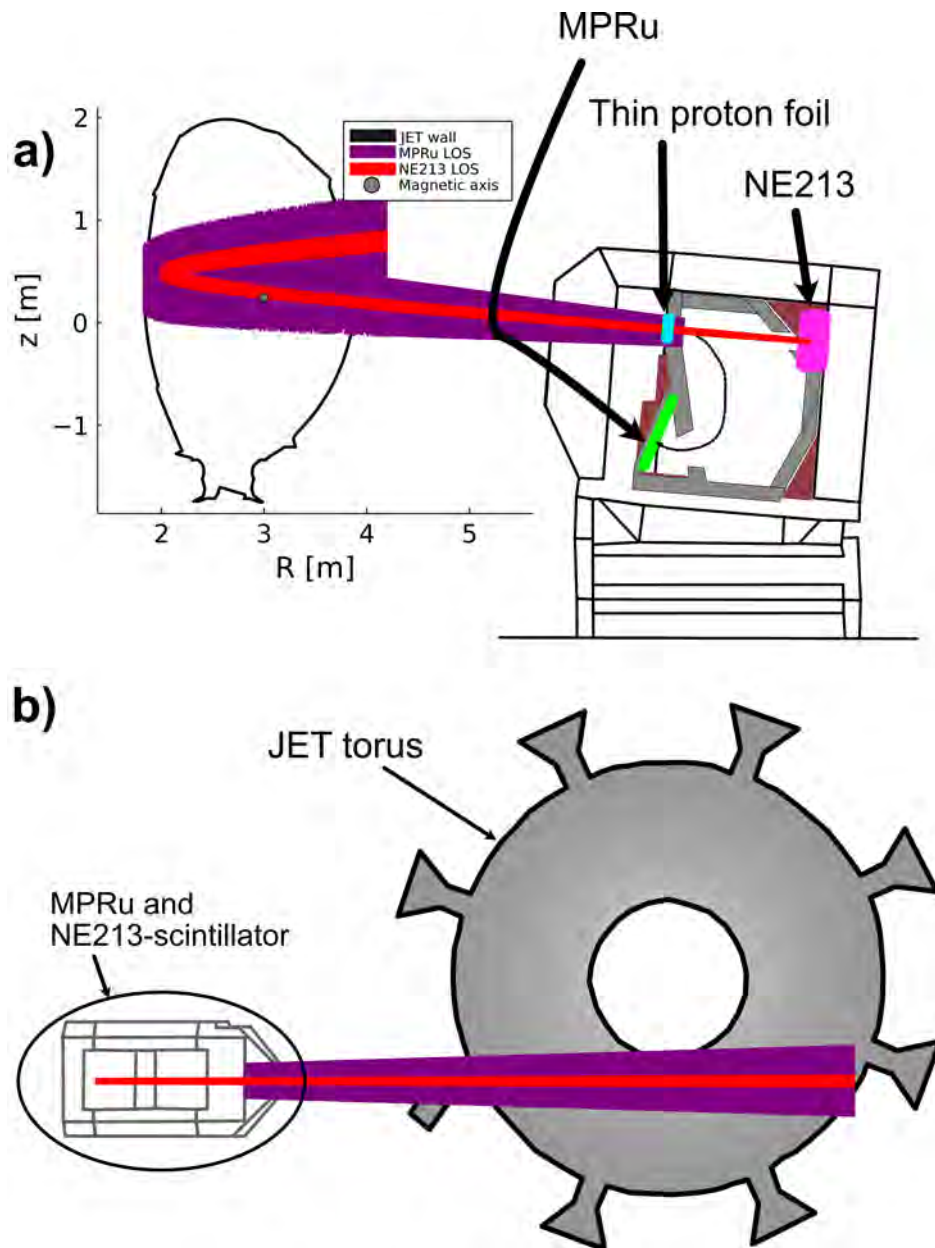


Figure 3.2: a) A poloidal and b) top-view of the NE213 [73, 74] and MPRu [75] diagnostics at JET. The neutrons hit a thin foil (turquoise) and knock off protons that travel in the magnetic field of the MPRu, and hit the detector (green). Some neutrons will pass through the thin foil and instead reach the NE213 detector. The NE213 and MPRu detectors observe JET plasma in the counter-clockwise direction, viewed from above.

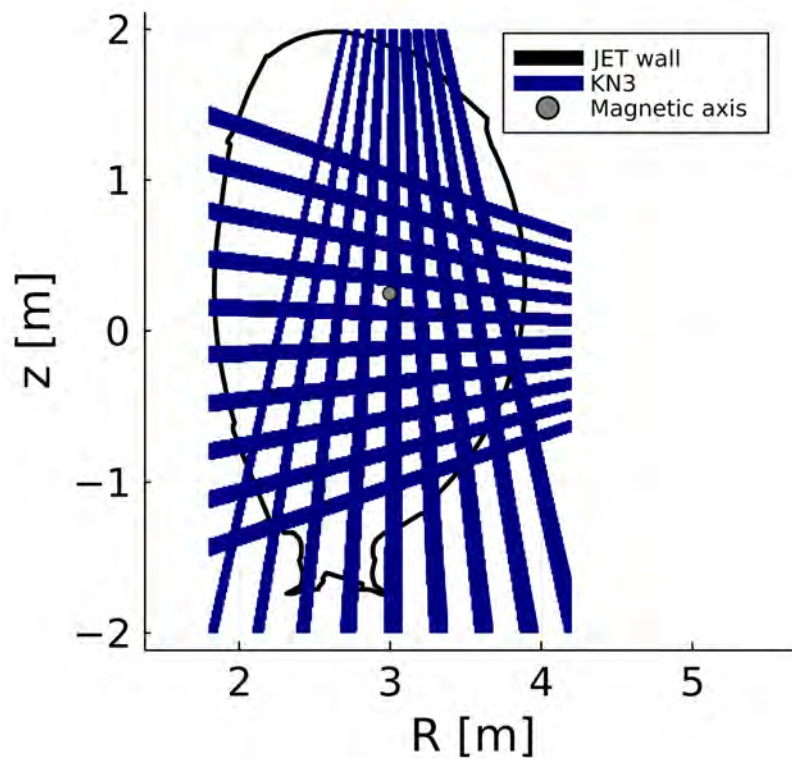


Figure 3.3: The KN3 [77] neutron camera system is comprised of 9 vertical and 10 horizontal LOS. They all face the plasma at an angle almost completely perpendicular to the magnetic field. The magnetic axis of JET shot 96100 has been superimposed for reference.

3.4 KN3 Neutron Camera System

As Figure 3.3 shows, the KN3 neutron camera system is comprised of two different sets of detectors implemented along 10 horizontal LOS and 9 vertical LOS [77]. Depending on the neutron energy of interest, different diagnostics are employed. For the measurement of 2.45 MeV DD neutrons, NE213 liquid scintillators are used while for 14 MeV DT neutrons thin plastic scintillation detectors are usually used. The KN3 has a digital acquisition system capable of operating at 0.2×10^9 samples/s with a sample size of 14 bits. In addition, the KN3 system is sensitive to both neutron (n) and gamma (γ) radiation which produce signals of different pulse shapes. The Short/Long gate method [78] combined with tomographic methods are used to separate the two spectra.

3.5 MPRu

The upgraded magnetic proton recoil (MPRu) diagnostic at JET is a thin-foil spectrometer with an oblique LOS [79]. The sightline is identical to that of the NE213-scintillator discussed in section 3.2, but with a less collimated LOS, as can be observed in Figure 3.2. In contrast to scintillators and time-of-flight (and semiconductor) detectors, the MPRu measures the energy of incoming neutrons via the recoil of protons scattered from a thin foil. A schematic overview of the MPRu is shown in Figure 3.4.

Neutrons from the plasma pass through a neutron collimator, forming a neutron beam into the detector. The neutron beam then intersects a thin polythene ($\text{CH}_2\dots$) foil target, where some neutrons scatter elastically on the protons of the foil. The forward scattered protons are then selected and enter a magnetic system, where they are spatially separated according to their momentum. The position of the proton impact is then detected via an array of scintillators, and the original neutron energy can then be deduced. For 14 MeV DT-born neutrons, the MPRu has a signal count rate of 0.61 MHz with a signal-to-background noise (S/B) ratio of 2×10^3 . The S/B for 2.5 MeV DD-neutrons is 10^{-1} , thus making the MPRu suitable for detecting DT-born, but not DD-born, neutrons.

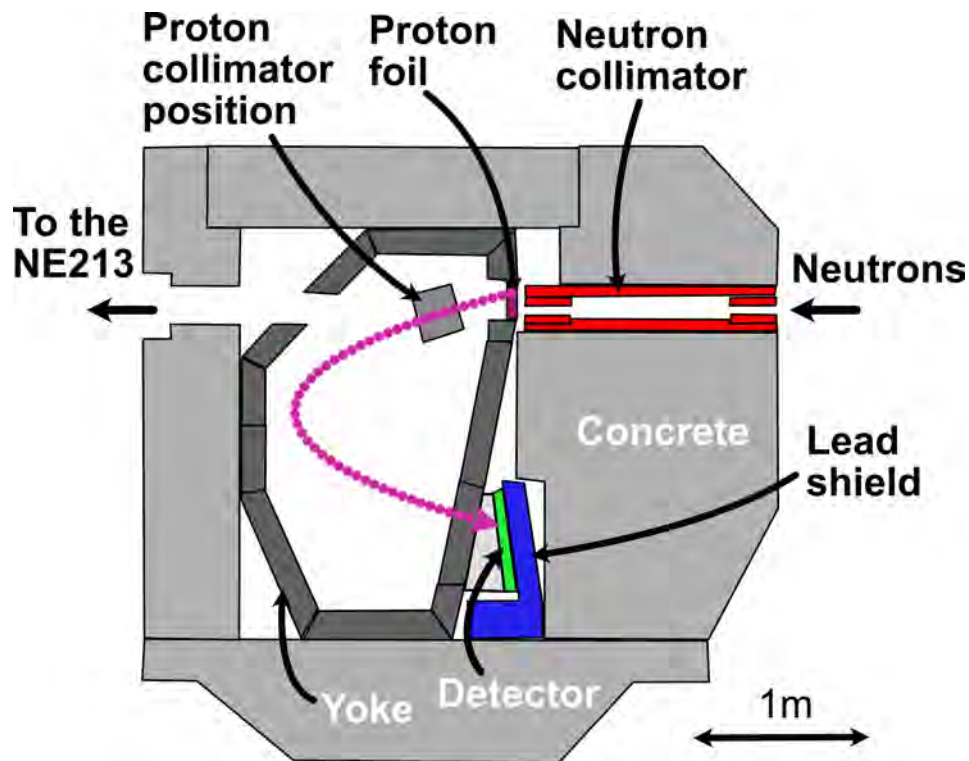


Figure 3.4: A schematic drawing of the MPRu [75] diagnostic at JET. A neutron enters a collimator and might elastically knock off a proton from the thin foil. If it doesn't, it continues to the NE213 [73, 74] diagnostic. The proton travels through a collimator, and in a curved trajectory (pink) as a result of the internal magnetic field of the MPRu. The measurement of the impact position of the proton on a detector can then be used to determine the original energy of the incoming neutron.

CHAPTER 4

Orbit sensitivity of fast-ion diagnostics

Fast-ion diagnostics possess a varying probability to detect measurements depending on the fast-ion orbit origin of interest. This varying probability is called the *orbit sensitivity* and it can be quantified and mapped using orbit weight functions. As discussed in H. Järleblad *et al.*, Nucl. Fusion, 2022 (Paper II, [2]), the diagnostic signal s and the fast-ion distribution f can be related via a weight function w as

$$s(E_{1,d}, E_{2,d}) = \int w(E_{1,d}, E_{2,d}, \mathbf{x}, \mathbf{v}) f(\mathbf{x}, \mathbf{v}) d\mathbf{x}d\mathbf{v}, \quad (4.1)$$

where $E_{1,d}$ and $E_{2,d}$ denote the lower and upper boundaries of the diagnostic measurement bin of interest, respectively. \mathbf{x} and \mathbf{v} denote the position and velocity of the ion. The time dependence of the full six-dimensional fast-ion distribution $f(\mathbf{x}, \mathbf{v})$ is outside the scope of this work. We can re-write (4.1) for our (E, p_m, R_m) orbit-space of interest as

$$s(E_{1,d}, E_{2,d}) = \int w(E_{1,d}, E_{2,d}, E, p_m, R_m) f(E, p_m, R_m) dE dp_m dR_m, \quad (4.2)$$

where we have assumed toroidal symmetry, a guiding-centre picture and unperturbed fast-ion orbits as discussed in section 2.2. We can observe in equation 4.2 how a linear relationship between s and f is assumed. This assumption is valid as long as the signal contribution from fast ions (fi) reacting with the bulk plasma is much greater than other contributions. That is

$$s_{fi,bulk} \gg s_{fi,fi} \quad (4.3)$$

where $s_{A,B}$ is the signal from the reaction between A and B . By utilizing 4.2 for

many different diagnostic energy bins $(E_{1,d}, E_{2,d})$ and discretizing our problem in (E, p_m, R_m) orbit-space, we can write the matrix equation

$$S = WF \quad (4.4)$$

where S is a vector with length equal to the number of diagnostic measurement bins of interest. W is the so-called *weight matrix* with number of rows equal to the length of S and number of columns equal to the number of valid orbits for our discretized (E, p_m, R_m) -space of interest. F is the fast-ion distribution for our (E, p_m, R_m) orbit-space of interest but in vectorized format.

As discussed in H. Järleblad *et al.*, Rev. Sci. Instrum., 2021 (Paper I) and H. Järleblad *et al.*, Nucl. Fusion, 2022 (Paper II), orbit weight functions can be computed as follows:

1. Compute all (E, p, R, z) points for an orbit with a particular (E, p_m, R_m) coordinate, given a resolution in time or space.
2. Weight each (E, p, R, z) point by the fraction of the poloidal transit time τ_p the ion spends between that point and the next.
3. Let all weighted (E, p, R, z) points constitute a fast-ion distribution f and feed it into the code of your synthetic diagnostic of interest.
4. Let the 1D output signal of the forward model be a unique column in a matrix.
5. Repeat 1-4 for all (E, p_m, R_m) coordinates of interest.
6. The rows of your matrix now constitute orbit weight functions for that specific diagnostic measurement bin.

Mathematically, this can be expressed by setting $f(E, p_m, R_m) = \delta(E - E_i)\delta(p_m - p_{m,j})\delta(R_m - R_{m,k})$ in equation 4.2 as

$$\begin{aligned} s(E_{1,d}, E_{2,d}) &= \int w(E_{1,d}, E_{2,d}, E, p_m, R_m) \delta(E - E_i) \delta(p_m - p_{m,j}) \delta(R_m - R_{m,k}) dE dp_m dR_m \\ &= w(E_{1,d}, E_{2,d}, E_i, p_{m,j}, R_{m,k}), \end{aligned} \quad (4.5)$$

where δ is Dirac's delta distribution and $(E_i, p_{m,j}, R_{m,k})$ is the orbit-space coordinate of interest. Equation 4.5 is then evaluated for all orbit-space coordinates and diagnostic measurement bins of interest.

For a given diagnostic measurement bin $[E_{d,1}, E_{d,2})$ and fast-ion energy E , the value of the weight function at (p_m, R_m) is determined by:

- The time fraction of the poloidal projection of the orbit trajectory in the diagnostic sightline.
- The pitch (and by extension, the projection of the fast-ion velocity onto the diagnostic line-of-sight) of the fast ion when it is inside the diagnostic sightline.
- The temperature and density of the bulk plasma when the fast ion is inside the diagnostic sightline.
- The cross-section of the fusion reaction.
- The solid angle and toroidal extension of the diagnostic sightline where the fast-ion orbit trajectory crosses.

For more details, explanations and illustrations, please see H. Järleblad *et al*, *Comp. Phys. Comm.*, *Submitted* (Paper **III**).

Let us now take a look at some of examples of orbit weight functions for fast-ion diagnostics. We will visualize them by 'slicing up' orbit space by fast-ion energy E , i.e. keeping E constant while varying p_m and R_m . This allows us to superimpose the topological boundaries between orbit types while examining the orbit sensitivity. Since all orbit types are present for a given fast-ion energy E , and not at a given p_m or R_m , this way of examining orbit space in terms of 'slices' of constant E can be argued to be the most informative way of viewing three-dimensional orbit-space quantities.

4.1 TOFOR

In the previous section, a brief description of how to compute orbit weight functions was given. However, in practice a lot of additional quantities and parameters need to be specified. For example, the so-called 'forward model' can be any numerical framework that computes synthetic signals for fast-ion diagnostics.

In the case of TOFOR, a JET time-of-flight NES diagnostic discussed in section 3.1, the DRESS code [80] has been used as the forward model to compute orbit weight functions. TOFOR is optimized for detecting neutrons with an energy roughly equal to that of the DD-fusion reaction nominal neutron birth energy, i.e. 2.45 MeV. Therefore, the $D(D,n)^3\text{He}$ fusion reaction was used to compute orbit weight functions, mapping the corresponding TOFOR orbit-space sensitivity.

For NES diagnostics and the $D(D,n)^3\text{He}$ reaction, the orbit-space sensitivity will vary depending on the neutron energy measurement bin ($E_{1,d}, E_{2,d}$) of interest. The relation between the motional state of the reactants and the neutron birth energy E_n can be described as [81]

$$E_n = \frac{1}{2}m_n V_{COM}^2 + \frac{m_{pr}}{m_n + m_{pr}} (Q + K) + (V_{COM} \cos \theta) \left(\frac{2m_n m_{pr}}{m_n + m_{pr}} (Q + K) \right)^{1/2}, \quad (4.6)$$

which is a slight correction of the expression used in equation (4) in H. Järleblad *et al.*, Rev. Sci. Instrum, 2021 (Paper I). Here m_n is the neutron mass and $V_{COM} = |\mathbf{V}_{COM}|$ where $\mathbf{V}_{COM} = (m_1 \mathbf{v}_1 + m_2 \mathbf{v}_2) / (m_1 + m_2)$ is the center-of-mass (COM) velocity of the two reactant ions, described by their masses m_1 and m_2 and velocities \mathbf{v}_1 and \mathbf{v}_2 . m_{pr} is the mass of the second product of the fusion reaction, Q is the nuclear energy release of the reaction, $K = m_1 m_2 v_{rel}^2 / (2(m_1 + m_2))$ is the relative kinetic energy of the reactants where $v_{rel} = |\mathbf{v}_2 - \mathbf{v}_1|$ and θ indicates the angle between \mathbf{V}_{COM} and the neutron velocity vector in the COM frame. Notice how the first two terms in equation 4.6 are positive definite.

In the limiting case of one reactant being stationary, the following equation for E_n can be used (lab frame) [67]

$$E_n = \frac{m_{pr}}{m_{pr} + m_n} Q + \frac{m_{pr} - m_1}{m_{pr} + m_n} E_1 + \frac{m_1 m_n}{m_{pr} + m_n} uv_n \quad (4.7)$$

where m_1 and E_1 are the mass and kinetic energy of the non-stationary (fast) particle, respectively. u is the velocity component of the fast ion along the line-of-sight towards the diagnostic detector and v_n is the speed of the neutron.

To showcase how the orbit sensitivity varies around the nominal neutron birth energy, it is illuminating to divide the investigation into three categories. Let E_d denote the center of a diagnostic energy bin and $E_{n,nominal}$ the value of E_n when $V_{COM} = K = 0$. For the $D(D,n)^3\text{He}$ reaction $Q = 3.27$ MeV [8] so we get that $E_{n,nominal} = 2.45$ MeV as stated above. Then, the three categories are $E_d < E_{n,nominal}$, $E_d \approx E_{n,nominal}$ and $E_d > E_{n,nominal}$ corresponding to down-shifted, nominal and up-shifted neutron energies, respectively.

4.1.1 $E_d < E_{n,nominal}$

At heavily down-shifted neutron energies, the orbit-space sensitivity is relatively high for potato orbits and counter-stagnation orbits, as can be observed in Figure

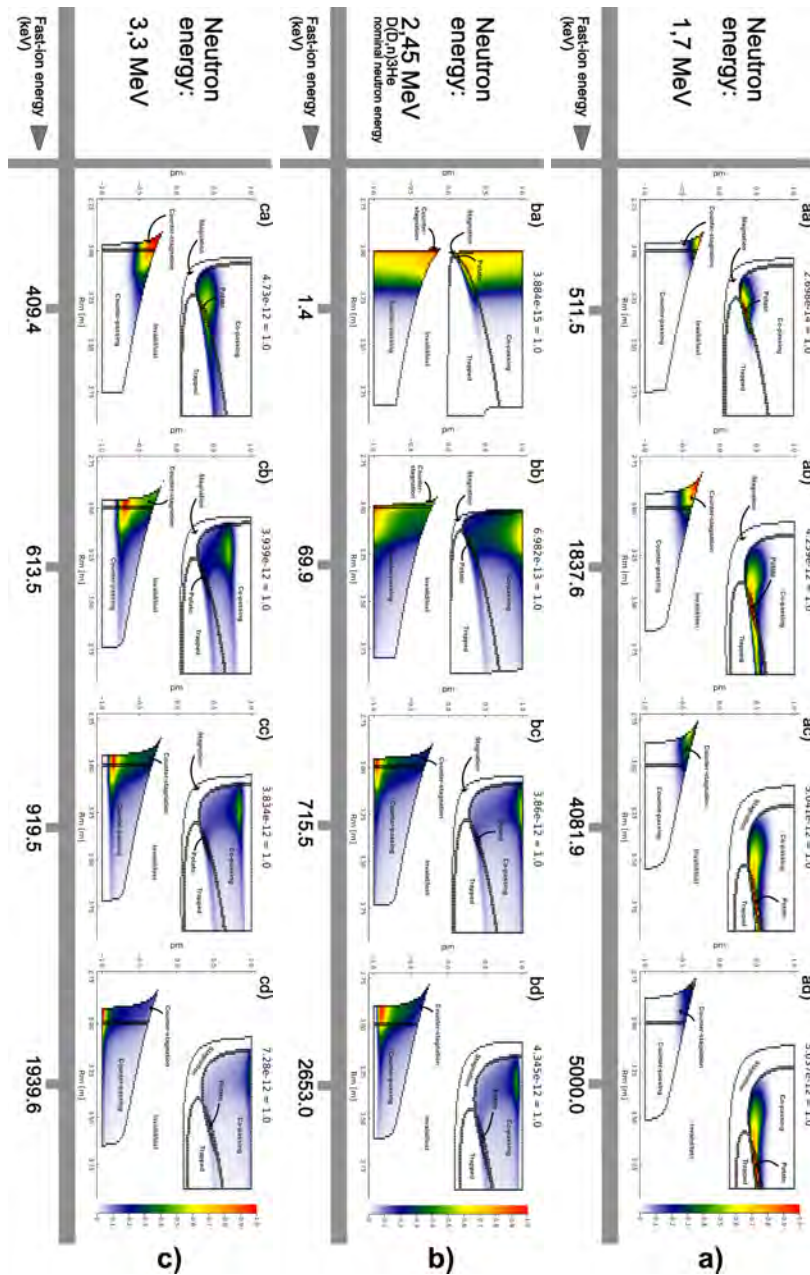


Figure 4.1: Three orbit weight functions for TOFOR. The $D(D,n)^3\text{He}$ has been studied. One orbit weight functions is for a measurement bin corresponding to a down-shifted neutron energy (a), one at the nominal $D(D,n)^3\text{He}$ neutron energy (b) and one at an up-shifted neutron energy (c). The fast-ion energy refers to one of the fusing deuterium ions. JET shot No. 94701 at 10.8 s. The figure examines different neutron energies than H. Järleblad *et al*, Nucl. Fusion, 2022 (Paper II, [2]) and is thus original.

4.1a. For the chosen neutron energy of 1.7 MeV (and magnetic equilibrium as well as fast-ion and thermal distributions) the weights are all zero for fast ions with an energy below ≈ 500 keV. This is because fast ions with such a low energy are not able to produce neutrons with enough down-shift of $E_{n,nominal}$ for the 1.7 MeV diagnostic energy bin. At fast-ion energies above ≈ 500 keV but still below the MeV range (Figure 4.1aa), the non-zero weights are concentrated around the potato region and towards the tip of the counter-stagnation region. The concentration around the potato region is due to two factors. First, when an ion is moving around on a potato orbit, it is moving away (negative z direction) from the TOFOR detector when passing through the TOFOR viewing cone (Figure 3.1). This will give rise to neutrons that are down-shifted in energy when detected by TOFOR, because of conservation of momentum (and energy). Second, the poloidal projection of a potato orbit has a relatively large fraction of its (R, z) trajectory within the TOFOR viewing cone. This results in a relatively high sensitivity. As we move away from the potato region (in the $p_m > 0$ region), these two factors decrease and thus the sensitivity decreases.

Furthermore, the concentration towards the tip of the counter-stagnation region can also be attributed to two factors. First, an ion on a counter-stagnation orbit does not change its pitch much as it moves around the orbit. Thus, the p_m coordinate is representative for the pitch of the ion at all points along the counter-stagnation orbit. As we approach the tip of the counter-stagnation region, the perpendicular velocity component of the ion increases for all points along the orbit overall (because p_m gets closer to 0.0, and thus $p = v_{||}/v$ gets closer to 0.0 and v_{\perp}/v gets closer to 1.0 for all (E, p, R, Z) points in general). Since the TOFOR sightline is almost completely in the perpendicular direction, a deuterium ion with a large perpendicular velocity component taking part in a $D(D,n)^3\text{He}$ fusion reaction will be able to give rise to a neutron with a large down-shifted nominal energy. Hence, at down-shifted neutron energies and low fast-ion energies, the orbit sensitivity increases towards the tip of the counter-stagnation region. Second, an ion on a counter-stagnation orbit has its poloidal projection almost completely within the TOFOR sightline, which naturally results in a relatively high sensitivity.

At fast-ion energies in the low MeV range (Figure 4.1ab), the sensitivity concentration diffuses outwards from the potato region and the tip of the counter-stagnation region, as more coordinates gain non-zero weight values. This is

because, at these higher fast-ion energies, even orbits that do have p_m - and p -values relatively close to 0.0 are able to produce neutrons with heavily down-shifted nominal energies. We can also notice how a narrow region of high sensitivity appears in the upper part of the trapped region. This phenomena was discussed in [1](Paper I) and corresponds to trapped orbits whose 'banana' tips lie within the TOFOR sightline where an ion spends a relatively large fraction of its poloidal transit time.

Lastly, at fast-ion energies in the several MeVs range (Figure 4.1ac and ad), the sensitivity of potato-like orbits increases relative to counter-stagnation orbits. This is likely due to the fact that, at such high fast-ion energies, simply having the poloidal projection of the orbit completely within the TOFOR sightline is not sufficient for high orbit sensitivity. As can be observed in equation 4.6, the down-shift of the neutron energy is proportional to the cosine of the angle between the COM velocity vector of the reactants and the neutron velocity vector in the COM frame ($\cos \theta = \mathbf{V}_{\text{COM}} \cdot \mathbf{v}_n / V_{\text{COM}} v_n$). We can approximate \mathbf{V}_{COM} to be the fast-ion velocity vector and $\cos \theta = -1$ to be when the fast-ion and neutron velocity vectors point in the negative and positive z -direction, respectively. In that case, it can be understood that unless $v_{\perp}/v \rightarrow 1$ as the fast ion travels within the TOFOR sightline, not enough down-shift of the neutron nominal energy will be possible. In the several MeVs range, this only happens for potato-like orbits (counter-stagnation orbits never reach $v_{\perp}/v \rightarrow 1$).

4.1.2 $E_d \approx E_{n,nominal}$

At neutron energies close to the nominal energy, the weights are non-zero all the way down to thermal ion energies of a few keVs, as can be observed in Figure 4.1 b). This is because we do not need to produce any down- or up-shift at those neutron energies, and thus it is possible even for thermal ions to contribute to a measurement signal (Figure 4.1 ba). However, the contribution is marginal as can be seen by observing the absolute value of the largest weight ($3.884 \cdot 10^{-15}$) and comparing it with the absolute value of the largest weights at the fast-ion energies of 69.9 keV ($6.982 \cdot 10^{-13}$, Figure 4.1 bb), 715.5 keV ($3.86 \cdot 10^{-12}$, Figure 4.1 bc)) and 2653.0 keV ($4.345 \cdot 10^{-12}$, Figure 4.1 bd). As we examine those increasingly high fast-ion energies, the orbit sensitivity gets more and more concentrated towards $p_m = \pm 1.0$ (Figure 4.1 bb). As we approach $p_m = \pm 1.0$ the average pitch (p) of all points along an orbit approaches ± 1.0 and the deviation of p from p_m tends to zero. We thus get that $v_{\parallel}/v \rightarrow 1.0$ and $v_{\perp}/v \rightarrow 0.0$. Since the TOFOR sightline is almost completely in the vertical (perpendicular)

direction and we do not want any down- or up-shift of the neutron energy for $E_d \approx E_{n,nominal}$, at higher fast-ion energies the orbit sensitivity will tend towards orbits that are able to produce the least amount of down- or up-shift of the neutron energy in the TOFOR sightline. Those orbits can be found at $p_m \rightarrow \pm 1.0$. The orbit sensitivity is highest in the counter-stagnation region since those orbits have their poloidal projection almost completely within the TOFOR sightline (Figure 4.1 bc).

As we increase the fast-ion energy even higher into the several MeVs (Figure 4.1 bd), the areas of highest orbit sensitivity move slightly away from the $p_m \pm 1.0$ boundaries. As we examine higher and higher fast-ion energies, the areas of highest sensitivity will move further and further away from $p_m \pm 1.0$. This is likely due to the interplay between the terms in equation 4.6, where we can observe that as we go to higher and higher fast-ion energies, the first and second term will contribute more and more to the neutron energy E_n . To ensure that the resulting neutron ends up in the same diagnostic energy bin ($E_d = 2.45$ MeV), the third term needs to counteract the increase of the first two terms. This counteraction would be maximized if $\cos \theta \rightarrow -1.0$, which occurs for TOFOR approximately when $p \rightarrow 0.0$. That is, for orbits away from the $p_m \pm 1.0$ boundaries that are potato-like (in the positive p_m half plane) and orbits close to the tip of the counter-stagnation region (in the negative p_m half plane).

4.1.3 $E_d > E_{n,nominal}$

At heavily up-shifted neutron energies, as shown in Figure 4.1 c), we can see sensitivity features similar to those found at both $E_d < E_{n,nominal}$ and $E_d \approx E_{n,nominal}$. At low fast-ion energies (Figure 4.1 ca), the sensitivity is concentrated around the potato region and towards the tip of the counter-stagnation region. This is because, similar to the $E_d < E_{n,nominal}$ case, fast ions on those orbits spend a relatively large fraction of their poloidal transit times within the viewing cone of TOFOR, and have pitch values that go to zero as they cross the TOFOR sightline. The former results in a high sensitivity in general while the latter is necessary to be able to produce enough up-shift of the nominal neutron energy. We can also observe the characteristic narrow region of relatively high sensitivity that runs through the trapped topological region. This narrow region corresponds to trapped orbits with their tips inside the diagnostic sightline, where the fast ions spend a relatively large fraction of their poloidal transit times. This results in a relatively high sensitivity.

As we look at higher and higher fast-ion energies (Figure 4.1 cb, cc and cd), the area of highest sensitivity moves outwards towards the $p_m \pm 1.0$ boundaries. This is because the higher the total fast-ion energy the less fraction of perpendicular energy we need to produce the required up-shift of the nominal neutron energy. As we know from the previous section, $p_m \rightarrow \pm 1.0$ implies $p \rightarrow \pm 1.0$ in general. However, not shown in Figure 4.1 c), it can be assumed that at fast-ion energies of many MeVs (> 5.0 MeV), the area of highest sensitivity would start to wander inwards back towards the potato region and the $p_m = 0.0$ region. This is to maximize the counteraction of the increase of the first two terms in equation 4.6, so that $\cos \theta \rightarrow -1.0$, as discussed towards the end of section 4.1.2. However, at fast-ion energies of the several MeVs, the usage of guiding-centre picture starts to become increasingly dubious, since the variation of the magnetic equilibrium on the scale of the Larmor radius becomes too great, bringing it outside the scope of this analysis.

4.2 NE213-scintillator

In contrast to TOFOR, the sightline of the NE213-scintillator (Figure 3.2) is at an oblique angle to the magnetic field, which results in a different orbit sensitivity.

4.2.1 $E_d < E_{n,nominal}$

At heavily down-shifted neutron energies, the orbit sensitivity is relatively high for counter-passing, counter-stagnation and stagnation orbits, as can be observed in Figure 4.2a. At low fast-ion energies (Figure 4.2aa), the weights are non-zero almost exclusively for counter-passing and counter-stagnation orbits. Three peaks of high sensitivity can be observed in the counter-passing region at $R_m \approx 3.05$ m, $R_m \approx 3.30$ m and $R_m \approx 3.70$ m. These peaks correspond to counter-passing orbits that satisfy two criteria. First, the fraction of the poloidal projection of their orbit trajectory within the viewing cone of NE213 is maximized, resulting in a relatively high sensitivity. Second, when crossing the viewing cone of NE213, the pitch (p) of those counter-passing orbits is optimal for giving just the right amount of down-shift of the neutron nominal birth energy for the diagnostic energy bin of interest ($E_d = 2.1$ MeV). The viewing cone of NE213 points in the counter-passing direction and thus, to be able to produce sufficient down-shifted neutron energies at low fast-ion energies, the ion has to travel in the same direction (counter-passing). Hence, almost all weights in the co-passing direction ($p_m > 0.0$) are zero.

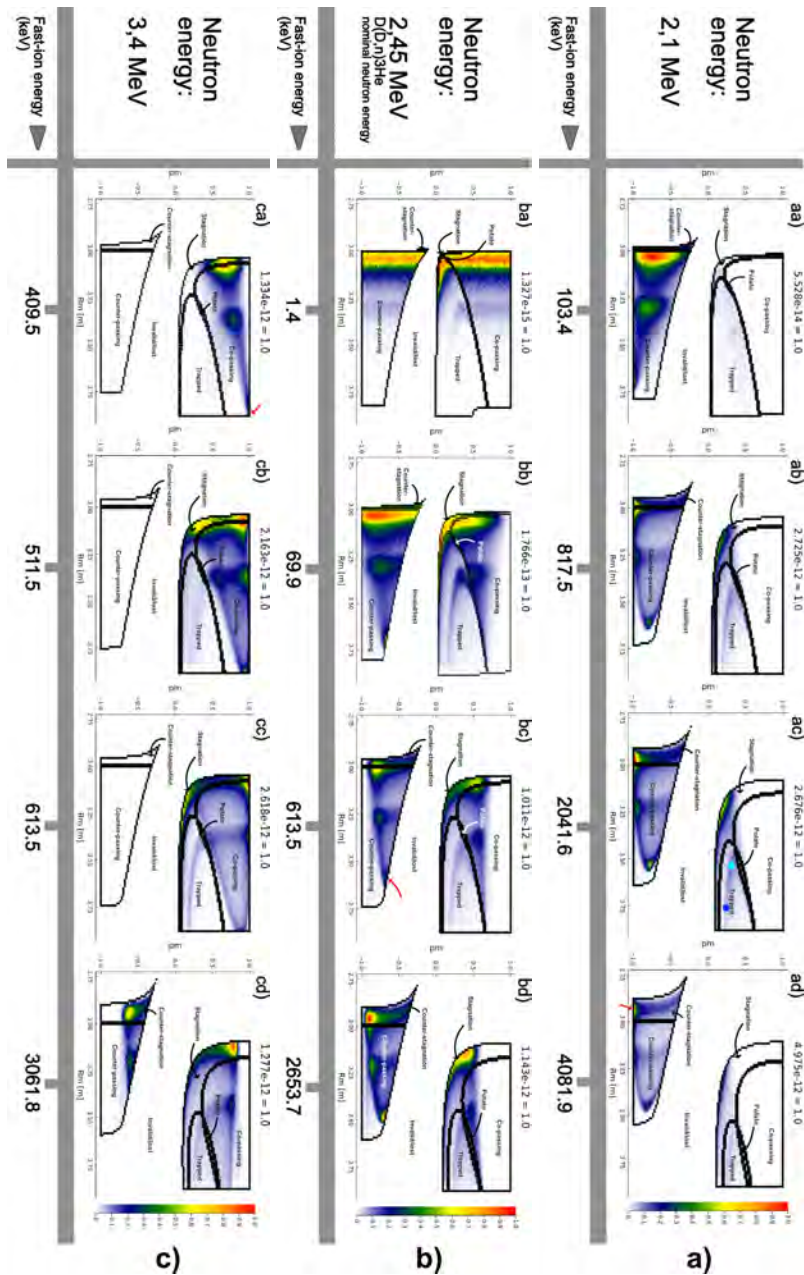


Figure 4.2: Three orbit weight functions for NE213. The $D(D,n)^3\text{He}$ has been studied. One orbit weight functions is for a measurement bin corresponding to a down-shifted neutron energy (a), one at the $D(D,n)^3\text{He}$ neutron nominal energy (b) and one at an up-shifted neutron energy (c). The fast-ion energy refers to one of the fusing deuterium ions. The two colored dots in ac) mark the coordinates of the trapped orbits in Figure 4.3. The figure examines different neutron energies than H. Järleblad *et al*, Nucl. Fusion, 2022 (Paper II, [2]) and is thus original.

At fast-ion energies close to, but still below, 1.0 MeV (Figure 4.2ab) the area of highest sensitivity has moved downwards towards the $p_m = -1.0$ boundary. Since we are now looking at higher fast-ion energies, we are going to need a larger fraction of the ion motion to be in the counter-passing direction to be able to produce just the right amount of down-shift of the neutron nominal birth energy for the diagnostic energy bin of interest. Hence, the area of highest sensitivity is closer to the $p_m = -1.0$ boundary but at roughly the same R_m coordinates. The area of highest sensitivity that was previously at $R_m = 3.70$ m and $p_m = -1.0$ has moved away from the $p_m = -1.0$ boundary however. This is due to another phenomenon, where the farther we go from the $p_m = -1.0$ boundary the more energy is in the perpendicular direction in general and the more the ions deviate from the flux surfaces as they go around their counter-passing orbits. As the ions deviate from the flux surfaces their pitch changes. For the peak at approximately $R_m = 3.70$ and $p_m = -0.8$, just enough energy is in the perpendicular direction when the ion crosses the viewing cone of NE213 so as to produce just the right amount of down-shift of the neutron nominal birth energy for the diagnostic energy bin of interest. Hence, the sensitivity peaks at this counter-passing orbit.

At fast-ion energies in the MeV range (Figure 4.2 ac), we start to get an area of significant sensitivity in the stagnation region (this was also present at fast-ion energies close to, but still below, 1.0 MeV). These stagnation orbits have the poloidal projection of their trajectories almost completely within the viewing cone of NE213, giving them the prerequisites for a relatively high sensitivity to begin with. In addition, the fraction of their energy in the perpendicular direction is likely just right for the $\cos \theta$ -term in equation 4.6 to produce the correct amount of down-shift of the neutron nominal birth energy for the diagnostic energy bin of interest. This corresponds to u being just right in equation 4.7. Finally, as we could also observe in Figure 4.2ab, there is a narrow region of relatively high sensitivity in the trapped region. This corresponds to trapped orbits whose upper 'banana' tip exactly coincides with the upper leg of the NE213 sightline. This has been illustrated in Figure 4.3

At fast-ion energies in the many MeV range (Figure 4.2 ad), the non-zero sensitivity is once again almost completely concentrated to the $p_m < 0.0$ region of orbit space. This is because at such high fast-ion energies, there is simply no way to produce sufficient down-shift of the neutron nominal birth energy without having the ion move away from the NE213 viewing cone (counter-passing

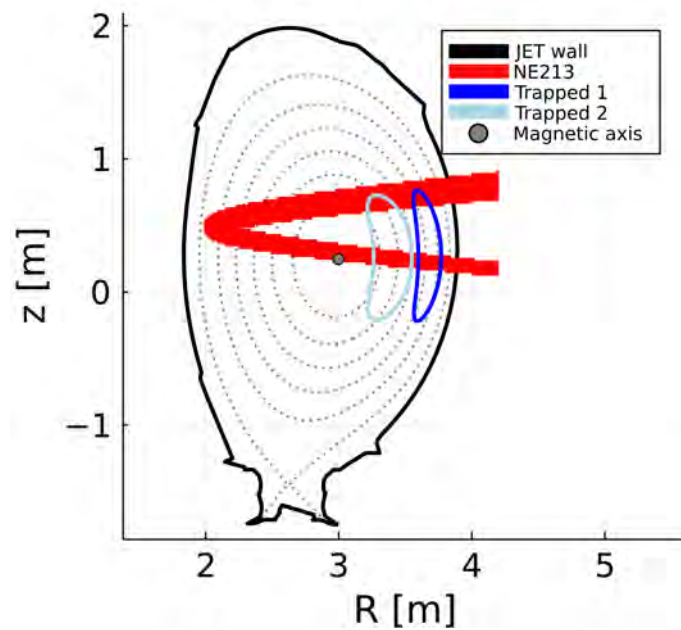


Figure 4.3: Two examples of trapped orbits whose upper 'banana' tip coincides with the upper leg of the NE213 sightline. The dark and light blue orbits have orbit-space coordinates $(E [\text{keV}], p_m [-], R_m [\text{m}]) = (2041.6, 0.23, 3.77)$ and $(E [\text{keV}], p_m [-], R_m [\text{m}]) = (2041.6, 0.3, 3.55)$, respectively. They have been marked in Figure 4.2ac. Orbits computed for deuterium fast ions in JET shot 94701 at 10.8 seconds.

direction). Hence, the orbit sensitivity is non-zero almost exclusively for counter-passing and counter-stagnation orbits. The counter-stagnation orbit with the very highest sensitivity has been marked with a red arrow.

4.2.2 $E_d \approx E_{n,nominal}$

At neutron energies close to the nominal energy, the weights are non-zero all the way down to thermal energies of a few keVs, as can be observed in Figure 4.2 b). This is the same as for TOFOR. The sensitivity is highest for orbits whose trajectory has a poloidal projection that lies completely within the NE213 sightline; that is, orbits with an R_m coordinate close to the magnetic axis at $R_m = 3.0$ m.

However, as soon as we increase the fast-ion energy into the tens of keVs (Figure 4.2 bb) distinct sensitivity patterns start to emerge. In the $p_m > 0.0$ half-plane, we can once again observe the narrow region of relatively high sensitivity in the trapped region. We can also observe an area of relatively high sensitivity in the co-passing region at around $R_m = 3.30$ m and $p_m = 0.6$. These are orbits that fulfill the two criteria of having a relatively high fraction of their poloidal projection within the viewing cone of NE213, as well as having a pitch value just right to produce as little down- and up-shift of the neutron nominal energy as possible when crossing the viewing cone. Furthermore, similar to TOFOR, the region of highest sensitivity in the $p_m > 0.0$ half-plane can be found for orbits with an R_m coordinate close to the magnetic axis at $R_m = 3.0$ m. There we have stagnation and co-passing orbits heavily localized around the magnetic axis, almost completely within the NE213 sightline, resulting in a relatively high sensitivity. However, the region of high sensitivity does not extend all the way up to the $p_m = 1.0$ boundary (as it did for thermal ion energies). Orbits with a p_m coordinate close to 1.0 have pitch p values close to 1.0 for all points along the orbit in general. Since the neutron energy diagnostic bin of interest is close to the nominal neutron birth energy and the NE213 sightline is an oblique viewing cone with respect to the magnetic field, such orbits would produce too much up-shift. Thus, the sensitivity goes to zero for orbits with p_m coordinates close to 1.0. In the $p_m < 0.0$ half-plane, we see a similar sensitivity pattern to the one in Figure 4.2aa. However, it is tilted upwards through the counter-passing region instead of downwards. This is likely because at neutron energies close to the neutron nominal birth energy, we would like as little down-shift as possible. Since the NE213 sightline is pointing in the counter-passing direction, in the $p_m < 0.0$ half-plane we would expect to find regions of relatively high sensitivity where the fraction of poloidal projection

of orbit trajectory in the NE213 viewing cone is maximized and the pitch values while crossing the sightline are minimized. This corresponds exactly to the peaks of relatively high sensitivity that we observe in Figure 4.2bb.

4.2.3 $E_d > E_{n,nominal}$

At heavily up-shifted neutron energies, the non-zero weights are mostly concentrated to the $p_m > 0.0$ half-plane, as can be observed in Figure 4.2c. The orbits in the $p_m < 0.0$ half-plane will result in ion motion moving exclusively away from the NE213 sightline. Ions on these orbits are therefore mostly unable to produce the up-shift required for the neutron energy of interest. For low fast-ion energies (Figure 4.2ca), there are three areas of relatively high sensitivity. The area of the highest sensitivity can be found heavily localized at approximately $(R_m, p_m) = (3.85\text{m}, 1.0)$ (marked with a red arrow). Orbits close to this coordinate will have the possibility to have almost all of their energy concentrated in the direction of the NE213 sightline while crossing. They will thus be able to produce the largest amount of up-shift of the neutron nominal birth energy. Similarly, we have an area of relatively high sensitivity at $(R_m, p_m) = (3.35\text{m}, 0.75)$. Here, albeit a significant fraction, not as much of the fast-ion energy will be concentrated parallel to the NE213 line-of-sight (LOS). Hence, the sensitivity will not be as high. Finally, at around $(R_m, p_m) = (3.07\text{m}, 0.7)$ we find the third and largest area of relatively high sensitivity for the fast-ion energy of interest. This area corresponds to orbits with trajectories whose poloidal projections are heavily localized and with a majority inside the viewing cone of the NE213-scintillator. A majority of the poloidal projection of the orbit trajectory within the viewing cone results in a higher sensitivity compared to the area of relatively high sensitivity at $(R_m, p_m) = (3.35\text{m}, 0.75)$. The size (number of valid orbits for a given orbit-space grid) of the areas of relatively high sensitivity increases as $R_m \rightarrow 3.0$ m (magnetic axis) because of the following reasons:

1. The poloidal projections of the orbit trajectories become increasingly localized around/near the magnetic axis
2. The NE213 sightline runs almost right through the magnetic axis
3. Varying p_m in the $p_m > 0.0$ half-plane for R_m values smaller than the trapped orbit with the smallest R_m value does not change the localization of the poloidal projection of the orbit trajectory as much as varying R_m

Hence, for the NE213-scintillator the areas of relatively high sensitivity tend to grow in size as $R_m \rightarrow 3.0$ m (magnetic axis) as can be seen in general in Figure 4.2.

Continuing, as we increase the fast-ion energy by approximately 100 keV (Figure 4.2cb), several areas of relatively high sensitivity can be observed. It can be seen how the three regions of relatively high sensitivity from Figure 4.2ca now seem to have split into two branches (one upper and one lower with a common area of high sensitivity at approximately $(R_m, p_m) = (3.85 \text{ m}, 0.95)$). One possible explanation for this is that at 511.5 keV, there might be more ways of achieving the required up-shift for the neutron energy of interest. Thus a split into several areas of high sensitivity might be the result, which is what we are seeing in Figure 4.2cb.

As we increase the fast-ion energy by approximately 100 keV again (Figure 4.2 cc) we can observe how the areas of highest sensitivity separate further and drift towards $p_m = 1.0$ as well as the part of the stagnation region closest to $p_m = 0.0$. We can also observe how a thin region of relatively high sensitivity appears in the trapped region and seems to continue upwards through the co-passing region. This thin region corresponds to trapped orbits whose 'banana' tips coincide with the upper leg of the NE213 sightline. And the continuation upwards into the co-passing region corresponds to co-passing orbits with a trajectory whose poloidal projection has an upper part that coincides with the upper leg of the NE213 sightline. Furthermore, at this higher fast-ion energy ($E = 613.5 \text{ keV}$) the areas of highest sensitivity will correspond to orbits that result in just the right amount of up-shift of the neutron nominal birth energy when the ion crosses the NE213 sightline.

At very high fast-ion energies in the MeV range (Figure 4.2 cd), the weights close to $p_m = 1.0$ start to become zero and weights in the $p_m < 0.0$ half-plane start to become non-zero. The weights close to $p_m = 1.0$ start to become zero because the ions on those orbits have too much energy in the oblique direction and will result in too much up-shift of the neutron nominal birth energy for the neutron bin ($E_d = 3.4 \text{ MeV}$) of interest (because the sightline of the NE213-sightline is mostly an oblique view). On the contrary, the weights in the $p_m < 0.0$ half-plane start to become non-zero because of the first and second term in equation 4.6 being positive definite. Even though ions on those counter-passing and counter-stagnation orbits are moving mostly away from the NE213 detector, they are so energetic that they can still cause V_{COM}^2 and K (equation 4.6) to be large enough to produce neutrons with high enough energy for the diagnostic energy bin of interest.

4.3 GRS

In the previous sections of this chapter, we have examined orbit weight functions for the $D(D,n)^3\text{He}$ reaction where the neutron is the emitted, and detected, particle. As was done in H. Järleblad *et al*, Nucl. Fusion, 2022 (Paper II), it can be helpful to investigate cases where the measurement is made using detected photons instead (to be precise, photons are both particles and waves, but that is besides the point here), which are massless. For this goal, we will be using the $T(p,\gamma)^4\text{He}$ reaction, which is a one-step fusion reaction with an emitted gamma photon.

The intended GRS diagnostic examined here has the same sightline as TOFOR. Therefore, the weight functions will have similar orbit sensitivity due to geometrical reasons, but differences due to the masslessness of the $T(p,\gamma)^4\text{He}$ gamma photon.

4.3.1 $E_d < E_{g,nominal}$

As can be seen in Figure 4.4a, the orbit sensitivity for gamma energies lower than the gamma nominal birth energy is relatively low. The sensitivity is mostly concentrated around the tip of the counter-stagnation region in the $p_m < 0.0$ half-plane and the potato region in the $p_m > 0.0$ half-plane. These regions correspond to orbits that have ions with pitch p values closest to zero when crossing the high-purity germanium diagnostic sightline and thus are able to produce the maximum possible amount of red-shift of the gamma nominal birth energy. However, because the gamma photon is massless, it does not take part in the conservation of momentum equation (at non-relativistic speeds), only the conservation of energy. Therefore, as we look at higher fast-ion energies (Figure 4.4ac and ad) the sensitivity tends towards zero because the high fast-ion energy will result in too high a gamma energy relative to the red-shift it produces.

4.3.2 $E_d \approx E_{g,nominal}$

At gamma energies close to the gamma nominal birth energy, the orbit sensitivity is non-zero down to thermal ion energies and up to the several hundreds of keVs, as can be observed in Figure 4.4b. At thermal ion energies of a few keVs (Figure 4.4 ba), the sensitivity is similar to the sensitivity for TOFOR for fast-ion energies at neutron energies close to the neutron nominal birth energy. The sensitivity is relatively homogeneous for orbits with $R_m < 3.25$ m and starts to decrease sharply as we look at larger R_m values (with the exception of trapped orbits whose 'banana' tips are within the viewing cone of the GRS diagnostic sightline). This is simply because orbits with $R_m < 3.25$ m have a relatively large fraction of the

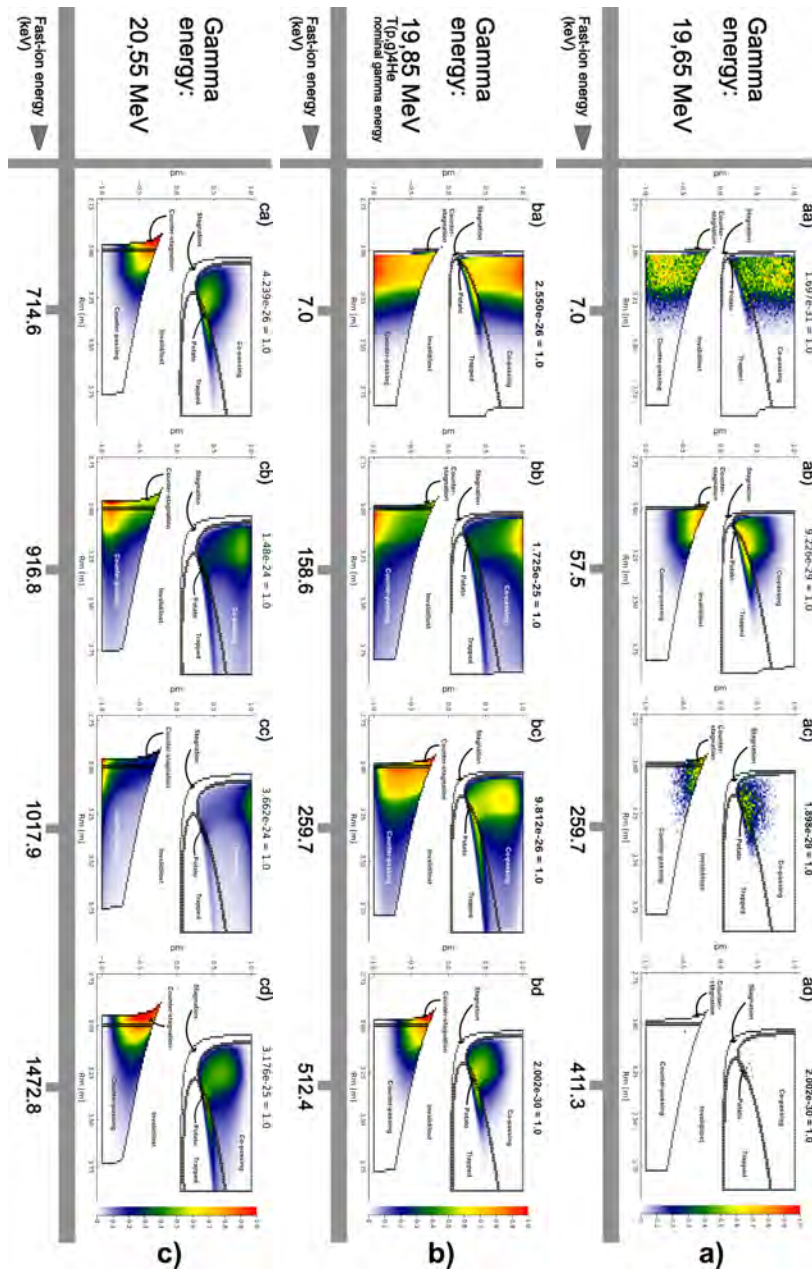


Figure 4.4: Three orbit weight functions for a GRS diagnostic sharing the TOFOR sightline. The $T(p,\gamma)^4\text{He}$ reaction has been studied. One orbit weight functions is for a measurement bin corresponding to (a) a red-shifted gamma energy, (b) one at the $T(p,\gamma)^4\text{He}$ gamma nominal energy and (c) one at blue-shifted gamma energies. The fast-ion energy refers to the proton energy. The figure examines different gamma energies than H. Järleblad *et al*, Nucl. Fusion, 2022 (Paper II, [2]) and is thus original.

poloidal projection of their trajectories within the viewing cone of the diagnostic. As we look at larger R_m values, the poloidal projection of the orbit trajectories becomes less and less localized poloidally. As the ion crosses the viewing cone of the diagnostic it will do so during an increasingly smaller fraction of the poloidal transit time, resulting in lower sensitivity.

At FI energies between 100.0 – 200.0 keV (Figure 4.4bb), the areas of relatively high sensitivity start to move outwards towards the $p_m \pm 1.0$ boundaries. This once again corresponds to orbits whose energy is almost completely concentrated parallel to the magnetic field, producing the least amount of red-/blue-shift w.r.t. the viewing cone of the diagnostic. Since we are looking at gamma energies close to the gamma nominal birth energy, these orbits will have a relatively high sensitivity. In terms of R_m , the sensitivity is concentrated at $R_m < 3.25$ m corresponding to orbits that follow magnetic flux surfaces whose high-field side (HFS) part is almost completely within the viewing cone of the diagnostic.

As we increase the gamma energy (Figure 4.4bc), the area of highest sensitivity starts to wander inwards towards the potato region ($p_m > 0.0$ half-plane) and the tip of the counter-stagnation region ($p_m < 0.0$ half-plane). This is because, at higher fast-ion energies we need to produce a certain amount of red-shift for the energy of the gamma photon to match the diagnostic energy bin of 19.85 MeV. The birth energy of the product gamma photon will increase as the energy of the reactant fast ion increases, and thus a certain amount of red-shift will be required for the gamma photon to be detected in the 19.85 MeV diagnostic energy bin.

Finally, at fast-ion energies of around half an MeV and above (Figure 4.4bd), the sensitivity starts to get heavily concentrated around the potato region and tip of the counter-stagnation region. At such high fast-ion energies, the additional energy added to the gamma birth energy must be counteracted by heavy red-shift, if the gamma photon is to be detected in the 19.85 MeV diagnostic energy bin. This is only possible for fast ions travelling away from the viewing cone of the diagnostic at high speeds when crossing the sightline. This happens for potato orbits and counter-stagnation orbits with a pitch p value as close to zero as possible (resulting in almost all of the fast ion energy being concentrated in the perpendicular direction) when the ion crosses the viewing cone of the diagnostic (which points in the negative z -direction almost completely perpendicular to the magnetic field). This consequently results in a relatively high sensitivity.

4.3.3 $E_d > E_{g,nominal}$

At gamma energies above the gamma nominal birth energy, the orbit sensitivity follows a predictable pattern as we scan the fast-ion energies. At relatively low fast-ion energies (Figure 4.4ca), the sensitivity is concentrated around the potato region and tip of the counter-stagnation region. This is because these orbit types have pitch p values that tends relatively close to zero when crossing the viewing cone of the diagnostic, and are able to produce sufficient blue-shift for the gamma photon to be detected in the 20.55 MeV diagnostic energy bin.

As we increase the fast-ion energy (Figure 4.4cb and cc), the sensitivity gets more and more concentrated towards the $p_m \pm 1.0$ boundaries. At these fast-ion energies, the energy of the reactants is enough to result in a gamma energy with sufficient energy to be detected in the diagnostic energy bin of interest. Therefore, the sensitivity is relatively high for orbits with a large fraction of their energy concentrated in the direction parallel to the magnetic field.

At fast-ion energies above 1.0 MeV (Figure 4.4cd), the area of highest sensitivity wanders once again inwards towards the potato region and the tip of the counter-stagnation region. The fast-ion energy will result in a gamma energy too high for the diagnostic energy bin of interest. This can be counteracted via red-shift, which is only possible for potato-like orbits and counter-stagnation orbits with a p_m value close to 0.0. Hence, the sensitivity is relatively high for those orbit types.

4.4 KN3 orbit weight functions

Using the KN3 neutron camera system at JET, we are going to illustrate how the orbit sensitivity varies depending on the LOS. As has been illustrated in Figure 4.5, the orbits with non-zero weights will vary depending on the poloidal projection of the LOS. The same goes for the areas of highest sensitivity. As the figure explains, as we look at diagnostics with horizontal sightlines closer to the magnetic axis, the orbit sensitivity will move 'inwards' i.e. $R_m \rightarrow R_{axis}$ where $R_{axis} = 3.0$ m is the major radius position of the magnetic axis at JET for the considered magnetic equilibrium.

As has been illustrated in Figure 4.6, this pattern is also valid for vertical sightlines. As the LOS crosses the plasma closer to the magnetic axis, the non-zero weight and the area of highest sensitivity tend towards R_m values close to R_{axis} .

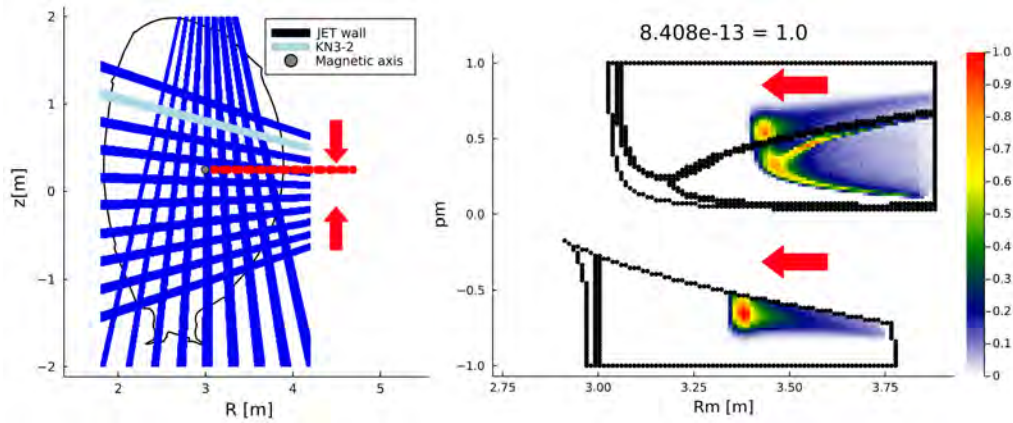


Figure 4.5: Example of an orbit weight function (OW) for one of the KN3 neutron cameras at JET, discharge No 94701. The $D(D,n)^3\text{He}$ reaction has been studied. The OW for the KN3-2 neutron camera is used as example. The red dots mark the vertical coordinate of the magnetic axis.

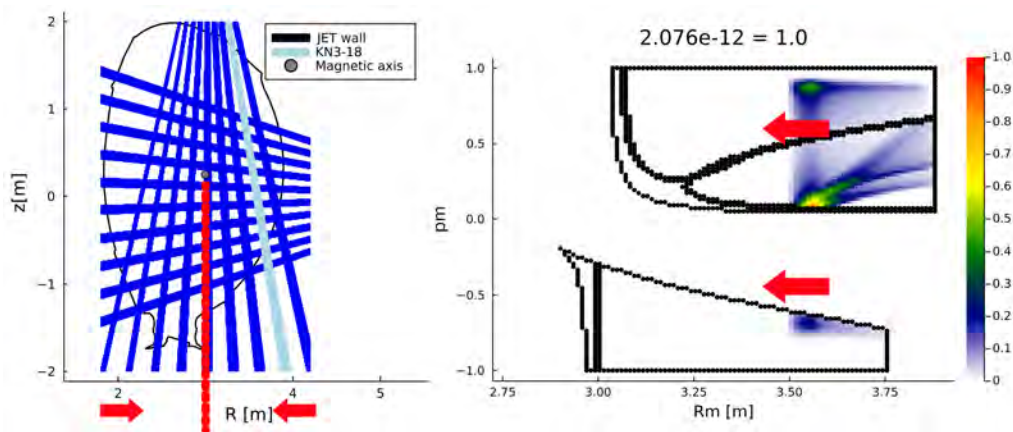


Figure 4.6: Example of an orbit weight function (OW) for one of the KN3 neutron cameras at JET, discharge No 94701. The $D(D,n)^3\text{He}$ reaction has been studied. The OW for the KN3-18 neutron camera is used as example. The red dots mark the major radius coordinate of the magnetic axis.

It should be noted that all of the KN3 neutron cameras are diagnostics with sightlines perpendicular to the toroidal direction. Since the magnetic field in JET discharges is approximately toroidal, this means that even though the KN3 neutron camera system might be useful for differentiating between signals originating from various orbits in the poloidal plane, the KN3 system will in general be unable to differentiate between signals originating from co- and counter-passing orbits. This is because most of the up- or down-shift of a nominal signal is achieved via the gyro-motion as the ion crosses a sightline perpendicular to the magnetic field. This gyro-motion is identical for co- and counter-passing ions with the same energy. In contrast, the up- or down-shift of a nominal signal detected using a diagnostic with an oblique sightline w.r.t. magnetic field can also be due to the co- and/or counter-passing toroidal motion of the ion. In the orbit weight functions for perpendicular sightlines in general, and the KN3 sightlines in particular, this manifests via a similar magnitude of the orbit sensitivity in both the co- and counter-passing regions, as can be observed in Figure 4.5.

4.5 MPRu

The MPRu diagnostic shares the sightline of the NE213-scintillator. However, it is less collimated due to its placement in front of the NE213. As we can observe from Figure 3.2, the projection of the MPRu sightline covers a significant fraction of the poloidal plane. Compared to the NE213-scintillator, this will result in the non-zero weights covering a larger fraction of all the valid orbits for each fast-ion energy orbit-space slice. This can be observed in Figure 4.7. In both a) and b), the sensitivity pattern is very similar to the NE213-pattern obtained for the same JET shot, timepoint, neutron energy and fast-ion energy (Figure 4.2ca and aa, respectively). The separate regions of relatively high sensitivity observed for the NE213 scintillator have merged. This is because of the MPRu having one large connected poloidal projection of its LOS, as opposed to the NE213-scintillator which LOS has one upper and lower 'leg'. The regions of non-zero weights are also larger for the MPRu, reflecting its larger LOS compared to the NE213-scintillator. Finally, the values of the non-zero weights are larger in general for the MPRu, reflecting the fact that a larger fraction of the poloidal projection of the fast-ion orbit trajectories will be inside the MPRu LOS, compared to the NE213 LOS.

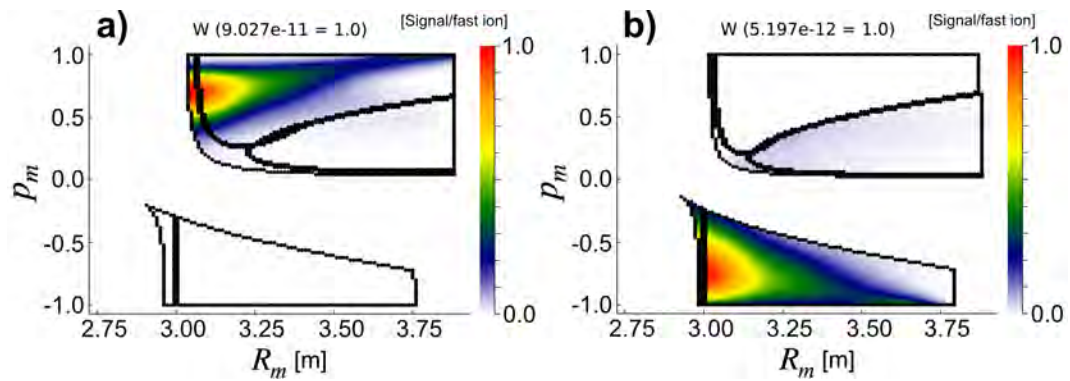


Figure 4.7: Two MPRu orbit weight function slices of constant fast-ion energy. The $D(D,n)^3\text{He}$ reaction has been studied. In a), $E_d = 3.4$ MeV and $E = 409.5$ keV, which is the same values as in Figure 4.2ca. In b), $E_d = 2.1$ MeV and $E = 103.4$ keV, which is the same values as in Figure 4.2aa. Deuterium. JET discharge 94701 at 10.8 seconds. TRANSP ID 94701V01.

CHAPTER 5

Orbit-space origin of diagnostic signals

Using orbit weight functions, the origin of diagnostic signals can be examined in detail in terms of fast-ion orbits. Given a measurement and a fast-ion distribution function, we can split up the measurement into its orbit-type constituents and provide information on what fractions of orbit types amount to the total signal. The fast-ion distribution can also be pointwise multiplied with the orbit weight functions in orbit space. This will result in a detailed map of where in orbit space the signal is most likely to originate from. Lastly, we can split the fast-ion distribution itself into its orbit-type constituents. This is useful for various purposes, such as verifying certain heating schemes (e.g. the three-ion heating scheme which contains a large population of high-energy co-passing orbits despite the use of ICRF heating) and understanding how the orbit types make up the fast-ion distribution. For example, this can be understood both in terms of relative population as well as via the dependence on the three orbit coordinates E , p_m and R_m .

5.1 Weight function signals split into orbit types

As was described in H. Järleblad *et al*, Nucl. Fusion, 2022 (Paper II, [2]), if we have confirmed that $S = WF$ (where S is the diagnostic signal, W our orbit weight matrix and F our fast-ion orbit-space distribution) we can use the weight functions to derive the origin of a (synthetic) diagnostic measurement in terms of orbit types. This can be written as

$$WF = \sum_h W_h F_h \quad (5.1)$$

where h refers to the different orbit types (co-passing, trapped, etc). W_h and F_h are the weight matrix and fast-ion orbit-space distribution decomposed according to orbit type, respectively. In Figure 5.1a, we can observe a diagnostic signal

(green WF points) and its likely orbit-type constituents below. In general, most of the signal can be expected to originate from co-passing orbits (green) and about a quarter can be expected to originate from trapped orbits. We can see how the orbit-type contributions are almost completely symmetrical with respect to the nominal DT-neutron energy of $E_{d,n} \approx 14$ MeV. This is a result of the KM14 sightline being almost completely vertical, as we will discuss further in later sections and chapter 6.

To enable analysis of the orbit-type constituents at the extrema of the signal spectrum (≈ 13 and ≈ 15 MeV), we can normalize the sum of the orbit-type constituents to 1.0 for each diagnostic measurement bin $E_{d,n}$. This has been done in Figure 5.1b. We can see how, at the extrema, the contributions from potato and trapped orbits increase (relative to all other orbit types). We can also observe how the decomposition into orbit types is not completely symmetrical w.r.t. the nominal DT-neutron energy of $E_{d,n} \approx 14$ MeV. This is because the KM14 sightline is not completely vertical and because a symmetrical up- and down-shift in velocity ($v_{d,n} \pm \Delta v$) does not result in a perfectly symmetrical up- and down-shift in energy ($\sim E_{d,n} \pm m(v_{d,n} \pm \Delta v)^2$). As discussed in earlier chapters and in H. Järleblad *et al.*, Nucl. Fusion, 2022 (Paper II, [2]), in real experimental data, the low-energy part of the neutron spectrum is generally plagued by down-scattered neutrons not directly originating from fusion reactions. This makes that part of the spectrum unsuitable for fast-ion analysis.

We can make barplots for the diagnostic sensitivity (weight matrix) split into orbit types, W_h , and the fast-ion distribution, F_h , on their own. In Figure 5.2a, we can observe how the most populous orbit type is the trapped orbit. One might therefore expect the majority of the diagnostic signal to originate from trapped orbits. However, as we saw in Figure 5.1, the majority of the signal is likely to originate from co-passing orbits. This is because the diagnostic's orbit sensitivity for co-passing orbits is much greater, as we can observe in Figure 5.2b, where the so-called orbit *weight average* \bar{w} has been plotted for each orbit type. How to compute the orbit weight average will be discussed further in chapter 6.3. The weights of the orbit weight functions determine where in orbit space, and thus to which orbit types, the diagnostic is most sensitive. But can we perform a more detailed analysis?

Yes, we can perform a so-called *split of the split*. That is, we can examine where the orbit-type constituents of the diagnostic signal originate from as functions of

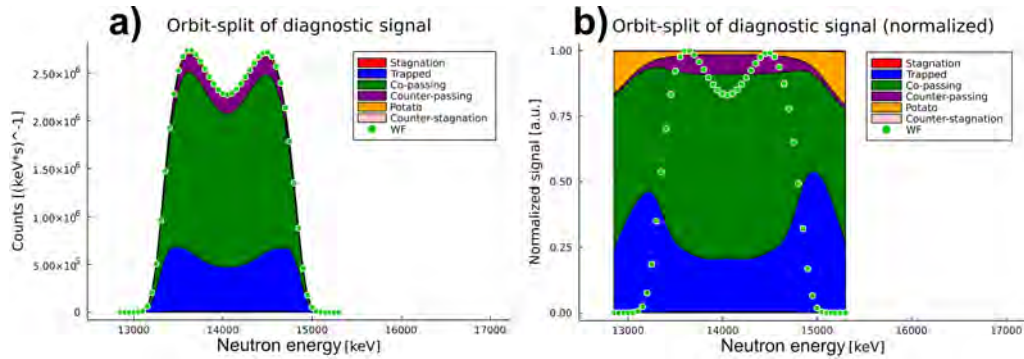


Figure 5.1: An example of a synthetic diagnostic signal WF split into its orbit-type constituents. In a), the absolute values of the signal and orbit contributions have been used, and in b) the sum of all orbit contributions have been normalized to 1.0 for all diagnostic measurement bins E_d . Also in b), the normalized synthetic diagnostic signal has been superimposed for clarity. Signal computed for the LOS of the KM14 [82] neutron scintillator at JET [19] with an almost completely vertical sightline. JET shot No 99500 at 7.4 s, TRANSP ID V05.

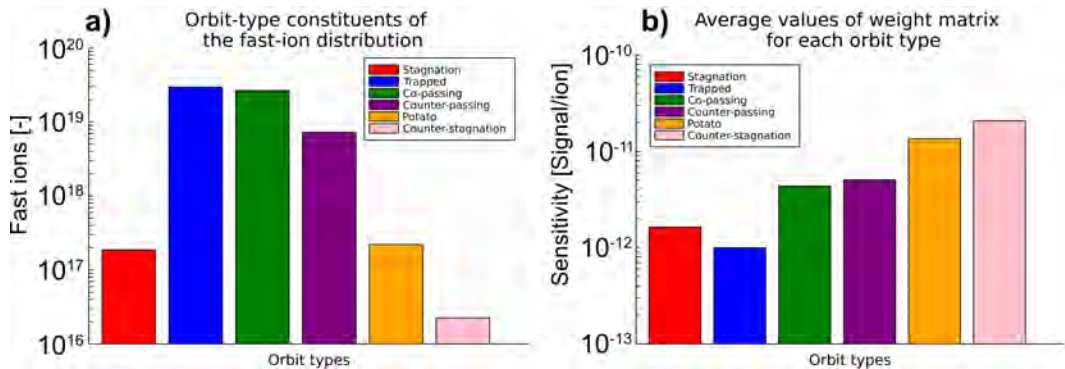


Figure 5.2: An example of a) a fast-ion distribution and b) an orbit weight function matrix, split into their orbit-type constituents. The orbit sensitivity is computed for the LOS of the KM14 [82] neutron scintillator at JET [19] with an almost completely vertical sightline. The diagnostic measurement bin range is $E_d = [12.5, 16.5)$ MeV and the fast-ion energy range is $E = [0.5, 172]$ keV. To compute a bar in b), the corresponding orbit-type elements are identified in the weight matrix, and then averaged over. JET shot No 99500 at 7.4 s, TRANSP ID V05.

E , p_m and R_m , respectively. Mathematically, this can be expressed as examining the hidden coordinate integrands of equation 5.1

$$\sum_h W_h F_h = \sum_h \int_h w(E, p_m, R_m) f(E, p_m, R_m) dE dp_m dR_m \quad (5.2)$$

and integrating out two out of the three orbit coordinates at a time. We will thus acquire the *diagnostic signal density* $w(E)f(E)$, $w(p_m)f(p_m)$ and $w(R_m)f(R_m)$ for each orbit type (for the given distribution function). Figure 5.3 shows an example of an orbit-split of the diagnostic signal density for the $E_d = 14.75$ MeV measurement bin of the KM14 [82] neutron scintillator diagnostic at JET. We can observe how most of the measured neutrons for this measurement bin can be expected to have originated from co-passing orbits with a fast-ion energy $E = 100$ keV. There is also a significant contribution from trapped orbits, peaked slightly below the co-passing peak in terms of fast-ion energy. Not much contribution to the 14.75 MeV neutrons can be expected to have originated from below $E \approx 60$ keV.

We can also perform an analogous analysis for p_m by integrating out E and R_m instead. This has been done in Figure 5.4. For the given fast-ion distribution, we can observe how most of the measured 14.75 MeV neutrons can be expected to have originated from co-passing and trapped orbits with a pitch maximum value equal to $p_m \approx 0.5$. The trapped peak is located slightly below the co-passing peak in p_m , partly because the (barycentric) center of the trapped topological region is located slightly below the center of the co-passing region, for the fast-ion energies of interest.

Finally, we can integrate out E and p_m to obtain the signal density as a function of maximum major radius R_m . This has been plotted in Figure 5.5. We can observe how most of the measured 14.75 MeV neutrons can be expected to have originated from co-passing orbits with a maximum major radius position of $R_m \approx 3.25$ m. Outside of $R_m \approx 3.3$ m however, most of the 14.75 MeV neutrons can be expected to have originated from trapped orbits.

5.2 Orbit sensitivity split into orbit types

We can perform the same analysis as for the signal density wf , but for the orbit weight functions instead, i.e. $w(E)$, $w(p_m)$ and $w(R_m)$. This is useful for determining e.g. for which fast-ion energies a certain diagnostic is most sensitive

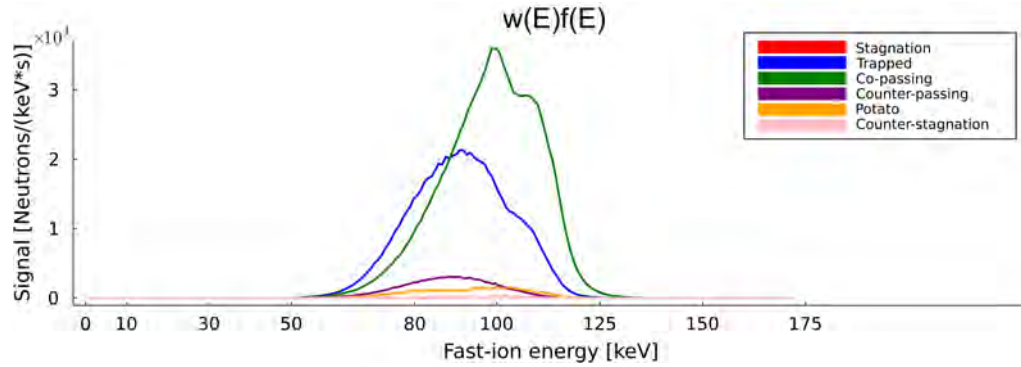


Figure 5.3: An example of the diagnostic signal density wf as a function of fast-ion energy E , split into its orbit-type constituents. Diagnostic measurement bin $E_d = 14.75$ MeV. LOS corresponds to KM14 [82] neutron scintillator, JET shot No 99500 at 7.4 s, TRANSP ID V05.

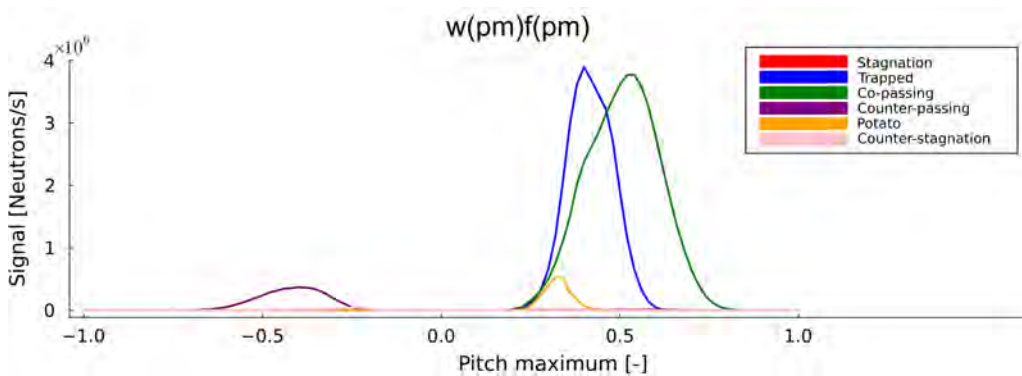


Figure 5.4: An example of the diagnostic signal density wf as a function of pitch p_m at the maximum major radius position of the fast-ion orbit, split into its orbit-type constituents. Diagnostic measurement bin $E_d = 14.75$ MeV. LOS corresponds to KM14 [82] neutron scintillator, JET shot No 99500 at 7.4 s, TRANSP ID V05.

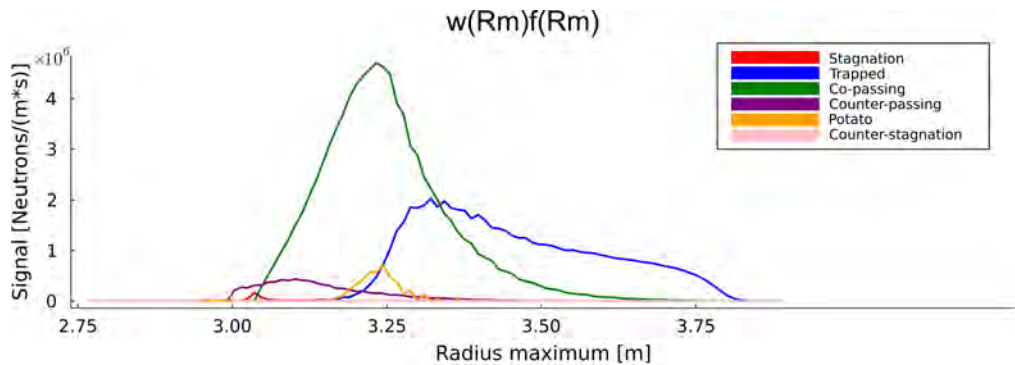


Figure 5.5: An example of the diagnostic signal density wf as a function of maximum major radius position R_m of the fast-ion orbit, split into its orbit-type constituents. Diagnostic measurement bin $E_d = 14.75$ MeV. LOS corresponds to KM14 [82] neutron scintillator, JET shot No 99500 at 7.4 s, TRANSP ID V05.

to in terms of orbit types (and in general). However, when computing e.g. $w(E)$ for trapped orbits, we have to normalize by the number of orbit-space points corresponding to trapped orbits for each fast-ion energy E , when integrating over p_m and R_m (effectively computing averages). This is to be able to take the metric of our orbit-space into account (i.e. for a finite grid resolution, the fraction of points ending up in the trapped region in the (E, p_m, R_m) space will be different compared to e.g. the $(E, \mu, P_\phi; \sigma)$ space). Analogous averages are performed for the other dimensions (p_m, R_m) and orbit types (co-passing, counter-passing, etc).

In Figure 5.6, we can observe an example plot of an orbit weight function where the p_m and R_m dependence has been integrated out. We can thus examine $w(E)$ while also splitting it into the different orbit types. It can be observed how, for the $E_d = 14.75$ MeV diagnostic measurement bin of interest, the orbit sensitivity tends to zero below approximately $E = 60$ keV, regardless of orbit type. This is because orbits with $E \lesssim 60$ keV are unable to produce sufficient up-shift of the neutron nominal birth energy $E_{d,n} = 14.06$ MeV to be detected in the $E_d = 14.75$ MeV diagnostic measurement bin. Above approximately $E = 60$ keV, the orbit sensitivity rises sharply for potato and counter-stagnation orbits. This reflects the fact that those two orbit types will spend a relatively large fraction of their poloidal transit time inside the KM14 (same as TOFOR) LOS. We can also observe the interesting fact that the sensitivity is higher towards counter-stagnation orbits compared to stagnation orbits in general. This is because the LOS is almost completely vertical and passes through the plasma just on the HFS of the magnetic

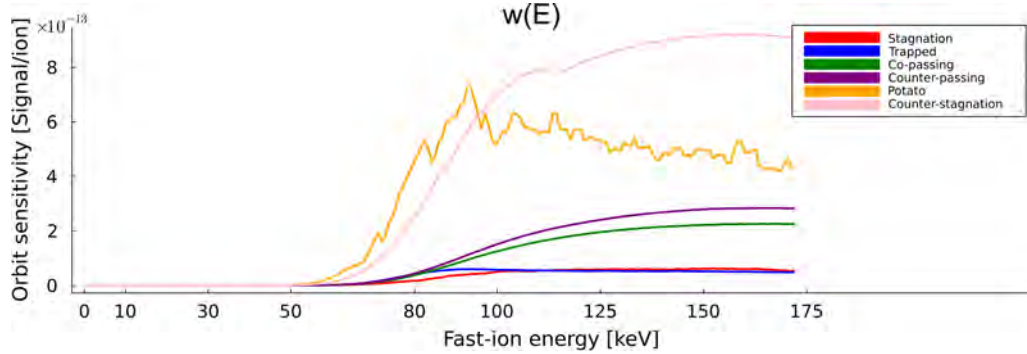


Figure 5.6: An example of an orbit weight function as a function of fast-ion energy, split into its orbit-type constituents. The dependence on p_m and R_m has been integrated out. The lines correspond to averages, for each fast-ion energy. The potato line is noisy because of limited orbit-space grid resolution. Diagnostic measurement bin $E_d = 14.75$ MeV. LOS corresponds to KM14 [82] neutron scintillator, JET shot No 99500 at 7.4 s, TRANSP ID V05.

axis, but not as much on the LFS of the magnetic axis. The area just on the HFS of the magnetic axis is where the counter-stagnation orbits 'live' and the area just on the LFS of the magnetic axis is where the stagnation orbits live. Thus, for this particular LOS, the sensitivity will be relatively high for counter-stagnation orbits, compared to stagnation orbits.

Next, the same process can be repeated for p_m . Co-going orbits (co-passing, trapped (both co- and counter-precessing), stagnation and potato) will be found for $p_m > 0$ and counter-going orbits (counter-passing and counter-stagnation) will be found for $p_m < 0$. We can thus examine for which orbit 'kingdom' ($p_m > 0$ and $p_m < 0$) the diagnostic is most sensitive to. For example, in Figure 5.7, we can observe how the diagnostic is most sensitive to counter-stagnation and potato orbits, which is similar to that in Figure 5.6. We can also observe how, even though we are only examining the orbit sensitivity of the diagnostic for fast-ion energies below $E \approx 175$ keV, the sensitivity for counter-stagnation orbits is relatively high. This suggests that the diagnostic LOS is localized just on the HFS of the magnetic axis, which supports the conclusion regarding the LOS geometry already drawn from Figure 5.6.

Finally, we can examine $w(R_m)$ by integrating over the other two orbit coordinates. Since orbits with $R_m \rightarrow R_{axis}$, where R_{axis} is the major radius position of the

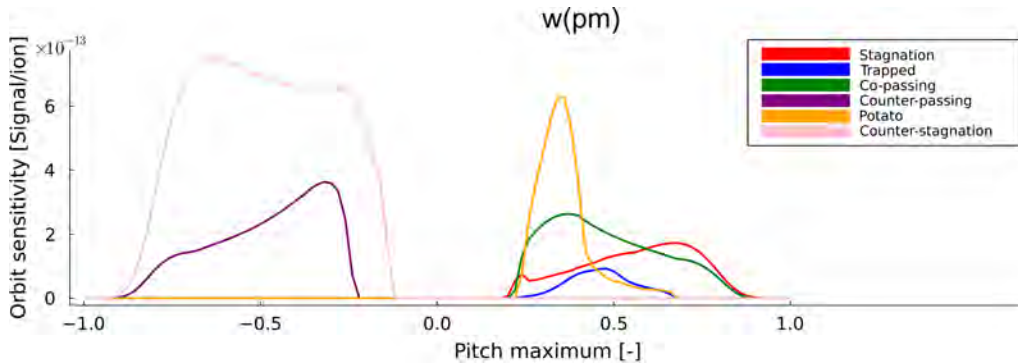


Figure 5.7: An example of an orbit weight function as a function of pitch maximum, split into its orbit-type constituents. The dependence on E (from 1 keV to ~ 175 keV) and R_m has been integrated out. The lines correspond to averages, for each pitch maximum value. Diagnostic measurement bin $E_d = 14.75$ MeV. LOS corresponds to KM14 [82] neutron scintillator, JET shot No 99500 at 7.4 s, TRANSP ID V05.

magnetic axis, correspond to orbits heavily localized around the magnetic axis, we can examine how sensitive a diagnostic is to orbits near the plasma center versus orbits that might transport fast ions far away from the magnetic axis (e.g. out to the plasma separatrix). In Figure 5.8 we can observe how, as we examine R_m values close to $R_{axis} \approx 3.0$ m, the sensitivity for counter-going (counter-passing and counter-stagnation) orbits is relatively high, while the sensitivity for the co-going orbits is relatively low. As with Figure 5.6 and 5.7, this supports the conclusion that the diagnostic LOS is localized just on the HFS of the magnetic axis, since this is where the counter-going orbits 'live'.

In short, without actually knowing what the diagnostic LOS looks like, we can combine our knowledge of fast-ion topology in tokamaks with the integrated orbit weight functions $w(E)$, $w(p_m)$ and $w(R_m)$, split into orbit types, to 'reverse-engineer' our way towards what the diagnostic LOS must look like, given the orbit-split profiles. In the process this also results in new insight, such as how the diagnostic LOS might be changed to increase its sensitivity to certain orbit types.

5.3 Fast-ion distribution split into orbit types

To examine the FI distribution in terms of orbit types, we simply transform the FI distribution into orbit space and use a topological map to keep track of where each orbit type region is. Thereafter, we can identify how much of the FI distribution is

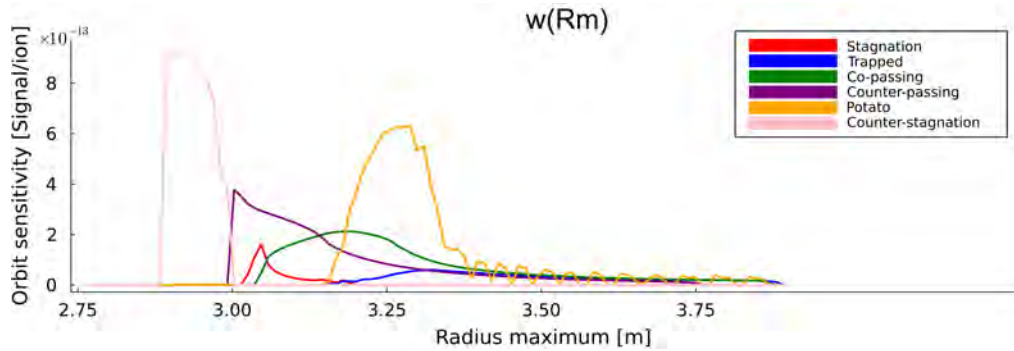


Figure 5.8: An example of an orbit weight function as a function of major radius maximum, split into its orbit-type constituents. The dependence on E (from 1 keV to ~ 175 keV) and p_m has been integrated out. The lines correspond to averages, for each radius maximum value. The potato line is fluctuating because of limited orbit-space grid resolution. Diagnostic measurement bin $E_d = 14.75$ MeV. LOS corresponds to KM14 [82] neutron scintillator, JET shot No 99500 at 7.4 s, TRANSP ID V05.

comprised of every orbit type. This can then be visualized in various ways. One of the most intuitive ways is simply to view the dependence on E , p_m and R_m one by one, having integrated the other two.

In Figure 5.9, we can observe how the p_m and R_m coordinates of the orbit-type constituents of the fast-ion distribution have been integrated out. We can thus examine the energy dependence of the fast-ion distribution $f(E)$ for the different orbit types. We can observe how the fast-ion distribution is comprised of mostly trapped orbits below $E \approx 60$ keV, and mostly co-passing orbits above. It can also be noted how, at the highest neutral beam injection (NBI) energy of $E \approx 125$ keV, the populated orbits are exclusively co-going. As we examine lower and lower fast-ion energies, the counter-passing population grows relative to the co-going population. Thus, by examining Figure 5.9, we might suspect that the NBI beam was injected in the co-going direction and, as the fast ions slowed down, the scattering produced counter-going orbits.

Similarly, we can integrate out the E and R_m coordinates to obtain the p_m dependence $f(p_m)$ of the orbit-type constituents of the fast-ion distribution. This enables detailed examination of the ratio between the populated co- and counter-going orbits of the fast-ion distribution. In Figure 5.10, we can observe how the

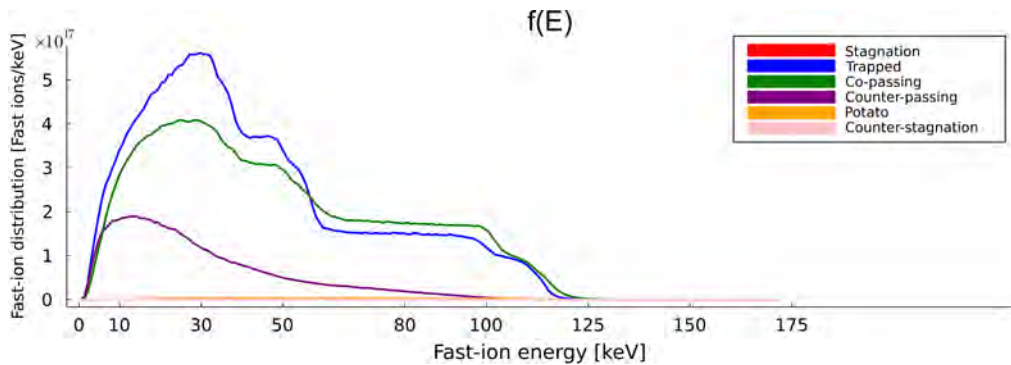


Figure 5.9: An example of a fast-ion distribution as a function of energy, split into its orbit-type constituents. The dependence on p_m and R_m has been integrated out. JET shot No 99500 at 7.4 s, TRANSP ID V05.

most populated orbit type is the trapped orbit, and how the trapped distribution is peaked at $p_m \approx 0.5$. The second most populated orbit type is the co-passing orbit. However, the co-passing distribution peaks at $p_m \approx 0.6$. This is partly due to the fact that the co-passing topological region is, in general, located at larger values of p_m than the co-passing region. In contrast to Figure 5.9, we can also observe how we have a small population of potato orbits located at $p_m \approx 0.3$.

Lastly, we can integrate over the E and p_m coordinates to obtain the R_m dependence $f(R_m)$ of the orbit-type constituents of the fast-ion distribution. In general, the larger the R_m value, the more an orbit is likely to be localized to the outer magnetic flux surfaces, and vice versa. We can therefore use $f(R_m)$ to investigate roughly for which magnetic flux surfaces we might expect the orbit types to be populated. We can observe in Figure 5.11 how the co-passing population peaks at $R_m \approx 3.25$ m while the trapped population peaks at $R_m \approx 3.7$ m. We can also observe how we have a small population of stagnation and counter-stagnation orbits close to the maximum major radius position corresponding to the magnetic axis $R_{m,axis} \approx 3.0$ m. This is to be expected since this is where the stagnation-type orbits 'live'.

5.4 Orbit weight function signal density detailed analysis

In section 5.1, we saw how we could 'split the split' of the diagnostic signal, and examine the origin of measurements in terms of orbit types and as a function of

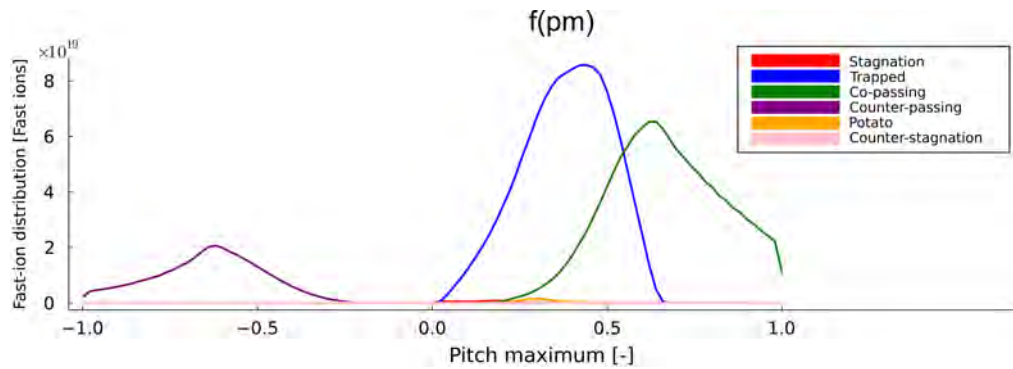


Figure 5.10: An example of a fast-ion distribution as a function of pitch maximum, split into its orbit-type constituents. The dependence on E (from 1 keV to ~ 175 keV) and R_m has been integrated out. JET shot No 99500 at 7.4 s, TRANSP ID V05.

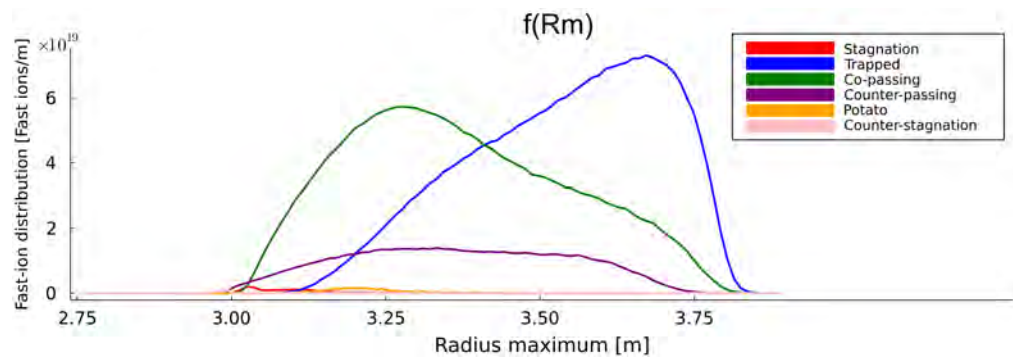


Figure 5.11: An example of a fast-ion distribution as a function of maximum major radius, split into its orbit-type constituents. The dependence on E (from 1 keV to ~ 175 keV) and p_m has been integrated out. JET shot No 99500 at 7.4 s, TRANSP ID V05.

the orbit coordinates E , p_m and R_m one by one. But why stop there? Instead of integrating out one or more of the coordinates, we can also keep the three-dimensional signal density $w(E, p_m, R_m)f(E, p_m, R_m)$ as is, and examine the origin of measurements in detail. This can be achieved by slicing up the orbit space into slices of constant fast-ion energy, as was done for the orbit weight functions in chapter 4, and superimposing the topological boundaries between different orbit types. Figure 5.12c shows an example of a slice of WF signal density as a result of point-wise multiplication between an orbit weight function slice (Figure 5.12a) and a fast-ion distribution slice (Figure 5.12b). We can notice how, even though a large fraction of the co-passing and trapped regions are populated with fast ions, only a smaller fraction will actually contribute to the 14.75 MeV neutron measured by the KM14 [82] scintillator. This smaller fraction of orbits correspond to orbits whose poloidal trajectory projections lie to a large extent within the LOS of the KM14 scintillator. As they cross the LOS, these orbits also have a pitch value that favors the birth of a neutron with the correct amount of up-shift to end up in the 14.75 MeV measurement bin.

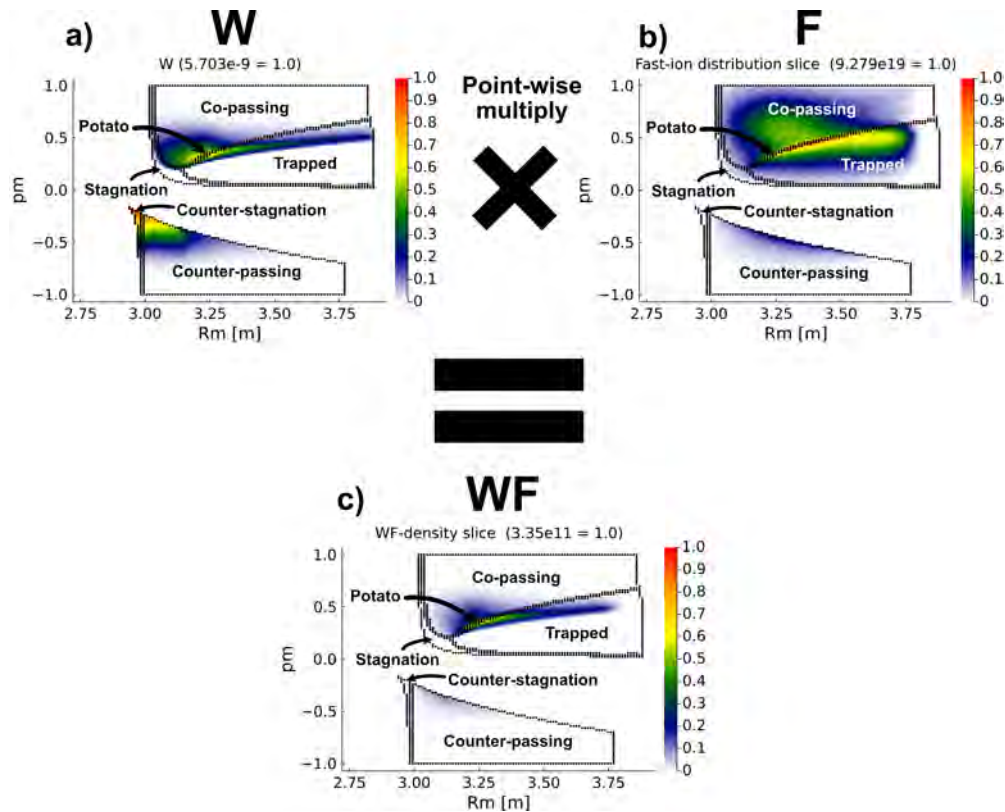


Figure 5.12: An example of a point-wise multiplication between an orbit weight function and a fast-ion distribution, without summing up all the contributions. W , F and WF have dimensions *signal per ion*, *ion per orbit-space volume* and *signal per orbit-space volume*, respectively. $E_d = 14750$ keV and $E = 80$ keV, LOS corresponding to KM14 [82] scintillator. JET shot No 99500 at 7.4 s, TRANSP ID V05.

CHAPTER 6

Discussion on orbit tomography

This chapter will provide a short discussion on the experience gained from the attempts to reconstruct the orbit-space fast-ion distribution during this PhD project. Although a successful reconstruction was not achieved, useful insight was obtained that is deemed to be of future use. Since all attempts at a successful reconstruction during this project were performed using synthetic measurements, caution is advised when reconstructing the fast-ion distribution from experimental measurements. The recommendations provided in this chapter might need to be altered or improved upon to facilitate a successful reconstruction when attempting to use experimental data.

6.1 Attempts at reconstructing from synthetic measurements

There were several attempts at reconstructing the fast-ion distribution in JET. The most notable example was an attempt to reconstruct the high-energy tail of a deuterium fast-ion distribution in a DD plasma. The fast-ion distribution was a result of heating by deuterium neutral beam injection (NBI) and ion-cyclotron resonance heating (ICRH). The discussion will therefore focus on this specific example, and illuminate the conclusions with its help. Other attempts at reconstructing the fast-ion distribution naturally also contributed to the gained insights. However, we will use this specific example to illustrate our points.

The energy dependence of the fast-ion distribution with the high-energy tail that was to be reconstructed is shown in Figure 6.1. Please note that the whole 3D orbit-space fast-ion distribution above $E \approx 150$ keV was to be reconstructed. This was to be accomplished using synthetic measurements from TOFOR [72], an NE213 neutron scintillator [73, 74] and the KN3 neutron camera system [77], whose combined lines-of-sight (LOS) have been plotted in Figure 6.2. At first sight, it might look like there should be enough diagnostic sightlines to be able

to reconstruct the full fast-ion distribution in three-dimensional (E, p_m, R_m) orbit space (which we could later transform into an (E, p) distribution for every poloidal cross-sectional (R, z) point). However, as we shall see, that is not necessarily so.

Using the TRANSP [32] NUBEAM [33]-computed fast-ion deuterium distribution $f(E, p_m, R_m)$ (with $f(E)$ in Figure 6.1) with TRANSP ID 94701V01 at 10.8 seconds, and the pertaining thermal plasma profiles, together with the sightlines in Figure 6.2, we can compute the expected synthetic diagnostic signals. This was done using the Orbit Weight Computational Framework (OWCF) [83] with the DRESS code [80]. The resulting synthetic signals have been visualized in Figure 6.3.

Using the synthetic diagnostic signals in 6.3 and their corresponding orbit weight functions, we can attempt to reconstruct the fast-ion distribution in (E, p_m, R_m) orbit space. This has been illustrated in Figure 6.4. As we can observe, the reconstruction is not successful apart from certain features. It successfully identifies a fast-ion distribution consisting of more co-passing than counter-passing orbits, but it heavily overestimates the number of counter-passing orbits (Figure 6.4b). We will further discuss why this is the case in section 6.3. The reconstruction also successfully identifies the peak of the fast-ion distribution in R_m (Figure 6.4c), but it overestimates the population of fast-ion orbits that are localized at the outer magnetic flux surfaces ($R_m \gtrsim 3.3$ m). In section 6.4, we will discuss how this could be improved upon.

Finally, we can observe how the reconstruction completely fails to recreate the energy dependence of the fast-ion distribution (Figure 6.4a). This is likely due to several factors. First, there is simply too few measurements (2038) to be able to reconstruct the number of unknowns (3210). For future tomographic reconstruction of the fast-ion distribution in orbit space to be successful, given limited prior information, it can be argued that the number of measurements needs to at least match, and preferably exceed, the number of unknowns. It is important to understand that it is not enough to simply match the number of unknowns with the same number of measurements to obtain a good tomographic reconstruction. The provided measurements also need to contain all the information needed to reconstruct all parts of the fast-ion distribution (this is discussed further in section 6.3).

Second, the 0th order Tikhonov tomographic algorithm that is used to reconstruct

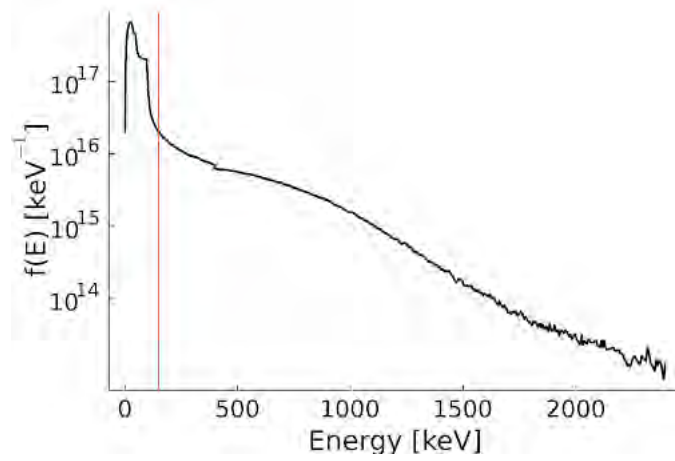


Figure 6.1: The energy dependence of the JET deuterium fast-ion distribution obtained from the TRANSP [32] NUBEAM [33]-simulation with ID 94701V01. The lower bound ($E \approx 150$ keV) of the high-energy tail to be reconstructed has been marked with a vertical red line.

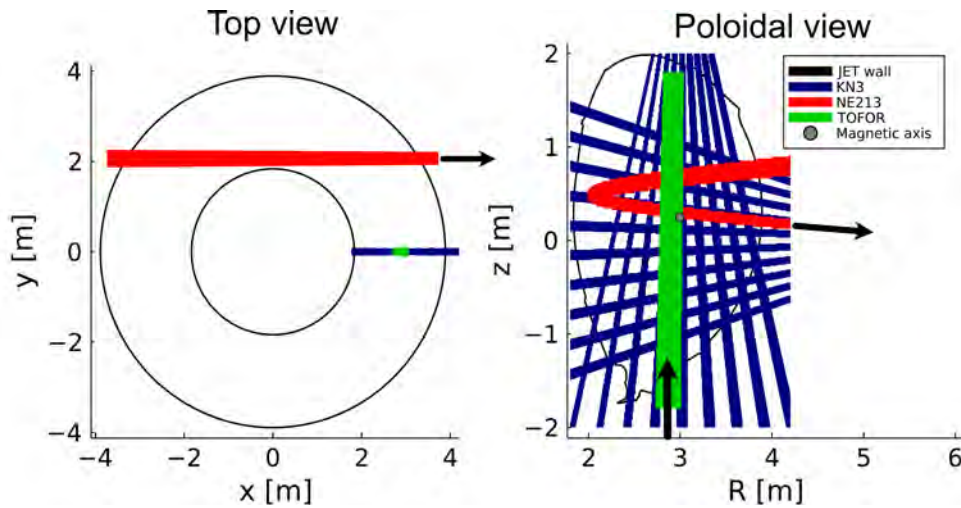


Figure 6.2: The LOS of all the (synthetic) diagnostics used to attempt the reconstruction of the 3D orbit-space fast-ion distribution above $E \approx 150$ keV with TRANSP ID 94701V01. The black arrows point in the direction of the respective detectors.

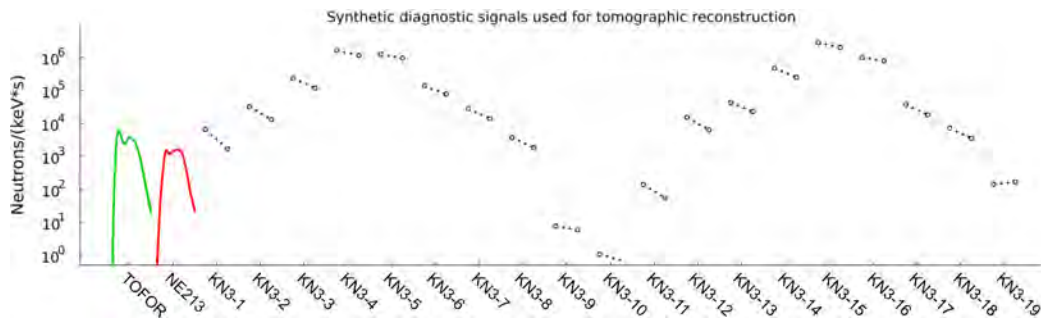


Figure 6.3: The synthetic diagnostic signals for TOFOR [72], an NE213-scintillator [73, 74] and the KN3 [77] neutron camera system, given the fast-ion distribution of TRANSP [32] run 94701V01 at 10.8 seconds and the corresponding thermal plasma profiles. Since the fusion reaction of interest for the JET discharge is the $D(D,n)^3\text{He}$ reaction with a neutron nominal birth energy of 2.45 MeV, the diagnostic measurement range was set to $E_{d,min} = 1$ MeV and $E_{d,max} = 5$ MeV. This was done to ensure capture of all the possible up- or downshift of the neutron nominal birth energy. The TOFOR and the NE213-scintillator diagnostic signals were comprised of 1000 measurements, respectively. Each of the 19 cameras of the KN3 neutron camera system was assumed to be able to resolve the [1, 5] MeV neutron energy range into only two measurement bins. The total number of synthetic measurements was thus 2038. A background noise level of 5 % and signal noise level of 7 % were added to the signals, to emulate real experimental data.

the fast-ion distribution in (E, p_m, R_m) orbit space penalizes large values relative to small values. The energy dependence of fast-ion distributions such as that of Figure 6.1 thus becomes difficult to reconstruct. More flat profiles for the fast-ion distribution are more likely according to the algorithm, when little measurement data is provided. It is envisioned that the concept of so-called *null orbits* could help overcome this issue. This is discussed further in section 6.2.

Third, the energy range of the high-energy tail (of the fast-ion distribution to be reconstructed) spans more than 2 MeV ($150 < E < 2400$ keV). This is a large energy range. It can be understood how 10 energy grid points (Figure 6.4) are likely not enough to accurately resolve the necessary phase-space details required for a good reconstruction. However, more phase-space points means more unknowns to reconstruct. The number of measurements then has to increase to preserve an accurate reconstruction. Hence, a conflict between phase-space resolution and number of measurements naturally arises. At a certain point, an increase in the number of phase-space grid points and measurements will also result in a problem of, potentially, inadequate computational resources (such as RAM memory and processing power).

6.2 Null measurements (null orbits)

When future reconstructions of the orbit-space fast-ion distribution from experimental measurements are to be performed, the available data is likely going to be scarce. A way of reducing the number of unknowns via reasonable assumptions would therefore be advantageous, as already discussed above and in [49, 84]. One way of doing so is by looking at the diagnostic signal and identifying measurement bins where the signal is zero ($s = 0$). Orbit-space points with non-zero weights ($w > 0$) are then deduced to be zero in terms of fast-ion distribution ($s = 0$ and $w > 0 \Rightarrow f = 0$) and can be removed from the equation. This is because, if there were fast ions populating those orbit-space points, since $s = wf$ and $w > 0$, we could not have that $s = 0$ [27, 30, 49]. Note that, for the argument to hold, we assume that $f \geq 0$ and $w \geq 0$, since $f < 0$ and $w < 0$ is unphysical. Thus, we can define null orbits as valid orbits (i.e possible orbits, given the magnetic equilibrium) that are not populated by a large enough number of fast ions to be detected.

In practice, instead of zero, we have to use $s < \epsilon_S$ and $w > \epsilon_W$ where ϵ_S, ϵ_W are small values. This has been illustrated in Figure 6.5. In the example, every row

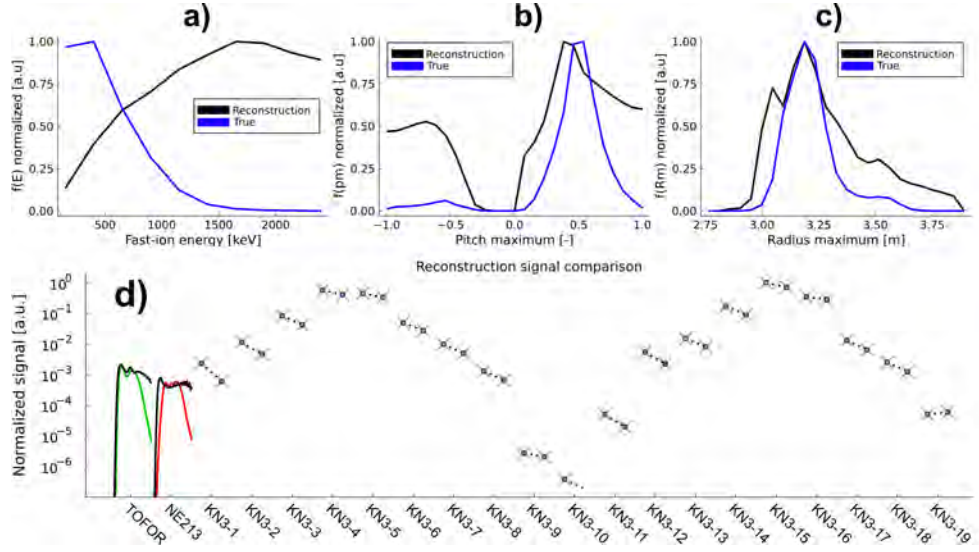


Figure 6.4: The reconstruction of the fast-ion distribution F_{rec} , using the synthetic diagnostic measurements in Figure 6.3 and orbit weight functions for the diagnostic measurement bins of interest. The orbit weight functions (and, by extension, F_{rec}) were computed on an orbit-space grid with size $10 \times 27 \times 25$ ($Exp_m \times R_m$). The ranges in E , p_m and R_m are shown in a), b) and c). The number of valid orbits for the orbit-space grid was 3210 (the number of unknowns to tomographically reconstruct). In a), b) and c), the E -, p_m - and R_m -dependence of the reconstructed and true fast-ion distributions are shown in black and blue, respectively. The two other coordinates have been integrated out in each of the plots. In d), the normalized S and WF_{rec} signals are shown in colors and black, respectively. For the KN3 neutron camera signals, the WF_{rec} signals are plotted as x-crosses.

$$\begin{array}{c}
 \left[\begin{array}{c}
 \textcircled{< \epsilon_S} \\
 \epsilon_S \\
 > \epsilon_S \\
 \vdots \\
 > \epsilon_S \\
 > \epsilon_S \\
 \textcircled{< \epsilon_S}
 \end{array} \right] = \begin{array}{c}
 \left[\begin{array}{ccccccc}
 < \epsilon_W & \epsilon_W & \dots & \textcircled{> \epsilon_W} & < \epsilon_W & \epsilon_W & \\
 \epsilon_W & > \epsilon_W & \dots & \epsilon_W & < \epsilon_W & \epsilon_W & \\
 < \epsilon_W & > \epsilon_W & \dots & > \epsilon_W & \epsilon_W & < \epsilon_W & \\
 \vdots & \vdots & \dots & \vdots & \vdots & \vdots & \\
 \epsilon_W & < \epsilon_W & \dots & > \epsilon_W & \epsilon_W & \epsilon_W & \\
 < \epsilon_W & \epsilon_W & \dots & < \epsilon_W & < \epsilon_W & < \epsilon_W & \\
 < \epsilon_W & < \epsilon_W & \dots & < \epsilon_W & < \epsilon_W & \textcircled{> \epsilon_W}
 \end{array} \right]
 \left[\begin{array}{c}
 o_1 \\
 o_2 \\
 \vdots \\
 \textcircled{o_{N-2}} \\
 \textcircled{o_{N-1}} \\
 \textcircled{o_N}
 \end{array} \right]
 \end{array}
 \end{array}$$

S
W
F

Figure 6.5: The measurements with an amplitude smaller than ϵ_S (red circles) are identified as null measurements. The corresponding orbit weight function is then scanned for weights larger than ϵ_W (blue circles). The corresponding elements of the vectorized fast-ion distribution are then identified as null orbits (orange circles).

of the weight matrix W corresponds to a 3D orbit weight function that has been reshaped into a 1D array.

For a diagnostic measurement bin where $s < \epsilon_S$, the orbit weight function can be reshaped back into its 3D-array format and the orbit-space coordinates of the null orbits can be examined for e.g. slices of constant fast-ion energy. This has been done in Figure 6.6. We can observe how the (p_m, R_m) coordinates with too large orbit weights are identified as 'null-orbit coordinates', that are likely to correspond to unpopulated orbits in terms of fast-ion distribution. Via this visual method, an overview of where the null orbits are located in orbit-space can be gained. The null measurements ($s < \epsilon_S$) are often found at the extrema of a spectrum, with the nominal diagnostic measurement value (roughly) in the middle. This is because the fast-ion distribution is often monotonically decreasing in energy, which results in most of the signal ending up at, and close to, the nominal diagnostic measurement value. The presence of null orbits thus often grows as we look at increasingly high fast-ion energies. This is because large energies are required to be able to produce an up-/down-shift of the nominal diagnostic measurement value to the extrema of the spectrum.

The method of including null orbits as prior information to the tomographic reconstruction of orbit-space fast-ion distributions was attempted during this project. However, the right thresholds were not accurately found, resulting in

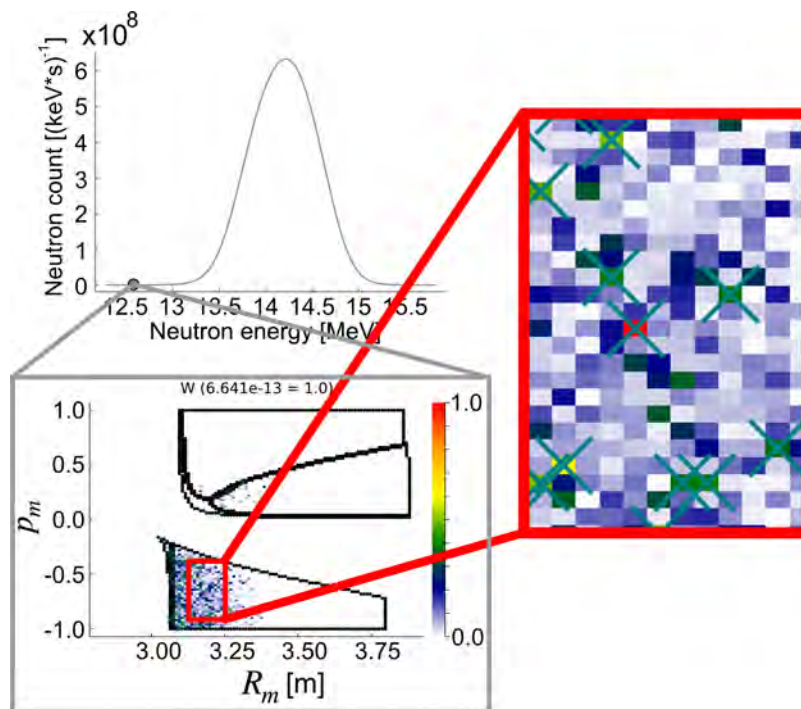


Figure 6.6: The orbit weight function for a signal measurement (gray dot) below a certain threshold (ϵ_S) can be examined slice-by-slice in terms of fast-ion energy. The (p_m, R_m) coordinates of weights above another threshold (ϵ_W) are identified as null-orbit coordinates (crosses).

either too few or too many orbit-space coordinates being labelled as null-orbit coordinates. This could naturally be improved upon, but there was simply not enough time during the project to do so.

Given the prospect of null orbits, is there something else we could do to facilitate the successful reconstruction of the orbit-space fast-ion distribution from diagnostic measurements? In short: yes, there is. However, we must first examine the measurements themselves. An important question would be: 'Does increasing the ratio of the number of measurements to the number of unknowns result in a better tomographic reconstruction?' As we shall discuss in the next section, the answer might *not* necessarily be 'yes'.

6.3 Importance of varying sightlines

At first sight, the problem of where the sightline of a fast-ion diagnostic should run through the plasma might seem trivial. As long as the poloidal projection of the sightline runs through the plasma center, a good detection of signals originating from the fast-ion distribution would seem to be ensured (see for example Figure 1.3). However, as was discussed in [85](H. Järleblad *et al*, Nucl. Fusion, *to be submitted*, Paper IV), that does not have to be the case. As can be seen in Figure 6.7, some valid orbits are localized away from the magnetic axis. If a diagnostic sightline such as that of TOFOR (e.g. Figure 6.2) is used to obtain e.g. neutron measurements, it will completely miss neutrons originating from fast-ion orbits such as those in Figure 6.7. However, as can be seen in Figure 1.3, the fast-ion distribution is often heavily peaked at the magnetic axis. Orbits such as those in Figure 6.7 are therefore relatively unpopulated. In addition, the temperature and density profiles of the thermal plasma are often approximately monotonically decreasing outwards from the magnetic axis. Given the above, most (but not all) of the diagnostic signals involving the fast-ion distribution can be expected to originate from the orbits localized around the magnetic axis. However, the inversion algorithms that are utilized to reconstruct the fast-ion distribution from diagnostic measurements have no information about this fact. This might result in inaccurate tomographic reconstructions.

If we wanted to ensure that our diagnostic LOS is able to observe all of the fast-ion distribution, we could simply orient a sightline that poloidally crosses through the equatorial midplane of the fusion plasma, as has been illustrated in Figure 6.8. This would ensure that, at least parts of, all fast-ion orbits are

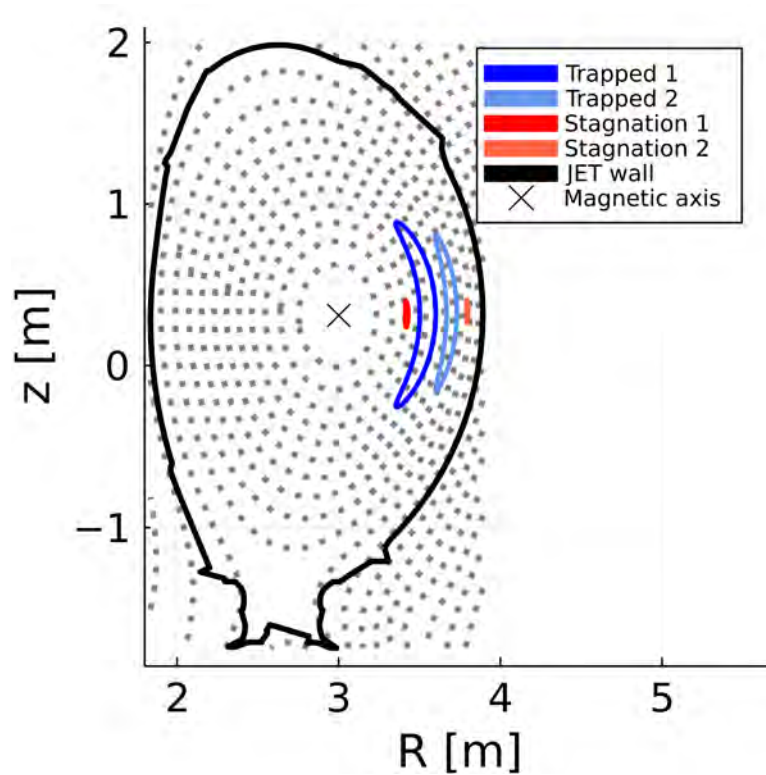


Figure 6.7: Four examples of valid fast-ion orbits that are localized away from the magnetic axis. The energy was arbitrarily set to $E = 250$ keV for all of them. The $(p_m[-], R_m[m])$ coordinates are $(0.25, 3.6)$ and $(0.18, 3.73)$ for trapped orbits 1 and 2, and $(0.07, 3.43)$ and $(0.05, 3.8)$ for stagnation orbits 1 and 2, respectively. JET equilibrium 96100 at 13 seconds. The magnetic flux surfaces are depicted as gray dots.

observed by the diagnostic, since all (standard) fast-ion orbits cross the equatorial midplane at some point. Would an LOS like the one in Figure 6.8 be able to (theoretically) ensure a sufficient set of measurements for reconstructing the full fast-ion distribution in (E, p_m, R_m) orbit space? Unfortunately, that is not necessarily so.

For the next discussion, we have to introduce the so-called orbit *weight average* $w(E_{d,1}, E_{d,2})$. The orbit weight average can be computed as follows:

1. Compute the orbit weight function $w(E_{d,1}, E_{d,2}, E, p_m, R_m)$.
2. Average over all orbit-space grid points:

$$\bar{w}(E_{d,1}, E_{d,2}) = \left(\int dE dp_m dR_m \right)^{-1} \int w(E_{d,1}, E_{d,2}, E, p_m, R_m) dE dp_m dR_m$$

The orbit weight average can be viewed as the synthetic diagnostic signal, given only the orbit-space variation of the orbit weight function. In addition, we can examine the orbit weight average for each orbit type as

$$\bar{w}_h(E_{d,1}, E_{d,2}) = \left(\int_h dE dp_m dR_m \right)^{-1} \int_h w(E_{d,1}, E_{d,2}, E, p_m, R_m) dE dp_m dR_m \quad (6.1)$$

where $h = \text{co-passing, trapped, etc}$ and the integral \int_h is taken over topological region for orbit type h . By comparing $\bar{w}_h(E_{d,1}, E_{d,2})$ for the different orbit types, we can examine how relatively sensitive a measurement in $(E_{d,1}, E_{d,2})$ is to the different orbit types, on average. This has been done for a set of diagnostic measurement bins $([E_{1,d}, E_{2,d}], [E_{2,d}, E_{3,d}], \dots, [E_{n-1,d}, E_{n,d}])$ for a vertical and oblique line-of-sight in Figure 6.9a and 6.9b, respectively.

As we can observe in Figure 6.9, the set of orbit weight averages is almost symmetric with respect to the nominal measurement bin $E_{\text{nominal}} = 14.1$ MeV for the vertical line-of-sight, and asymmetric for the oblique line-of-sight. This means that, for the vertical line-of-sight, a measurement at $E_{\text{nominal}} + \Delta E_d$ will contain the same information about the ratio between populated co- and counter-going orbits as a measurement at $E_{\text{nominal}} - \Delta E_d$ (where ΔE_d is an arbitrary number)(approximately). For the oblique line-of-sight, as can be seen in Figure 6.9b, this is not the case. Measurements on one side of E_{nominal} will contain more information about co-going fast ions and measurements on the other side

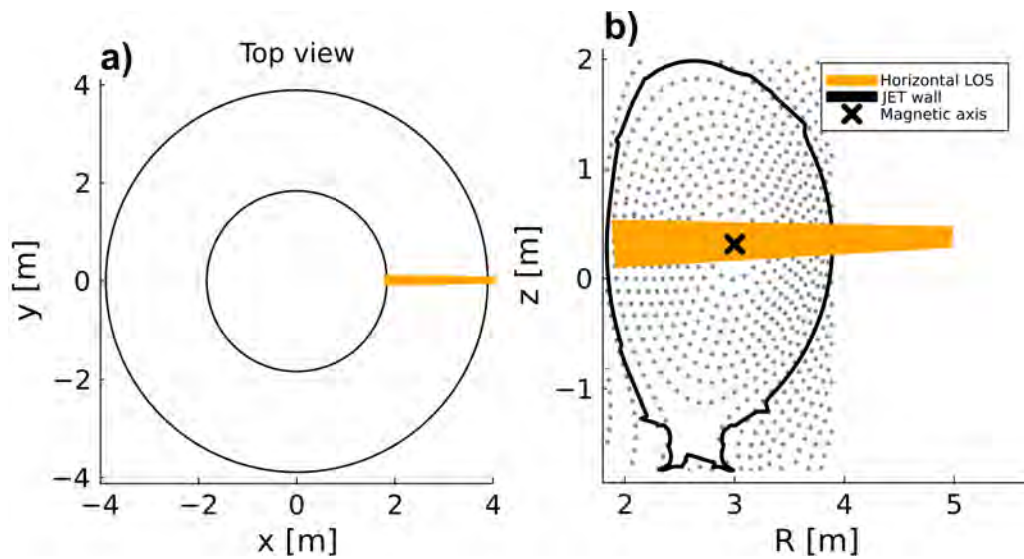


Figure 6.8: An illustration of a) the top view and b) the poloidal projection of an imaginary fast-ion diagnostic with a perpendicular line-of-sight at JET. The flux surfaces of the magnetic equilibrium of JET shot 96100 at 13 seconds have been included in b) as gray dots for reference.

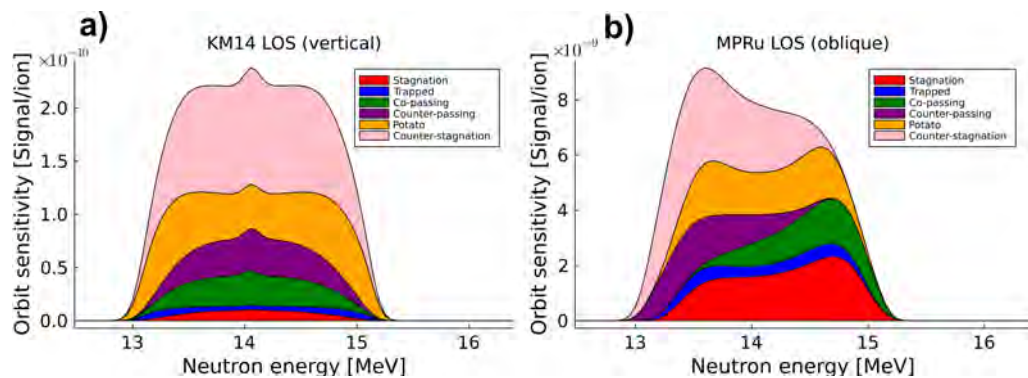


Figure 6.9: The orbit weight averages for each orbit type for a) a vertical and b) an oblique LOS, corresponding to the sightlines for the KM14 [82] diagnostic (a neutron diamond matrix for DT-neutrons with approximately the same vertical LOS as TOFOR) and the MPRu [75] diagnostic, respectively. The plots are not cumulative; the areas should be compared, not the y-axis values. JET shot 99500 at 7.44 seconds. TRANSP ID 99500V05.

of E_{nominal} will contain more information about counter-going fast ions. However, as discussed in previous chapters, for neutron fast-ion diagnostics in practice, the signal in measurement bins with $E_d < E_{\text{nominal}}$ will be dominated by contributions originating from neutrons with down-scattered energies. Therefore, measurement bins with $E_d < E_{\text{nominal}}$ are generally unusable for the reconstruction of the fast-ion distribution from neutron measurements.

Given the discussion above, it is possible to envision a set-up of diagnostic sightlines that, when combined, would likely have the potential to provide (neutron) measurements with enough information to reconstruct the full fast-ion distribution function. Such a set-up has been illustrated in Figure 6.10. With an assumed counter-clockwise co-going direction (viewed from above), the measurement bins with $E_d > E_{\text{nominal}}$ of diagnostic 1 (orange-colored LOS) will be more sensitive to co-going fast ions. For diagnostic 2 (blue-colored LOS), the corresponding measurement bins ($E_d > E_{\text{nominal}}$) will be more sensitive to counter-going fast ions. The conclusions for diagnostics 1 and 2 would naturally be the same for a clockwise co-going direction (viewed from above), but with flipped information content. Also, the JET tokamak was used as example, but the conclusions would hold for tokamaks in general.

Together, the $E_d > E_{\text{nominal}}$ measurement bins of diagnostic 1 and 2 should contain the necessary information for reconstructing both the co- and counter-going orbits of the fast-ion distribution. Diagnostic 3 (green) is included to provide a vertical sightline for reference; the LOS is placed so as to view both the HFS and LFS of the magnetic axis.

Let's imagine that we have an optimal set-up of diagnostic sightlines, but that we still do not have enough measurements to be able to reconstruct the full fast-ion distribution. Is there anything that we could do to include additional physics as prior information, which could improve the reconstruction? There are options [27, 86], and in section 6.4 we will explore yet another possible source of prior information envisioned as a result of this work.

6.4 Magnetic flux surfaces in (E, p_m, R_m) coordinates

In tokamaks, the fast-ion distribution can be expected to be approximately constant along the magnetic flux surfaces, compared to the perpendicular direction. Is there a way to use this fact as prior information in a reconstruction of the fast-ion orbit-space distribution function? The short answer is: possibly. If one

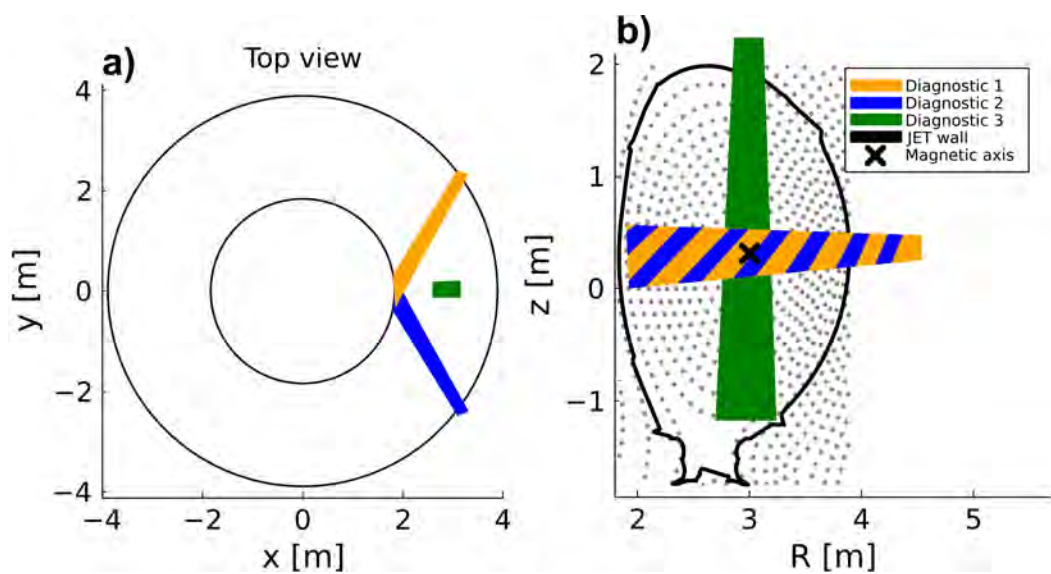


Figure 6.10: An illustration of a hypothetical set of fast-ion diagnostic sightlines, a) viewed from above and b) projected onto the poloidal plane. The poloidal projections of diagnostic 1 and 2 would look similar; this has been illustrated with a striped orange-blue color in b). The detectors of diagnostic 1 and 2 are envisioned to be placed on the LFS. The magnetic flux surfaces of JET shot 96100 at 13 seconds have been included for reference, depicted as gray dots.

could find a way to define magnetic flux surfaces in e.g. (E, p_m, R_m) orbit space, a suitable regularizer could be created for the (E, p_m, R_m) coordinates corresponding to the same magnetic flux surfaces. In this work, one way of mapping magnetic flux surfaces from (R, z) to (E, p_m, R_m) coordinates was developed. This method is discussed below.

Magnetic flux surfaces in tokamaks can be described via a set of (R, z) points. Thus, in 4D (E, p, R, z) guiding-centre phase space, the magnetic flux surfaces can be thought of as hyper-tubes that would look the same no matter which 3D cube of constant energy you look at. Such a 3D cube with a 3D cut of a flux-surface hyper-tube has been illustrated in Figure 6.11. In terms of fast-ion orbits, one could interpret a magnetic flux surface as a collection of orbits that all intersect this hyper-tube at some point along their trajectories. Therefore, to map a magnetic flux surface from (R, z) to (E, p_m, R_m) , one could take all the (R, z) points along a flux surface, compute the resulting orbits for all possible pitch and energy values, and identify their respective (E, p_m, R_m) coordinates.

This has been done in Figure 6.12. We can observe in Figure 6.12b, c and d how the width of the R_m -range of orbits that intersect the $\rho_{pol} = 0.5$ ($\sim R_m = 7.4$ m) magnetic flux surface increases with fast-ion energy. This is because the deviation from magnetic flux surfaces increases as the fast-ion energy increases, thus resulting in a broader R_m -range of fast-ion orbits that intersect the $\rho_{pol} = 0.5$ flux surface.

In future tomographic reconstructions of the fast-ion orbit-space distribution from diagnostic measurements, it is envisioned that many magnetic flux surfaces be mapped to (E, p_m, R_m) coordinates. These magnetic flux surfaces in orbit space can then serve as the basis for a suitable regularization scheme, that incorporates the fact that the fast-ion distribution can be expected to be approximately constant along magnetic flux surfaces. More precisely, the gradients along flux surfaces are likely much smaller than across flux surfaces.

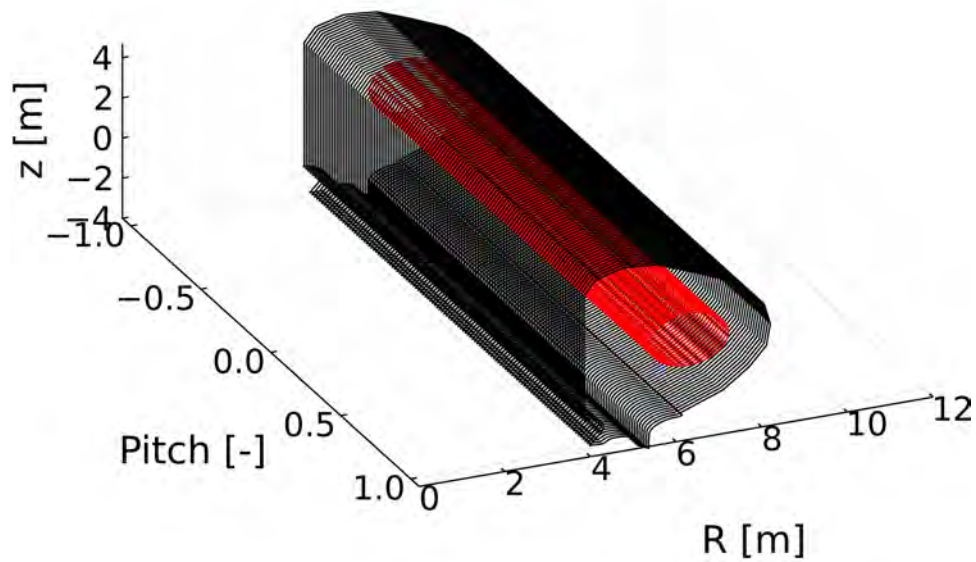


Figure 6.11: An example of how to interpret magnetic flux surfaces in (E, p, R, z) phase space. For a 3D cube of constant energy E , the magnetic flux surface (red) takes the shape of a tube running from pitch -1 to $+1$. The tokamak first wall has been included in black for reference. ITER 80 MW heating test magnetic equilibrium with $B_0 = 5$ T, magnetic flux surface at $\rho_{pol} = 0.5$.

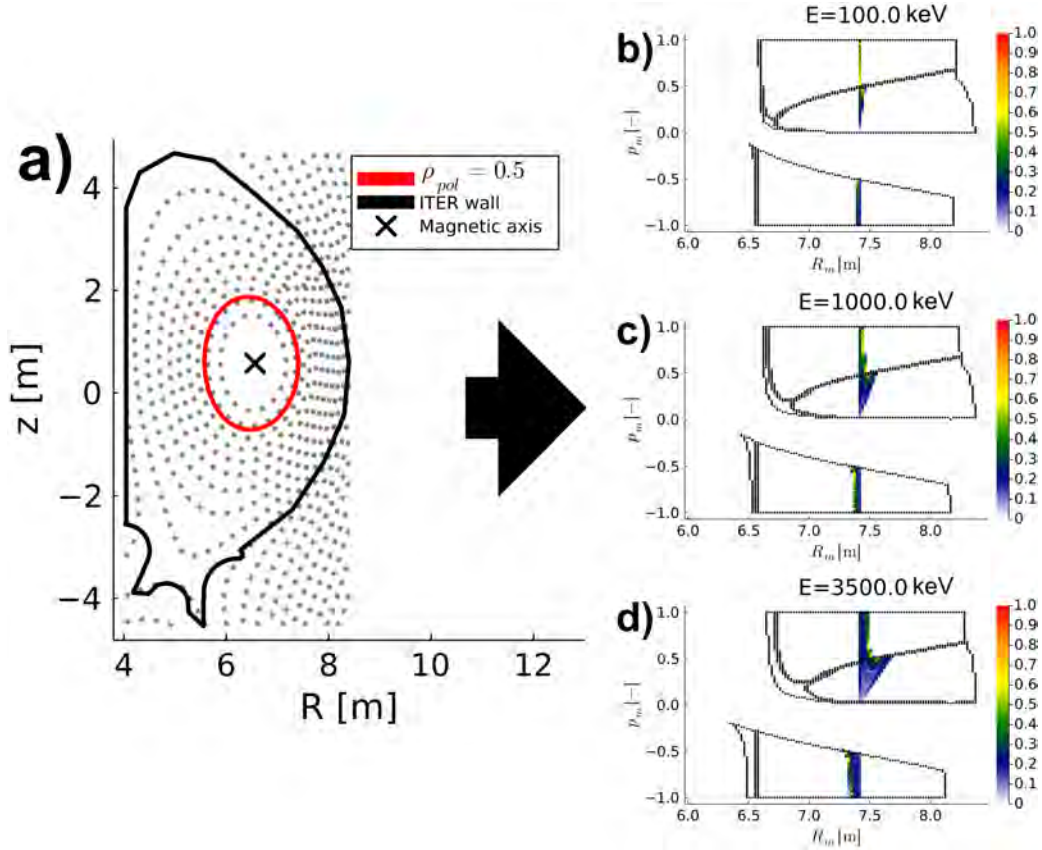


Figure 6.12: An illustration of a magnetic flux surface with $\rho_{pol} = 0.5$ in a) (R, z) coordinates that has been mapped to (E, p_m, R_m) coordinates. The magnetic flux surface was discretized into ~ 700 (R, z) coordinates and, for every fast-ion energy level, the $(-1, 1)$ pitch range was discretized into 101 points. In b), c) and d), (R_m, p_m) coordinates with higher values (closer to 1.0 on the color bar) correspond to orbits on which the fast ion intersects the $\rho_{pol} = 0.5$ flux surface more often as it goes around the orbit. The opposite is true for (R_m, p_m) coordinates with lower values (closer to 0.0 on the color bar). Orbits computed for α -particles in ITER test equilibrium with 80 MW heating and $B_0 = 5$ T.

CHAPTER 7

The Orbit Weight Computational Framework (OWCF)

This chapter will briefly discuss the computational framework that was developed during this project; it is known as the orbit weight computational framework (OWCF). A detailed discussion can be found in H. Järleblad *et al* (Comp. Phys. Comm., Submitted, 2022), which has been included as appendix Paper **III** to this dissertation. This chapter will therefore focus on the background of the OWCF and some of the parts that did not make the Comp. Phys. Comm. manuscript, as well as future work for the OWCF. The interested reader is kindly referred to the Comp. Phys. Comm. manuscript in the appendix for a technical and scientific discussion.

7.1 Background

During the beginning of this project, it was realized that many similar computations would need to be performed. The methods for computing orbit weight functions for neutron and gamma-ray emission spectroscopy were being developed, and a trial-and-error approach was adopted to make progress. Via this process, many minor 'bugs' and errors were being corrected as soon as they were identified. Naturally, such a repetitive process is made efficient via standardization. Templates for testing different scenarios were developed, as well as templates for submitting batch jobs to a computational cluster. Already at this early stage, a framework-like structure started to take shape. However, it was yet too early to stand on its own as a code framework.

Shortly after, it was realized that an intuition for the topology of (E, p_m, R_m) orbit space needed to be developed. This was because e.g. the sensitivity patterns of the orbit weight functions needed to be understood. An often efficient way to build intuition is via interaction and real-time feedback. Therefore, interactive applications were developed in which the user could change the (E, p_m, R_m)

coordinate and the corresponding guiding-center orbits would be computed and visualized in real time. It was also during this stage that specific color-coding for the different orbit types were developed, as well as ways of identifying the boundaries between topological regions. These were quickly incorporated into the applications.

Before long, a structure of standardized scripts and interactive applications had started to take shape. While the work of this project was almost completely focused on developing orbit weight functions for NES and one-step GRS, a small amount of time was allocated to solidify this structure into a framework. At the time, there was no way to know if the work put into this code framework would be worthwhile. This concern was (rightfully) expressed by the supervisors. Nevertheless, the work continued solely on the initiative, and overtime work, of the PhD student.

In the final year of the project, it became clear that a positive result regarding the reconstruction of the JET fast-ion distribution using synthetic measurements was not possible to obtain within the timeframe of the project. The likely reasons for this was discussed in Chapter 6. To add further value to the project, it was then decided that the OWCF code framework be further developed and that a pertaining publication be submitted to the journal of Computer Physics Communications. By this point, this was a straightforward task. The structure and scope of the OWCF had already been subsequently refined and broadened, making it suitable to be published as a standalone code framework.

7.2 Compatibility with computational clusters

The OWCF is usable on supercomputers, also known as computational clusters. As of version 1.0 of the OWCF (the version submitted to Comp. Phys. Comm.), the framework template files are written to be used on SLURM [87, 88] computational clusters. This is because the OWCF was developed and tested on a SLURM computational cluster. In the future, in later versions of the framework, it will be straightforward to add template files that would make the OWCF usable on other types of computational clusters (e.g. PBS [89]).

To use the OWCF on a SLURM cluster, the user can utilize a Shell [90, 91] (.sh) template submit file. The SLURM cluster manager will then execute the OWCF start file via the .sh submit file, as has been depicted in Figure 7.1.

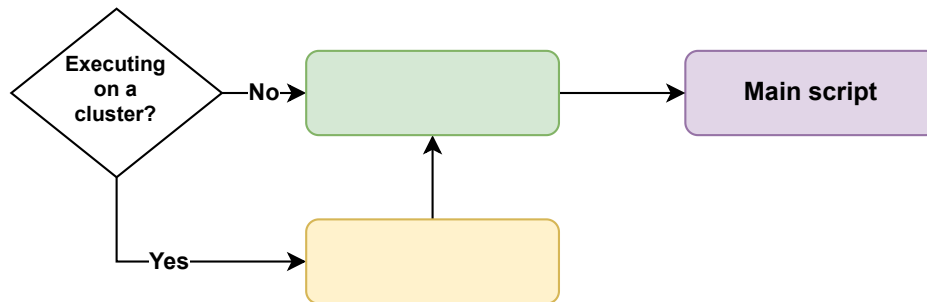


Figure 7.1: A graphical illustration of how the OWCF scripts are run on computational clusters, compared to on local machines. On computational clusters, the submit file (.sh) communicates with the workload manager, and then executes the OWCF start file (.jl) from within.

7.3 Orbit web app

The orbit web app is an interactive plotting tool that allows the user to visualize individual guiding-center orbits in detail. As Figure 7.2 shows, the user can change the (E, p_m, R_m) coordinate by modifying the 'E', 'pm' and 'Rm' input slots. The app will then respond by computing and displaying the corresponding guiding-center orbit in real-time. The 'i' slider can then be used to change what fraction of the guiding-center orbit trajectory is being plotted. This can be useful to e.g. examine the pitch value at a specific point along the orbit trajectory. It can also be used by students, to develop an intuition for what the motion of fast ions in tokamaks looks like for different orbit coordinates. An animation of the motion of the fast ion as it travels around the orbit trajectory is displayed in the bottom right-hand plot.

7.4 Constants-of-motion web app

Even though the OWCF mainly uses the (E, p_m, R_m) coordinates for computation and analysis of guiding-center orbits, the user also has the option to examine certain results in the $(E, \mu, P_\phi; \sigma)$ constants-of-motion coordinates. One tool that provides this utility is the so-called **comWebApp.jl** web application. A screenshot of the comWebApp can be observed in Figure 7.3. With this web application, the user can visualize fast-ion orbits in a fully customizable Solov'ev magnetic equilibrium. The following parameters can be interactively changed: the inverse aspect ratio, the plasma elongation, the triangularity, the minor radius, the (vacuum) magnetic field on axis, the fast-ion energy E , the magnetic moment

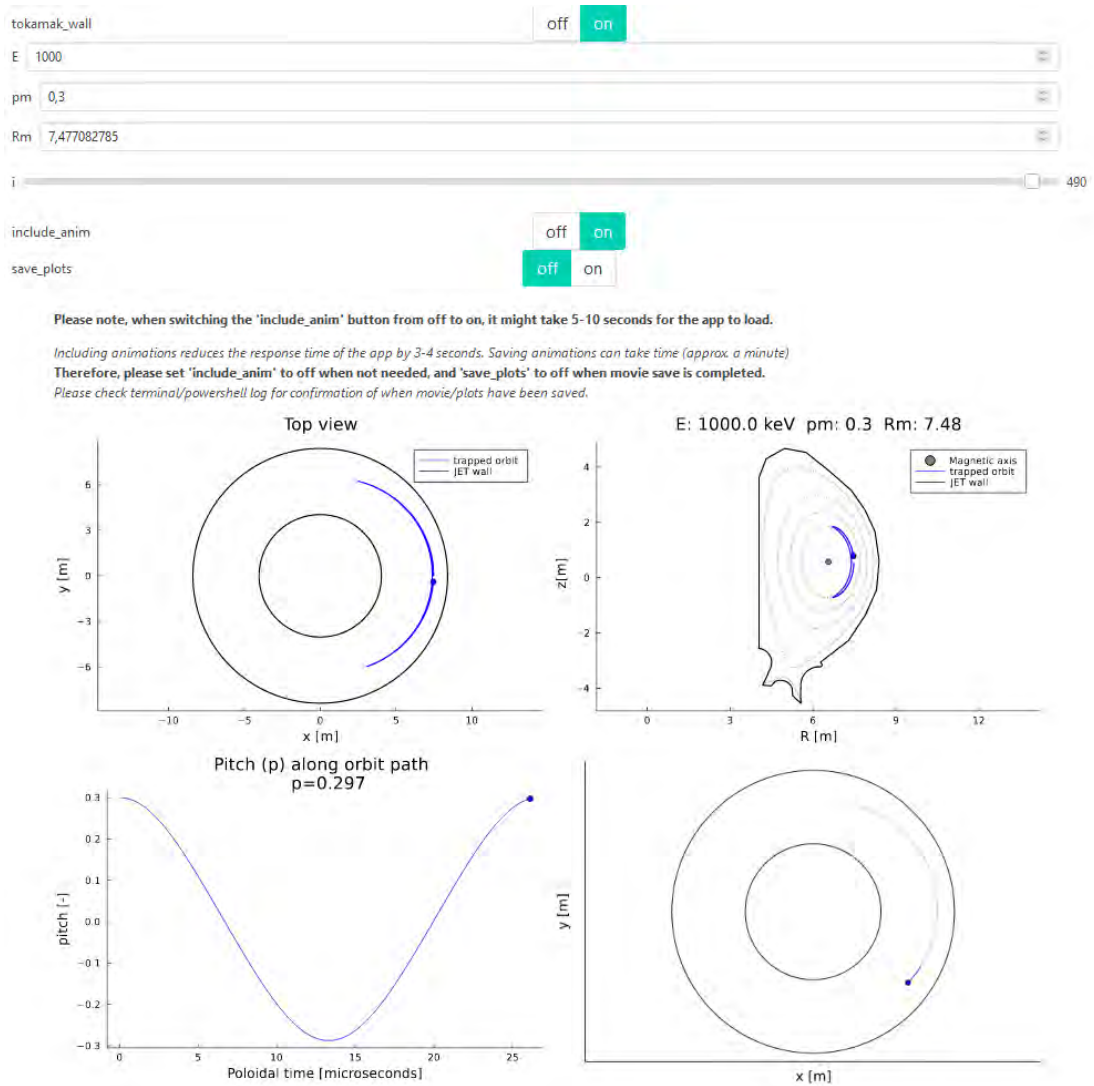


Figure 7.2: A screenshot of the orbitWebApp.jl web application, included with the OWCF (as of version 1.0). The magnetic equilibrium is an ITER test equilibrium with 80 MW of heating.

μ and the toroidal canonical angular momentum P_ϕ . When these parameters are changed, the app will respond by computing a new Solov'ev equilibrium and fast-ion orbit in real-time, and plot them. If there are two fast-ion orbits corresponding to the same (E, μ, P_ϕ) triplet, the app will plot both of them. The comWebApp can be used both as a quick investigative research tool, or as a pedagogical tool for teaching.

7.5 Future work

In future versions of the OWCF, some updates are already planned. These include:

- To optimize the performance of all scripts and apps of the OWCF. As of version 1.0 of the OWCF, there are several scripts and apps that were written to ensure functionality, but not optimal performance. These include some of the OWCF web applications, that have a long loading time. To ensure that the OWCF stays relevant in the future, performance upgrades should be conducted.
- To enable the user to compute orbit weight functions using TRANSP [32] output data without a NUBEAM [33] output file. As of version 1.0 of the OWCF, the user has to input both a TRANSP (.cdf) shot file and a NUBEAM fast-ion output file for the OWCF algorithm to know which timepoint to extract data from. In a future version of the OWCF, the user should be able to specify a timepoint without the need for a NUBEAM output file.
- To include a script that automatically transforms magnetic flux surfaces from (R, z) coordinates into (E, p_m, R_m) orbit space. Additionally, the **distrWebApp.jl** should be upgraded to allow for parallel viewing of many 3D orbit-space quantities, e.g. many transformed magnetic flux surfaces. This could enable an increased understanding of magnetic flux surfaces in orbit space.
- To upgrade the **ps2WF.jl** script to be able to compute analytical high-resolution WF signals. As of version 1.0 of the OWCF, the ps2WF.jl script can not compute WF signals using analytical orbit weight functions, i.e. that have been computed from projected velocities. This could be implemented in future versions, to enable comparison of high-resolution WF signals from numerical and analytical orbit weight functions.
- To improve the barycentric interpolation algorithm used to convert a TRANSP fast-ion distribution, defined on a spiral grid in (R, z) , to a regular

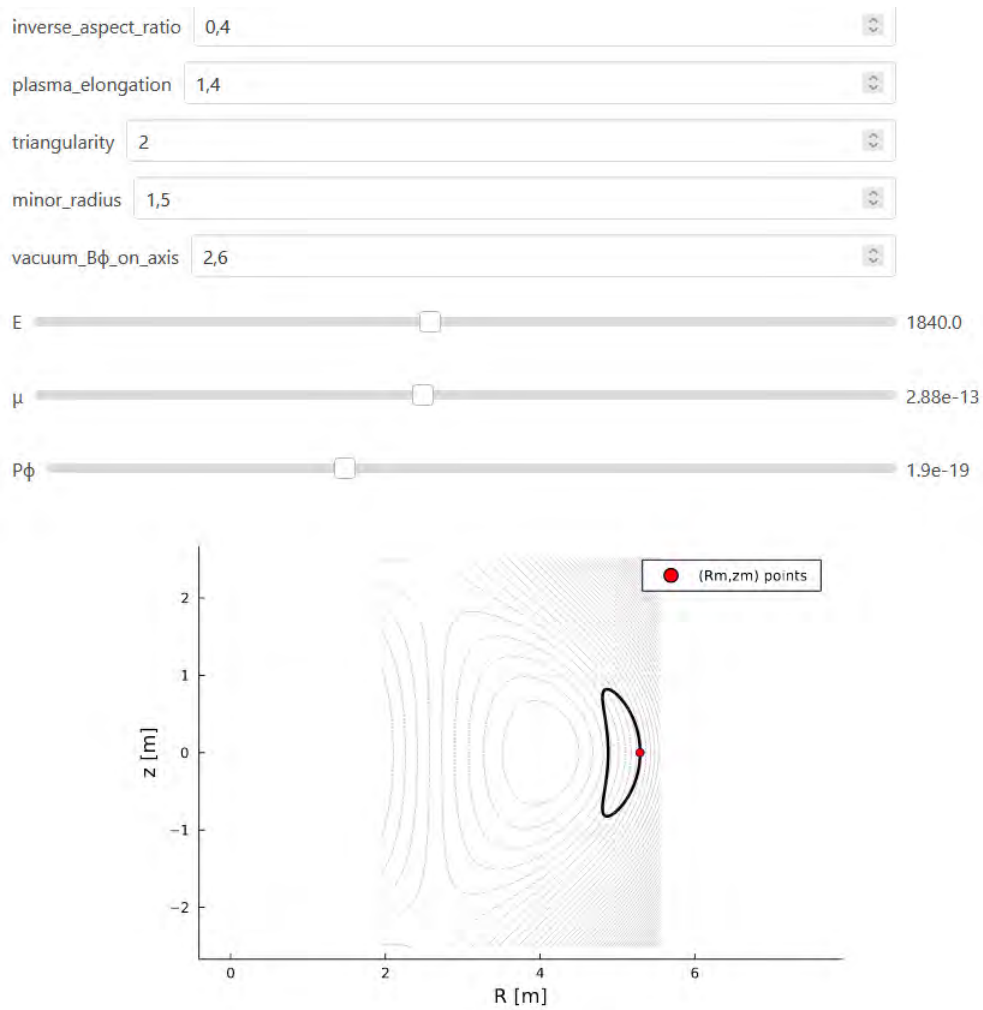


Figure 7.3: A screenshot of the `comWebApp.jl` web application. The user can interactively modify the parameters for the Solov'ev magnetic equilibrium, as well as the constants-of-motion. The app will then respond by plotting contours of the corresponding Solov'ev equilibrium, and the fast-ion guiding-center orbit(s).

grid in (E, p, R, z) . This would result in smoother fast-ion distributions, enabling more exact analysis.

- To improve the mapping of e.g. orbit weight functions from (E, p_m, R_m) to $(E, \mu, P_\phi; \sigma)$. As of version 1.0 of the OWCF, points on the very edge of the orbit-space regions of valid orbits might not be mapped sufficiently exact. The error goes to zero as the grid resolution increases. However, the problem could be avoided all together by including a nearest neighbour extrapolation scheme for points just outside the orbit-space regions of valid orbits.
- To include the option for the user to provide an instrumental response function matrix as input to e.g. **calcOrbWeights.jl**. The OWCF could then compute orbit weight functions, run them through the instrumental response function matrix and then save the resulting weight functions in an additional output file.

To some degree, all of the future work listed above could have been performed during this project, but there was simply not enough time to do so. In addition, there is also future work of larger size, that could be performed to extend and upgrade the OWCF. This includes:

- To design and write new IO pipelines and scripts, to be able to connect additional synthetic diagnostics codes with the OWCF, e.g. FIDASIM [92, 93]. As stated in the Comp. Phys. Comm. manuscript in the appendix, version 1.0 of the OWCF is ready to send orbit data to additional synthetic diagnostics codes. However, to correctly prepare input and process output from additional synthetic diagnostics codes, new scripts within the OWCF are naturally going to have to be designed and written.
- To enable the input of diagnostic sightlines in more file formats than only the LINE21 [94] output files, when using the OWCF together with the DRESS [80] code. This would increase the flexibility of the OWCF in general, and the computation of NES and GRS quantities in particular. To achieve this, a future OWCF script named e.g. **createSightline.jl** can be imagined, that outputs a .jld2 (or .h5/.hdf5) file readable by the OWCF-DRESS interface. Via the inputs to createSightline.jl, the user could fully customize the geometry of a synthetic diagnostic sightline. It can also be imagined that such input could be provided via a file, e.g. a MATLAB-data file (.mat).
- To enable the computation of NES and GRS spectra from two-step fusion

reactions. This would include reactions such as the ${}^9\text{Be}(\alpha,n){}^{12}\text{C}$ reaction, which happens in two steps. This future work is already planned and will likely be performed in the near future. The options likely include to upgrade the DRESS code or to connect the OWCF with the GENESIS [71,95] code.

CHAPTER 8

Conclusion and outlook

Prior to this work, the methods for reconstructing the fast-ion distribution from diagnostic measurements in terms of fast-ion orbits had just been developed for fast-ion D-alpha spectroscopy and neutral particle analyzers. This was done using orbit weight functions. The immediate goal of this project was to develop orbit weight functions for neutron emission and gamma-ray spectroscopy diagnostics. This was completed and results were published in both the journal of Review of Scientific Instruments (H. Järleblad *et al*, 2021, Paper I) and a special issue of Nuclear Fusion (H. Järleblad *et al*, 2022, Paper II). However, for gamma-ray spectroscopy, the more complicated two-step reactions were deferred to future work.

A code framework for computing orbit weight functions was built as a foundation to facilitate such future advancement. The so-called Orbit Weight Computational Framework (OWCF) provides a starting point for the computation of orbit weight functions. The trajectories of guiding-center orbits are weighted, effectively functioning as a fast-ion distribution function, and can be sent to synthetic diagnostics codes via customized I/O pipelines. Furthermore, the OWCF also functions as a hub for easy and accessible analysis. This is enabled via e.g. user-friendly and customizable template scripts, as well as interactive web applications that re-compute and re-plot figures in real-time.

The development of such analysis tools would not have been possible had it not been for the work done by L. Stagner [38, 39, 56], which served as the starting point for this project. However, albeit foundational, the work of L. Stagner was expanded upon in various ways. For example, prior to this project, fast-ion orbits completely confined to the high-field side area of the magnetic axis had not been considered relevant for (E, p_m, R_m) orbit-space analysis, i.e. fast-ion orbits with $R_m < R_{axis}$ (where R_{axis} is the major radius position of the magnetic axis). This project identified such orbits as counter-stagnation orbits

and showed that their topological region grows with increasing fast-ion energy. If a diagnostic sightline views the co-going direction, and measurement bins for heavily up-shifted nominal birth energies are examined, the contribution from counter-stagnation orbits could be significant. In future fusion plasmas with a significant fusion-born fast-ion population, because the total birth distribution of fusion products is approximately isotropic, the counter-stagnation orbits might constitute a considerable fraction of the fast-ion distribution.

This project continued to break new ground by introducing the concept of decomposing a diagnostic signal according to the contribution from the different fast-ion orbit types. This orbit-splitting of a diagnostic signal can be used to e.g. confirm heating schemes such as the three-ion heating scheme, where a relatively large population of high-energy co-passing orbits are created. It can also be used to provide an easy overview of which orbit types a diagnostic is able to observe, thus providing insight into the design of future fast-ion diagnostics.

Furthermore, the concept of mapping the poloidal and toroidal transit times for all fast-ion orbits was developed, thanks to an idea by M. Salewski. These maps can then be visualized interactively via a simple slice-by-slice approach in terms of constant fast-ion energy. As is described in the OWCF manuscript (H. Järleblad *et al*, *Submitted to Comp. Phys. Comm.*, Paper III), this can also be performed in (E, p, R, z) phase space. The tools can be used to e.g. interactively investigate which orbit types pass through a certain (R, z) point of a tokamak cross section, as well as their respective poloidal and toroidal times.

Using the OWCF tools developed during this project, an analysis of JET DT discharge 99965 was performed. As ICRH was switched off, a decrease in the (synthetic) signals of the KM14 diamond matrix and MPRu proton recoil diagnostics was observed. The diagnostic signals and the decrease were found to likely originate mostly from co-passing orbits. Even though the fast-ion distribution consisted mostly of trapped orbits, the orbit sensitivities of the diagnostics lifted the co-passing signal contribution up above the trapped signal contribution. The analysis is being prepared in a manuscript (H. Järleblad *et al*, Paper IV) to be submitted to the journal Nuclear Fusion.

Finally, there is plenty of future work that can be imagined following this PhD project. Some has already been mentioned in this chapter, and further future work includes the following. First, orbit weight functions for two-step fusion reactions

can be developed, such as the ${}^9\text{Be}(\alpha, n){}^{12}\text{C}^* \rightarrow {}^9\text{Be}(\alpha, n \gamma){}^{12}\text{C}$ reaction. This is imagined to be of great importance for reconstructing the α -particle distribution in e.g. JET and future ITER DT-plasmas. The process for computing such two-step orbit weight functions could be implemented in e.g. the OWCF. Continuing, there are several ways in which the OWCF can be further developed; including more optimized performance, I/O pipelines for more synthetic diagnostics codes and the usage of diagnostic sightlines described by other file formats than the LINE21 file format. Regarding the orbit weight functions, future work also includes new attempts at reconstructing the fast-ion orbit-space distribution in JET. With the new insights and methods discussed in Chapter 6, it is imagined that a successful reconstruction should be possible, given the right conditions and approach.

This PhD project has paved the way for future research in the area. The gained insights will help improve the understanding of the behaviour of fast ions in tokamak fusion plasmas. The orbit weight functions for neutron emission and gamma-ray spectroscopy diagnostics will help illuminate the relation between fast-ion orbits and diagnostic measurements. The OWCF will provide tools that enable more efficient, effective and pedagogical analysis of fast-ion orbits. This will help prepare the current and next generation of plasma physicists for the coming era of burning fusion plasmas. An era of fusion power plants and virtually limitless sustainable energy.

Bibliography

- [1] H. Järleblad *et al.* Fast-ion orbit sensitivity of neutron emission spectroscopy diagnostics. *Rev. Sci. Instrum.*, 92:043526, 2021.
- [2] H. Järleblad *et al.* Fast-ion orbit sensitivity of neutron and gamma-ray diagnostics for one-step fusion reactions. *Nucl. Fusion*, 62:112005, 2022.
- [3] We Finally Know How Much Energy Humans Actually Need to Live a Decent Life. <https://www.sciencealert.com/this-is-how-much-energy-we-all-need-to-fill-our-needs-and-live-a-modestly-decent-life>. Accessed 2022-01-25.
- [4] N.D. Rao *et al.* Energy requirements for decent living in India, Brazil and South Africa. *Nat. Energy*, 4:1025–1032, 2019.
- [5] Energy use per person, 2019. <https://ourworldindata.org/grapher/per-capita-energy-use>. Accessed 2022-01-25.
- [6] International Energy Agency. World Energy Outlook 2020, 2020.
- [7] John Wesson. *Tokamaks (3rd edition)*. Clarendon Press, Oxford, 2004.
- [8] M. Kikuchi, K. Lackner & M.Q. Tran. *Fusion Physics*. International Atomic Energy Agency, Vienna, Austria, 2012.
- [9] World Nuclear Association. Heat Values of Various Fuels. <http://precog.iiitd.edu.in/people/anupama>, October 2022.
- [10] International Energy Agency. OECD – Coal calorific values, October 2022.
- [11] H.-S. Bosch *et al.* Final integration, commissioning and start of the Wendelstein 7-X stellarator operation. *Nucl. Fusion*, 57:116015, 2017.
- [12] P. Brunzell *et al.* Initial results from the rebuilt EXTRAP T2R device. *Plasma Phys. Control. Fusion*, 43:1457, 2001.
- [13] U. Shumlak. Z-pinch fusion. *Journal of Applied Physics*, 127:200901, 2020.
- [14] K.F. McKenna and R.E. Siemon. Theta-pinch research at Los Alamos. *Nucl. Fusion*, 25:1267, 1985.
- [15] A. Boxer *et al.* Turbulent inward pinch of plasma confined by a levitated dipole magnet. *Nature Physics*, 6:207–212, 2010.

-
- [16] Editorial. Fusion news ignites optimism. *Nat. Photon.*, 15:713, 2021.
- [17] G.A. Wurden *et al.* Magneto-Inertial Fusion. *J Fusion Energ*, 35:69–77, 2016.
- [18] R.P. Taleyarkhan *et al.* Evidence for Nuclear Emissions During Acoustic Cavitation. *Science*, 295:1868–73, 2002.
- [19] E. Joffrin *et al.* Overview of the JET preparation for deuterium-tritium operation with the ITER like-wall. *Nucl. Fusion*, 59:112021, 2019.
- [20] R.S. Cohen *et al.* The electrical conductivity of an Ionized Gas. *Phys. Rev.*, 80(2):230, 1950.
- [21] L. Spitzer *et al.* Physics of Fully Ionized Gases. *American Journal of Physics*, 31 (11):890–891, 1963.
- [22] Max Planck Institute for Plasma Physics. Ohmic Heating. <https://www.ipp.mpg.de/1766292/oheizung>, October 2022.
- [23] Max Planck Institute for Plasma Physics. Neutral Particle Heating. <https://www.ipp.mpg.de/1766120/nteilchenheizung>, October 2022.
- [24] Max Planck Institute for Plasma Physics. High-frequency heating. <https://www.ipp.mpg.de/1766064/hfheizung>, October 2022.
- [25] S.D. Pinches *et al.* Observation and modelling of fast ion loss in JET and ASDEX upgrade. *Nucl. Fusion*, 46:S904–S910, 2006.
- [26] W.W. Heidbrink. Basic Physics of Alfvén instabilities driven by energetic particles in toroidally confined plasmas. *Physics of Plasmas*, 15:055501, 2008.
- [27] B. Madsen *et al.* Fast-ion velocity-space tomography using slowing-down regularization in EAST plasmas with co- and counter-current neutral beam injection. *Plasma Phys. Control. Fusion*, 62:115019, 2020.
- [28] W.W. Heidbrink and G.J. Sadler. The behaviour of fast ions in tokamak experiments. *Nucl. Fusion*, 34:535, 1994.
- [29] M. Salewski *et al.* Tomography of fast-ion velocity-space distributions from synthetic CTS and FIDA measurements. *Nucl. Fusion*, 52:103008, 2012.
- [30] B. Madsen *et al.* Tomography of the positive-pitch fast-ion velocity distribution in DIII-D plasmas with Alfvén eigenmodes and neoclassical tearing modes. *Nucl. Fusion*, 60:066024, 2020.
-

-
- [31] A. Bierwage *et al.* Representation and modeling of charged particle distributions in tokamaks. *Computer Physics Communications*, 275:108305, 2022.
- [32] Joshua Breslau, Marina Gorelenkova, Francesca Poli, Jai Sachdev, Alexei Pankin, and Gopan Perumpilly. TRANSP. [Computer Software] <https://doi.org/10.11578/dc.20180627.4>, jun 2018.
- [33] A. Pankin, D. McCune, R. Andre *et al.* The Tokamak Monte Carlo Fast Ion Module NUBEAM in the National Transport Code Collaboration Library. *CPC*, 159,3:157–184, 2004.
- [34] M. Salewski *et al.* Combination of fast-ion diagnostics in velocity-space tomographies. *Nucl. Fusion*, 53(6):063019, 2013.
- [35] M Salewski *et al.* On velocity-space sensitivity of fast-ion D-alpha spectroscopy. *Plasma Phys. Control. Fusion*, 56(10):105005, 2014.
- [36] M. Salewski *et al.* Velocity-space observation regions of high-resolution two-step reaction gamma-ray spectroscopy. *Nucl. Fusion*, 55(9):093029, 2015.
- [37] M. Salewski *et al.* Fast-ion energy resolution by one-step reaction gamma-ray spectrometry. *Nucl. Fusion*, 56(4):046009, 2016.
- [38] L Stagner and W.W. Heidbrink. Action-angle formulation of generalized, orbit-based, fast-ion diagnostic weight functions. *Phys. Plasmas*, 24:092505, 2017.
- [39] L. Stagner *et al.* Orbit tomography of energetic particle distribution functions. *Nucl. Fusion*, 62:026033, 2022.
- [40] W.W. Heidbrink *et al.* Phase-space sensitivity (weight functions) of 3 MeV proton diagnostics. *Plasma Phys. Control. Fusion*, 63:055008, 2021.
- [41] B Geiger *et al.* Fast-ion D-alpha measurements at ASDEX Upgrade. *Plasma Physics and Controlled Fusion*, 53(6):065010, 2011.
- [42] A.S. Jacobsen *et al.* Velocity-space sensitivity of neutron spectrometry measurements. *Nuclear Fusion*, 55(5):053013, 2015.
- [43] A.S. Jacobsen *et al.* Velocity-space sensitivities of neutron emission spectrometers at the tokamaks JET and ASDEX Upgrade in deuterium plasmas. *Review of Scientific Instruments*, 88(7):073506, 2017.
- [44] J Eriksson *et al.* Measuring fast ions in fusion plasmas with neutron diagnostics at JET. *Plasma Physics and Controlled Fusion*, 61(1):014027, 2018.
-

-
- [45] M. Nocente *et al.* Conceptual design of the radial gamma ray spectrometers system for α particle and runaway electron measurements at ITER. *Nuclear Fusion*, 57(7):076016, 2017.
- [46] B.S. Schmidt *et al.* Determining 1D fast-ion velocity distribution functions from ion cyclotron emission data using deep neural networks. *Review of Scientific Instruments*, 92(5):053528, 2021.
- [47] M. Salewski *et al.* On velocity space interrogation regions of fast-ion collective Thomson scattering at ITER. *Nucl. Fusion*, 51:083014, 2011.
- [48] M. Salewski *et al.* Measurement of a 2D fast-ion velocity distribution function by tomographic inversion of fast-ion D-alpha spectra. *Nucl. Fusion*, 54:023006, 2014.
- [49] M. Salewski *et al.* High-definition velocity-space tomography of fast-ion dynamics. *Nucl. Fusion*, 56:106024, 2016.
- [50] M. Salewski *et al.* MeV-range velocity-space tomography from gamma-ray and neutron emission spectroscopy measurements at JET. *Nucl. Fusion*, 57:056001, 2017.
- [51] M. Salewski *et al.* Alpha-particle velocity-space diagnostic at ITER. *Nucl. Fusion*, 58:096019, 2018.
- [52] M. Salewski *et al.* Diagnostic of fast-ion energy spectra and densities in magnetized plasmas. *JINST*, 14:C05019, 2019.
- [53] W.W. Heidbrink *et al.* Measurements of fast-ion acceleration at cyclotron harmonics using Balmer-alpha spectroscopy. *Plasma Phys. Control. Fusion*, 49:1457–1475, 2007.
- [54] J. Galdon-Quiroga *et al.* Velocity-space sensitivity and tomography of scintillator-based fast-ion loss detectors. *Plasma Phys. Control. Fusion*, 60:105005, 2018.
- [55] M. Salewski *et al.* Bayesian Integrated Data Analysis of Fast-ion Measurements by Velocity-Space Tomography. *Fusion Sci. Technol.*, 74:1-2:23–36, 2018.
- [56] Luke Stagner. *Inference of the fast-ion distribution function*. PhD thesis, University of California, Irvine, 2018.
- [57] B. Bigot. Progress toward ITER’s First Plasma. *Nucl. Fusion*, 59:112001, 2019.
- [58] Francis F. Chen. *Introduction to plasma physics*. Springer, New York, United States of America, 1974.
-

-
- [59] M. Salewski. *An Introduction to Fusion Plasma Physics*. Technical University of Denmark, Kgs. Lyngby, Denmark, 2022.
- [60] E. Noether. Invariante Variationsprobleme. *Nachrichten von der Gesellschaft der Wissenschaften zu Göttingen, Mathematisch-Physikalische Klasse*, 1918:235–237, 1918.
- [61] J.A. Rome and Y-K.M. Peng. The topology of tokamak orbits. *Nucl. Fusion*, 19:1193, 1979.
- [62] Y.V. Petrov and R.W. Harvey. A fully-neoclassical finite-orbit-width version of the CQL3D Fokker-Planck code. *Plasma Phys. Control. Fusion*, 58:115001, 2016.
- [63] X. Tao, A.A. Chan and A. J. Brizard. Hamiltonian theory of adiabatic motion of relativistic charged particles. *Phys. Plasmas*, 14:092107, 2007.
- [64] J. Bezanson *et al.* Julia: A fresh approach to numerical computing. *SIAM review*, 59(1):65–98, 2017.
- [65] J. Revels, M. Lubin, T. Papamarkou. Forward-Mode Automatic Differentiation in Julia. arXiv(cs-MS):1607.07892.
- [66] S. Benjamin. Distribution transforms for orbit tomography. Master’s thesis, The Australian National University, July 2021.
- [67] M. Salewski. Fast-ion diagnostic in fusion plasmas by velocity-space tomography, January 2020. Dr. techn. thesis.
- [68] S.B. Korsholm *et al.* Collective Thomson scattering capabilities to diagnose fusion plasmas. *Nuclear Instruments and Methods in Physics Research Section A: Accelerators, Spectrometers, Detectors and Associated Equipment*, 623(2):677, 2010.
- [69] W.W. Heidbrink *et al.* Hydrogenic fast-ion diagnostic using Balmer-alpha light. *Plasma Phys. Control. Fusion*, 46(12):1855, 2004.
- [70] J. Eriksson *et al.* Dual sightline measurements of MeV range deuterons with neutron and gamma-ray spectroscopy at JET. *Nucl. Fusion*, 55(12):076004, 2015.
- [71] Massimo Nocente. *Neutron and gamma-ray emission spectroscopy as fast ion diagnostics in fusion plasmas*. PhD thesis, Università Degli Studi Di Milano Bicocca, Facoltà de Scienze Matematiche, Fisiche e Naturali, 2011.
- [72] M. Gatu Johnson *et al.* The 2.5-MeV neutron time-of-flight spectrometer TOFOR for experiments at JET. *Nucl. Instrum. Meth. Phys. Res. A*, 591:417–430, 2008.
-

- [73] F. Binda *et al.* Forward fitting of experimental data from a NE213 neutron detector installed with the magnetic proton recoil upgraded spectrometer at JET. *Rev. Sci. Instrum.*, 85:11E123, 2014.
- [74] C. Cazzaniga *et al.* Single crystal diamond detector measurements of deuterium-deuterium and deuterium-tritium neutrons in Joint European Torus fusion plasmas. *Rev. Sci. Instrum.*, 85:043506, 2014.
- [75] E. Andersson Sundén *et al.* The thin-foil magnetic proton recoil neutron spectrometer MPRu at JET. *Nucl. Instrum. Meth. Phys. Res. A*, 610:682–699, 2009.
- [76] M. Nocente *et al.* Energy resolution of gamma-ray spectroscopy at JET plasmas with a LaBr₃ scintillator detector and digital data acquisition. *Rev. Sci. Instrum.*, 81:10D321, 2010.
- [77] L. Giacomelli *et al.* Neutron emission profiles and energy spectra measurements at JET. *AIP Conference Proceedings*, 1612:113, 2014.
- [78] L. Giacomelli *et al.* Evaluation of a digital data acquisition system and optimization of n- γ discrimination for a compact neutron spectrometer. *Rev. Sci. Instrum.*, 82:013505, 2011.
- [79] E. Andersson Sundén *et al.* The thin-foil magnetic proton recoil neutron spectrometer MPRu at JET. *Nucl. Instrum. and Methods in Phys. Res. A*, 610:682–699, 2009.
- [80] J. Eriksson *et al.* Calculating fusion neutron energy spectra from arbitrary reactant distributions. *Comp. Phys. Comm.*, 199:40–46, 2016.
- [81] H. Brysk. "fusion neutron energies and spectra". *Plasma Phys.*, 15(7):611, 1973.
- [82] A. Muraro *et al.* First neutron spectroscopy measurements with a pixelated diamond detector at JET. *Rev. Sci. Instrum.*, 87:11D833, 2016.
- [83] H. Järleblad *et al.* A framework for synthetic diagnostics using energetic-particle orbits in tokamaks, 2022. Submitted.
- [84] Birgitte Madsen. *Reconstructing the fast-ion distribution from sparse datasets*. PhD thesis, Department of Physics, Technical University of Denmark, 2020.
- [85] H. Järleblad *et al.* Fast-ion orbit origin of neutron measurements in the jet dte2 campaign, 2023. In preparation.
- [86] B. S. Schmidt *et al.* 4d and 5d phase-space tomography using slowing-down physics regularization, 2022. In preparation.

-
- [87] A. Yoo, M. Jette, and M. Grondona. SLURM: Simple Linux Utility for Resource Management. *Job Scheduling Strategies for Parallel Processing*, 2862 of *Lecture Notes in Computer Science*:44–60, 2003.
- [88] SLURM workload manager Version 22.05. Overview, August 2021. Accessed 2022-10-26.
- [89] Altair Engineering Inc. Altair PBS Professional, 2022. Accessed 2022-10-26.
- [90] M.D. McIlroy. A Research Unix Reader: annotated excerpts from the Programmer’s Manual, 1987. CSTR. Bell Labs. 139.
- [91] Stephen .R. Bourne. The Unix Shell. *BYTE*, page 187, October 1983.
- [92] B. Geiger *et al.* Progress in modelling fast-ion D-alpha spectra and neutral particle analyzer fluxes using FIDASIM. *Plasma Physics and Controlled Fusion*, 62:105008, 2020.
- [93] L. Stagner, B. Geiger, and W.W. Heidbrink. FIDASIM: A Neutral Beam and Fast-ion Diagnostic Modeling Suite.
- [94] S. Conroy. Line21 code. Private communication.
- [95] M. Tardocchi *et al.* Spectral broadening of characteristic γ -ray emission peaks from $^{12}\text{C}(^3\text{He}, p\gamma)^{14}\text{N}$ reactions in fusion plasmas. *Phys. Rev. Lett.*, 107:205002, 2011.

Appendices

Daily Human Energy Need

The arguably simplest possible method of estimating the daily energy need for a human, is to use Fourier's law to estimate the power, and subsequently the energy, needed to maintain a body temperature of 37 degrees Celcius:

$$\frac{\partial q}{\partial t} = -k \frac{dT}{dx} \quad (8.1)$$

where $\partial q/\partial t$ is the heat flux in $\text{Jm}^{-2}\text{s}^{-1}$, k is the thermal conductivity in $\text{Wm}^{-1}\text{K}^{-1}$ and dT/dx is the temperature gradient in Km^{-1} . We can approximate the thermal conductivity of a human with the thermal conductivity of water, $k = 0.591 \text{ W/mK}$ ¹, $dT/dx \approx \Delta T/\Delta x$, $\Delta T = (37 + 273.15) - (20 + 273.15) = 17 \text{ K}$ and $\Delta x = 0.1 \text{ m}$. We then get

$$\frac{\partial q}{\partial t} \approx 100 \text{ Jm}^{-2}\text{s}^{-1}. \quad (8.2)$$

We can then multiply with the total area A of the human body to estimate the power ($\text{Js}^{-1}=\text{W}$) needed to maintain a temperature difference of 17 degrees Celcius between the human body and the outside. We get

$$P = A \frac{\partial q}{\partial t} \approx 1.0 \times 100 = 100 \text{ W} \quad (8.3)$$

where we have approximated the area of the human body as $A \approx 1 \text{ m}^2$. If we then multiply with 24 hours, we can finally estimate the daily human energy need to be

$$E = P \times t = 100 \text{ W} \times 24 \text{ h} = 2.4 \text{ kWh}. \quad (8.4)$$

¹<https://whatsinsight.org/thermal-conductivity-of-water/>

Paper I

Fast-ion orbit sensitivity of neutron emission spectroscopy diagnostics

Cite as: Rev. Sci. Instrum. **92**, 043526 (2021); <https://doi.org/10.1063/5.0040696>

Submitted: 15 December 2020 . Accepted: 23 March 2021 . Published Online: 07 April 2021

 H. Järleblad,  L. Stagner,  M. Salewski,  J. Eriksson, S. Benjamin,  B. Madsen,  M. Nocente,  J. Rasmussen, and  B. S. Schmidt






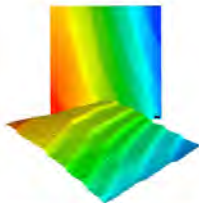

View Online



Export Citation



CrossMark

	<p>Nanopositioning Systems</p> 	<p>Modular Motion Control</p> 	<p>AFM and NSOM Instruments</p> 	<p>Single Molecule Microscopes</p> 
---	--	---	---	--

Fast-ion orbit sensitivity of neutron emission spectroscopy diagnostics

Cite as: Rev. Sci. Instrum. 92, 043526 (2021); doi: 10.1063/5.0040696

Submitted: 15 December 2020 • Accepted: 23 March 2021 •

Published Online: 7 April 2021



H. Järleblad,^{1,a)}  L. Stagner,²  M. Salewski,¹  J. Eriksson,³  S. Benjamin,⁴  B. Madsen,¹  M. Nocente,⁵ 
J. Rasmussen,¹  and B. S. Schmidt¹ 

AFFILIATIONS

¹Department of Physics, Technical University of Denmark, DK-2800 Kgs. Lyngby, Denmark

²General Atomics, P.O. Box 85608, San Diego, California 92186-5608, USA

³Department of Physics and Astronomy, Uppsala University, 751 20 Uppsala, Sweden

⁴Mathematical Sciences Institute, Australian National University, Canberra ACT 2601, Australia

⁵Department of Physics, University of Milano-Bicocca, 20126 Milano, Italy

Note: Paper published as part of the Special Topic on Proceedings of the 23rd Topical Conference on High-Temperature Plasma Diagnostics.

^{a)}Author to whom correspondence should be addressed: henrikj@dtu.dk

ABSTRACT

Fast ions in fusion plasmas often leave characteristic signatures in the plasma neutron emission. Measurements of this emission are subject to the phase-space sensitivity of the diagnostic, which can be mapped using weight functions. In this paper, we present orbit weight functions for the TOFOR and NE213 neutron diagnostics at the Joint European Torus, mapping their phase-space sensitivity in 3D orbit space. Both diagnostics are highly sensitive to fast ions that spend a relatively large fraction of their orbit transit times inside the viewing cone of the diagnostic. For most neutron energies, TOFOR is found to be relatively sensitive to potato orbits and heavily localized counter-passing orbits, as well as trapped orbits whose “banana tips” are inside the viewing cone of TOFOR. For the NE213-scintillator, the sensitivity is found to be relatively high for stagnation orbits.

Published under license by AIP Publishing. <https://doi.org/10.1063/5.0040696>

I. INTRODUCTION

The age of burning plasmas is quickly approaching. With the ITER tokamak^{1,2} and smaller projects such as SPARC,³ burning plasmas will pose novel challenges in regard to dominant alpha particle heating. Fast alpha particles are created in fusion reactions between fast deuterium (D) and tritium (T) ions, which will be further explored in the upcoming DT campaign at Joint European Torus (JET).⁴ The behavior of these fast ions may lead to undesired losses in energy and fast-ion density⁵ of varying severity, such as via the development of energetic particle modes,⁶ via the interaction with Alfvén eigenmodes,^{7–9} and via the interaction with sawteeth instabilities.^{10–13} Understanding the behavior and physics of these fast ions is therefore considered paramount.^{14–16} Prior to the development of the tools of velocity-space tomography,^{9,17–23} an assessment of how the fast ions are distributed in velocity space was only possible by simulations of the fast-ion distribution

function and finding the simulation matching the experimental data the best.^{23,24} With velocity-space tomography, a reconstruction of the fast-ion distribution from measurements became possible via weight functions.¹⁴ A weight function w is the phase-space sensitivity of a diagnostic. When its product with the fast-ion distribution f is integrated over phase space (\mathbf{x}, \mathbf{v}) , the diagnostic signal s is obtained. This can be expressed as

$$s(E_{1,d}, E_{2,d}) = \iint w(E_{1,d}, E_{2,d}, \mathbf{x}, \mathbf{v}) f(\mathbf{x}, \mathbf{v}) d\mathbf{x}d\mathbf{v}, \quad (1)$$

where $E_{1,d}, E_{2,d}$ are used to indicate the boundaries of an energy bin in which particles or photons are detected by the diagnostic. From here on, the dependence on $E_{1,d}, E_{2,d}$ will be omitted for brevity. For a single diagnostic energy bin, the weight functions used in velocity-space tomography are two-dimensional, with energy (E) and pitch (p) dependence. Utilizing velocity-space weight

functions with tomography, it is possible to infer the fast-ion distribution in a small measurement volume around a single cross-sectional point (R, Z) . Velocity-space weight functions have been developed for various fast-ion diagnostics, including fast-ion D- α spectroscopy (FIDA),^{25,26} collective Thomson scattering,^{5,28} gamma-ray spectroscopy,^{28,29} fast-ion loss detectors,³⁰ neutral particle analyzers,²⁷ neutron emission spectroscopy (NES),^{31,32} and 1D weight functions for ion cyclotron emission diagnostics.³³ However, with velocity-space tomography, the full 3D fast-ion distribution of all ions in the tokamak eludes reconstruction. Orbit weight functions solve this problem by using the physical correlation of the points along fast-ion orbits. This enables an inference of the complete fast-ion distribution (assuming toroidal symmetry, guiding-center picture and neglecting collisions) in three-dimensional orbit space.³⁴ The distribution in orbit space can then be transformed into the corresponding distribution in (E, p, R, Z) . Processes for calculating orbit weight functions have been developed for neutron scintillators, NPA, and FIDA.³⁵ This paper concerns the development of orbit weight functions for NES diagnostics. At the JET tokamak, neutron spectroscopy is well-established,³⁶ velocity-space weight functions have already been developed,^{31,32} and it is used as a main diagnostic for fast-ion studies.^{36,37} The development of NES orbit weight functions will enable more detailed studies of fast ions in burning plasmas at JET in the upcoming DT campaign.

This paper is organized as follows: In Sec. II, the choice of orbit coordinates is motivated, the coordinates are explained, and orbit space is described. In Sec. III, an overview of how to calculate orbit weights is presented and described in more detail for the TOFOR³⁸ and a NE213-scintillator³⁹ at JET. In Sec. IV, orbit weight functions for NES at JET are presented and visualized. Thereafter, a conclusion and outlook follow in Sec. V.

II. ORBIT SPACE (E, p_m, R_m)

There are several possible choices when it comes to labeling orbits in a tokamak plasma.^{40,41,42} The labeling can be done via a chosen set of coordinates. The usual constants of motion coordinates $(E, \mu, p_\phi) = (\text{energy, magnetic moment, toroidal canonical angular momentum})$ do not uniquely identify orbits.⁴¹ Therefore, to be able to work with a purely 3D phase space, we have chosen to work with the so-called orbit-space coordinates (E, p_m, R_m) .³⁵ Here, E is the kinetic energy of the fast ion, and p_m is the pitch (ion velocity parallel to the magnetic field divided by total ion velocity magnitude) at the maximum major radius position R_m of (the guiding-center of) the orbit. Given a tokamak equilibrium and geometry, an (E, p_m, R_m) triplet uniquely labels any orbit (Z_m is implicitly fixed). Some example orbits are shown in Fig. 1, illustrating the concept of an (E, p_m, R_m) triplet. All orbits and relevant orbit-space quantities in this paper are calculated for a deuterium ion.

In orbit space, there are specific topological regions corresponding to the different types of orbits. In contrast to particle space (E, p, R, Z) , the gradient of the fast-ion distribution is usually not continuous across topological boundaries in orbit space. This is because continuity implies correlation, and it is not always the case that topological regions that are close together in orbit space are correlated. When crossing the boundary between two topological regions, the orbit trajectory can change dramatically. It is even possible that areas that are far apart in orbit space are more closely

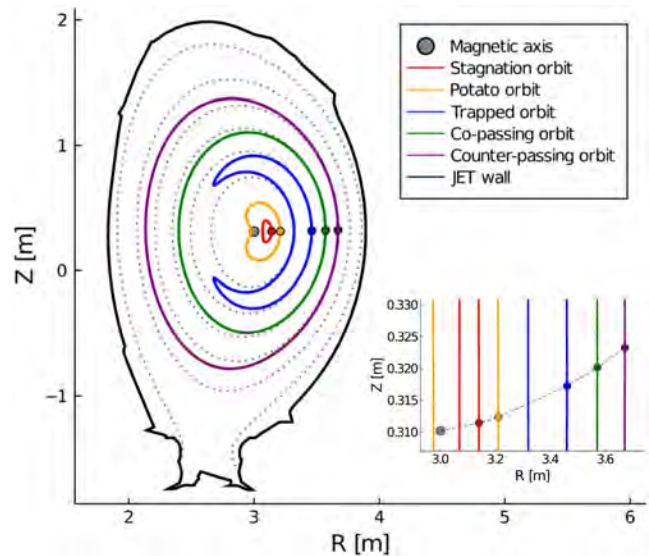


FIG. 1. Example orbits with $(E[\text{keV}], p_m[-], R_m[\text{m}])$ -coordinates $(80, 0.15, 3.14)$ (stagnation), $(80, 0.29, 3.21)$ (potato), $(80, 0.47, 3.46)$ (trapped), $(80, 0.88, 3.57)$ (co-passing), and $(80, -0.88, 3.67)$ (counter-passing) for JET shot No. 96100 at 13.0012 s. The colored lines correspond to the trajectories of the fast-ion guiding-center. The dotted lines correspond to the magnetic flux surfaces. The colored points mark the R_m -coordinates of the orbits. Note how the Z -coordinates of the R_m -points are slightly increasing with R_m , as a result of the specific magnetic equilibrium.

correlated than areas that are near to each other.⁴³ From Fig. 2, we can observe how a large portion of orbit space (gray region) corresponds to invalid and lost orbits. Lost orbits are orbits that intersect the tokamak wall or the divertor. Invalid orbits are orbits that are impossible to realize, given the magnetic equilibrium. The size of this gray region can vary between tokamaks, time-stamps, etc. However, as previously investigated⁴³ for the DIII-D tokamak, it seems to

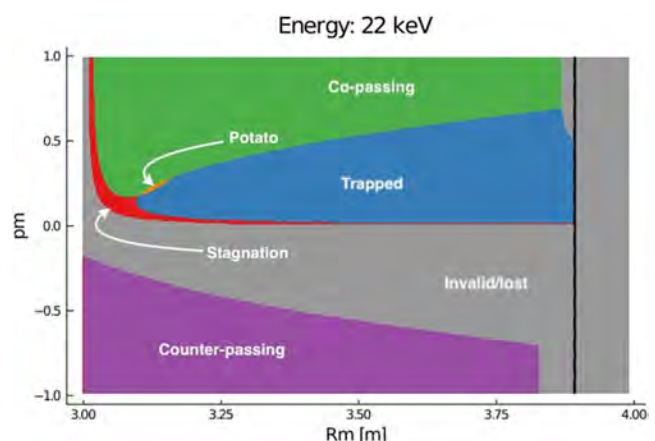


FIG. 2. Orbit-space topology for JET shot No. 96100 at 13.0012 s with energy $E = 22.0$ keV held constant. The black line marks the low-field side JET wall.

consistently extend over a large portion of orbit space. Slices through orbit space at other energies are qualitatively similar.

III. CALCULATING ORBIT WEIGHTS

To calculate a weight, one calculates the signal produced by an ion at a specific action coordinate \mathbf{J} , averaged over the angle coordinates Θ . It can be stated generally as⁴³

$$w(\mathbf{J}) = \left(\prod_i \frac{1}{\tau_i} \right) \int_0^{\tau_1} \dots \int_0^{\tau_i} S(\mathbf{J}, \Theta) d\Theta, \quad (2)$$

where w is the weight, τ_i is the final value before the corresponding angle coordinate repeats, and S is the (synthetic) diagnostic signal. For our orbit space of interest, $\mathbf{J} = (E, p_m, R_m)$ and $\Theta = (t, \gamma, \phi_0)$, where t is the time, γ is the gyro-angle, and ϕ_0 is the initial toroidal angle. Equation (2) can thus be written specifically as

$$w = \frac{1}{4\pi^2 \tau_p} \int_0^{2\pi} \int_0^{2\pi} \int_0^{\tau_p} S(E, p_m, R_m, t, \gamma, \phi_0) dt d\gamma d\phi_0, \quad (3)$$

where $w = w(E, p_m, R_m)$ is the orbit weight for a single (E, p_m, R_m) coordinate. The orbit weights are the signal per fast ion on that orbit. In practice, the orbit weight functions are then calculated by discretizing (3), calculating synthetic signals via a forward model for distributions consisting of just one non-zero orbit-space voxel (a representation of a delta function), averaging over (t, γ, ϕ_0) , and structuring the signals into a matrix W . Calculating W can be written as the following step-by-step process:

1. Let $f = n_f \delta(E - E_i) \delta(p_m - p_{m,j}) \delta(R_m - R_{m,k})$, where f is the test fast-ion distribution and n_f is a test fast-ion density
2. Transform f into the format needed by the forward model as input

3. Use the forward model to calculate the signal S for that delta function
4. Average over (t, γ, ϕ_0)
5. Repeat for all $(E_i, p_{m,j}, R_{m,k})$ points of interest.

In the case of NES, we are interested in how different orbits produce different neutron spectra or, equivalently, how sensitive a measurement at a specific neutron energy is to different areas of orbit space. We have focused on the TOFOR³⁸ diagnostic and the NE213-scintillator³⁹ diagnostic, both installed at JET. TOFOR is installed so as to view a collimated neutron flux coming up vertically from the plasma. As can be seen in Fig. 3, TOFOR and NE213 are able to observe neutrons originating from fusion reactions along the part of the orbit that lies in the viewing cone of the diagnostic. Depending on the orbit, the fast ion will spend a varying amount of time inside the viewing cone. For both diagnostics (or any diagnostic), this will result in different parts of orbit space acquiring different weights. The neutron energy E_n can be related to the known motional state of the reactants via the following equation:^{37,44}

$$E_n = \frac{1}{2} m_n V_{cm}^2 + \frac{m_n}{m_n + m_f} (Q + K) + (V_{cm} \cos \theta) \left(\frac{2m_n m_f}{m_n + m_f} (Q + K) \right)^{1/2}. \quad (4)$$

Here, m_n is the neutron mass, and $V_{cm} = |\mathbf{V}_{cm}|$ where $\mathbf{V}_{cm} = (m_1 \mathbf{v}_1 + m_2 \mathbf{v}_2) / (m_1 + m_2)$ is the center-of-mass velocity of the two reactant ions, described by their masses m_1 and m_2 and velocities \mathbf{v}_1 and \mathbf{v}_2 . m_f is the mass of the second product of the fusion reaction, Q is the nuclear energy release of the reaction, $K = m_1 m_2 v_{rel}^2 / (2(m_1 + m_2))$ is the relative kinetic energy of the reactants, where $v_{rel} = |\mathbf{v}_2 - \mathbf{v}_1|$ and θ indicates the angle between \mathbf{V}_{cm} and the neutron velocity vector in the center-of-mass frame. In

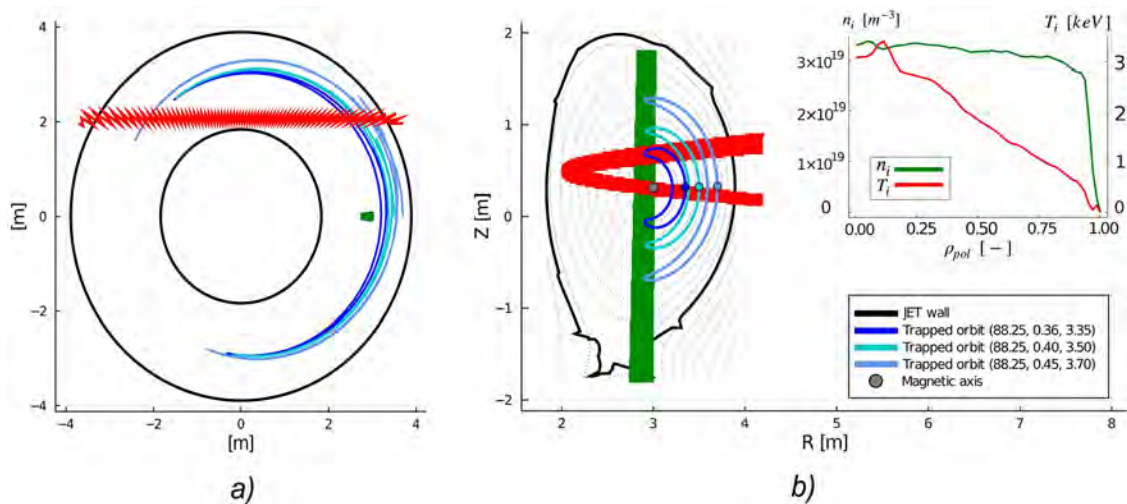


FIG. 3. Viewing cones of the TOFOR and NE213 diagnostics are shown by green and red areas, respectively. Depicted as examples in (a) and (b), both diagnostics observe part of the fast-ion guiding-center trajectories for the trapped orbits with shown $(E[\text{keV}], p_m[-], R_m[\text{m}])$ coordinates. The equilibrium is the same as in Fig. 1. The ion temperature and density profiles are shown in (b) as an inset.

practice, the process of calculating an NES orbit weight (for a given plasma equilibrium and a given bulk ion temperature profile and density profile) is as follows. An orbit is calculated for an (E, p_m, R_m) triplet. Toroidal symmetry is assumed, which means that the orbit is characterized by its projection onto the (R, Z) plane and by the energy and pitch values at each (R, Z) point. Hence, this is effectively an (E, p, R, Z) distribution representing the orbit. For a given instrument (TOFOR or NE213), the expected diagnostic signal from this distribution can then be calculated with Monte Carlo methods.⁴⁵ We normalize these calculations to the total number of points on the orbit, which gives the signal that one ion on this orbit would give rise to, which is precisely the orbit weight that we are after. The orbit weight functions presented in this work have been calculated for a $100 \times 100 \times 100$ orbit-space grid with $E : [20.65, 149.35]$ keV, $p_m : [-0.99, 0.99]$, and $R_m : [3.03, 3.80]$ m. To achieve these relatively smooth weight functions, no more than 500 (E, p, R, Z) points were used for each orbit. Often, the number of (E, p, R, Z) points was significantly lower. The computational time is dependent on a number of factors. To calculate the orbit weight functions presented in this paper, 40 Intel(R) Xeon(R) Scalable Gold CPUs 6148 2.20 GHz were used, with an estimated maximum of 17.21 GB utilized RAM memory and a total computational time of ~ 25 h (including programming package initialization and calculation of the orbits). However, it should be noted that an orbit weight function calculated on a $100 \times 100 \times 100$ orbit-space grid uses about five orders of magnitude more valid orbits than what is needed to accurately mimic the physics of the forward model in this case. For JET shot No. 96100, an orbit weight function using just the valid orbits of a $17 \times 15 \times 13$ orbit-space grid (for example) is enough to closely reproduce the expected diagnostics signal when multiplied with the fast-ion distribution [Eq. (1)]. The number of valid orbits needed to correctly mimic the physics of the forward model with the orbit weight functions will depend on the size of the non-zero areas of the fast-ion distribution in phase space as well as the phase-space resolution requirements for both the fast-ion distribution and the diagnostic.

IV. VISUALISATION OF ORBIT WEIGHT FUNCTIONS

Since orbit weight functions are three-dimensional, the process of visualization is difficult. For every point in three-dimensional orbit space, there is a corresponding weight. Thus, the data are four-dimensional (one phase-space location and one weight). Previous work has visualized orbit weight functions via projection onto the three orthogonal coordinate planes.³⁵ To be able to get a detailed picture of how the sensitivity is distributed in terms of different orbit types, this work has chosen to instead examine the orbit weight functions slice-by-slice in terms of fast-ion energy E . The topological boundaries for a specific energy can then be superimposed onto the orbit weight function to easily identify the topological areas of highest sensitivity. In Fig. 4, it can be observed how, for the given fast-ion energy and TOFOR neutron energy bin, large weights can be found for potato orbits and heavily localized counter-passing orbits. It can also be noted how a narrow region of large weights extends from the potato region, through the trapped region, and out to the JET wall. This is due to the “banana tips” of those trapped orbits coinciding with the TOFOR viewing cone, where the fast ions then spend a relatively large fraction of their poloidal transit times. Hence, the

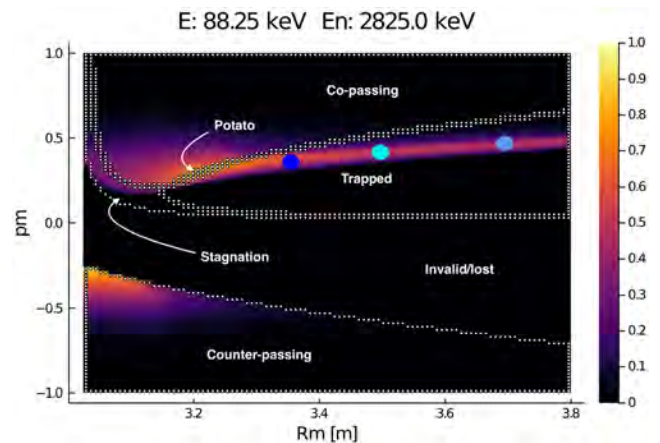


FIG. 4. A slice of a normalized TOFOR orbit weight function with superimposed topological boundaries. For a fast-ion orbit with $E = 88.25$ keV, the TOFOR neutron energy bin with $(E_{1,d}, E_{2,d}) = (2.775, 2.875)$ MeV will be most sensitive to potato orbits and counter-passing orbits heavily localized around the magnetic axis (small R_m value). The three colored points indicate the coordinates of the trapped orbits depicted in Figs. 3(a) and 3(b). The equilibrium is the same as in Fig. 1. The colorbars indicate normalized weight.

sensitivity is higher. For the NE213-scintillator, the general structure of the orbit weight functions differs, as can be seen in Fig. 5. For the given fast-ion energy and neutron energy bin, the sensitivity to stagnation orbits is relatively high. This is in agreement with expectations since many stagnation orbits will have their poloidal orbit projection completely within the NE213 viewing cone. The slices presented in Figs. 4 and 5 are typical for most neutron energy bins and fast-ion energies, albeit great variations do exist. Note that the above results have been obtained assuming DD reactions only

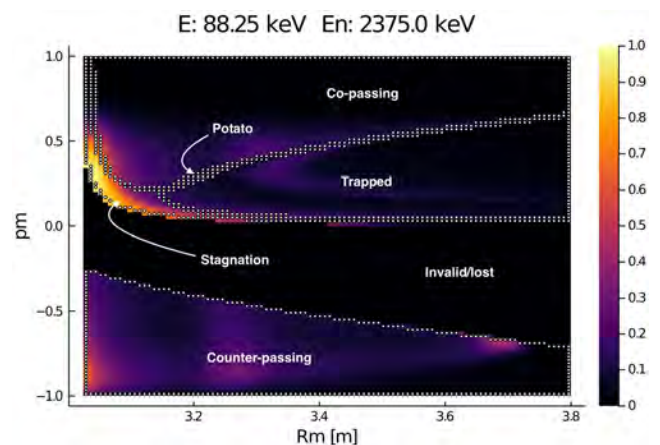


FIG. 5. A slice of a normalized NE213 orbit weight function with superimposed topological boundaries. For a fast-ion orbit with $E = 88.25$ keV, the NE213 neutron energy bin with $(E_{1,d}, E_{2,d}) = (2.325, 2.425)$ MeV will be most sensitive to stagnation orbits. The equilibrium is the same as in Fig. 1. The colorbars indicate normalized weight.

and exclusively beam-target neutron yield. The orbit-space sensitivity will likely vary for other scenarios. Recall also that the topology of orbit space itself will vary depending on the magnetic equilibrium. However, the discussion regarding orbits with a relatively high sensitivity attributable to a relatively large fraction of the time being spent within the viewing cone of the diagnostic is valid in general.

V. CONCLUSION AND OUTLOOK

Orbit weight functions have been developed for the TOFOR and NE213-scintillator diagnostics at JET. They are comprised of weights where each weight is the signal per fast ion on a unique orbit. On their own, they describe the orbit-space sensitivity, that is, for a given diagnostic, how sensitive a measurement of a specific energy bin is to the different regions of orbit space. The weight functions show that both diagnostics are highly sensitive to orbits whose fast ions spend a large fraction of their orbit transit times inside the viewing cone of the diagnostic. In particular, TOFOR is found to have relatively large weights for potato orbits and heavily localized counter-passing orbits. The NE213-scintillator is found to have relatively large weights for stagnation orbits. Together with a TOFOR- or NE213-signal originating from a fast-ion distribution, the orbit weight functions can be used to reconstruct the orbit-space fast-ion distribution, which can then be transformed to obtain the four-dimensional, gyro- and toroidally averaged fast-ion distribution function in energy, pitch, R, and Z. This will be shown in future work.

ACKNOWLEDGMENTS

We thank the ITPA Energetic Particle Physics Topical Group for its support. This work was carried out within the framework of the EUROfusion Consortium and has received funding from the Euratom Research and Training Programme 2014–2018 and 2019–2020 under Grant Agreement No. 633053. The views and opinions expressed herein do not necessarily reflect those of the European Commission.

DATA AVAILABILITY

Raw data were generated at the JET large scale facility. Derived data supporting the findings of this study are available from the corresponding author upon reasonable request.

REFERENCES

- ¹M. Salewski *et al.*, *Nucl. Fusion* **58**, 096019 (2018).
- ²B. Bigot, *Nucl. Fusion* **59**, 112001 (2019).
- ³P. Rodriguez-Fernandez *et al.*, *J. Plasma Phys.* **86**, 865860503 (2020).
- ⁴E. Joffrin *et al.*, *Nucl. Fusion* **59**, 112021 (2019).
- ⁵M. Salewski *et al.*, *Nucl. Fusion* **51**, 083014 (2011).
- ⁶S. Briguglio *et al.*, *Phys. Plasmas* **14**, 055904 (2007).
- ⁷W. W. Heidbrink, *Phys. Plasmas* **9**, 2113 (2002).
- ⁸W. W. Heidbrink, *Phys. Plasmas* **15**, 055501 (2008).
- ⁹B. Madsen *et al.*, *Nucl. Fusion* **60**, 066024 (2020).
- ¹⁰F. B. Marcus *et al.*, *Nucl. Fusion* **34**, 687 (1994).
- ¹¹J. P. Graves *et al.*, *Plasma Phys. Controlled Fusion* **47**, B121 (2005).
- ¹²D. J. Campbell *et al.*, *Phys. Rev. Lett.* **60**, 2148 (1988).
- ¹³Y. I. Kolesnichenko *et al.*, *Nucl. Fusion* **40**, 1325 (2000).
- ¹⁴M. Salewski, *Fast-Ion Diagnostic in Fusion Plasmas by Velocity-Space Tomography* (Technical University of Denmark, Kongens Lyngby, Denmark, 2019).
- ¹⁵M. Salewski *et al.*, *J. Instrum.* **14**, C05019 (2019).
- ¹⁶J. Eriksson *et al.*, *Nucl. Fusion* **55**, 123026 (2015).
- ¹⁷M. Salewski *et al.*, *Nucl. Fusion* **54**, 023005 (2014).
- ¹⁸A. S. Jacobsen *et al.*, *Plasma Phys. Controlled Fusion* **58**, 045016 (2016).
- ¹⁹M. Weiland *et al.*, *Plasma Phys. Controlled Fusion* **58**, 025012 (2016).
- ²⁰M. Weiland *et al.*, *Nucl. Fusion* **57**, 116058 (2017).
- ²¹M. Salewski *et al.*, *Nucl. Fusion* **57**, 056001 (2017).
- ²²B. Madsen *et al.*, *Plasma Phys. Controlled Fusion* **62**, 115019 (2020).
- ²³M. Salewski *et al.*, *Nucl. Fusion* **50**, 035012 (2010).
- ²⁴M. Salewski *et al.*, *Nucl. Fusion* **53**, 063019 (2013).
- ²⁵M. Salewski *et al.*, *Plasma Phys. Controlled Fusion* **56**, 105005 (2014).
- ²⁶W. W. Heidbrink *et al.*, *Plasma Phys. Controlled Fusion* **49**, 1457 (2007).
- ²⁷M. Salewski *et al.*, *Fusion Sci. Technol.* **74**, 23 (2018).
- ²⁸M. Salewski *et al.*, *Nucl. Fusion* **55**, 093029 (2015).
- ²⁹M. Salewski *et al.*, *Nucl. Fusion* **56**, 046009 (2016).
- ³⁰J. Galdon-Quiroga *et al.*, *Plasma Phys. Controlled Fusion* **60**, 105005 (2018).
- ³¹A. S. Jacobsen *et al.*, *Nucl. Fusion* **55**, 053013 (2015).
- ³²A. S. Jacobsen *et al.*, *Rev. Sci. Instrum.* **88**, 073506 (2017).
- ³³B. S. Schmidt *et al.*, “Determining 1D fast-ion velocity distribution functions from ion cyclotron emission data using deep neural networks,” *Rev. Sci. Instrum.* (submitted) (2021).
- ³⁴L. Stagner, “Orbit tomography of energetic particle distribution functions” (to be published) (2021).
- ³⁵L. Stagner and W. W. Heidbrink, *Phys. Plasmas* **24**, 092505 (2017).
- ³⁶J. Eriksson *et al.*, *Plasma Phys. Controlled Fusion* **61**, 014027 (2019).
- ³⁷D. Moseev *et al.*, *Rev. Mod. Plasma Phys.* **2**, 7 (2018).
- ³⁸M. Gatu Johnson *et al.*, *Nucl. Instrum. Methods Phys. Res., Sect. A* **591**, 417 (2008).
- ³⁹F. Binda *et al.*, *Rev. Sci. Instrum.* **85**, 11E23 (2014).
- ⁴⁰R. B. White, *The Theory of Toroidally Confined Plasmas*, 2nd ed. (Imperial College Press, 2001).
- ⁴¹J. A. Rome and Y. K. M. Peng, *Nucl. Fusion* **19**, 1193 (1979).
- ⁴²Y. V. Petrov and R. W. Harvey, *Plasma Phys. Controlled Fusion* **58**, 115001 (2016).
- ⁴³L. Stagner, “Inference of the fast-ion distribution function,” Ph.D. thesis, University of California, Irvine, 2018.
- ⁴⁴H. Brysk, *Plasma Phys.* **15**, 611 (1973).
- ⁴⁵J. Eriksson *et al.*, *Comput. Phys. Commun.* **199**, 40 (2016).

Paper II

PAPER

Fast-ion orbit sensitivity of neutron and gamma-ray diagnostics for one-step fusion reactions

To cite this article: H. Järleblad *et al* 2022 *Nucl. Fusion* **62** 112005

View the [article online](#) for updates and enhancements.

You may also like

- [Vibration energy harvesting based on a piezoelectric nonlinear energy sink with synchronized charge extraction interface circuit](#)
Zhaoyu Li, Liuyang Xiong, Lihua Tang et al.
- [Noise-induced phenomena in the dynamics of groundwater-dependent plant ecosystems with time delay](#)
Zheng-Lin Jia and Dong-Cheng Mei
- [Observation of a nuclear-elastic-scattering effect caused by energetic protons on deuteron slowing-down behaviour on the Large Helical Device](#)
H. Matsuura, S. Sugiyama, K. Kimura et al.

Fast-ion orbit sensitivity of neutron and gamma-ray diagnostics for one-step fusion reactions

H. Järleblad^{1,*}, L. Stagner², M. Salewski¹, J. Eriksson³, M. Nocente⁴,
J. Rasmussen¹, Ž. Štancar^{5,6}, Ye.O. Kazakov⁷, B. Simmendefeldt¹
and JET Contributors^a

¹ Department of Physics, Technical University of Denmark, DK-2800 Kgs. Lyngby, Denmark

² General Atomics, PO Box 85608, San Diego, CA 92186-5608, United States of America

³ Department of Physics and Astronomy, Uppsala University, 751 20 Uppsala, Sweden

⁴ Department of Physics, University of Milano-Bicocca, 20126 Milano, Italy

⁵ Jožef Stefan Institute, 1000 Ljubljana, Slovenia

⁶ UKAEA, Culham Centre for Fusion Energy, Abingdon, Oxfordshire, OX14 3DB,
United Kingdom of Great Britain and Northern Ireland

⁷ Laboratory for Plasma Physics, LPP-ERM/KMS, TEC Partner, 1000 Brussels, Belgium

E-mail: henrikj@dtu.dk

Received 4 February 2022, revised 17 March 2022

Accepted for publication 4 April 2022

Published 29 September 2022



CrossMark

Abstract

Fast ions in the MeV-range can be diagnosed by neutron emission spectroscopy (NES) and gamma-ray spectroscopy (GRS). In this work, we present orbit weight functions for one-step fusion reactions, using NES and GRS diagnostics on perpendicular and oblique lines-of-sight (LOS) at Joint European Torus (JET) as examples. The orbit weight functions allow us to express the sensitivities of the diagnostics in terms of fast-ion (FI) orbits and can be used to swiftly reproduce synthetic signals that have been computed by established codes. For diagnostically relevant neutron energies for the $D(D, n)^3\text{He}$ reaction, the orbit sensitivities of the NES diagnostics follow a predictable pattern. As the neutron energy of interest increases, the pattern shifts upwards in FI energy. For the GRS diagnostic and the $T(p, \gamma)^4\text{He}$ reaction, the orbit sensitivity is shown to be qualitatively different for red-shifted, blue-shifted and nominal gamma birth energies. Finally, we demonstrate how orbit weight functions can be used to decompose diagnostic signals into the contributions from different orbit types. For a TRANSP simulation of the JET discharge (a three-ion ICRF scenario) considered in this work, the NES signals for both the perpendicular and oblique LOS are shown to originate mostly from co-passing orbits. In addition, a significant fraction of the NES signal for the oblique LOS is shown to originate from stagnation orbits.

Keywords: tomography, plasma diagnostics, neutron emission, gamma-ray emission, energetic particle physics, energetic particle diagnostics, one-step fusion reactions

(Some figures may appear in colour only in the online journal)

* Author to whom any correspondence should be addressed.

^a See Mailloux *et al* 2022 (<https://doi.org/10.1088/1741-4326/ac47b4>) for the JET Contributors.

1. Introduction

In future fusion reactors and experiments, fast ions will play a vital role in maintaining the self-sustained heating of burning plasmas [2]. However, the interaction of fast ions with the fusion plasma may lead to unstable magnetohydrodynamic mode growth [3–5]. Fast ions can also be subject to anomalous transport [3] and be lost from the plasma [6], which may lead to a reduced heating efficiency and damage to first-wall components [7]. An understanding of the coupling between fast ions and the background plasma is therefore seen as imperative for the success of fusion energy as a viable energy source [6, 8–10].

The dynamics of fast ions is determined by the fast-ion (FI) distribution function in phase-space, which consists of position- and velocity-space. With velocity-space tomography [11–18], the velocity-space FI distribution function can be reconstructed from measurements by using the velocity-space sensitivity of the diagnostics. This sensitivity can be expressed in the form of two-dimensional weight functions. Velocity-space weight functions have been developed for numerous FI diagnostics: fast-ion D- α spectroscopy (FIDA) [19, 20], collective Thomson scattering [21], one-step [22] and two-step [23] gamma-ray spectroscopy (GRS), FI loss detectors [24, 25], neutral particle analyzers (NPAs) [18], neutron emission spectroscopy (NES) [26, 27] as well as 1D weight functions for ion cyclotron emission diagnostics [28]. However, velocity-space weight functions only map the phase-space sensitivity at a single point in position space. Hence, the FI distribution function can only be reconstructed in a small measurement volume at one major radius position R and vertical position z . Orbit weight functions overcome this limitation by using the known physical relationship between the points along charged particle orbits to link isolated (R, z) points to each other. Assuming magnetic equilibrium [29], toroidal symmetry, a guiding-centre picture and low collisionality ($\nu\tau_p \ll 1$ where ν is the ion–ion collisional frequency and τ_p is the orbit poloidal transit time), the complete FI distribution function can be reconstructed in terms of orbits [30], which can then be transformed into a distribution in energy E and pitch $p = v_{\parallel}/v$ for all R and z . Orbit weight functions have so far been developed for neutron scintillators [31], NPA [31], FIDA [31] and NES [32].

In this work, we map out how the orbit sensitivity of NES [33] and GRS [34] diagnostics vary with FI- and fusion product energy (detected by the diagnostic). We examine the orbit weight functions in detail for several fusion-product energies using a perpendicular and an oblique line-of-sight (LOS) as examples, as relevant for e.g. the time-of-flight diagnostic TOFOR [35], a LaBr₃ detector [36, 37] and an NE213-scintillator [38] diagnostic at the Joint European Torus (JET) [1]. However, the methods developed in this work can be used to compute orbit weight functions for any diagnostic sightline and one-step fusion reaction with a neutron or gamma-photon product. The more complicated two-step fusion reactions are deferred to future work since these would require a reformulation of the methods presented in this work via the treatment

of random variables [23]. Furthermore, we demonstrate that the weight functions are able to reproduce the forward model that predicts the diagnostic energy spectrum for a given fusion reaction. Lastly, the orbit weight functions are combined with FI distribution functions to analyze diagnostic signals in terms of their orbit-type constituents.

The paper is organized as follows. In section 2, orbit space and its various topological regions are introduced and the dependence on energy is explained. In section 3, we discuss the formalism behind orbit weight functions and how they can be used to rapidly compute synthetic diagnostic signals. Orbit weight functions are presented and discussed for a perpendicular sightline in section 4 (relevant for TOFOR [35] and the LaBr₃ GRS diagnostic [36, 37]) and for an oblique sightline in section 5 (relevant for the NE213-scintillator [38]). In section 6, orbit weight functions are used to split synthetic signals into their orbit-type constituents as well as to examine from where in orbit space the signal can be expected to originate. Lastly, a conclusion is presented in section 7.

2. Orbit space (E, p_m, R_m) , including the MeV range

The full six-dimensional charged particle motion in space \mathbf{x} and velocity \mathbf{v} can be dimensionally reduced under relevant assumptions. If we assume toroidal symmetry, we can reduce the number of spatial dimensions by one. Similarly, by assuming the variation of the magnetic field to be negligible on the scale of the gyro-motion of the ion, so that the gyro-motion is approximately a rotation around a circle, we can reduce the number of velocity dimensions by one. If we also assume the motion of the ion to have been unperturbed as it revisits the same (R, z) coordinate, we can uniquely label all charged particle trajectories in a magnetic equilibrium with just one spatial coordinate and two velocity coordinates. Given these assumptions, the particle motion is periodic and follows fixed spatial trajectories called orbits. Since our aim is to ultimately utilize three-dimensional orbit phase space for tomographic inversion, the coordinates should be chosen carefully. It is arguably preferable to choose the coordinates so that the space has clear, finite boundaries and does not mix position and velocity space [39]. Therefore, in this work, we use the (E, p_m, R_m) orbit-space coordinates [31]. E is the kinetic energy of the particle, and p_m is the pitch (v_{\parallel}/v) at the maximum major radius position R_m of (the guiding-centre of) the orbit. All possible orbits in a given tokamak equilibrium can be uniquely identified with an (E, p_m, R_m) triplet. For a given FI energy E , orbit space is bounded by $[-1, 1]$ in p_m and $[R_{\text{axis}} - \delta R, R_{\text{LFS}}]$ in R_m , where R_{axis} and R_{LFS} are the major radius positions of the magnetic axis and the low-field side wall, respectively. δR can vary but has a natural maximum of $\delta R = R_{\text{axis}} - R_{\text{HFS}}$ where R_{HFS} is the location of the high-field side wall. However, in practice, $\delta R = 1/5(R_{\text{axis}} - R_{\text{HFS}})$ is usually enough to include all possible populatable orbits when working with orbit space.

In this work, all orbit-space quantities have been computed assuming the magnetic equilibrium of JET shot No. 94701

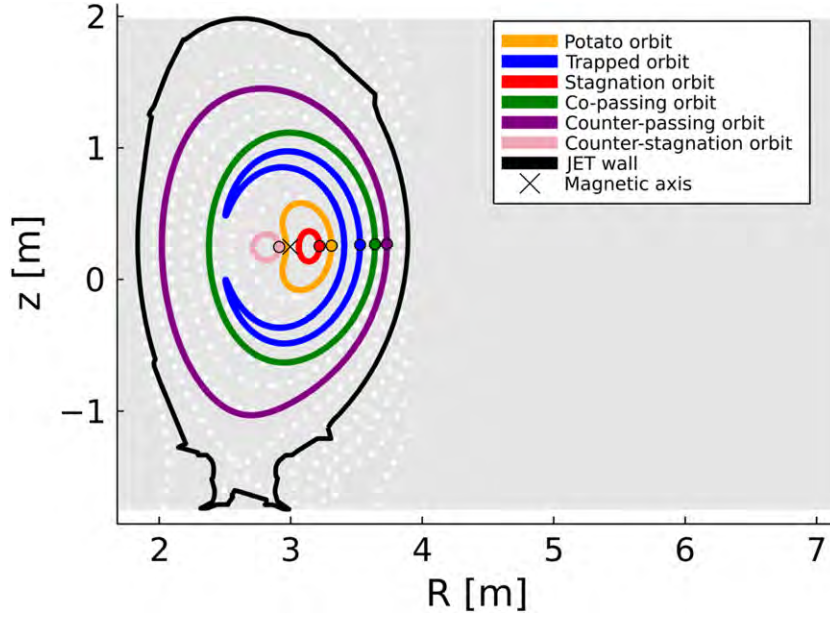


Figure 1. Example (deuterium) orbits with $(E$ [keV], p_m [—], R_m [m]) coordinates (412.6, 0.333, 3.31) (potato), (69.9, 0.535, 3.53) (trapped), (2125.9, 0.333, 3.22) (stagnation), (481.1, 0.758, 3.64) (co-passing), (138.5, -0.980 , 3.73) (counter-passing) and (2262.9, -0.333 , 2.91) (counter-stagnation) for JET shot No. 94701 at 10.79 s. The colored lines show the poloidal projections of the guiding-centre trajectories. The dotted white lines correspond to the magnetic flux surfaces. The colored points mark the R_m -coordinates of the orbits.

at 10.79 s [34, 40–42], a three-ion ICRF scheme with core-localized FI generation. Examples of the different orbit types and their corresponding (E, p_m, R_m) coordinates are shown in figure 1.

Together, the three coordinates span a three-dimensional space, named orbit space, where every point corresponds to a unique orbit. As can be seen in figure 2, orbit space can be divided into different topological regions where every region corresponds to a specific orbit type. The exact shape, position and size of a topological region depend on the magnetic equilibrium, particle species and FI energy. Near thermal energies of a few keV, there are primarily three regions of appreciable size: co-passing, trapped and counter-passing. At higher energies, three additional regions grow to significant size: potato, stagnation and counter-stagnation. At the same time, the trapped, co- and counter-passing regions shrink. This means that at progressively higher FI energies, an increasing fraction of the populatable orbits will be potato, stagnation and counter-stagnation orbits. This is relevant for fusion-born ions [such as DT-born alpha particles (3.52 MeV), DD-born protons (3.02 MeV) and ^3He ions (0.82 MeV), and D^3He -born protons (14.7 MeV) [43]]. Furthermore, a large portion of orbit space will contain invalid and lost orbits (gray and brown regions in figure 2, respectively). Invalid orbits are orbits whose (E, p_m, R_m) coordinates correspond to unrealizable particle trajectories given the magnetic equilibrium. Lost orbits are orbits with trajectories that intersect the tokamak wall. The lost region also grows at increasingly high FI energies.

Lastly, the orbit-space topology depends on the particle species and magnetic equilibrium. This can be understood from the Lorentz force law $m\mathbf{a} = q(\mathbf{E} + \mathbf{v} \times \mathbf{B})$ which determines the particle acceleration and hence trajectory.

3. Weight function formalism

To derive the phase-space sensitivity of diagnostics, consider a fast ion with position coordinate \mathbf{x} and velocity coordinate \mathbf{v} . A weight function can be viewed as a mapping between a general FI distribution $f(\mathbf{x}, \mathbf{v})$ and the resulting diagnostic signal s via the following relation [19, 20, 44]:

$$s(E_{1,d}, E_{2,d}) = \int w(E_{1,d}, E_{2,d}, \mathbf{x}, \mathbf{v}) f(\mathbf{x}, \mathbf{v}) d\mathbf{x} d\mathbf{v} \quad (1)$$

where $E_{1,d}$ and $E_{2,d}$ mark the lower and upper boundaries of a diagnostic energy bin and $w(E_{1,d}, E_{2,d}, \mathbf{x}, \mathbf{v})$ is the weight function. Both the signal and the weight function will thus depend on the diagnostic energy bin for which the measurement is considered. Equation (1) can then be written specifically for our (E, p_m, R_m) orbit space as follows

$$s(E_{1,d}, E_{2,d}) = \int w(E_{1,d}, E_{2,d}, E, p_m, R_m) \times f(E, p_m, R_m) dE dp_m dR_m. \quad (2)$$

Here, we have assumed toroidal symmetry, a guiding-centre picture and low collisionality as explained in section 1. Equation (2) can then be discretized to give

$$s(E_{1,d}, E_{2,d}) = \sum_{i,j,k} w(E_{1,d}, E_{2,d}, E_i, p_{m,j}, R_{m,k}) \times f(E_i, p_{m,j}, R_{m,k}) \Delta E \Delta p_m \Delta R_m. \quad (3)$$

To get a practical relationship between the signal of a diagnostic, which consists of several energy bins, and the FI orbit-space distribution, we write the matrix equation

$$S = WF, \quad (4)$$

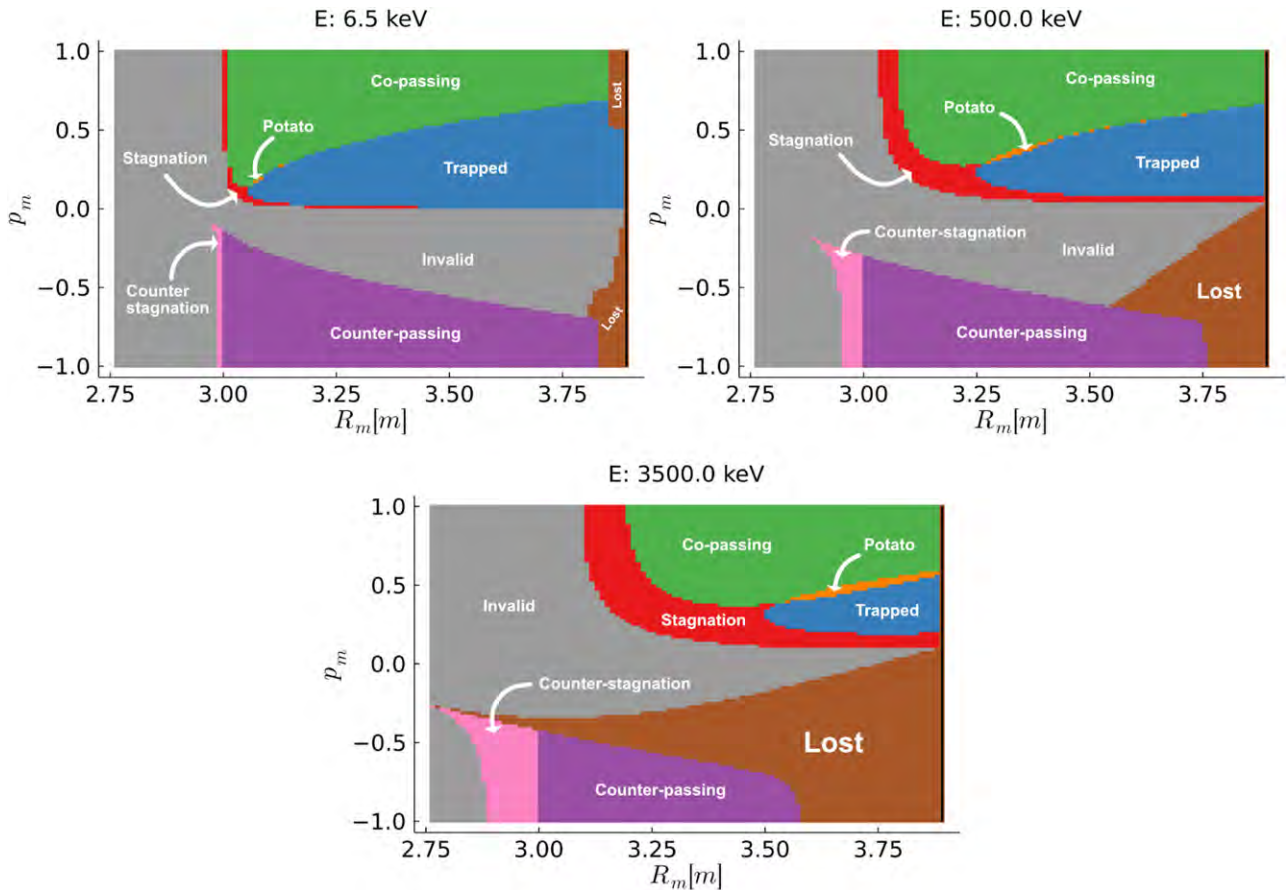


Figure 2. Orbit-space topology for JET shot No. 94701 at 10.79 s for three energy slices (FI energy held constant). The black line marks the JET low-field side wall. The topology was computed for deuterium ions. 6.5 keV is the temperature of the bulk ion distribution at the magnetic axis. 500 keV and 3500 keV were chosen to illustrate the energy dependence of the orbit-space topology.

where S has the size *number of diagnostic energy bins* $\times 1$, W has the size *number of diagnostic energy bins* \times *number of valid orbits* and F has the size *number of valid orbits* $\times 1$. The factor $\Delta E \Delta p_m \Delta R_m$ has been absorbed into W . We have thus vectorized our orbit-space quantities and stacked the weight functions row by row into a matrix. Hence, every row of equation (4) is a case of equation (3). Equation (4) is mathematically the same equation as is used for velocity-space tomography (and position-space tomography).

At this point, it can be helpful to introduce and explain some nomenclature. In the context of orbit space,

- a *weight* relates a single diagnostic energy bin to a single (E, p_m, R_m) grid point. For a specific diagnostic energy bin $(E_{1,d}, E_{2,d})$, it describes the sensitivity of the diagnostic to the orbit at that particular orbit-space grid point. It has the dimensions of *signal per ion* (the dimensions of the signal depend on what diagnostic is used).
- a *weight function* relates a single diagnostic energy bin to all points in orbit space. A discretized weight function is thus comprised of many individual weights. It is a function of the three orbit-space coordinates as $w(E, p_m, R_m)$.
- a *weight function matrix* (or weight matrix for short) is a matrix where each row is a vectorized discretized weight function. Each row corresponds to a specific diagnostic

energy bin and each column corresponds to a particular orbit.

From here on, the label ‘discretized’ will be omitted for brevity.

3.1. Computing weight matrices and orbit weight functions

To compute a weight matrix, the forward model of the diagnostic is used to compute predicted signals for all valid orbits of a particular orbit grid. A set of diagnostic energy bins of interest ($[E_{1,d}, E_{2,d}]$, $[E_{2,d}, E_{3,d}]$, \dots , $[E_{n-1,d}, E_{n,d}]$), reflecting the spectral resolution of the diagnostic, must be assumed for the weight matrix. Each valid orbit is assumed to be populated by only a single particle (to achieve correct normalization) and the orbit is split up into its (E, p, R, z) constituent points. Each (E, p, R, z) point is then weighted according to the fraction of the total poloidal transit time spent by the particle on a path length dl between that (E, p, R, z) point and the next. The number of (E, p, R, z) points needed to accurately represent an orbit will vary depending on the required numerical accuracy [45], the complexity of the orbit as well as the width of the (R, z) -projection of the viewing cone of the diagnostic. In this work, ≥ 500 points were used throughout. For one orbit, all weighted points effectively constitute an (E, p, R, z) distribution for which the expected signal can

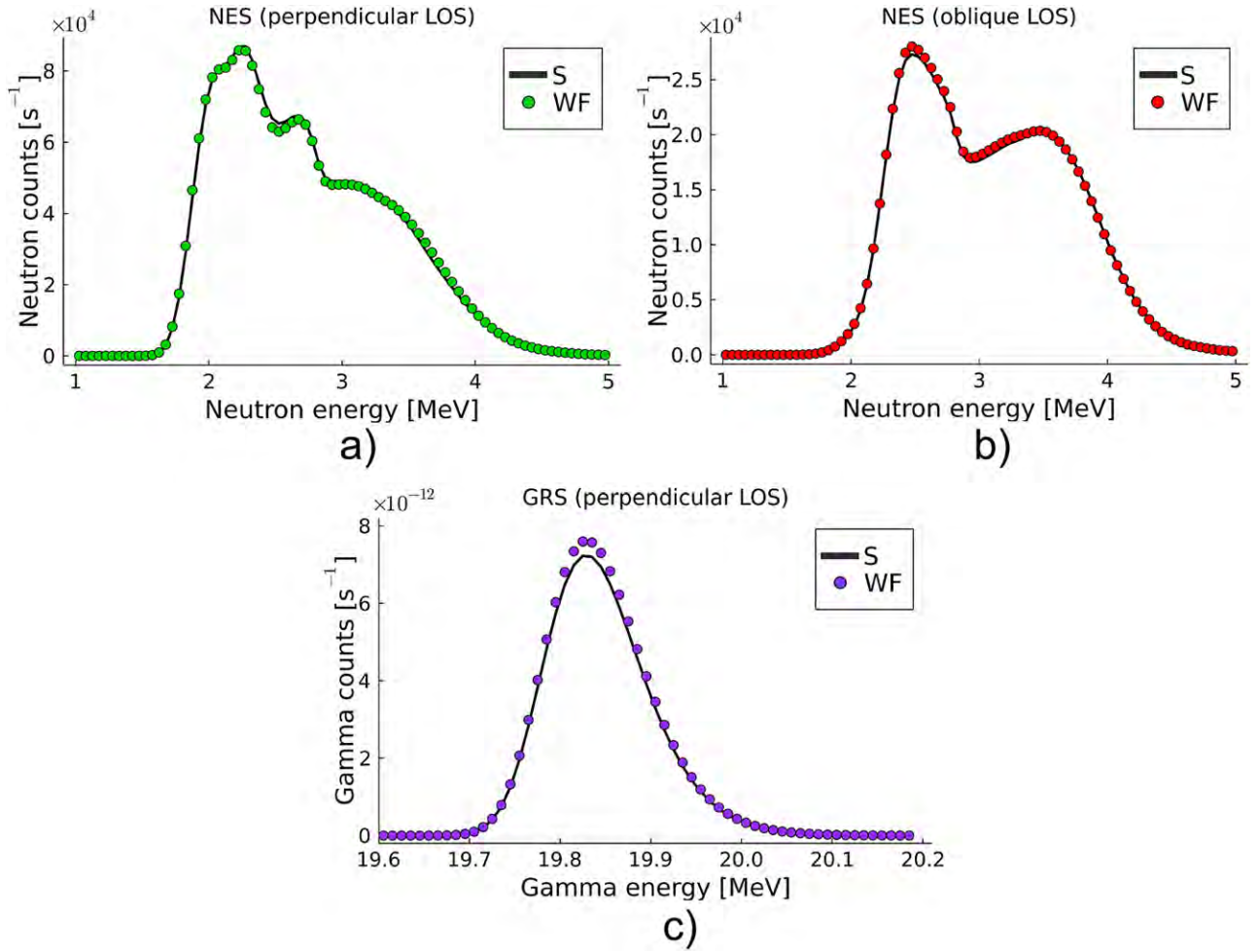


Figure 3. The predicted diagnostic signals computed via the forward model (S) and via the weight matrix (WF) for NES with a perpendicular sightline (a) and an oblique sightline (b), as well as for GRS with a perpendicular sightline (c). The NES signals are computed using the $D(D, n)^3\text{He}$ reaction and the GRS signal is computed using the $T(p, \gamma)^4\text{He}$ reaction. The NES WF signals were computed using a $2400 \times 102 \times 104$ grid in orbit space with $E = [1.4, 2400.0]$ keV, $p_m = [-1.0, 1.0]$ and $R_m = [2.76, 3.89]$ m. The GRS WF signal was computed using the same grid points in p_m and R_m but with 600 grid points in FI energy E and $E = [1.4, 600.0]$ keV. Please note that this relatively high orbit-space grid resolution was only used in order to validate that the WF and S signals converge as grid resolution increases.

be computed with the forward model [46] for a given instrument (e.g. TOFOR). This signal represents one column in the weight matrix and the process is then repeated for all valid orbits, resulting in the complete weight matrix. Every row of the matrix then corresponds to an orbit weight function and describes the orbit-space sensitivity for a specific diagnostic energy bin.

Mathematically, this way of computing the weight functions can be understood via equation (2) and setting $f(E, p_m, R_m) = \delta(E - E_i)\delta(p_m - p_{m,j})\delta(R_m - R_{m,k})$ to model the single-particle valid orbit. We get

$$\begin{aligned}
 s(E_{1,d}, E_{2,d}) &= \int w(E_{1,d}, E_{2,d}, E, p_m, R_m) \delta(E - E_i) \\
 &\quad \times \delta(p_m - p_{m,j}) \delta(R_m - R_{m,k}) dE dp_m dR_m \\
 &= w(E_{1,d}, E_{2,d}, E_i, p_{m,j}, R_{m,k}), \quad (5)
 \end{aligned}$$

where $(E_i, p_{m,j}, R_{m,k})$ denotes the orbit-space coordinate of interest. Note that equation (5) simply describes the sensitivity in orbit space but does not yet account for the extent to which these orbits are actually populated (via F). As can be understood from equation (4), for a given FI distribution F , the weight matrix W can be used to very rapidly compute the expected diagnostic signal S instead of performing the more time-consuming computations usually needed to compute synthetic signals. This is advantageous if synthetic signals for many distribution functions are to be computed.

3.2. Validating orbit weight functions

To confirm that the weight matrix is equivalent to the standard forward model, synthetic signals S (computed via the DRESS code [46] forward model) are plotted together with the 'weight matrix signals' WF for given FI distributions in figure 3. This

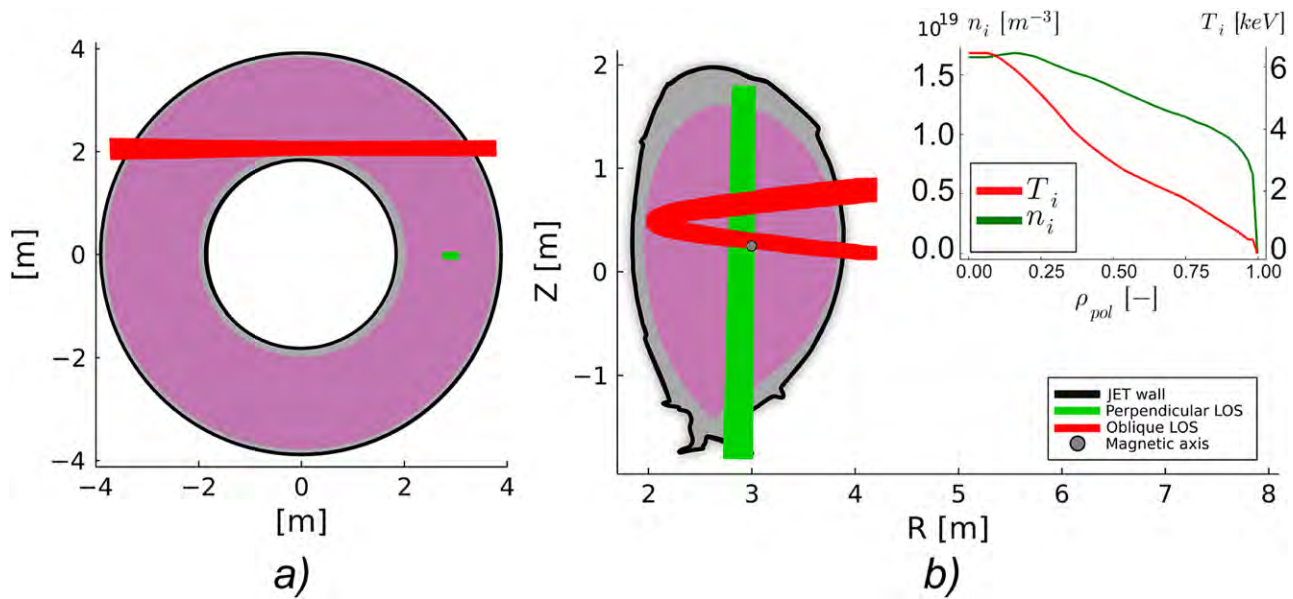


Figure 4. The viewing cones of the perpendicular (green) and oblique (red) sightlines, projected onto a toroidal (a) and poloidal (b) view. The plasma within the last closed flux surface (LCFS) is depicted in indigo. The bulk (deuterium) density n_i and temperature T_i profiles for JET shot No. 94701, averaged over our time window of interest, are shown as an inset. The electron density n_e and temperature T_e were measured with high resolution Thomson scattering, after which $T_i = T_e$ was assumed. n_i was estimated from n_e together with measurements of Z_{eff} made by visible bremsstrahlung diagnostics and the assumption that impurity ions are exclusively beryllium. The n_i and T_i profiles correspond to data between R_{axis} and R_{LCFS} at z_{axis} and are representative for the plasma as a whole.

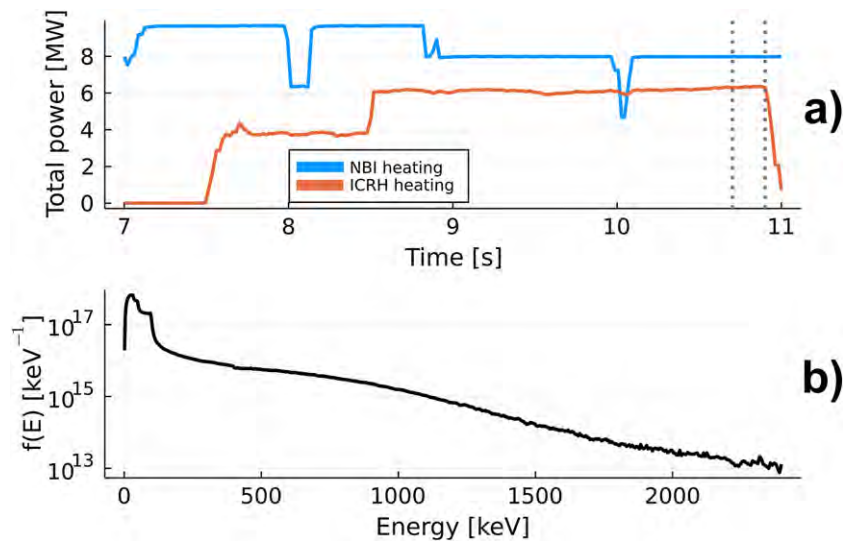


Figure 5. The total injected NBI and ICRH power as functions of time for JET shot No. 94701 are shown in (a). The dotted lines delimit the time window of this work. The corresponding average TRANSP NUBEAM-computed FI deuterium distribution function for the time window is shown in (b) as a function of energy.

has been done for NES and GRS diagnostics with perpendicular sightlines (corresponding to the LOS of TOFOR [35] and a LaBr_3 gamma-ray detector [36, 37]) and for an additional NES diagnostic with an oblique sightline (corresponding to the LOS of a NE213-scintillator [38]). Their sightlines are illustrated in figure 4. The $\text{D}(\text{D}, n)^3\text{He}$ reaction was used for the NES diagnostics and the $\text{T}(\text{p}, \gamma)^4\text{He}$ reaction was used for the GRS diagnostic.

For the NES diagnostics, the average FI deuterium distribution function was computed for JET shot No. 94701 for our time window of interest using the TRANSP [47] code (v19.2) with the NUBEAM [48] module coupled to TORIC [49] (for

the RF-acceleration of the ions) together with the RF kick operator [50, 51]. The magnetic equilibrium at 10.79 s is thus used as the average magnetic equilibrium for our time window. The time traces of the neutral beam injection (NBI) and ion cyclotron resonance heating (ICRH) power are shown in figure 5(a), and the FI deuterium distribution function is plotted as a function of energy in figure 5(b) (where the other dimensions have been integrated out). The thermal deuterium distribution is plotted as an inset in figure 4.

For the GRS diagnostic, the same n_i and T_i profiles as in figure 4 were used for the thermal tritium distribution but the n_i profile was re-normalized so that $n_{\text{T}} = 10^{13} \text{ m}^{-3}$ on-axis.

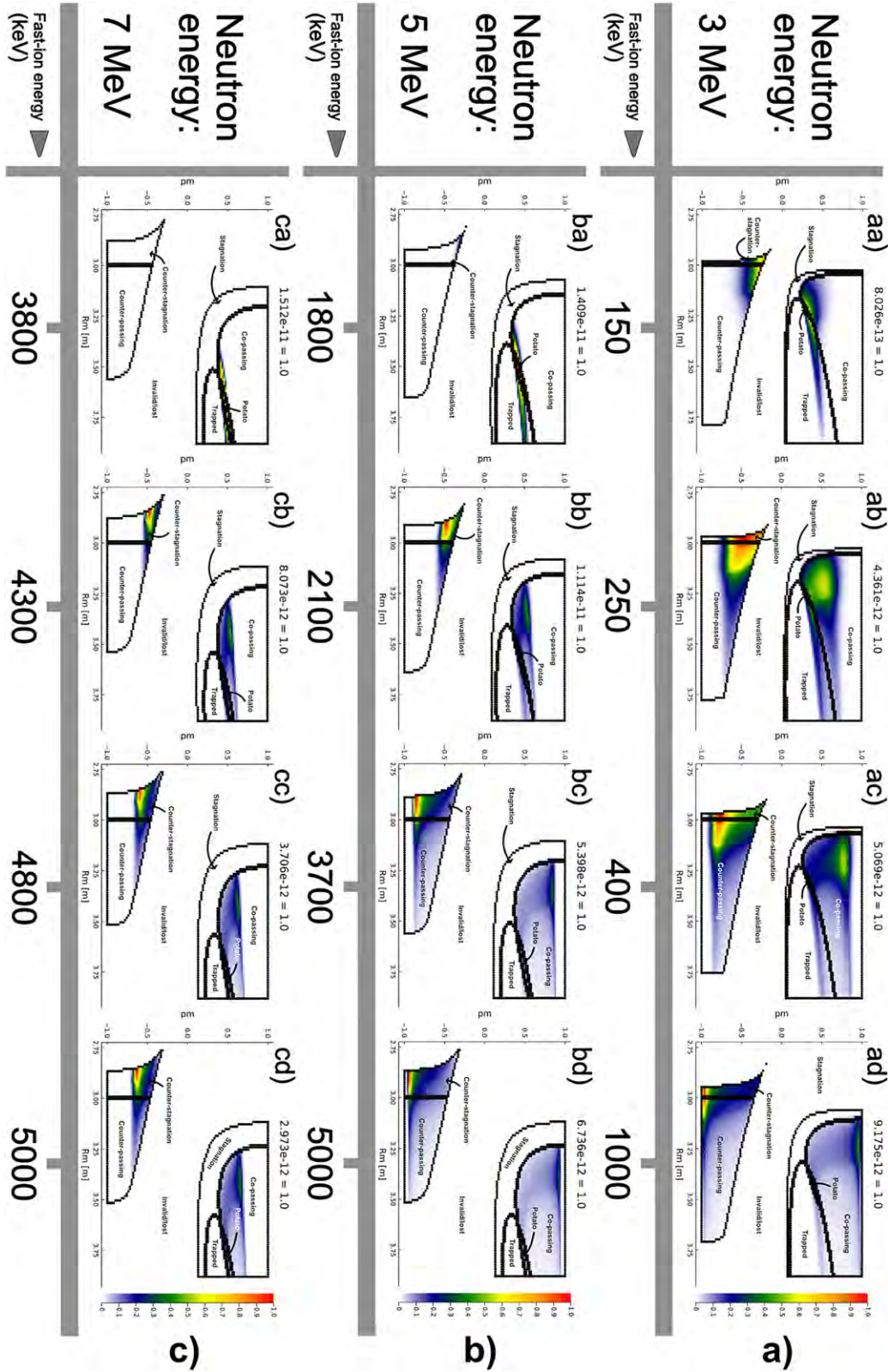


Figure 6. Three orbit weight functions for the perpendicular sightline (corresponding to the LOS of e.g. TOFOR [35]) and $D(D, n)^3\text{He}$ reaction. The number of grid points in p_m and R_m is 100. The neutron energies of (a) 3, (b) 5 and (c) 7 MeV were chosen because neutron energies down-shifted below the nominal $D(D, n)^3\text{He}$ birth energy of 2.45 MeV are diagnostically indistinguishable from scattered neutrons. The FI energy refers to one of the fusing deuterium ions. For ease of visualization, the data in each energy slice has been normalized to have a maximum value of 1.0. The actual maximum value $w_{E,\max}$ is found in the title of each slice plot as $w_{E,\max} = 1.0$.

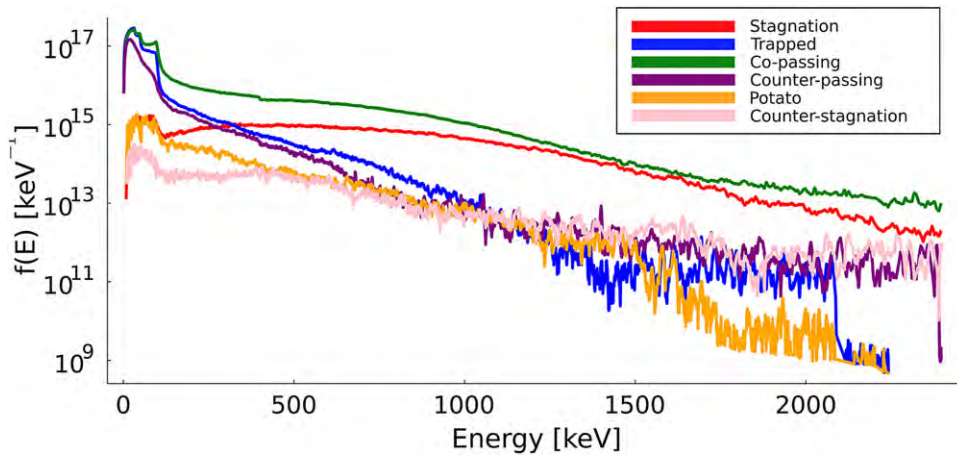


Figure 7. The same TRANSP NUBEAM-computed FI deuterium distribution function as shown in figure 5(b), but split into its orbit-type constituents. The sum of all the colored lines equals the black line in figure 5(b). The significant population of MeV-range co-passing fast ions for three-ion ICRF schemes at JET has been discussed in [52]. The noise at high energies is due to sampling and can be reduced if we increase the number of orbit samples when transforming the FI distribution to orbit space.

For the fast protons, a Maxwellian distribution was used with $T = 30$ keV and with the same 2D (R, z) density profile as that of the TRANSP FI deuterium distribution used in this work. The total number of fast protons was set to $N_p = 6 \times 10^{13}$.

As we can observe from figure 3, the signals produced by multiplying the orbit weight functions (W) with the FI distribution functions (F) closely match the signals computed via the conventional forward model (S). This confirms that the orbit weight functions are computed correctly and provide an accurate map of the orbit-space sensitivity of the diagnostics, which we will examine in sections 4 and 5.

4. Orbit weight functions for perpendicular sightlines

4.1. Neutron emission spectroscopy

Based on the formalism in sections 2 and 3, figure 6 shows examples of the orbit sensitivity of the perpendicular sightline at JET (the sightline of TOFOR) for selected FI energies E and diagnostic (neutron) energies E_d . For each diagnostic energy of an NES (or GRS) spectrum, we will show three selected slices of the corresponding 3D orbit weight function. The orbit sensitivity displays a complicated dependence on the orbit-space coordinates and diagnostic (here neutron) energy E_d . Nevertheless, certain general features can be identified. For all three neutron energies, the orbit sensitivity is relatively concentrated around the potato region (figures 6(aa), (ba) and (ca)) for the lowest E considered here and then widens outwards towards the $p_m = \pm 1.0$ boundaries at increasing FI energies ((ab)–(ad), (bb)–(bd) and (cb)–(cd)). For potato orbits, the ion spends a large fraction of its poloidal transit time inside the LOS and $v_{\parallel} \rightarrow 0$ ($v_{\perp}/v \rightarrow 1$) at the same time. Ions on potato orbits are thus able to produce a large amount of up-shift of the neutron nominal birth energy (which is most important at low FI energies) for a large fraction of the poloidal transit time. This results in a relatively large orbit sensitivity for

the E and E_d of interest (figures 6(aa), (ba) and (ca)). Furthermore, the narrow region of relatively high sensitivity of trapped orbits (most clearly visible in figures 6(aa)–(ad)) is due to the ‘banana tips’ perfectly coinciding with the perpendicular sightline [32]. The ions spend a relatively large fraction of their poloidal transit time at these banana tips, which results in a relatively large sensitivity. At higher FI energies, the counter-stagnation region becomes the area of highest sensitivity. This is because counter-stagnation orbits have the poloidal projection of their trajectories almost completely within the perpendicular sightline. For the TRANSP FI deuterium distribution examined in this work, the counter-stagnation orbits are scarcely populated, as shown in figure 7. However, in future fusion devices, the counter-stagnation orbits are likely going to be populated by fusion-born alpha particles because of their high energy and (approximately) isotropic birth pitch distribution.

As we look at increasingly higher neutron energies, the features of the weight functions stay roughly the same but the 3D structures are translated ‘upwards’ to higher FI energies.

4.2. Gamma-ray spectroscopy

The GRS diagnostic examined in this paper has the same sightline as the perpendicular NES diagnostic. Therefore, the NES and GRS orbit weight functions will have similar orbit sensitivity due to the usage of the same sightline, but differences due to the masslessness of the $T(p, \gamma)^4\text{He}$ gamma photon [22]. As can be seen in figure 8(a), the orbit sensitivity for gamma energies below the nominal birth energy is relatively low (maximum $w_{E,\text{max}}$ in figure 8(a) is an order of magnitude smaller than maximum $w_{E,\text{max}}$ in figure 8(b) and three orders of magnitude smaller than maximum $w_{E,\text{max}}$ in figure 8(c)). This is consistent with the often strongly asymmetric shape of one-step reaction GRS spectra, which have low signal levels below the nominal gamma nominal birth energy [53]. The

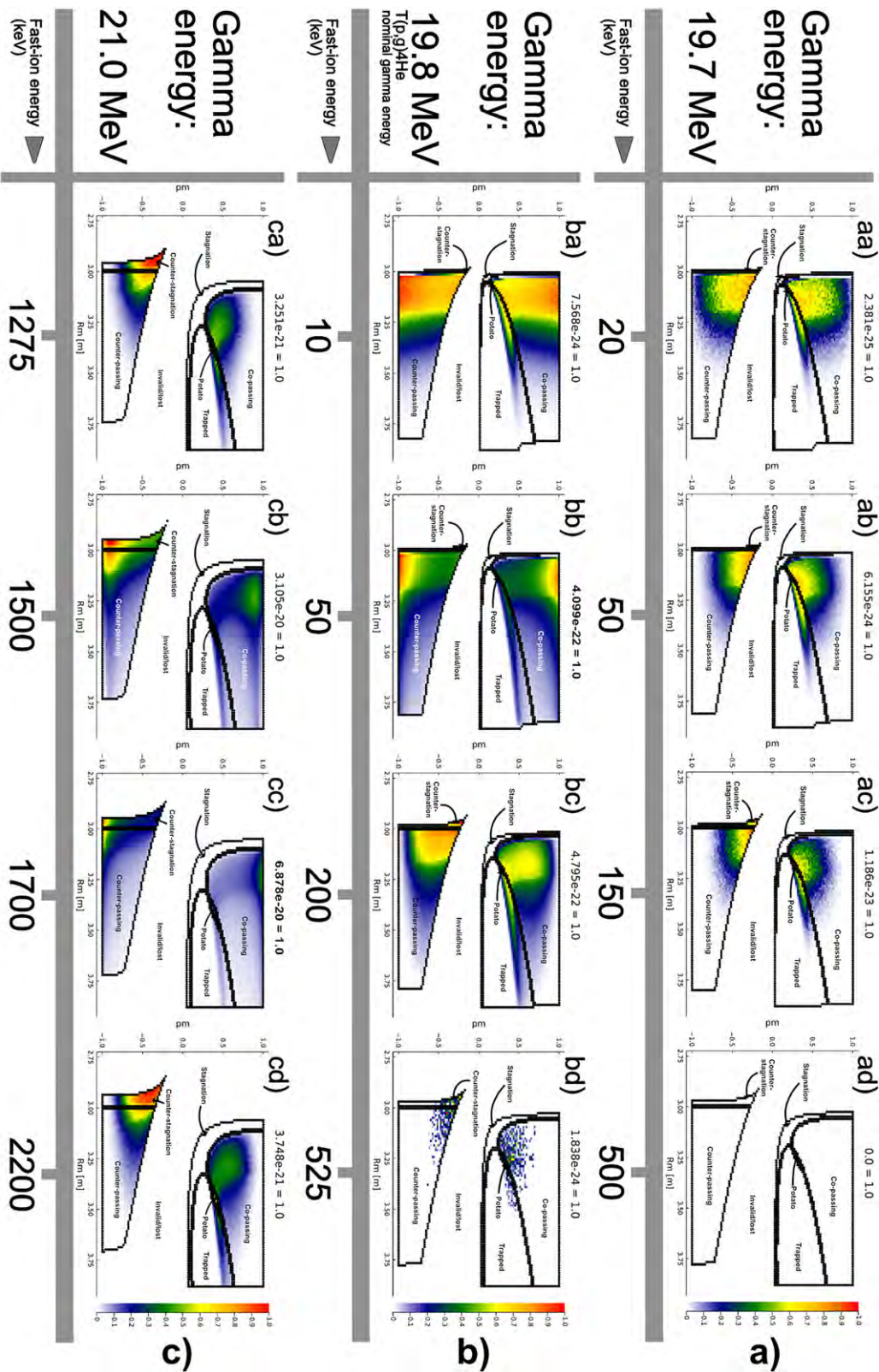


Figure 8. Three orbit weight functions for the perpendicular sightline (corresponding to the LOS of e.g. the LaBr₃ diagnostic [36, 37]) and T(p, γ)⁴He reaction. One at red-shifted gamma energies (a), one at the T(p, γ)⁴He gamma nominal energy (b) and one at blue-shifted gamma energies (c). The number of grid points in p_m and R_m is 100. The FI energy refers to the proton energy of the T(p, γ)⁴He fusion reaction. For ease of visualization, the data in each energy slice has been normalized to have a maximum value of 1.0. The actual maximum value $w_{E,\max}$ is found in the title of each slice plot as $w_{E,\max} = 1.0$.

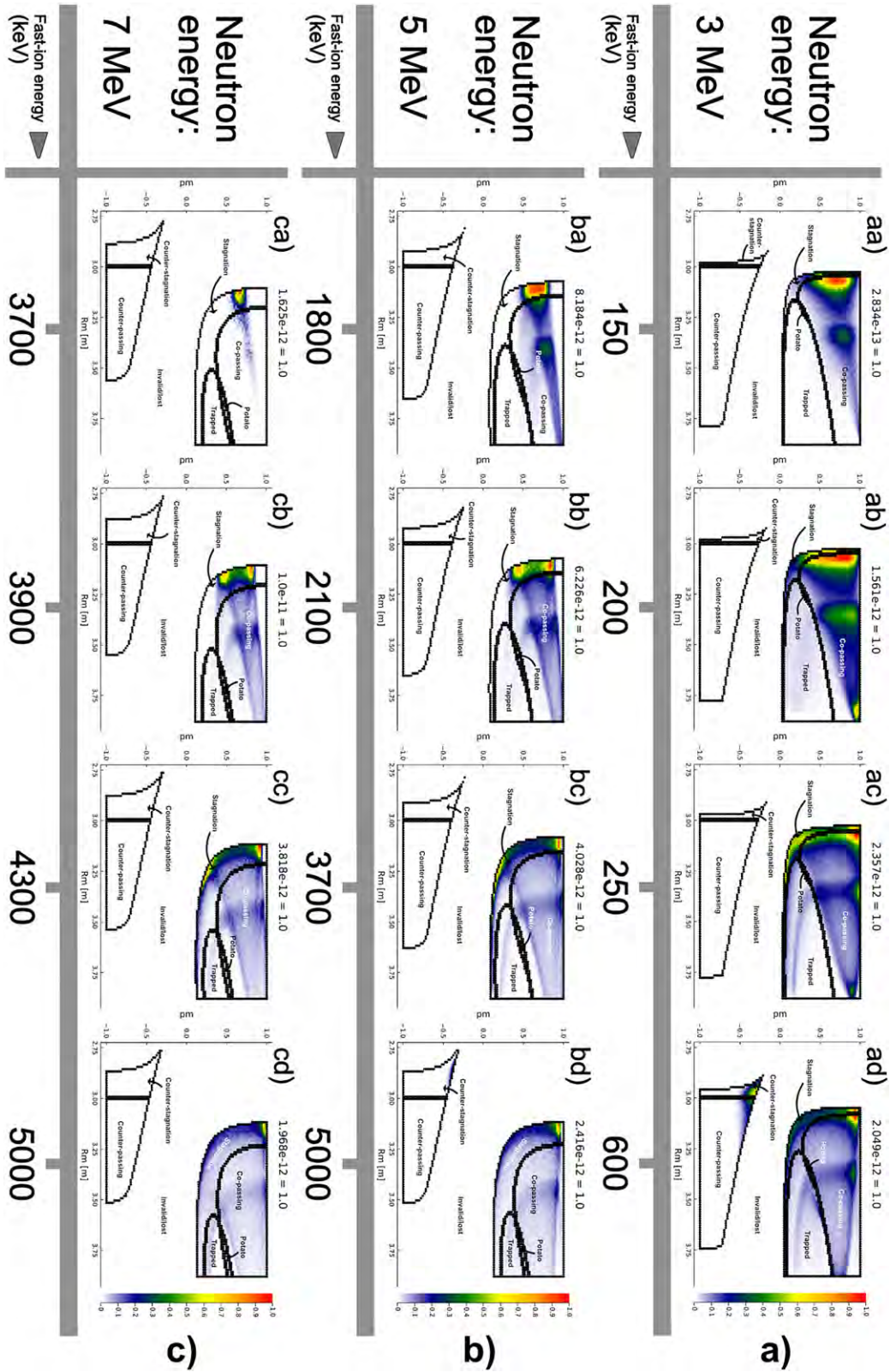


Figure 9. Three orbit weight functions for the oblique sightline (corresponding to the LOS of e.g. the NE213-scintillator diagnostic [38]) and $D(D, n)^3\text{He}$ reaction. The number of grid points in p_m and R_m is 100. The FI energy refers to one of the fusing deuterium ions. For ease of visualization, the data in each energy slice has been normalized to have a maximum value of 1.0. The actual maximum value $w_{E,max}$ is found in the title of each slice plot as $w_{E,max} = 1.0$.

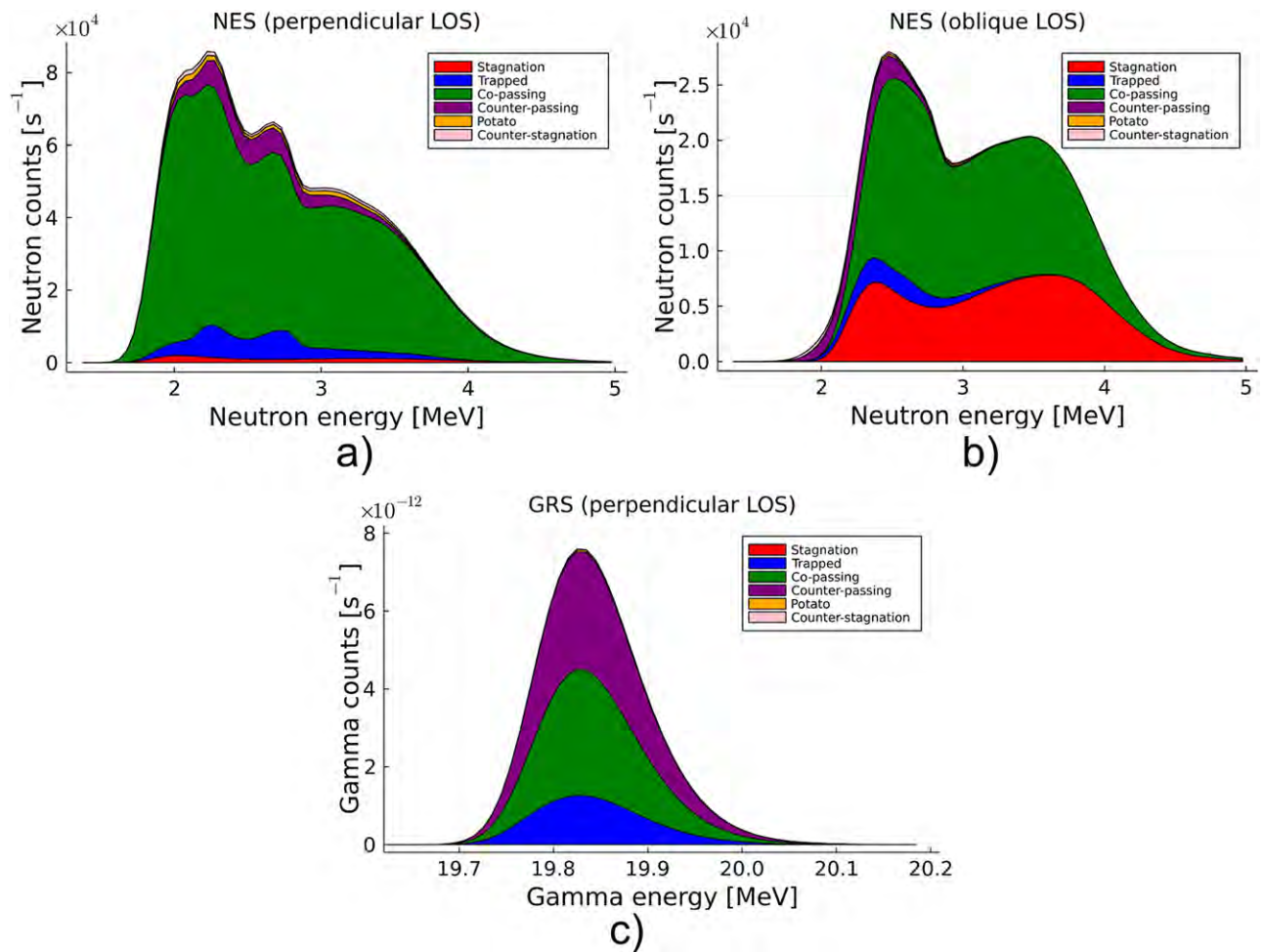


Figure 10. Diagnostic signals split into their orbit type constituents for (a) NES with perpendicular LOS, (b) NES with oblique LOS and (c) GRS with perpendicular LOS. The same orbit-space grid points, FI- and bulk distributions were used as those in figure 3.

sensitivity is mostly concentrated around the tip of the counter-stagnation region in the $p_m < 0.0$ half-plane and the potato region in the $p_m > 0.0$ half-plane. All weights become zero for higher FI energies (figure 8(ad)). This is because fast ions with such a high energy will result in gamma photons with too high energy for the 19.7 MeV diagnostic energy bin. At gamma energies close to the nominal birth energy, the orbit sensitivity is non-zero down to thermal ion energies and up to the several hundreds of keVs, as can be observed in figure 8(b). Just above thermal ion energies, the area of highest sensitivity tends outwards towards the $p_m = \pm 1.0$ boundaries (figure 8(bb)) before reverting back in towards the tip of the counter-stagnation and potato regions (figure 8(bc)) at increasing E . Similar to the orbit weight function for the 19.7 MeV diagnostic energy bin, all weights become zero for sufficiently high FI energies.

At gamma energies above the nominal birth energy, the orbit sensitivity follows a predictable pattern. At relatively low FI energies (figure 8(ca)), the sensitivity is mainly concentrated around the potato region and tip of the counter-stagnation region. This is similar to the orbit sensitivity for gamma energies below the nominal birth energy

(figures 8(aa)–(ac)), but the reason is now due to the need for blue-shift instead of red-shift of the gamma birth energy. At increasing FI energy (figures 8(cb) and (cc)) the sensitivity becomes more concentrated towards the $p_m = \pm 1.0$ boundaries, but again migrates inward towards the potato region and the tip of the counter-stagnation region at $E \approx 2$ MeV (figure 8(cd)). At FI energies above ≈ 2500.0 keV, all weights become zero for the 21.0 MeV diagnostic energy bin. For increasingly high gamma energy bins ($E_d > 21.0$ MeV), the whole pattern observed for the 21.0 MeV orbit weight function will stay roughly the same and move ‘upwards’ to higher FI energies.

5. Orbit weight functions for an oblique sightline (NES)

The viewing cone of the NE213-scintillator NES diagnostic considered in this paper has an oblique sightline w.r.t. **B**. Therefore, the patterns of the weight functions will differ significantly compared to those associated with the perpendicular sightline. However, the non-zero weights will be found

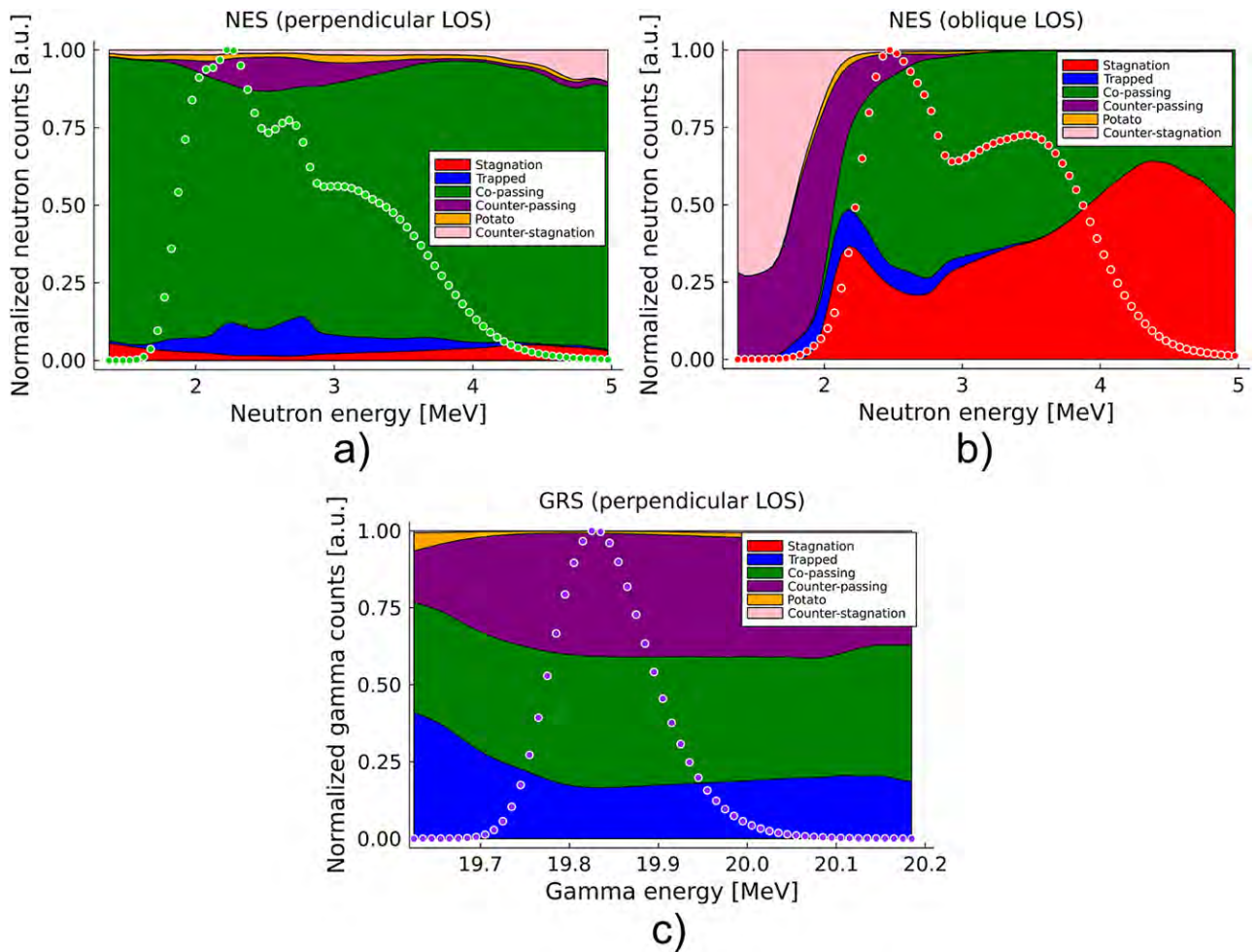


Figure 11. Same as figure 10, but the sum of the orbit constituents has been normalized to 1.0 for all diagnostic energies of interest. The normalized ‘WF’ signals taken from figure 3 have been superimposed for convenience.

in similar FI- and neutron energy ranges as for the perpendicular sightline because the same fusion reaction $D(D, n)^3$ He is being considered. In figure 9, we can observe how the non-zero weights are mostly concentrated to the $p_m > 0.0$ half-plane. The orbits in the $p_m < 0.0$ half-plane will result in ion motion exclusively away from the oblique NES diagnostic. Ions on these orbits are therefore mostly unable to produce the up-shift required for the neutron energies of interest. However, at high FI energies, the counter-stagnation orbits have enough energy and just the right pitch as they cross the oblique sightline that they can produce sufficient up-shift as well (figures 9(ad) and (bd)). Furthermore, the following similar overall features can be observed in all weight functions (figures 9(a)–(c)). The areas of highest sensitivity are concentrated to two islands close to the stagnation region and in the middle of the co-passing region. These areas then split at increasingly high FI energies. They tend toward the $p_m = 1.0$ boundary and the bottom of the stagnation region. At very high FI energies (figures 9(ad), (bd) and (cd)), the sensitivity close to the $p_m = 1.0$ boundary starts to become zero since ions on those orbits will now produce too much up-shift for the neutron energies of interest. Similar to the case of the perpendicular

diagnostics, for increasingly high neutron energies the 3D pattern will stay roughly the same and move ‘upwards’ to higher FI energies.

6. Orbit-space origin of diagnostic signals for given FI distribution functions

With orbit weight functions, we can split the predicted diagnostic signal of a FI distribution function into orbit-type constituents. Mathematically, this can be expressed as

$$WF = \sum_h W_h F_h, \quad (6)$$

where h labels all the different orbit types (co-passing, trapped, etc). The FI distribution function in terms of orbit types (F_h) can be obtained by transforming the FI distribution function into orbit space to obtain $f(E, p_m, R_m)$, and identifying the (E, p_m, R_m) coordinates corresponding to a given orbit type. This is also the method which allows us to split e.g. $f(E)$ into its orbit-type constituents (as in figure 7). Via pointwise multiplication between F_h and $w(E, p_m, R_m)$, we can obtain signal contributions for every diagnostic energy bin in terms of orbit types. This allows us to re-examine the diagnostic signals of

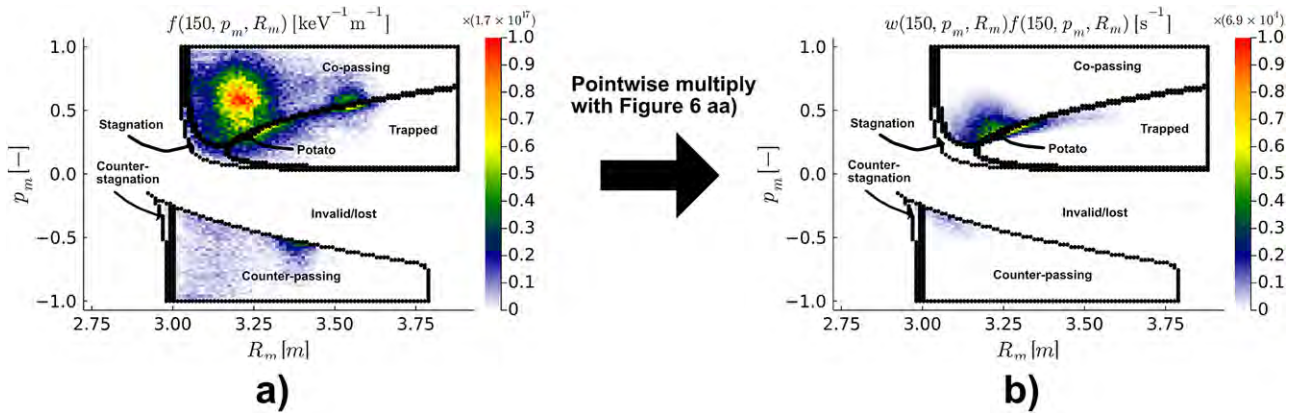


Figure 12. (a) An orbit-space energy slice of the average FI deuterium distribution function for JET shot No. 94701 for our time window of interest. (b) The data in panel (a) is pointwise multiplied with the NES orbit weight function $w(150, p_m, R_m)$ for the neutron energy $E_d = 3$ MeV, corresponding to the weight function slice in figure 6(aa).

figure 3 in terms of orbit types, as shown in figure 10. For the perpendicular LOS with NES and the average FI deuterium distribution function for JET shot No. 94701 for our time window of interest, the signal comes mainly from co-passing orbits for all neutron energies of interest. At neutron energies around the nominal birth energy (2.45 MeV), there are also significant contributions from trapped and counter-passing orbits to the signal generated by fast ions. However, this neutron energy range is difficult to diagnose due to the presence of down-scattered neutrons. For the oblique LOS with NES and the same FI distribution, in addition to co-passing orbits a large portion of the signal comes from stagnation orbits. For the perpendicular LOS with GRS and the Maxwellian FI test distribution (discussed in section 3.2), the signal comes from co-passing, counter-passing and trapped orbits in comparable fractions.

By normalizing the signal to 1.0 for all neutron energies of interest (figure 11), we can examine the signal contributions from different orbit types more closely. For the diagnostics with the perpendicular LOS (figures 11(a) and (c), respectively), the normalized plots confirm the deductions made from figures 10(a) and (c). For the oblique LOS with NES (figure 11(b)), we can observe how the contributions from all orbit types but counter-passing and counter-stagnation orbits vanish for neutron energies below 2.0 MeV. This is because heavy down-shift of the neutron nominal birth energy is required for a neutron to be detected in those diagnostic energy bins. The only orbit types that can produce that type of down-shift, given the oblique sightline, are counter-passing and counter-stagnation orbits. However, note that the absolute magnitude of the diagnostic signal starts to vanish for such heavily down-shifted neutron energies. In addition, the signal at those neutron energies is usually heavily dominated by scattered neutrons, which makes the neutron energy range unusable for diagnosing fast ions [2].

Finally, we can also examine the expected origin of the diagnostic signal in orbit space in detail. This is illustrated in figure 12. At $E = 150$ keV, we have populated orbits of all types, and we might expect them all to contribute to the signal.

However, when pointwise multiplied with an NES orbit weight function, such as the $w(150 \text{ keV}, p_m, R_m)$ for neutron energy $E_d = 3$ MeV (corresponding to figure 6(aa)), we can observe that almost all NES signal will originate from potato-like orbits for the neutron and FI energies of interest. This is because at $E = 150$ keV and $E_d = 3$ MeV, the NES orbit weight function for the perpendicular LOS (e.g. TOFOR) is non-zero almost exclusively for potato-like orbits.

7. Conclusion

In this work, orbit weight functions have been presented for one-step fusion reactions, using a perpendicular and an oblique LOS with NES and GRS diagnostics as examples. The orbit weight functions have been examined for different diagnostic- and FI-energies for the first time. Sensitivity patterns can be identified and understood via slice-by-slice examination in terms of FI energy, while superimposing the topological boundaries between different orbit types.

For the perpendicular LOS and the $D(D, n)^3\text{He}$ reaction, at relatively low FI energies the sensitivity is highest for potato and counter-stagnation orbits. At increasingly high FI energies, the area of highest sensitivity tends toward the $p_m = \pm 1.0$ boundaries, corresponding to co- and counter-passing orbits with ion pitch (v_{\parallel}/v) values close to 1.0. Orbit weight functions for increasingly high neutron energies have 3D patterns that remain qualitatively similar but are shifted 'upward' to increasingly high FI energies. The results can be used to conclude that TOFOR [35] (and any diagnostic sharing the LOS) is in general sensitive to neutrons originating from fast ions on potato orbits but not sensitive at all to neutrons originating from fast ions on stagnation orbits. This is because stagnation orbits at JET are mostly localized outside the viewing cone of TOFOR.

For the perpendicular LOS and the $T(p, \gamma)^4\text{He}$ reaction, the orbit sensitivity is generally low for gamma energies below the gamma nominal birth energy and is concentrated to potato-like and counter-passing orbits localized near the magnetic axis. At the nominal birth energy, the weights are non-zero

down to thermal energies where the sensitivity decreases as R_m increases. At $E \approx 50$ keV, the sensitivity is relatively high for orbits localized close to the magnetic axis with $p_m \rightarrow \pm 1.0$. At increasingly high FI energies, the area of highest sensitivity tends towards potato-like and counter-stagnation orbits, before all weights become zero for sufficiently high FI energies.

For the oblique LOS and the $D(D, n)^3\text{He}$ reaction, the areas of highest orbit sensitivity correspond to co-passing and stagnation orbits. The sensitivity is almost exclusively zero for counter-passing and counter-stagnation orbits since ions on those orbits are unable to produce the upshift required for the neutron energies of interest ($E_d > 2.5$ MeV).

For all diagnostics, the orbit sensitivity is mostly determined by the location and orientation of the sightline (perpendicular, oblique, co-current, counter-current, poloidal projection etc). For a given FI distribution function, the synthetic signals computed via the orbit weight functions are shown to closely match those computed with established forward models (in this work, the DRESS code [46] was used). In addition, the weight function signals can be split into their orbit-type constituents, which makes it possible to deduce signal origin in terms of orbit types. For JET shot No. 94701 and the time window of interest, the synthetic NES signals (corresponding to signals detectable by e.g. TOFOR [35] and the NE213-scintillator [38] but without an instrumental response function) are found to originate mostly from co-passing orbits. In addition, for the oblique LOS NES signal (e.g. the NE213-scintillator), a significant fraction originates from stagnation orbits.

In future work, orbit weight functions will be developed for two-step fusion reactions as well, which will enable us to express the sensitivities of diagnostics using e.g. alpha-particle FI orbits. In addition, orbit weight functions will be used to optimise the design of existing and new FI diagnostics via, for example, maximising the amount of non-zero weights in orbit space. Finally, orbit weight functions will be used to reconstruct the full (E, p, R, z) FI distribution function from fusion-product measurements via orbit tomography as was recently achieved for FIDA measurements [30]. This is expected to help illuminate key relationships between the behavior of fast ions (including alpha particles) and various plasma instabilities such as Alfvén eigenmodes, sawteeth and energetic particle modes, causing undesired redistribution of fast ions. This is highly relevant both for ongoing experiments such as JET and future tokamaks such as ITER where fast ions will be crucial to achieve self-sustained heating of burning plasmas.

Acknowledgments

This work has received support from the Niels Bohr Foundation which is a merger of The Niels Bohr Grant, The Emil Herborg Grantpart, The Grant of MA Marcus Lorenzen, The Ole Rømer Foundation and The Julie Marie Vinter Hansen Travel Grant. The views and opinions expressed herein do not necessarily reflect those of The Royal Danish Academy of Sciences

and Letters. This work has been carried out within the framework of the EUROfusion Consortium, funded by the European Union via the Euratom Research and Training Programme (Grant Agreement No. 101052200—EUROfusion). Views and opinions expressed are however those of the author(s) only and do not necessarily reflect those of the European Union or the European Commission. Neither the European Union nor the European Commission can be held responsible for them.

ORCID iDs

H. Järleblad  <https://orcid.org/0000-0003-1126-686X>

L. Stagner  <https://orcid.org/0000-0001-5516-3729>

J. Eriksson  <https://orcid.org/0000-0002-0892-3358>

M. Nocente  <https://orcid.org/0000-0003-0170-5275>

J. Rasmussen  <https://orcid.org/0000-0002-3947-1518>

References

- [1] Mailloux J. et al 2022 Overview of JET results for optimising ITER operation *Nucl. Fusion* accepted (<https://doi.org/10.1088/1741-4326/ac47b4>)
- [2] Moseev D., Salewski M., Garcia-Muñoz M., Geiger B. and Nocente M. 2018 *Rev. Mod. Plasma Phys.* **2** 7
- [3] Heidbrink W.W. and White R.B. 2020 *Phys. Plasmas* **27** 030901
- [4] Gorelenkov N.N., Berk H.L., Budny R., Cheng C.Z., Fu G.-Y., Heidbrink W.W., Kramer G.J., Meade D. and Nazikian R. 2003 *Nucl. Fusion* **43** 594
- [5] Pinches S.D. et al 2006 *Nucl. Fusion* **46** S904–10
- [6] Fasoli A. et al 2007 *Nucl. Fusion* **47** S264–84
- [7] Ding R. et al 2015 *Nucl. Fusion* **55** 023013
- [8] Salewski M. 2019 *Fast-Ion Diagnostic in Fusion Plasmas by Velocity-Space Tomography* (Kongens Lyngby, Denmark: Technical University of Denmark)
- [9] Eriksson J. et al 2015 *Nucl. Fusion* **55** 123026
- [10] Salewski M. et al 2019 *J. Instrum.* **14** C05019
- [11] Salewski M. et al 2012 *Nucl. Fusion* **52** 103008
- [12] Salewski M. et al 2013 *Nucl. Fusion* **53** 063019
- [13] Salewski M. et al 2014 *Nucl. Fusion* **54** 023005
- [14] Jacobsen A.S. et al 2016 *Plasma Phys. Control. Fusion* **58** 045016
- [15] Salewski M. et al 2016 *Nucl. Fusion* **56** 106024
- [16] Salewski M. et al 2017 *Nucl. Fusion* **57** 056001
- [17] Salewski M. et al 2018 *Nucl. Fusion* **58** 096019
- [18] Salewski M. et al 2018 *Fusion Sci. Technol.* **74** 23–36
- [19] Heidbrink W.W., Luo Y., Burrell K.H., Harvey R.W., Pinsker R.I. and Ruskov E. 2007 *Plasma Phys. Control. Fusion* **49** 1457–75
- [20] Salewski M. et al 2014 *Plasma Phys. Control. Fusion* **56** 105005
- [21] Salewski M. et al 2011 *Nucl. Fusion* **51** 083014
- [22] Salewski M. et al 2016 *Nucl. Fusion* **56** 046009
- [23] Salewski M. et al 2015 *Nucl. Fusion* **55** 093029
- [24] Galdon-Quiroga J. et al 2018 *Plasma Phys. Control. Fusion* **60** 105005
- [25] Heidbrink W.W., Garcia A., Boeglin W. and Salewski M. 2021 *Plasma Phys. Control. Fusion* **63** 055008
- [26] Jacobsen A.S., Salewski M., Eriksson J., Ericsson G., Korsholm S.B., Leipold F., Nielsen S.K., Rasmussen J. and Stejner M. 2015 *Nucl. Fusion* **55** 053013

- [27] Jacobsen A.S. *et al* 2017 *Rev. Sci. Instrum.* **88** 073506
- [28] Schmidt B.S., Salewski M., Reman B., Dendy R.O., Moseev D., Ochoukov R., Fasoli A., Baquero-Ruiz M. and Järleblad H. 2021 *Rev. Sci. Instrum.* **92** 053528
- [29] Heidbrink W.W. and Sadler G.J. 1994 *Nucl. Fusion* **34** 535
- [30] Stagner L., Heidbrink W.W., Salewski M., Jacobsen A.S. and Geiger B. (the DIII-D, ASDEX Upgrade Teams) 2022 *Nucl. Fusion* **62** 026033
- [31] Stagner L. and Heidbrink W.W. 2017 *Phys. Plasmas* **24** 092505
- [32] Järleblad H., Stagner L., Salewski M., Eriksson J., Benjamin S., Madsen B., Nocente M., Rasmussen J. and Schmidt B.S. *et al* 2021 *Rev. Sci. Instrum.* **92** 043526
- [33] Eriksson J. *et al* 2019 *Plasma Phys. Control. Fusion* **61** 014027
- [34] Nocente M. *et al* 2020 *Nucl. Fusion* **60** 124006
- [35] Johnson M.G. *et al* 2008 *Nucl. Instrum. Methods Phys. Res. A* **591** 417–30
- [36] Nocente M. *et al* 2010 *Rev. Sci. Instrum.* **81** 10D321
- [37] Nocente M. *et al* 2021 *Rev. Sci. Instrum.* **92** 043537
- [38] Binda F. *et al* 2014 *Rev. Sci. Instrum.* **85** 11E23
- [39] Rome J.A. and Peng Y.K.M. 1979 *Nucl. Fusion* **19** 1193
- [40] Kazakov Y.O. *et al* 2021 *Phys. Plasmas* **28** 020501
- [41] Štancar Ž. *et al* 2021 *Nucl. Fusion* **61** 126030
- [42] Kazakov Y.O. *et al* 2020 *Nucl. Fusion* **60** 112013
- [43] Kikuchi M., Lackner K. and Tran M.Q. 2012 *Fusion Physics* (Vienna: IAEA)
- [44] Stagner L. 2018 Inference of the fast-ion distribution function *PhD Thesis* University of California, Irvine
- [45] Bierwage A. *et al* 2021 Representation and modeling of charged particle distributions in tokamaks (arXiv:2111.08224v1 [physics.plasm-ph])
- [46] Eriksson J., Conroy S., Sundén E.A. and Hellesen C. 2016 *Comput. Phys. Commun.* **199** 40–6
- [47] Breslau J., Gorelenkova M., Poli F., Sachdev J., Pankin A. and Perumpilly G. 2018 *TRANSP (Computer Software)* USDOE Office of Science (SC), Fusion Energy Sciences (FES) (SC-24) (<https://transp.pppl.gov/index.html>)
- [48] Pankin A., McCune D., Andre R., Bateman G. and Kritz A. 2004 *Comput. Phys. Commun.* **159** 157–84
- [49] Brambilla M. 1999 *Plasma Phys. Control. Fusion* **41** 1
- [50] Kwon J.-M. *et al* 2006 Development of XGC-RF for global guiding-center particle simulation of minority ICRH heated plasmas in a general tokamak geometry *48th Annual Meeting of the Division of Plasma Physics* (Philadelphia, Pennsylvania October 30–November 3 2006) (<http://meetings.aps.org/link/BAPS.2006.DPP.VP1.115>)
- [51] Kwon J.-M., McCune D. and Chang C.S. 2007 Enhancement of nubeam for the simulation of fast ion and rf-wave interaction based on the quasi-linear theory *49th Annual Meeting of the Division of Plasma Physics* (Orlando, Florida November 12–16, 2007) vol 52 (<http://meetings.aps.org/link/BAPS.2007.DPP.UP8.83>)
- [52] Dreval M. *et al* 2022 *Nucl. Fusion* **62** 056001
- [53] Nocente M., Källne J., Salewski M., Tardocchi M. and Gorini G. 2015 *Nucl. Fusion* **55** 123009

Paper III

A Framework for Synthetic Diagnostics using Energetic-particle Orbits in Tokamaks

H. Järleblad^{a,*}, L. Stagner^b, M. Salewski^a, J. Eriksson^c, M. Nocente^d, B.S. Schmidt^a, M. Rud Larsen^a

^a*Department of Physics, Technical University of Denmark, DK-2800 Kgs. Lyngby, Denmark*

^b*General Atomics, P.O. Box 85608, San Diego, California 92186-5608, USA*

^c*Department of Physics and Astronomy, Uppsala University, 751 20 Uppsala, Sweden*

^d*Department of Physics, University of Milano-Bicocca, 20126 Milano, Italy*

Abstract

In fusion plasma physics, the trajectories of energetic particles in magnetic confinement devices are known as orbits. To effectively and efficiently be able to work with orbits, the Orbit Weight Computational Framework (OWCF) was developed. The OWCF constitutes a set of scripts, functions and applications capable of computing, visualizing and working with quantities related to fast-ion (FI) orbits in toroidally symmetric fusion devices. The current version is highly integrated with the DRESS code, which enables the OWCF to compute and analyze the orbit sensitivity for arbitrary neutron- and gamma-diagnostics. However, the OWCF is modular in the sense that any future codes (e.g. FIDASIM) can be easily integrated. The OWCF can also compute projected velocity spectra for FI orbits, which play a key role in many FI diagnostics. In terms of magnetic equilibrium, the OWCF accepts any magnetic equilibrium file used by the TRANSP code, as well as any user-specified Solov'ev magnetic equilibrium. The interactive applications of the OWCF can function both as tools for investigative research but also for intuitive pedagogical purposes. The OWCF will be used to analyze and simulate the diagnostic results of current and future fusion experiments such as ITER. The orbit weight functions computed with the OWCF can be used to reconstruct the FI distribution in terms of FI orbits from experimental measurements using tomographic inversion.

*Corresponding author.

E-mail address: henrikj@dtu.dk

Keywords: nuclear fusion; fast ions; orbits; weight functions.

1. Introduction

In magnetic confinement fusion devices, such as tokamaks, the population of particles can be categorized into two sets; thermal and energetic [36]. In tokamaks of size similar to the Joint European Torus (major radius ~ 3 meters)[16], the following distinction can be made. If we take three times the thermal velocity as a threshold, $3v_{\text{th}}$, the energetic fast ions are ~ 10 times more energetic than the thermal (bulk) ions. For a typical plasma temperature of $1 - 10$ keV ($\approx 1 - 11 \times 10^7$ K), the lower limit for energetic particles should arguably be placed around 10 keV. In reality, the transition from thermal to fast is naturally continuous. Even though the fast-ion (FI) population can be 2-3 orders of magnitude smaller than the thermal population[12], fast ions can cause damage to first-wall components[41] and drive plasma instabilities[42, 46]. Fast ions also need to be confined for a sufficient length of time (several slowing-down times, i.e. slowing down from fast to slow speeds) so as to heat the thermal ions and enable a self-sustained plasma burn[41].

Because of their relatively low energy, the thermal ions stay mostly confined to the magnetic flux surfaces, while the fast ions have more exotic motion that can deviate substantially from the magnetic flux surfaces[17, 12]. This exotic motion is commonly named a *fast-ion orbit* (FIO). The distance that the fast ions deviate from the flux surfaces is roughly proportional to the FI energy. Since $E_{\text{FI}} \approx 10E_{\text{bulk}}$, the FI drift speed is about 10 times larger than the thermal drift speed. In a tokamak, the FIOs constitute fixed trajectories that the fast ions must follow. A suitable analogy would be that the fast ions can be thought of as cars and the FIOs as highways. Since the fast ions must follow these highways, energy and particles flow along them and effectively define the FI distribution. The analogy also works for thermal ions, but with less exotic orbits as highways. The particle flow is dominated by the bulk (thermal) plasma, while energy flow is often carried to a significant fraction by the the fast ions.

Depending on the energy, starting position and angle of the particle velocity with respect to the magnetic field, the path of the FIOs can vary substantially. Therefore, it is of great importance to know how sensitive a diagnostic is to different FIOs, since various diagnosable particles or quanta

(e.g. fusion-born neutrons and γ -rays) might originate more strongly from certain FIOs[12]. Depending on the heating scheme of the tokamak plasma, certain FIOs will be more populated than others[12] and the exact shape of the diagnostic signal is thus dependent on a multitude of factors, including the magnetic equilibrium (which determines the shape of the topological FIO regions in phase space)[11] and the heating scheme, as well as the density and temperature profiles of the fusion plasma[14].

By knowing the sensitivity of a plasma diagnostic in phase space, the signal can be directly related to the FI distribution, given the assumption of a linear relationship between the signal and the FI distribution[32]. The sensitivity of the FI diagnostic can be expressed with varying dimensionality depending on the phase space of interest. For example, in velocity-space tomography[27, 28, 33, 35, 34], the sensitivity is two-dimensional and can be expressed as a so-called *weight function* of the parallel and perpendicular velocity components (v_{\parallel}, v_{\perp}) of the ion with respect to the magnetic field (or, equivalently, via the energy E and pitch $p = v_{\parallel}/v$ [6]). In terms of computational resources, this 2D weight function is almost always possible to compute on a regular laptop, for any phase-space grid resolutions of interest; both in terms of RAM and CPU power. However, these 2D weight functions can relate a diagnostic measurement to the FI distribution only at a single point (R, z) in position space[48, 23, 34, 30, 31, 29], where R is the major radius cylindrical coordinate and z the vertical coordinate. To be able to relate a measurement to the FI distribution at *all* (R, z) points via FIOs, three-dimensional so-called *orbit weight functions* (OWs) can be used[11, 12, 23, 22]. The (E, p_m, R_m) so-called orbit space is the 3D coordinate space of choice for the current version of the OWCF, due to its semi-bounded space and favorability for tomographic reconstructions[12]. E is the energy of the fast ion and p_m is the pitch (p) at the maximum major radius position R_m of the fast ion as it traverses its orbit. All quantities computed with the OWCF can be mapped to the standard $(E, \mu, P_{\phi}; \sigma)$ coordinates (where μ is the magnetic moment, P_{ϕ} is the toroidal canonical angular momentum and σ is a binary coordinate), provided that a Jacobian is not required. OWs, topological maps, poloidal and toroidal transit time maps are ok, but FI distributions are not, since distributions are defined *per phase-space volume*. This provides the user with the flexibility to analyze and export computed results in either (E, p_m, R_m) or $(E, \mu, P_{\phi}; \sigma)$ coordinates. This is useful for e.g. stability analysis, which is often performed in the $(E, \mu, P_{\phi}; \sigma)$ coordinates. It should be mentioned that, in addition to

OWs, other ways of relating a diagnostic signal to the full FI distribution exist. These include expressing the FI distribution in terms of a basis of slowing-down distribution functions[5, 7]. For orbit-space grid resolutions of interest, 3D OWs usually need to be computed using a computational cluster to be able to complete the calculation within a reasonable timeframe, due to both RAM and CPU requirements. Naturally, to be able to calculate, analyze and work with these 3D OWs, a speed-optimized framework written in a high-performance programming language is useful. To this end, the orbit weight computational framework (OWCF) was developed.

In short, the OWCF is a collection of scripts, utilities, structures and functions written in the Julia programming language[13]. The efficient computation of guiding-center FIOs (where the finiteness of the Larmor radius is not taken into account), made possible by the Julia language, serves as the foundation for the framework. The OWCF provides answers to several questions, such as:

- How to compute orbit weight functions efficiently
- How to analyze orbit weight functions effectively and intuitively
- How to streamline transformations of arbitrary fast-ion distributions into fast-ion orbits
- How to investigate populatable fast-ion orbits for every (R, z) point
- How to compute synthetic diagnostic signals using orbit weight functions with an exceptionally large amount of orbit-space grid points ($> 100 \times 100 \times 100$)
- How to decompose diagnostic signals into the contributions from fast-ion orbit types
- How to streamline the possibility of reconstructing fast-ion orbit distributions from measurements

In addition, even though the OWCF is currently heavily integrated with the DRESS[14] code for computing synthetic diagnostic neutron and γ -ray spectra, the OWCF maintains a modular approach towards synthetic diagnostics codes in general. This enables future codes to be easily integrated with the OWCF, for computing OWs via synthetic diagnostic FIO spectra.

This paper is structured as follows. In section 2, an overview of the OWCF is given. In sections 3 and 4, discussions on topological maps and orbit weight functions are provided, respectively. In 5, the capability of the OWCF to transform between (E, p_m, R_m) and (E, p, R, z) is outlined and in section 6 the tools of the OWCF for decomposing diagnostic signals in terms of orbit types are presented. Finally, a conclusion follows in section 7.

It should be mentioned that the OWCF contains more utilities and tools than can be included in this paper. For a complete and detailed breakdown of the whole OWCF, the reader is referred to the manual included with the OWCF.

2. Overview of the OWCF

At the time of publication, the current version of the OWCF (v1.0) comprises many scripts and file structures, and it is written almost entirely in the Julia programming language. It was chosen as a suitable language for the OWCF since it is high-level and yet maintains high-performance via efficient code compilation and execution[13]. Future code maintenance of the OWCF is therefore envisioned to be easily accessible without the need to sacrifice performance.

To help the reader understand the structure of the OWCF, a basic building block of the framework has been visualized in Figure 1a, and a basic relationship between different scripts has been visualized in Figure 1b. We can observe how the inputs and outputs form an I/O chain between the scripts, including optional inputs and integrated usage of dependencies. Together, this simple example serves as a basic illustration of the much larger system that is the full OWCF. Additionally, since two different scripts in the OWCF often require different inputs, the OWCF provides templates for input files used to specify the necessary inputs and to easily execute the pertaining script following input specification. These input files will be discussed further in later sections of this paper.

A graphical overview of the full OWCF (as it stands at the time of publication) is given in Figure 2. We can observe how there are four main groups of code (inside dotted lines): main scripts, apps, data and misc. The **main scripts** (colored purple) constitute the bulk of the computational tools of the OWCF. Depending on the quantity needed to be computed, one of the main scripts is used. The output of a main script can then be visualized by using, for example, one of the **apps** (colored red). The apps provide interactive

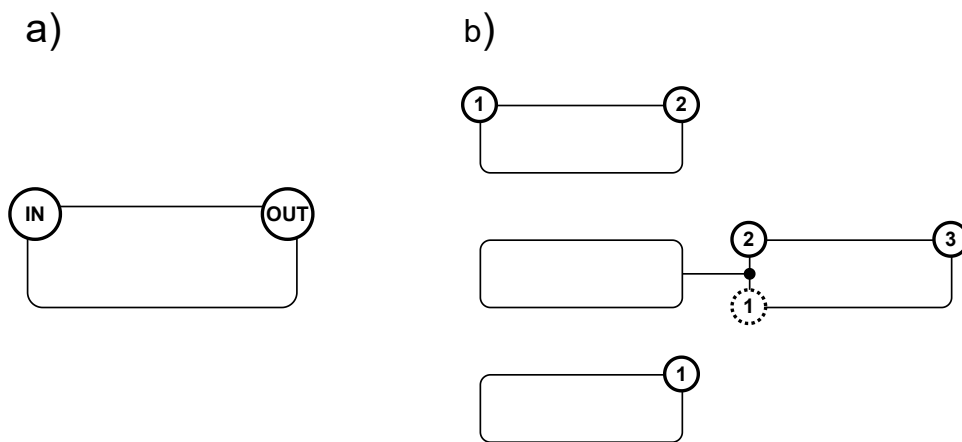


Figure 1: a) An illustration of a basic building block of the OWCF. The script has some input data visualized as an 'IN' circle in the top-left corner. The script has some output data visualized as an 'OUT' circle in the top-right corner. In b), we would like to compute output data '3' using *main script*. This '3' data can be an orbit weight function, an orbit signal etc. However, we can see that *main script* requires input data '2'. This '2' data is the output of *script B*, so we must execute *script B* prior to running *main script*. However, *script B* requires input data '1'. This '1' data is the output of *script A*, so we must run *script A* prior to running *script B*. Furthermore, the *main script* optionally accepts input data '1'; the optional input has been visualized with a dotted circle. We can also observe how a line runs **from dependencies to main script**. This means that *main script* is dependent on *dependencies*, i.e. it uses *dependencies* in an integrated way internally and cannot function without it.

analysis of computed quantities using web-based plotting, enabled via the *Interact.jl*[40] and *Mux.jl*[37] Julia packages. We shall explore the user interface and capabilities of the OWCF main scripts and apps in later sections. However, some outputs of the main scripts might need to be post-processed before being usable by the apps. This post-processing can be achieved by using the **helper functions and scripts** (colored blue). There are different helper scripts for different usage scenarios. Furthermore, with the OWCF, the user has the possibility of using various forms of data to perform analysis. As we can observe in Figure 2, there are five forms of basic data for the OWCF: a magnetic equilibrium, a fast-ion (FI) distribution in (E, p, R, z) coordinates, a diagnostic line-of-sight (LOS), a .cdf-file with TRANSP[8] discharge (shot) data and a .cdf-file with TRANSP NUBEAM[2] FI data. TRANSP is a 1.5D equilibrium and transport solver for interpretation and prediction of tokamak discharges. Its simulations and results are widely used in the plasma physics community, thus making its output a natural basic data input for the OWCF. NUBEAM is the FI module of TRANSP. Let us investigate the different forms of basic data for the OWCF in detail.

The magnetic equilibrium (D1) can be of two types. It can be provided as an .eqdsk file (e.g. used by TRANSP) containing estimated data for the magnetic equilibrium from experimental measurements, as well as data about the tokamak first wall. The magnetic equilibrium can also be generated from the fully customizable Solov'ev equilibrium template provided with the *Equilibrium.jl*[20, 3] package. In this case, a first wall of the hypothetical tokamak should be provided as data arrays of R and z values. This is to be able to distinguish between confined and lost orbits. The OWCF provides an easy way for the user to generate a Solov'ev equilibrium .jld2-file via the **compSolovev.jl** (E1) extra script.

The FI distribution in (E, p, R, z) coordinates (D2) can be provided as either a .jld2- or .h5 (.hdf5)-file type. Specific data keys are then required to be able to load the data correctly, such as 'f' identifying the 4D data array containing the (E, p, R, z) FI distribution. Sometimes, due to data conversion mismatch, this 4D array might be reversed in terms of dimensional order (i.e. $f(z, R, p, E)$) when loading from the .h5-file format. The OWCF therefore automatically re-reverses this order, if needed.

The inclusion of a diagnostic LOS (D3) is perhaps one of the less flexible features of the OWCF. As of this version of the framework, the LOS has to be provided either as a .txt-file containing data in the output format provided by the LINE21[39] code, or not specified at all, whereupon a spherical 4π sr

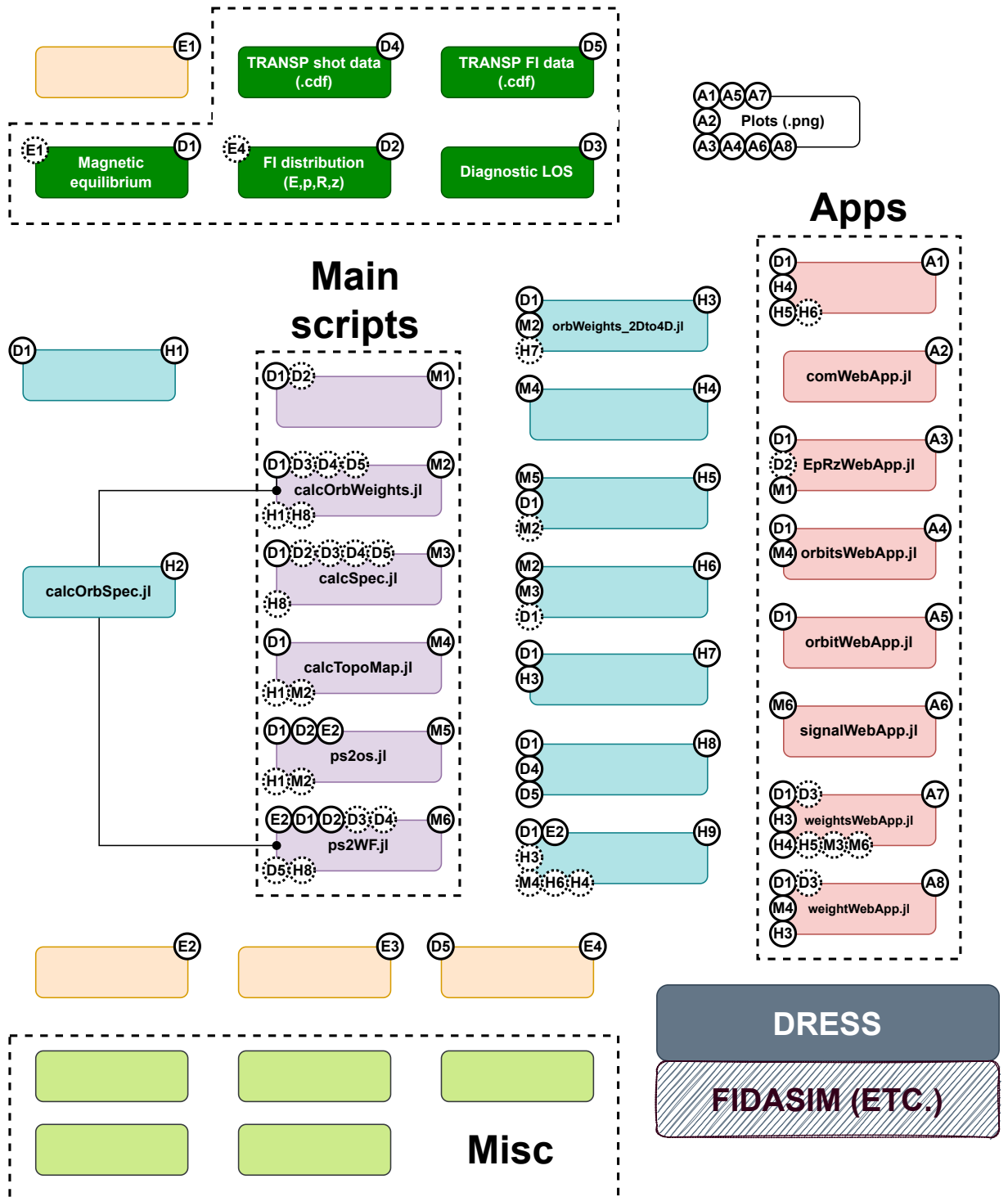


Figure 2: A graphical overview of the OWCF.

emission angle is assumed. However, this rather non-flexible feature is only required when using the OWCF together with the DRESS code. Should the user wish to compute orbit weight functions (or other quantities in orbit-space) using other codes, e.g. FIDASIM[45, 4], then the requirement for the LOS is given by that code.

The TRANSP shot (D4) and FI (D5) data are given in .cdf-file format and provided as output files of TRANSP runs. The TRANSP FI data is provided as output of the TRANSP-module NUBEAM[2]. The TRANSP FI data can be provided as input to the extra script **getEpRzFIDistrFrom-TRANSP.jl** (E4). The output will then be the TRANSP FI data converted into (E, p, R, z) coordinates, stored as a .jld2-file (D2). To clarify, in several OWCF scripts, the FI distribution can be provided either as a D2 or D5 data type. We can convert a D5 data type into a D2 data type via the E4 extra script.

Finally, the OWCF also contains some miscellaneous (**misc**) Julia files. These provide the framework with extra functionality that help the framework in various ways; such as keeping track of the fusion reactions currently supported by the DRESS code, a default normalized plasma temperature and density profile in case the user has provided none as input, and functions mapping simple ion species input ('D' for deuterium, 'T' for tritium etc) to properties such as mass and charge in kilograms and Coulombs, and atomic mass and charge units, respectively. The default plasma temperature and density profiles have been plotted in Figure 3. Lastly, the OWCF makes use of functions in **dependencies.jl** (E2) and **gui.jl** (E3) to serve as 'backend' and for non-interactive plotting, respectively.

3. Topological maps

Even though orbit weight functions are arguably the main feature of the OWCF, the true intelligibility can be found in the usage of topological maps (topoMaps) to easily interpret and analyze computed quantities in 3D (E, p_m, R_m) orbit space[17, 43, 22, 23, 11] and 4D (E, p, R, z) guiding-center phase space. By identifying which parts of phase space correspond to the six basic FIOs (co-passing, counter-passing, trapped, stagnation, counter-stagnation and potato)[11, 12, 47], we can identify the boundaries between the topological regions and use them to gain further insight about the phase-space quantities. The topological maps also serve as the 'discrete prism'

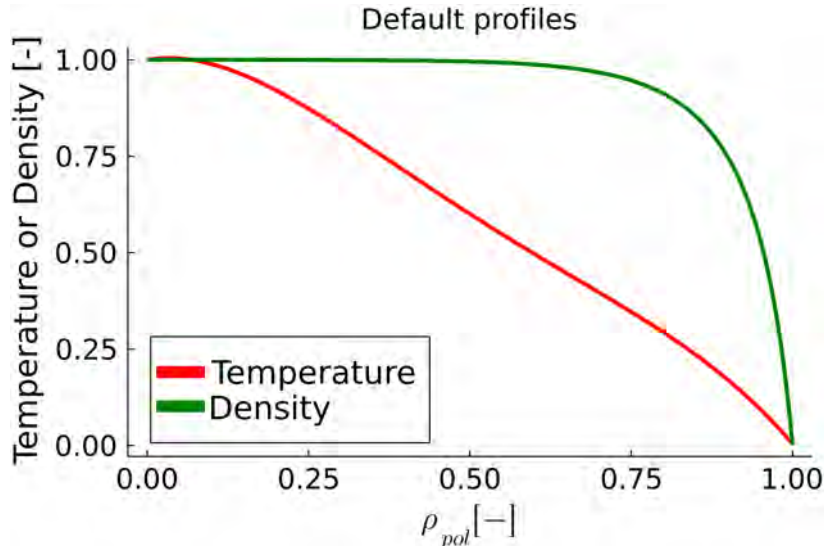


Figure 3: The default bulk temperature and density profiles used by the OWCF, in case the user provided none. The profiles can be re-scaled by specifying a temperature and density values on axis ($\rho_{pol} = 0$). The profiles are based on the temperature and density profiles of JET shot No 96100 at 13 seconds.

when splitting synthetic diagnostic signals into their orbit-type constituents, as we shall discuss in later sections.

3.1. (E, p_m, R_m) orbit space

The computation of topological maps in orbit space is done via the **calcTopoMap.jl** (M4) main script. As we can see in Figure 2, a magnetic equilibrium has to be provided as input. The specification of the grid points in (E, p_m, R_m) can be done in various ways, including automatically loading them by providing the filepath to the output of the **calcOrbGrid.jl** (H1) helper script or the **calcOrbWeights.jl** (M2) script. Additionally, the user can specify whether or not incomplete (i.e. problematic to integrate) and/or lost orbits should be included in the topological map, respectively. The option to save poloidal and toroidal transit times for all valid orbits is also provided. When all the inputs have been provided the **calcTopoMap.jl** script can be correctly executed. This can be advantageously achieved by modifying the OWCF template for a **calcTopoMap** input file and then simply executing the input file. The **calcTopoMap.jl** script will then compute a

3D topological map by computing 2D topological maps[11, 12] sequentially for each fast-ion energy E of interest, as illustrated in Figure 4.

With the M4 output, we can use the **orbitsWebApp.jl** (A4) to interactively visualize the orbit-space topology. A screenshot of the web application can be seen in Figure 5. As we change the value of the energy E slider, we can scan through the 2D 'slices' of constant energy and examine how the topology changes.

When examining the orbit-space topology, it makes most sense to look at slices of constant energy E , and not p_m or R_m . This is because only slices of constant E contain *all* orbit types. We can use the p_m and R_m sliders to interactively move the (p_m, R_m) coordinate for a given energy E and examine what the corresponding FIO looks like. Maps of the poloidal and toroidal transit times τ_p and τ_t for all valid orbits can be seen in the top-right and middle-left plot of the app, respectively. The top view and poloidal projections of the FIO are shown in the bottom left- and right-hand plots of the orbitsWebApp.jl, respectively. The FIOs are computed in real-time (~ 1 ms) thanks to the optimized algorithms of the *GuidingCenterOrbits.jl*[21] Julia package. The plots can be automatically saved as .png files by using the 'save_plots' toggle button. Finally, the user can easily switch from (E, p_m, R_m) to $(E, \mu, P_\phi; \sigma)$ via the toggle button. All the plots corresponding to a (p_m, R_m) 'slice' of constant fast-ion energy will then automatically change to a (μ, P_ϕ) slice. The $\sigma = +1$ slice is viewed when $p_m > 0$ and the $\sigma = -1$ slice is viewed when $p_m < 0$. This switch from (E, p_m, R_m) to $(E, \mu, P_\phi; \sigma)$ coordinates is illustrated in Figure 6.

3.2. (E, p, R, z) phase space

The OWCF can also compute topological maps for (E, p, R, z) phase space, as well as maps of τ_p and τ_t . This is done via the **calcEpRz-TopoMap.jl** (M1) main script. Topological maps for (E, p, R, z) phase space are useful when the user would like to know which orbit types pass through a certain (R, z) point, what the (E, p) topological map looks like and how that changes from one (R, z) point to another. As for the calcTopoMap.jl (M4) script, the required inputs are most easily specified using a template input file, readily provided by the OWCF. As we can see in Figure 2, a FI (E, p, R, z) distribution (D2) may be optionally provided as input to the calcEpRzTopoMap.jl script. The script will then automatically load the E -, p -, R - and z -arrays from the D2 file and compute the topological map for the same grid points.

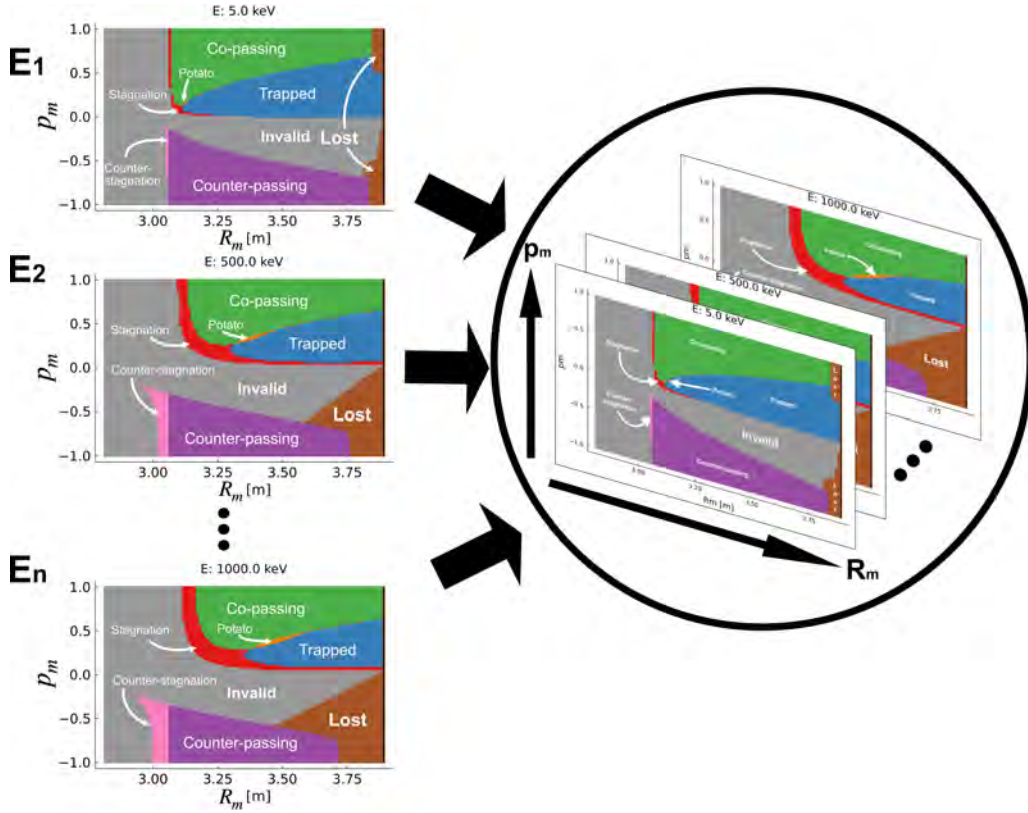


Figure 4: A graphical overview of the process by which the OWCF computes topological maps for the (E, p_m, R_m) coordinate space. Each valid orbit type (co-passing, counter-passing, trapped etc.) is numerically represented as an integer in $[1, 2, 3, 4, 5, 8]$. Lost orbits and invalid coordinate triplets are given the integers 7 and 9, respectively. This allows correct colors (green, purple, blue etc.) to represent the topological regions when plotting. All the energy slices (E_1, E_2, \dots, E_n) are computed sequentially and then put together into a 3D topological map of the whole (E, p_m, R_m) coordinate space.

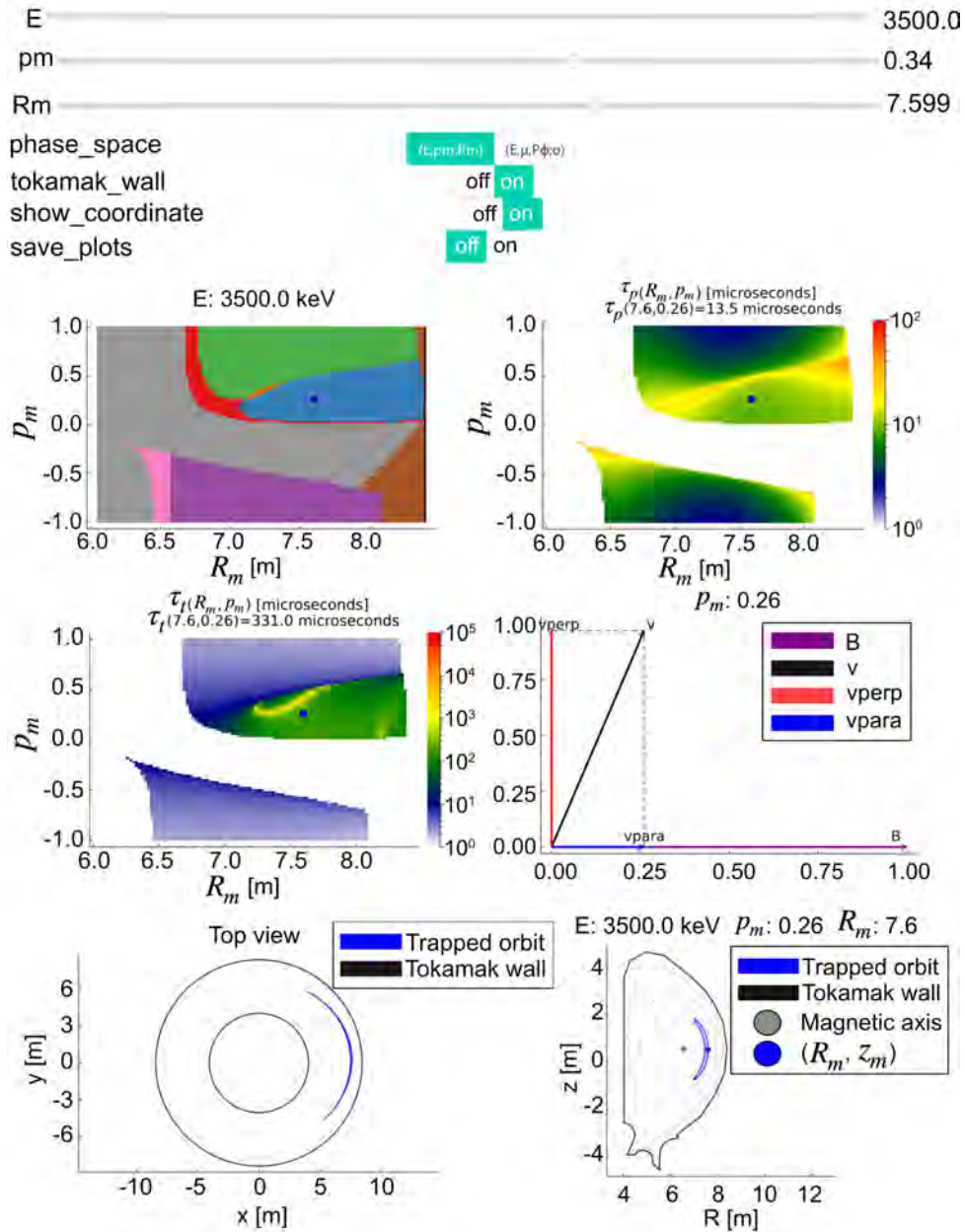


Figure 5: A screenshot of the orbitsWebApp.jl web application for interactively visualizing FIOs, topological maps, poloidal and toroidal transit time maps in (E, p_m, R_m) orbit space and $(E, \mu, P_\phi; \sigma)$ constants-of-motion space. By changing the values of the E , p_m and R_m sliders, the app will respond in real-time by computing the corresponding FIO and changing the topological map. The options to switch to constants-of-motion $(E, \mu, P_\phi; \sigma)$, to show the tokamak wall, to save the plots in .png-format or to show the (p_m, R_m) (or (μ, P_ϕ)) coordinate have been implemented via toggle buttons. ' $\tau_p(7.6, 0.26) = 13.5$ microseconds' means that τ_p at $(R_m, p_m) = (7.6 \text{ m}, 0.26)$ is 13.5 microseconds.

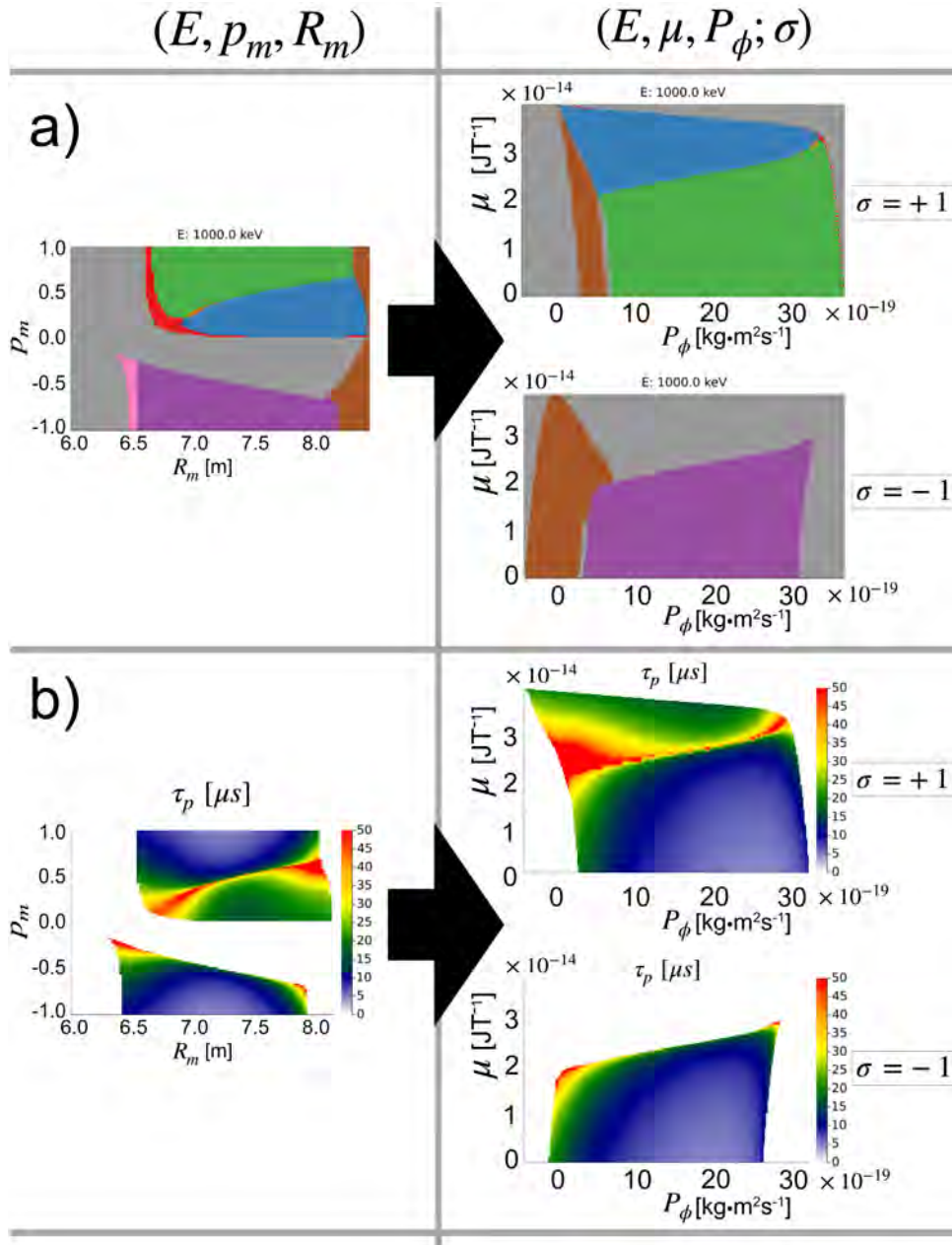


Figure 6: An example of how the OWCF can be used to map a) topological regions and b) poloidal transit times (τ_p) from (E, p_m, R_m) orbit coordinates to $(E, \mu, P_\phi; \sigma)$ constants-of-motion coordinates. The slices in b) correspond to the same energy slices as in a). The mapping can be done for quantities that do **not** require a Jacobian. We can observe how the apparent size of the topological regions change between the phase spaces. The lost region (brown) was not included for the poloidal transit times.

When the script has completed, the resulting topological map in (E, p, R, z) phase space can be visualized using the **EpRzWebApp.jl** (A3) web application. A screenshot of A3 can be seen in Figure 7. As we can observe, the user can explore the topological map by changing the values of the E -, p -, R - and z -sliders. The app will then respond by computing a new FIO in real-time and changing the topological map accordingly. To assist the user in judging the relative areas of the topological regions (bottom left plot), the **EpRzWebApp.jl** web application also includes a bar plot (top right) of the different populatable orbit types at (R, z) . The **EpRzWebApp.jl** web application is envisioned to assist fast-ion diagnostics that observe small (compared with minor radius) measurement volumes, e.g. fast-ion D- α diagnostics, in determining which orbit types are able to produce signals at given (R, z) points. Several other usage areas can also be imagined, such as for teaching and a deeper insight into the populated orbits for a fast-ion distribution given in (E, p, R, z) coordinates. For example, it can be imagined how students can use the OWCF apps to perform numerical experiments by modifying the orbit parameters interactively. This could provide a quick and effective way of teaching FIOs and orbit-space topologies, and help the students faster develop an intuition for FIOs and FIO-related quantities.

4. Orbit weight functions

The computation and visualization of orbit weight functions (OWs) are arguably the main features of the OWCF. Hence, the discussion concerning OWs will be given extra care, and it has therefore been split into two subsections: computation and visualization.

4.1. Computation

The computation of OWs is done via the **calcOrbWeights.jl** main script (M2). Similar to the computation of topological maps, the OWCF provides the user with several flexible options for the input quantities required to compute OWs, such as the grid in (E, p_m, R_m) orbit space. Using output from the **calcOrbGrid.jl** (H1) helper script to specify the grid and FIOs is advantageous since that ensures fidelity in terms of FIOs (the same grid and FIOs can be used in many scripts and apps).

The magnetic equilibrium is specified analogously to the computation of topological maps. The LOS may be either a data output file from the LINE21 code or simply not specified (for 4π sr emission). When computing OWs for

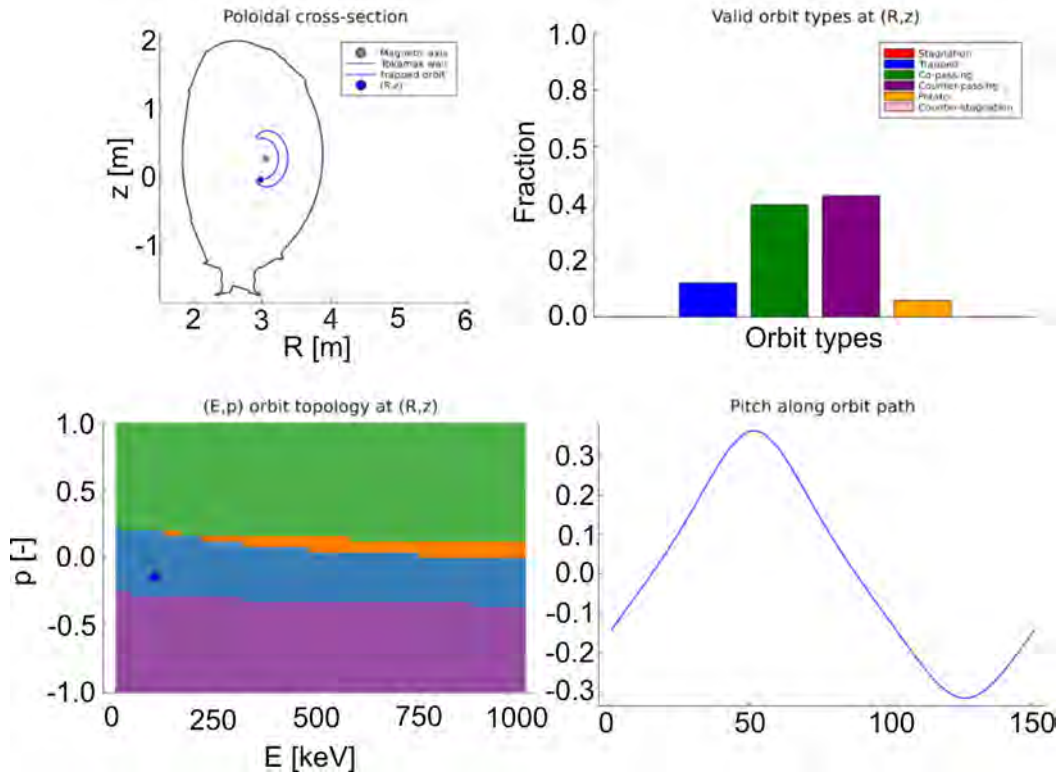


Figure 7: A screenshot of the EpRzWebApp.jl web application for interactively visualizing FIOs and topological maps in (E, p, R, z) orbit space. The app controls have been omitted for brevity. The app controls include E -, p -, R - and z -sliders, as well as toggle buttons for showing the tokamak wall, the fast-ion distribution, τ_p , τ_t and saving the plots. By changing the values of the E , p , R and z sliders, the app will respond in real-time by computing the corresponding FIO and changing the topological map. In addition, the user can also optionally include a fast-ion distribution in (E, p, R, z) coordinates, and visualize it with superimposed FIOs and topological boundaries in (E, p) . Finally, the EpRzWebApp.jl web application also includes a bar plot (top right) of the populatable orbit types at point (R, z) , as fractions of the total number of populatable orbits, and a plot of how the pitch of the fast ion changes (bottom right) as it goes around the FIO. If the user chooses to visualize a fast-ion distribution, the bar plot will instead show orbit type fractions of the total number of populated orbits for that fast-ion distribution at (R, z) .

e.g. neutron emission spectroscopy[15] or gamma-ray spectroscopy[25, 26] by coupling the OWCF to the DRESS code, there are several fusion reactions for the user to choose between. The following fusion reactions are currently supported by the OWCF (via DRESS)[24, 18]:

- $D + D \rightarrow n (2.45 \text{ MeV}) + {}^3\text{He} (0.82 \text{ MeV})$
- $D + T \rightarrow n (14.1 \text{ MeV}) + {}^4\text{He} (3.5 \text{ MeV})$
- $D + {}^3\text{He} \rightarrow p (14.7 \text{ MeV}) + {}^4\text{He} (3.6 \text{ MeV})$
- $T + p \rightarrow \gamma (19.8 \text{ MeV}) + {}^4\text{He}$

Please note however, that any other fusion reaction can be added to the list, by simply implementing the required cross-sectional data. Also, please note that the fusion-product proton from the $D({}^3\text{He},p){}^4\text{He}$ reaction has a non-zero charge. The proton trajectory would therefore have to be followed post-fusion to enable diagnostic investigation. As of v1.0 of the OWCF, this is not implemented. Instead, the resulting proton energy distribution for the plasma as a whole is returned (assuming 4π emission, i.e. ignoring any diagnostic LOS input). In future versions of the OWCF, implementation could utilize e.g. the methods developed in[49]. When it comes to providing the `calcOrbWeights.jl` script with data of the thermal plasma density n and temperature T profiles, the user has several options. 1) They can be provided by specifying the TRANSP shot data (D4) and the corresponding TRANSP FI data (D5) .cdf-files. The OWCF will then identify the timepoint of interest from D5 and load the corresponding n and T profiles from D4. In future versions of the OWCF, when computing OWs, the need to provide D5 together with D4 will be superseded by the user having to simply specify a timepoint t of interest, and a small increment dt around t . Continuing, the user may instead 2) specify their own n and T profiles as functions of the normalized flux coordinate ρ ,

$$\rho = \left(\frac{\psi - \psi_{\text{axis}}}{\psi_{\text{sep}} - \psi_{\text{axis}}} \right)^{1/2}, \quad (1)$$

where ψ is the magnetic flux function, ψ_{axis} is the magnetic flux at the magnetic axis and ψ_{sep} is the magnetic flux at the plasma separatrix. Finally, 3) the user may ignore to specify any n and/or T profiles. The OWCF will then respond by using its own default n and T profiles (Figure 3). If desired,

the user can choose to re-scale the default profiles by specifying the values of n and T on-axis.

Finally, `calcOrbWeights.jl` also gives the user the option of computing weights binned into projected velocities u instead of e.g. neutron energies. The projected velocity of a fast-ion can be written as[27]

$$u = v_{\parallel} \cos \phi + v_{\perp} \sin \phi \cos \Gamma, \quad (2)$$

where v_{\parallel} and v_{\perp} are the fast-ion velocity components parallel and perpendicular to the magnetic field, respectively. ϕ is the observation angle between the line-of-sight and the magnetic field vector and Γ is the gyrophase[9]. The projected velocity is a good proxy for spectral fast-ion diagnostics since it reflects essential features of the spectrum formation. u is an analytic measure of the sensitivity of a diagnostic in the sense that u does not require any thermal density and temperature data. When u has been computed, a value of w is added to its corresponding velocity bin. The binning weights w are

$$w = \frac{\Delta\tau_p}{\tau_p} \frac{\Omega\Delta\phi}{2\pi}, \quad (3)$$

where $\Delta\tau_p/\tau_p$ is the fraction of the total poloidal transit time for the FIO spent at the point of interest, Ω is the solid angle of the diagnostic viewing cone voxel and $\Delta\phi/2\pi$ is the toroidal angle fraction that the diagnostic viewing cone voxel of interest occupies. As mentioned earlier, the finiteness of the Larmor radius is not taken into account by the OWCF. The process of creating the resulting projected velocity spectrum has been illustrated in Figure 8.

The output of `calcOrbWeights.jl` will be a 2D matrix where the columns correspond to the expected synthetic diagnostic signals for every valid FIO of interest. Every row of the matrix is a 3D function that has been reshaped into a 1D vector.

4.2. Visualization

To be able to effectively visualize the M2 output, we have to inflate our 2D matrix to its full 4D form. The size of this 4D array will be $n_{E_d} \times n_E \times n_{p_m} \times n_{R_m}$ where

- n_{E_d} is the number of diagnostic measurement bins for the synthetic signals,

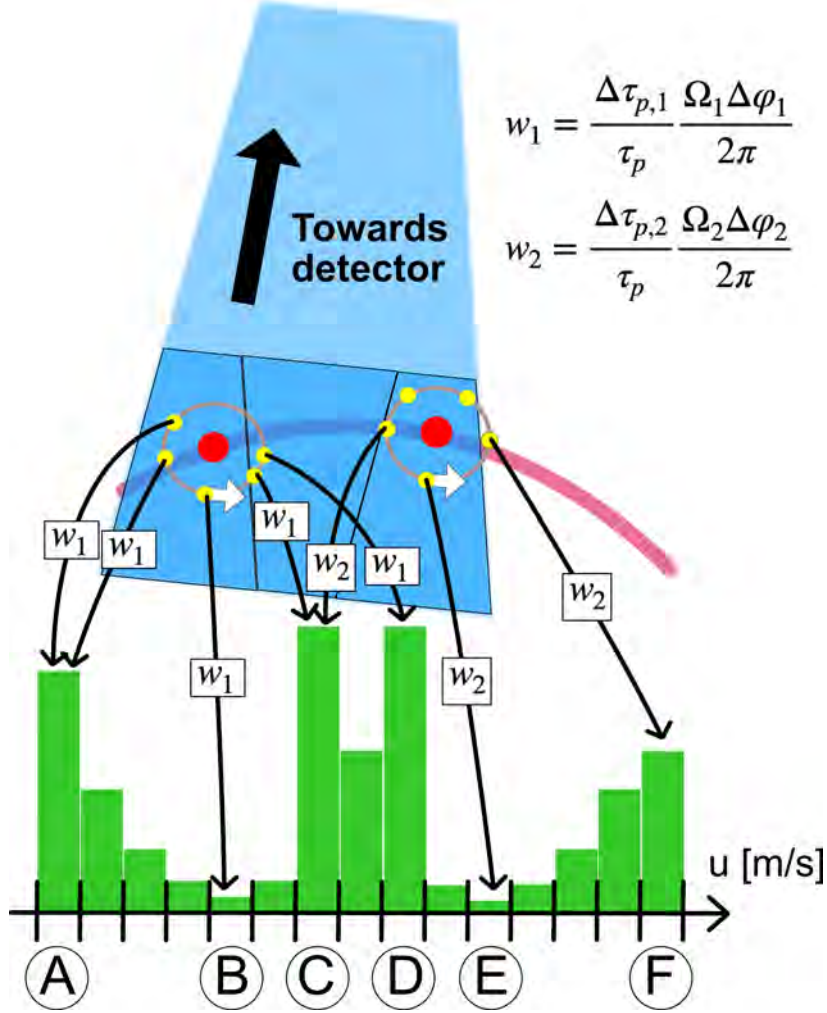


Figure 8: An illustration of the computation of projected velocity u spectrum by the OWCF. Let $u_{i,j}$ denote the projected velocity of sample j from gyro-center i . **A** Two samples (yellow), with projected velocities $u_{1,1}$ and $u_{1,2}$, along the gyro-orbit of the same guiding-center (red) end up in the same u -bin, even though $u_{1,1} \neq u_{1,2}$. This is because of the finite discretization of u , and $u_{1,1} \approx u_{1,2}$ so the samples end up in the same bin. **B** A sample with $u = v_{\parallel,1} \cos \phi$. Because of $\cos \Gamma$ in eq. (2), not many samples end up here. **C** Samples from both gyro-centers can end up in this bin. From the first point because of up-shift from $v_{\parallel,1} \cos \phi$ and from the second point because of down-shift from $v_{\parallel,2} \cos \phi$, where $v_{\parallel,1} < v_{\parallel,2}$. **D** Again, because of $\cos \Gamma$ a lot of samples will end up here, from both gyro-centers. **E** A sample with $v_{\parallel,2} \cos \phi$. **F** Even though this sample is outside of the LOS, the OWCF still includes it in the binning, since its guiding-center is inside of the LOS. The orbit trajectory is depicted as a pink line.

- n_E is the number of fast-ion energies of our grid used as input to M2,
- n_{p_m} is the number of pitch maximum grid points used as input to M2,
- n_{R_m} is the number of radius maximum grid points used as input to M2.

This will allow us to visualize the orbit sensitivity 'slice-by-slice' where every slice has constant fast-ion energy. The conversion from 2D to 4D can be done using **orbWeights_2Dto4D.jl** helper script (H3). The user can otherwise ask `calcOrbWeights.jl` to automatically call H3 when the 2D weight matrix has been computed, saving both a 2D- and a 4D-output array. The **os2com.jl** helper script (H9) can be used to map the (E_d, E, p_m, R_m) weight matrix H3 output to $(E_d, E, \mu, P_\phi; \sigma)$ constants-of-motion coordinates.

In Figure 9, we can see a screenshot of the **weightsWebApp.jl** (A7) web application, which is used to interactively analyze OWs. We can observe that the web application shows the user an extensive amount of information and consists of several interactive sliders. In addition to visualizing OWs slice-by-slice, the user can also choose to visualize a synthetic signal S and a weight function-computed signal WF simultaneously. The app will then keep track of what diagnostic measurement bin E_d the OW corresponds to, and visualize a marker (black dot in upper-left plot) that tracks the E_d as the user moves the E_d -slider. This functionality is useful when the S and WF do not match perfectly, and the OWs for the E_d values of interest need to be examined in detail.

In addition, the user can also choose to simultaneously visualize a fast-ion distribution in (E, p_m, R_m) coordinates. The so-called 'signal density' (WF -density) will then be computed automatically by the app and visualized as well. The WF -density is the OWs multiplied by the fast-ion distribution, as described in [12], but without summing up all the terms. It will thus still be a 3D quantity and a function of the three (E, p_m, R_m) coordinates. The WF -density tells the user where the signal is likely to have originated from in orbit space for the given fast-ion distribution.

Another way of thinking about OWs is: given an orbit with the coordinate (E, p_m, R_m) , what is the expected signal? What signal is that particular orbit likely to produce? To answer these questions, the **weightWebApp.jl** (please note the singular form *weight* in the name) (A8) web application was developed. The user can scan the valid orbits of orbit space and examine what their expected signals look like. In Figure 10, we can observe how the user can examine the expected signals for various orbits and orbit types by

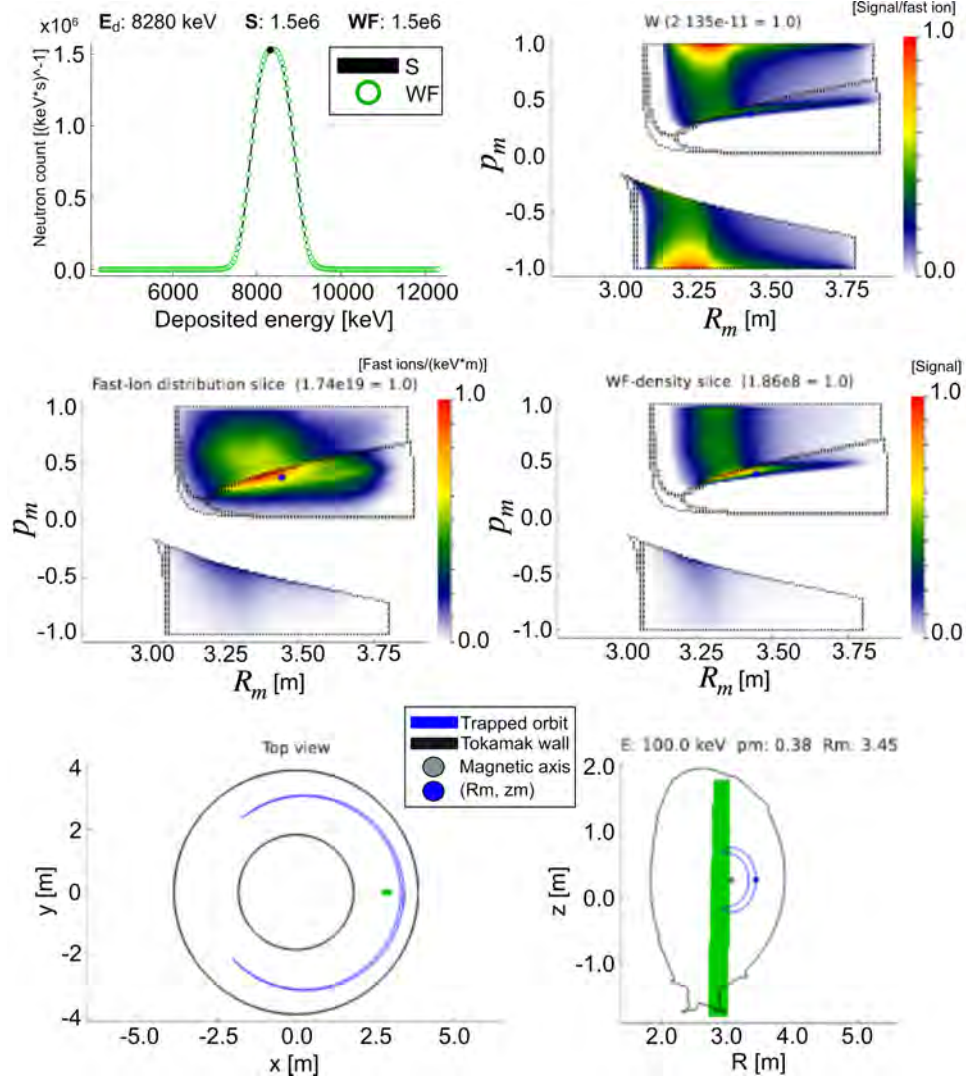


Figure 9: A screenshot of the `weightsWebApp.jl` web application for interactively visualizing orbit weight functions. The app controls have been omitted for brevity. The app controls include sliders for the diagnostic measurement bins, orbit-space grid points and for switching between several fast-ion distributions. They also include toggle buttons for the tokamak wall, the fast-ion distribution, colorbar scales, switch to $(E, \mu, P_\phi; \sigma)$ (not including fast-ion distribution and WF -density), show (p_m, R_m) coordinate and to save all plots in .png-format. The user can utilize the sliders to scan through 2D slices of OWs with topological boundaries superimposed as the figure shows.

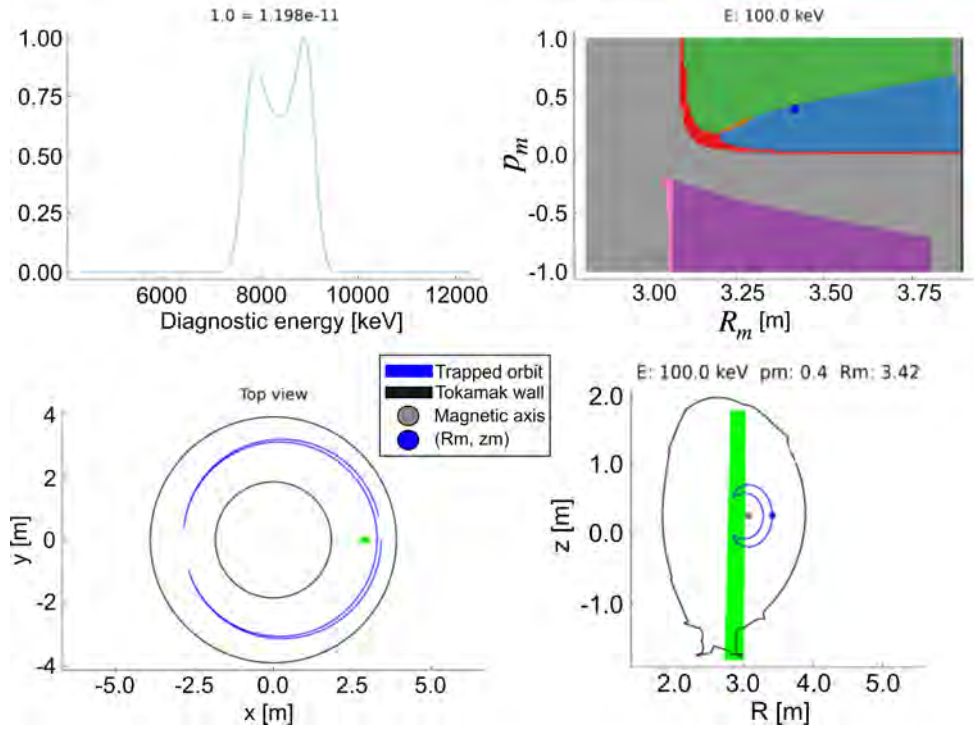


Figure 10: A screenshot of the `weightWebApp.jl` web application for interactively visualizing orbit weight functions. The top left-hand plot shows the expected signal for the orbit visualized in the bottom plots. The app controls have been omitted for brevity. They include sliders for the orbit-space grid points and toggle buttons for the tokamak wall, (p_m, R_m) , switch to $(E, \mu, P_\phi; \sigma)$ and to save all plots in `.png`-format.

changing the (E, p_m, R_m) coordinate with the sliders. It should be mentioned that, for every web application that includes poloidal projections of orbits, the option to show/hide the tokamak wall is always implemented. This is because some orbits, e.g. stagnation orbits, become so localized poloidally (i.e. approaching a point) for certain (E, p_m, R_m) coordinates that they need to be plotted without the tokamak wall for the user to be able to fully zoom in and accurately evaluate their trajectory.

5. Transforming to orbit space

To transform fast-ion distributions given on a rectangular grid in (E, p, R, z) coordinates (grid points need not be evenly spaced) to (E, p_m, R_m) orbit co-

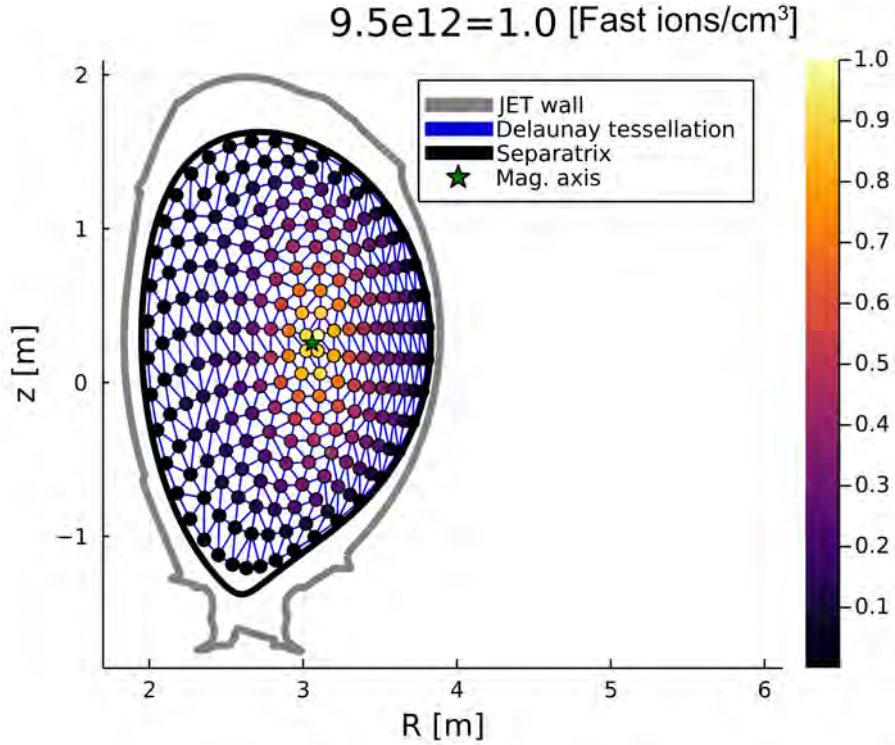


Figure 11: An example of a Delaunay tessellation performed on TRANSP fast-ion distribution data known only at discrete, irregular (R, z) points. The energy E and pitch p dependency of the distribution was integrated out to enable illustrative plotting, i.e. $f(R_i, z_i) = \int f(E, p, R_i, z_i) dE dp$. $f(R_i, z_i)$ was then normalized so that $\max(f(R_i, z_i))=1.0$ to enable clean plotting. The true maximum value of $f(R_i, z_i)$ is shown in the plot title as $\max(f(R_i, z_i))=1.0$.

ordinates, the user can utilize the `ps2os.jl` (M5) main script. However, let us say that the user instead only had the TRANSP fast-ion distribution in .cdf-file format (D5), which is given on an irregular grid spiraling outwards from the magnetic axis. How would the user transform such a distribution into orbit space? The user can then utilize the `getEpRzFIdistrFromTRANSP.jl` (E4) helper script. The E4 script takes D5 data and creates a Delaunay tessellation for the spiral (R, z) grid points[44, 23]. An example is shown in Figure 11.

Linear barycentric interpolation[19] can then be used to find the fast-ion distribution $f(E, p)$ at rectangular query points (R, z) . In `getEpRzFIdistr-`

From `TRANSP.jl`, the barycentric weights have been chosen as suggested by [10], that is

$$\mu(R, z, R_j, z_j) = \frac{\lambda(R, z, R_j, z_j)}{\sum_{j=1}^3 \lambda(R, z, R_j, z_j)} \quad (4)$$

with

$$\lambda(R, z, R_j, z_j) = \frac{1}{(R - R_j)^2 + (z - z_j)^2}. \quad (5)$$

where (R_j, z_j) are the individual coordinates of the three vertices of the Delaunay triangle containing the query point (R, z) . Query points outside of the Delaunay tessellation will be treated with nearest neighbour extrapolation, followed by forcing all $f(E, p)$ outside of the separatrix to be identically zero.

Once $f(E, p, R, z)$ has been obtained via the usage of H9, we can use the `ps2os.jl` (M5) main script to transform $f(E, p, R, z)$ into $f(E, p_m, R_m)$. It uses Monte-Carlo sampling of $f(E, p, R, z)$, followed by binning weighted samples into bins in (E, p_m, R_m) orbit space. More specifically, the Monte-Carlo sampling is done by 'spaghettifying' the 4D data array that is the discretized representation of $f(E, p, R, z)$. The cumulative sum vector is then computed and an evenly distributed random number between 0 and the last cumulative sum vector element is drawn. The corresponding element in the vector is identified, as well as the pertaining (E, p, R, z) coordinate. The FIO is then computed and the (E, p_m, R_m) coordinate of the FIO is identified. This is done for a sufficient number of Monte-Carlo samples and the $f(E, p_m, R_m)$ distribution is obtained. The $f(E, p, R, z) \rightarrow f(E, p_m, R_m)$ process has been visualized in Figure 12. Other methods of transforming $f(E, p, R, z) \rightarrow f(E, p_m, R_m)$ might be integrated in the OWCF in updated versions of the framework. This is discussed in the future work section of this paper.

Regardless of which method the user chooses to transform $f(E, p, R, z) \rightarrow f(E, p_m, R_m)$, the successfully transformed $f(E, p_m, R_m)$ 3D data array can be interactively visualized using the `distrWebApp.jl` (A1) web application. The A1 web app is similar to the `weightsWebApp.jl` (A7), but does not include OWs. In contrast to the A7 web app, the A1 web app allows the user to visualize and compare two fast-ion distributions in (E, p_m, R_m) coordinates,

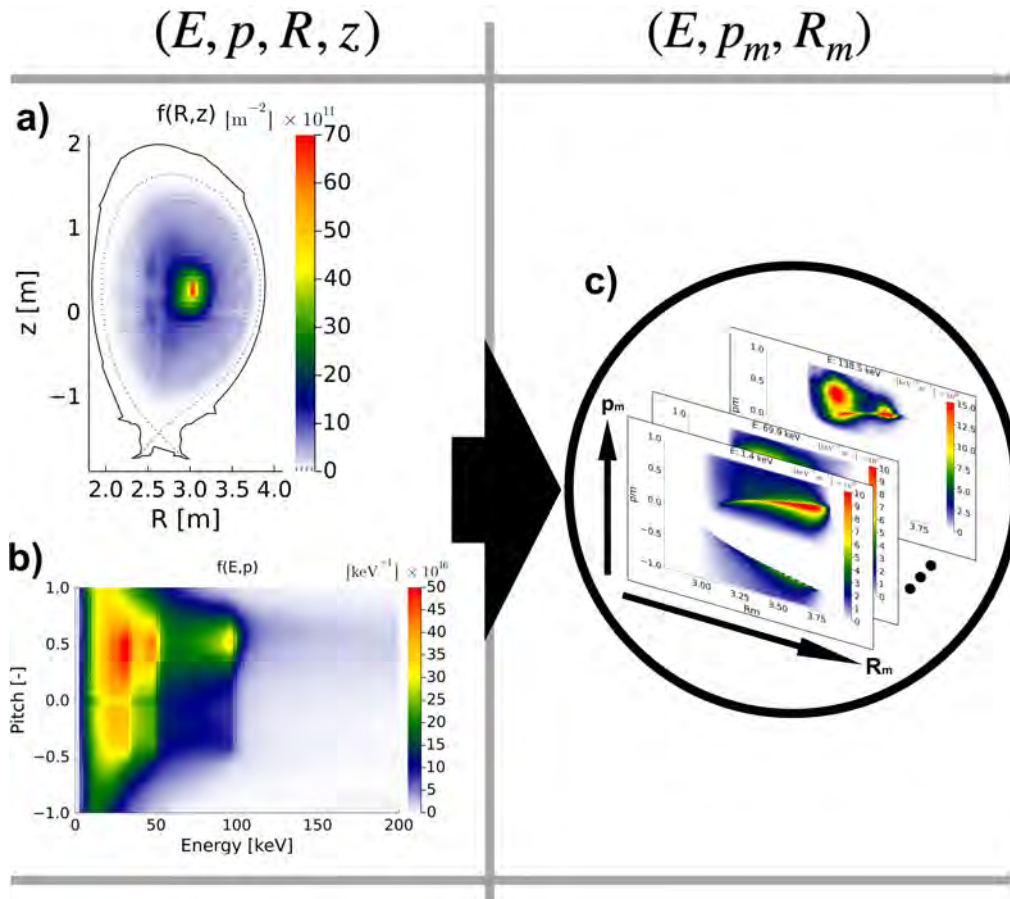


Figure 12: An example of a $f(E, p, R, z) \rightarrow f(E, p_m, R_m)$. In a) the $f(R, z)$ distribution has been illustrated, where the E - and p -dependences have been integrated out. In b) the opposite can be observed, i.e. $f(E, p)$. In c) the resulting fast-ion distribution in orbit-space $f(E, p_m, R_m)$ has been split into slices of constant E . It is usually helpful to use a new colorscale for every E -slice, to be able to observe detailed orbit-space dependencies.

to easily identify any differences between the two.

6. Orbit constituents of diagnostic signals

With the OWCF, the user can also decompose synthetic diagnostic signals into orbit type constituents, to investigate what fractions of orbit types are most likely to have produced a certain diagnostic measurement. Mathematically, this can be expressed as[12]

$$WF = \sum_h W_h F_h, \quad (6)$$

where 'h' stands for the different orbit types (co-passing, trapped etc). To investigate the dependency on (E, p_m, R_m) in terms of orbit types, we can further expand (6) as

$$\sum_h W_h F_h = \sum_h \sum_E W_{h,E} F_{h,E} \quad (7)$$

$$= \sum_h \sum_{p_m} W_{h,p_m} F_{h,p_m} \quad (8)$$

$$= \sum_h \sum_{R_m} W_{h,R_m} F_{h,R_m} \quad (9)$$

where e.g. $F_{h,E}$ is the fast-ion distribution for a particular orbit type h at a certain fast-ion energy E .

To compute these kinds of signal splits, the user can employ the **ps2WF.jl** (M6) main script. In addition to being able to compute orbit split signals, the M6 main script can also compute WF signals for ultra high-resolution grids in orbit space. That is, grids that consist of tens of millions of valid orbits and that require a computational cluster to compute within a reasonable timeframe. These kinds of grids can be useful when the $S = WF$ identity needs to be validated. S is the synthetic signal from e.g. a regular Monte-Carlo code and the validity of the OWs depends on the perfect match between the WF vector and the S vector. For too coarse grids, the identity $S = WF$ will likely not hold. This is because accurate representation of the orbit-space sensitivity (i.e. W) of the diagnostic requires a discretization of (E, p_m, R_m) space with a sufficiently high resolution.

The M6 output of the `ps2WF.jl` main script can be visualized using the **signalWebApp.jl** (A6) web application. Input-wise it is among the most simple of the OWCF web applications. Output-wise it is among the most complex, as Figure 13 shows.

We can see from Figure 13 that the user has several options when it comes to viewing the data. One-dimensional line plots will be displayed for the coordinate of interest (where the other coordinates have been integrated out). This provides the user with insight on which orbit types that make up a certain measurement. In the example shown, the user can also distinguish the energy dependence of the signal origin of the orbit types. This is also provided for the fast-ion distribution f and the orbit sensitivity w . For every measurement bin, a color-coded bar plot will show how much of the measurement is likely to originate from the different orbit types. The measurement bin of interest can be interactively changed by the user via the top slider (E_d). The `signalWebApp.jl` (A6) web application thus provides the possibility for detailed insight into where in orbit space a certain diagnostic measurement is likely to originate from.

In addition, if a simple overview of the orbit-type constituents of a diagnostic signal is sought, the user can utilize the `plotSignalOrbSplits()` function via loading the **gui.jl** (E3) extra Julia file. By providing the M6 output file as input, the function will save plots of a diagnostic signal decomposed into its likely orbit-type constituents, as shown in Figure 14. A quick overview of the fractions of orbit types that are likely to make up a diagnostic signal can thus be achieved. To know the likely orbit-type origin of diagnostic signals can be useful when e.g. verifying certain heating schemes, such as the three-ion heating scheme[50]. It can also be useful when investigating the orbit types of the birth distribution of alpha particles in burning plasmas, given a TRANSP simulation.

7. Conclusion

The OWCF is a framework of scripts, functions, routines and apps that combine to enable computation, visualization and analysis of fast-ion orbits and quantities in (E, p_m, R_m) (orbit-space) coordinates, such as orbit weight functions and fast-ion distribution functions. It is written in the Julia programming language to enable efficient computation of fast-ion orbits, pushing the computation time down to ~ 1 ms (deeply passing ~ 1 ms, marginally trapped ~ 3 ms). With the OWCF, the user can compute topological maps

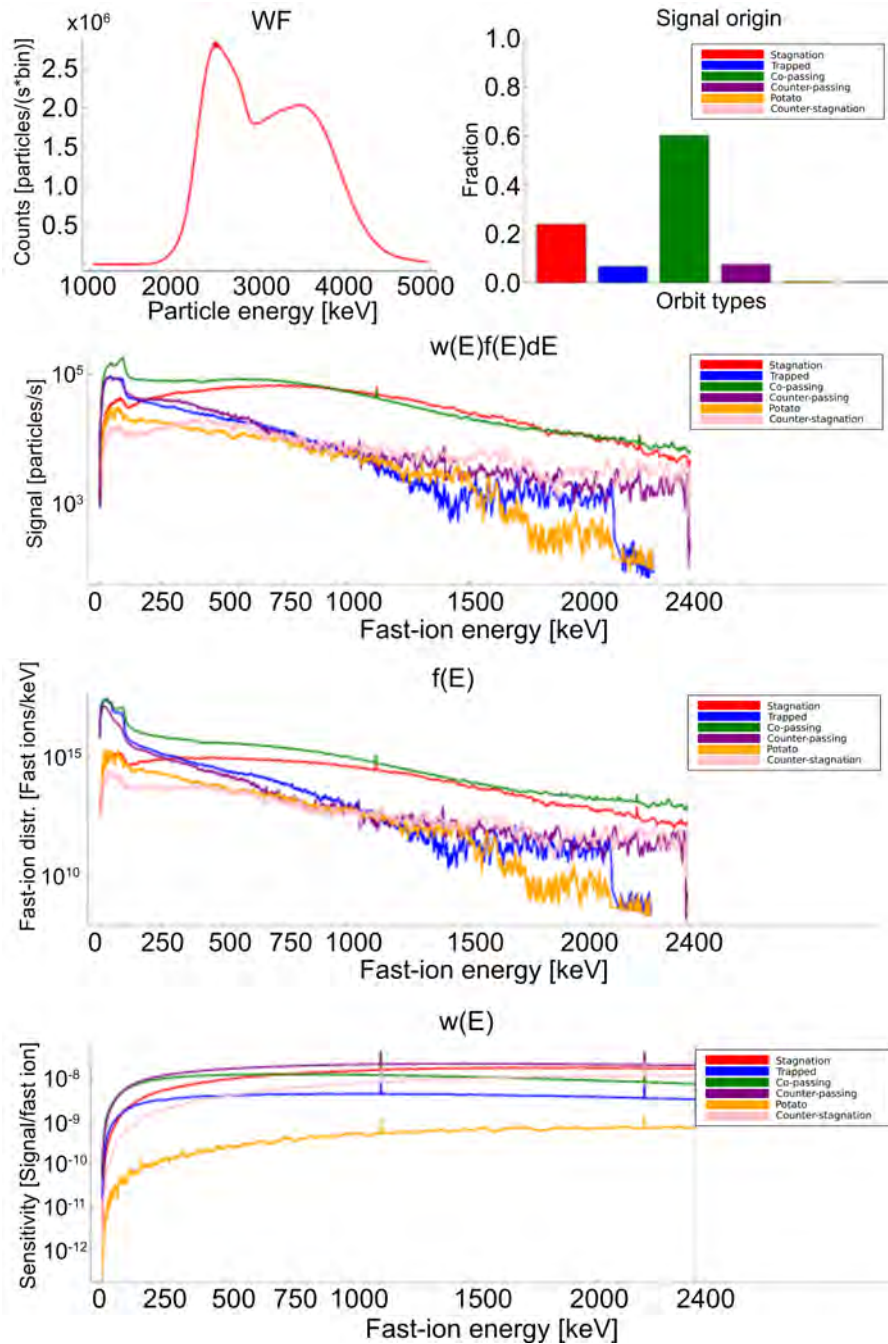


Figure 13: An example screenshot of the signalWebApp.jl (A6) web application. The user controls have been omitted for brevity. The coordinate of interest (E , p_m or R_m) is controlled via a toggle button. The app will then display the diagnostic signal and the orbit type decomposition (first plot row). The app will also display the signal density wf (second plot row), the fast-ion distribution f (third) and the orbit sensitivity w (fourth) as functions of the coordinate of interest. Additional user controls (orbit-type splitting, fractions, logarithmic and save plots) are accessed via toggle buttons. The app will respond by updating the plots in real-time.

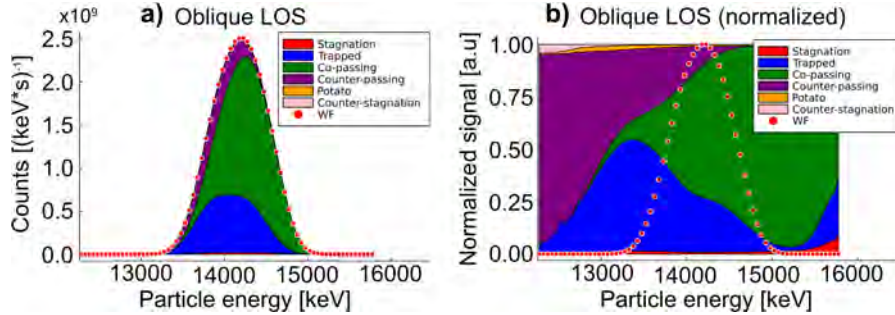


Figure 14: An example of a) a diagnostic signal WF split into its orbit-type constituents. In b) the signal amplitude has been set to 1.0 for all diagnostic measurement bins, to allow the orbit-type fractions to be examined in detail. The absolute and normalized diagnostic signal has been superimposed for reference in a) and b), respectively.

of the different orbit types in both (E, p_m, R_m) and (E, p, R, z) coordinates. The topological boundaries can then be superimposed onto e.g. orbit weight functions to analyze the sensitivity of fast-ion diagnostics to the different orbit types. The orbits and orbit-space quantities can be visualized interactively via the OWCF apps, where fast-ion orbits are computed in real-time based on the user's controls, made possible by the highly optimized guiding-center codes[44, 21].

The OWCF has been designed to be modular in terms of forward model codes. In addition to the already integrated DRESS code, future forward models such as FIDASIM can be added to the OWCF framework by simply altering a few lines of code.

Furthermore, the OWCF also contains tools for splitting synthetic diagnostic signals into their likely orbit-type constituents. This can be analyzed at varying levels of detail, depending on the needs of the user.

Tools that allow for transforming quantities back and forth between (E, p, R, z) and (E, p_m, R_m) are incorporated into the OWCF. This enables the user to e.g. reconstruct the fast-ion distribution in terms of fast-ion orbits using the orbit weight functions, and then transform the results to guiding-center phase space.

Future work for the OWCF includes continuing to make the scripts and apps more user-friendly by improving their efficiency and speed, making the OWCF compatible with additional forward models and computational cluster architectures, as well as adding further transformation capabilities to be able to transform more efficiently back and forth between (E, p_m, R_m) and

(E, p, R, z) . Such capabilities include the methods developed by [38] and [1], that transforms via grid-optimized automatic differentiation and marker distributions, respectively.

Finally, the versatility and standard of the OWCF will provide a useful and easy-to-use toolbox for understanding the complexity of fast-ion orbits in tokamaks. It will help pave the way for future tomographic reconstructions of fast-ion distributions, and contribute to the realization of fusion as a virtually limitless source of sustainable energy.

Acknowledgements

This work has received support from the Niels Bohr Foundation which is a merger of The Niels Bohr Grant, The Emil Herborg Grantpart, The Grant of MA Marcus Lorenzen, The Ole Rømer Foundation and The Julie Marie Vinter Hansen Travel Grant. The views and opinions expressed herein do not necessarily reflect those of The Royal Danish Academy of Sciences and Letters.

This work has been carried out within the framework of the EUROfusion Consortium, funded by the European Union via the Euratom Research and Training Programme (Grant Agreement No 101052200 — EUROfusion). Views and opinions expressed are however those of the author(s) only and do not necessarily reflect those of the European Union or the European Commission. Neither the European Union nor the European Commission can be held responsible for them.

References

- [1] A. Bierwage *et al*, 2022. Representation and modeling of charged particle distributions in tokamaks. *Computer Physics Communications* 275, 108305. doi:<https://doi.org/10.1016/j.cpc.2022.108305>.
- [2] A. Pankin, D. McCune, R. Andre *et al.*, 2004. The Tokamak Monte Carlo Fast Ion Module NUBEAM in the National Transport Code Collaboration Library. *CPC* 159,3, 157–184. doi:10.1016/j.cpc.2003.11.002.
- [3] A.J. Cerfon and J.P. Freidberg, 2010. 'One size fits all' analytic solutions to the Grad-Shafranov equation. *Phys. of Plasmas* 17, 032502. doi:10.1063/1.3328818.

- [4] B. Geiger *et al*, 2020. Progress in modelling fast-ion D-alpha spectra and neutral particle analyzer fluxes using FI-DASIM. *Plasma Physics and Controlled Fusion* 62, 105008. URL: <http://iopscience.iop.org/10.1088/1361-6587/aba8d7>.
- [5] B. Madsen *et al*, 2020a. Fast-ion velocity-space tomography using slowing-down regularization in EAST plasmas with co- and counter-current neutral beam injection. *Plasma Phys. Control. Fusion* 62, 115019. doi:10.1088/1361-6587/abb79b.
- [6] B. Madsen *et al*, 2020b. Tomography of the positive-pitch fast-ion velocity distribution in DIII-D plasmas with Alfvén eigenmodes and neo-classical tearing modes. *Nucl. Fusion* 60, 066024. doi:10.1088/1741-4326/ab82b5.
- [7] B. S. Schmidt *et al*, 2022. 4d and 5d phase-space tomography using slowing-down physics regularization. In preparation.
- [8] Breslau, J., Gorelenkova, M., Poli, F., Sachdev, J., Pankin, A., Perumpilly, G., 2018. *Transp.* [Computer Software] <https://doi.org/10.11578/dc.20180627.4>. doi:10.11578/dc.20180627.4.
- [9] *et al*, M.S., 2015. Velocity-space observation regions of high-resolution two-step reaction gamma-ray spectroscopy. *Nucl. Fusion* 55, 093029. doi:10.1088/0029-5515/55/9/093029.
- [10] F.F. Little *et al*, 1983. Convex combination surfaces. *Surfaces in Computer Aided Geometric Design* , 99–107.
- [11] H. Järleblad *et al*, 2021. Fast-ion orbit sensitivity of neutron emission spectroscopy diagnostics. *Rev. Sci. Instrum.* 92, 043526. doi:10.1063/5.0040696.
- [12] H. Järleblad *et al*, 2022. Fast-ion orbit sensitivity of neutron and gamma-ray diagnostics for one-step fusion reactions. *Nucl. Fusion* 62, 112005. doi:10.1088/1741-4326/ac63d3.
- [13] J. Bezanson *et al*, 2017. Julia: A fresh approach to numerical computing. *SIAM review* 59, 65–98. doi:10.1137/141000671.

- [14] J. Eriksson *et al*, 2016. Calculating fusion neutron energy spectra from arbitrary reactant distributions. *Comp. Phys. Comm.* 1996, 40–46. doi:10.1016/j.cpc.2015.10.010.
- [15] J Eriksson *et al*, 2018. Measuring fast ions in fusion plasmas with neutron diagnostics at JET. *Plasma Physics and Controlled Fusion* 61, 014027. doi:10.1088/1361-6587/aad8a6.
- [16] J. Mailloux *et al*, 2022. Overview of jet results for optimising iter operation. *Nucl. Fusion* 62, 042026. doi:10.1088/1741-4326/ac47b4.
- [17] J.A. Rome and Y-K.M. Peng, 1979. The topology of tokamak orbits. *Nucl. Fusion* 19, 1193. doi:10.1088/0029-5515/19/9/003.
- [18] J.E. Perry and S.J. Bame, Jr., 1955. $T(p,\gamma)He^4$. *Phys. Rev.* 99(5), 1386.
- [19] J.P. Berrut and G. Klein, 2014. Recent advances in linear barycentric rational interpolation. *Journal of Comp. Appl. Math.* 259, 195–107. doi:10.1016/j.cam.2013.03.044.
- [20] L. Stagner, 2022. Equilibrium.jl. <https://github.com/JuliaFusion/Equilibrium.jl>.
- [21] L. Stagner and H. Järleblad, 2022. Guidingcenterorbits.jl. <https://github.com/JuliaFusion/GuidingCenterOrbits.jl>.
- [22] L Stagner and W.W. Heidbrink, 2017. Action-angle formulation of generalized, orbit-based, fast-ion diagnostic weight functions. *Phys. Plasmas* 24, 092505. doi:10.1063/1.4990391.
- [23] L. Stagner *et al*, 2022. Orbit tomography of energetic particle distribution functions. *Nucl. Fusion* 62, 026033. doi:10.1088/1741-4326/ac3ed2.
- [24] M. Kikuchi, K. Lackner & M.Q. Tran, 2012. *Fusion Physics*. International Atomic Energy Agency, Vienna, Austria.
- [25] M. Nocente *et al*, 2010. Energy resolution of gamma-ray spectroscopy at JET plasmas with a $LaBr_3$ scintillator detector and digital data acquisition. *Rev. Sci. Instrum.* 81, 10D321. doi:10.1063/1.3501386.
- [26] M. Nocente *et al*, 2017. Conceptual design of the radial gamma ray spectrometers system for α particle and runaway electron measurements at ITER. *Nuclear Fusion* 57, 076016. doi:10.1088/1741-4326/aa6f7d.

- [27] M. Salewski, 2020. Fast-ion diagnostic in fusion plasmas by velocity-space tomography. Dr. techn. thesis.
- [28] M. Salewski *et al*, 2012. Tomography of fast-ion velocity-space distributions from synthetic CTS and FIDA measurements. Nucl. Fusion 52, 103008. doi:10.1088/0029-5515/52/10/103008.
- [29] M. Salewski *et al*, 2013. Combination of fast-ion diagnostics in velocity-space tomographies. Nucl. Fusion 53, 063019. doi:10.1088/0029-5515/53/6/063019.
- [30] M. Salewski *et al*, 2014. Measurement of a 2D fast-ion velocity distribution function by tomographic inversion of fast-ion D-alpha spectra. Nucl. Fusion 54, 023006. doi:10.1088/0029-5515/54/2/023005.
- [31] M. Salewski *et al*, 2014. On velocity-space sensitivity of fast-ion D-alpha spectroscopy. Plasma Phys. Control. Fusion 56, 105005. doi:10.1088/0741-3335/56/10/105005.
- [32] M. Salewski *et al*, 2016. High-definition velocity-space tomography of fast-ion dynamics. Nucl. Fusion 56, 106024. doi:10.1088/0029-5515/56/10/106024.
- [33] M. Salewski *et al*, 2017. MeV-range velocity-space tomography from gamma-ray and neutron emission spectroscopy measurements at JET. Nucl. Fusion 57, 056001. doi:10.1088/1741-4326/aa60e9.
- [34] M. Salewski *et al*, 2018a. Alpha-particle velocity-space diagnostic at ITER. Nucl. Fusion 58, 096019. doi:10.1088/1741-4326/aace05.
- [35] M. Salewski *et al*, 2018b. Bayesian Integrated Data Analysis of Fast-ion Measurements by Velocity-Space Tomography. Fusion Sci. Technol. 74:1-2, 23–36. doi:10.1080/15361055.2017.1380482.
- [36] Madsen, B., 2020. Reconstructing the fast-ion velocity distribution in fusion plasmas from sparse datasets. Ph.D. thesis. Technical University of Denmark.
- [37] M.J. Innes *et al*, 2022. Mux.jl. <https://github.com/JuliaWeb/Mux.jl>.
- [38] S. Benjamin, July 2021. Distribution transforms for orbit tomography. Master's thesis. The Australian National University.

- [39] S. Conroy, . Line21 code. Private communication.
- [40] S. Gowda *et al*, 2022. Interact.jl.
<https://github.com/JuliaGizmos/Interact.jl>.
- [41] SD Pinches *et al*, 2004. The role of energetic particles in fusion plasmas. *Plasma Phys. Control. Fusion* 46, B187. doi:10.1088/0741-3335/46/12B/017.
- [42] S.E. Sharapov *et al*, 2013. Energetic particle instabilities in fusion plasmas. *Nucl. Fusion* 53, 104022. doi:10.1088/0029-5515/53/10/104022.
- [43] Stagner, L., 2018a. Inference of the fast-ion distribution function. Ph.D. thesis. University of California, Irvine.
- [44] Stagner, L., 2018b. Inference of the Fast-ion Distribution Function. Ph.D. thesis. University of California, Irvine.
- [45] Stagner, L., Geiger, B., Heidbrink, W., . FIDASIM: A Neutral Beam and Fast-ion Diagnostic Modeling Suite. URL: <https://doi.org/10.5281/zenodo.1341369>, doi:10.5281/zenodo.1341369.
- [46] W.W. Heidbrink, 2008. Basic physics of Alfvén instabilities driven by energetic particles in toroidally confined plasmas. *Phys. Plasmas* 15, 055501. doi:10.1063/1.2838239.
- [47] W.W. Heidbrink and R.B. White, 2020. Mechanisms of energetic-particle transport in magnetically confined plasmas. *Phys. Plasmas* 27, 030901. doi:10.1063/1.5136237.
- [48] W.W. Heidbrink *et al*, 2007. Measurements of fast-ion acceleration at cyclotron harmonics using Balmer-alpha spectroscopy. *Plasma Phys. Control. Fusion* 49, 1457–1475. doi:10.1088/0741-3335/49/9/008.
- [49] W.W. Heidbrink *et al*, 2021. Phase-space sensitivity (weight functions) of 3 MeV proton diagnostics. *Plasma Phys. Control. Fusion* 63, 055008. doi:10.1088/1361-6587/abeda0.
- [50] Ye.O. Kazakov *et al*, 2021. Physics and applications of three-ion ICRF scenarios for fusion research. *Phys. Plasmas* 28, 020501. doi:10.1063/5.0021818.

Paper IV

Fast-ion Orbit Origin of Neutron Measurements in the JET DT Campaign

H. Järleblad¹, L. Stagner², M. Salewski¹, J. Eriksson³, M. Nocente⁴, K. Kirov⁵, M. Rud Larsen¹, B.S. Schmidt¹, M. Maslov⁵, D. Kinga⁶, D. Keeling⁶, C. Maggi⁶, J. Garcia⁷, E.A. Lerche⁸, P. Mantica⁹ and JET Contributors*

¹ Department of Physics, Technical University of Denmark, DK-2800 Kgs. Lyngby, Denmark

² General Atomics, P.O. Box 85608, San Diego, California 92186-5608, USA

³ Department of Physics and Astronomy, Uppsala University, 751 20 Uppsala, Sweden

⁴ Department of Physics, University of Milano-Bicocca, 20126 Milano, Italy

⁵ UKAEA, Culham Centre for Fusion Energy, Abingdon, Oxfordshire, OX14 3DB, UK

⁶ CCFE, Culham Science Centre, Abingdon, Oxfordshire, OX14 3DB, UK

⁷ CEA, IRFM, F-13108 Saint-Paul-lez-Durance, France

⁸ Laboratorium voor Plasmafysica, Koninklijke Militaire School - Belgische Staat, Ecole Royale Militaire, Brussels, 1000, Belgium

⁹ Istituto per la Scienza e Tecnologia dei Plasmi, CNR, via Cozzi 53, 20125 Milan, Italy

E-mail: henrikj@dtu.dk

September 2022

Abstract. In the JET DTE2 deuterium-tritium campaign, neutron diagnostics were employed to measure 14 MeV neutrons originating from $D(T,n)^4\text{He}$ reactions. In discharge 99965, a diamond matrix detector (KM14) and a magnetic proton recoil (MPRu) detector with a vertical and an oblique line-of-sight were used, respectively. Using a TRANSP simulation, a significant decrease in the expected signals can be observed as ion-cyclotron resonance heating (ICRH) is switched off. Analysis performed using orbit weight functions shows that the majority of the neutrons in the KM14 $E_d = 9.3$ MeV and MPRu $X_{cm} = 33$ cm measurement bins are likely to have originated from fast-deuterium ions on co-passing orbits. In contrast, at the timepoints of interest, the fast-ion distribution is likely to have been composed mostly of trapped orbits. This work explains why how this can be, and shows that the relative signal decrease as ICRH is switched off is largest for counter-passing orbits. Finally, for the magnetic equilibria of interest, it is shown how ~ 1 % of the fast-ion distribution, corresponding to stagnation orbits, was very likely completely unobservable by the KM14 diagnostic.

* See the author list of [1].

1. Introduction

The recent deuterium-tritium (DT) campaign [2, 3] at the Joint European Torus (JET) [1] marked an important milestone on the path to viable fusion energy for the production of electricity on a societal scale. Compared to the previous JET DT campaign in 1997 (JET-DTE1), this campaign (JET-DTE2) planned a twenty-fold increase in the budget of reprocessed tritium gas (~ 700 g vs ~ 35 g) and more than a five-fold increase in the budget of produced DT-neutrons (1.7×10^{21} vs 3×10^{20}) [2, 4]. To measure the fusion-born DT-neutrons during such plasma operation is therefore seen as vital; both to ensure that the neutron budget is respected and to confirm fusion power output, but also to provide experimental data to reconstruct the distribution of fast ions [5–7].

Compared to the 2.45 MeV neutrons produced in $D(D,n)^3\text{He}$ reactions, a different diagnostic setup is often required to measure the 14 MeV neutrons produced in $D(T,n)^4\text{He}$ reactions [8, 9]. For JET-DTE2, two fast-ion neutron diagnostics that were readily employed were the upgraded magnetic proton recoil diagnostic (MPRu) [9] and the KM14 diamond matrix diagnostic [10]. Given their frequent use, it can be argued to be of importance to investigate what type of fast ions that can produce the DT-neutrons measured by the MPRu and the KM14 diagnostics. Or, in other words, how sensitive these diagnostics are to fast ions with different energies, pitch ($p = v_{\parallel}/v$ where v is the speed and v_{\parallel} is the magnitude of the velocity component parallel to the magnetic field), major radius and vertical positions. Given the measurements of a certain number of neutrons with a certain energy, how many of those are likely to have originated from co-passing, counter-passing and trapped fast ions, and in what fractions? Are there fast-ion trajectories (also known as *orbits*) that are not observable at all by the MPRu and the KM14 diagnostics?

To answer these questions, we usually need to employ so-called *weight functions* [6, 11–18]. Given the assumption of a linear relationship between a measurement signal s and the fast-ion distribution f , the weight functions provide the link between the two as $s = \int w(\mathbf{x}, \mathbf{v})f(\mathbf{x}, \mathbf{v})d\mathbf{x}d\mathbf{v}$ [19–21], where \mathbf{x} is the position and \mathbf{v} the velocity, defining the phase space, and the integral is computed for the phase-space areas of interest. However, the validity of the linear relationship relies on the assumption that the fraction of neutrons originating from beam-thermal reactions is much larger than the fraction of neutrons originating from thermal-thermal and/or beam-beam reactions [14]. With ‘beam’, we mean the fast ions shot into the plasma via neutral beam injection (NBI). With ‘thermal’, we mean the bulk plasma below the fast-ion energy range. Fortunately, for the JET discharge

No 99965 examined in this paper, the beam-thermal reactions dominate (by a factor ≈ 4), making orbit weight functions suitable to use for analysis.

Together with fast-ion data (acquired either from e.g. TRANSP [22] via the NUBEAM [23] module, or via tomographic reconstruction), orbit weight functions can be used to decompose a synthetic diagnostic signal in terms of orbit-type constituents [19]. If the synthetic signal matches the experimental data adequately well, and $s \approx \int w(\mathbf{x}, \mathbf{v})f(\mathbf{x}, \mathbf{v})d\mathbf{x}d\mathbf{v}$ still holds after a discretization of phase space, the most likely fast-ion orbit origin of a diagnostic (e.g. neutron) measurement can be inferred. We can for example say in what fractions the fast-ion orbit types (co-passing, counter-passing, trapped, potato, stagnation and counter-stagnation) are likely to contribute to measurements of neutrons with a specific detected energy (which is up- or downshifted with respect to the nominal birth energy). With the orbit weight functions alone, we can also identify fast-ion orbits that are not observable by a certain diagnostic; thus providing the answer to all our questions above.

In this work, orbit weight functions have been used to perform a so-called *fast-ion orbit analysis* of the neutron measurements made by the MPRu and KM14 diagnostics in JET DT-shot No 99965 at 7.9 and 8.4 seconds. The difference between the signals at the two timepoints, corresponding to a decrease in measured neutrons, is also investigated and likely fast-ion orbits are identified. This paper is organized as follows...

2. Analysis setup

JET discharge No 99965 was a DT shot with a hydrogen minority $\mathcal{X}[\text{H}] \sim 1\%$ [24]. Heating schemes included NBI and ion-cyclotron resonance heating (ICRH). Deuterium beams were shot into a tritium-rich plasma where the mixture was $D/T \sim 0.15/0.85$. Time traces of the heating scheme can be seen in Figure 1a. For the ICRH heating, heating deuterium at the fundamental frequency of 29 MHz was used. The magnetic field strength on-axis was $B_0 = 3.85$ T and the plasma current was $I_p = 2.45$ MA. As we can see in Figure 1, when the ICRH was on at 7.9 seconds, the fast-ion distribution (Figure 1b) has a ‘tail’ that stretches up into the MeV range. When ICRH was off at 8.4 seconds, the fast-ion high-energy tail has almost completely disappeared, and only the energy distribution resulting from the NBI heating remains.

To investigate the measurement of DT-neutrons (originating from the interaction between the *fast-ion deuterium* distribution and the *thermal tritium* plasma), models of the MPRu and KM14 sightlines were used. They have been visualized in Figure 2.

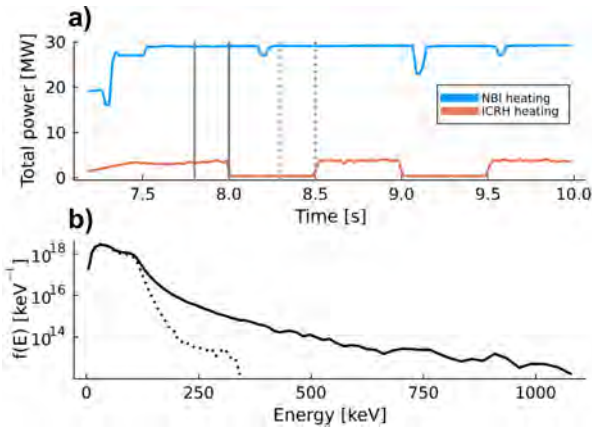


Figure 1. Time traces for the NBI and ICRH heating a) of JET shot No 99965. The energy dependence of the resulting deuterium fast-ion distribution has been plotted in b). The solid and dotted profiles correspond to the fast-ion distribution averaged over the solid and dotted time windows in a), respectively. The fast-ion distribution TRANSP ID is 99965K71.

The MPRu has an oblique line-of-sight (LOS) which views the plasma in the counter-clockwise direction. The KM14 has an almost completely vertical LOS and views the plasma from above.

To model the instrumental response (diagnostic resolution) of the diagnostics, the following response functions were used. For the MPRu, a transfer matrix between incoming neutrons energies and measured proton impact positions was used, and has been visualized in Figure 3. It was computed via Monte Carlo methods [9]. For the KM14, a Gaussian response function centered around 5.7 MeV and with a full-width at half-maximum of 100 keV was used as a proxy. This was deemed to be a good approximation of the true instrumental response function for the KM14 diagnostic.

With the model of the diagnostic sightlines in Figure 2 and the instrumental response functions, we can use the DRESS code [25] to compute the expected measurement signals given the deuterium fast-ion distributions in Figure 1b and the thermal tritium plasma profiles in Figure 4a and 4b. The resulting synthetic signals for the MPRu and the KM14 diagnostics can be viewed in Figure 5. We can observe how there is a decrease in the expected signals for both diagnostics when the ICRH has been switched off. This decrease is significant and noticeable across both diagnostic spectra. Most of the decrease is likely to originate from the loss of the fast-ion high-energy tail (Figure 1b) as ICRH is switched off. With the Orbit Weight Computational Framework (OWCF) [26], we can investigate the origin of this signal decrease more in detail by splitting the synthetic signals into their orbit-type constituents, allowing detailed analysis

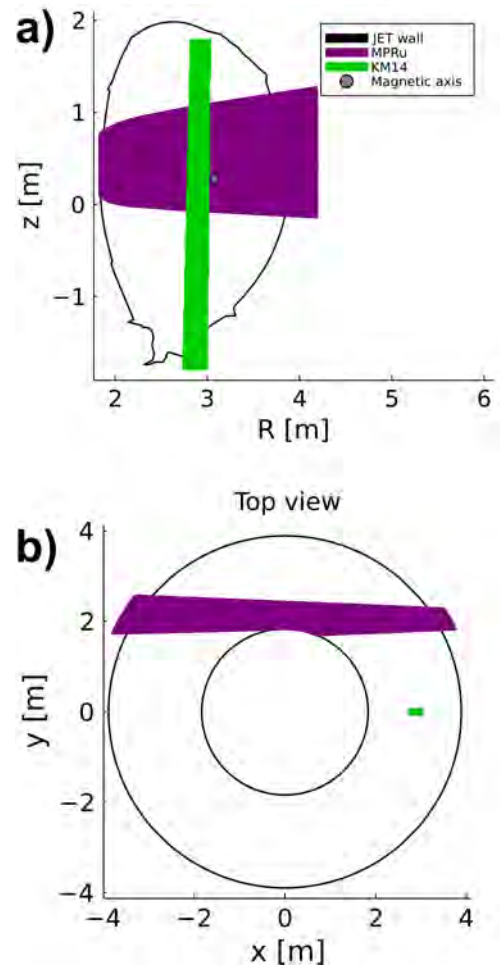


Figure 2. Sightlines for the MPRu and KM14 diagnostics, projected onto the JET poloidal cross-section in a) and viewed from above in b).

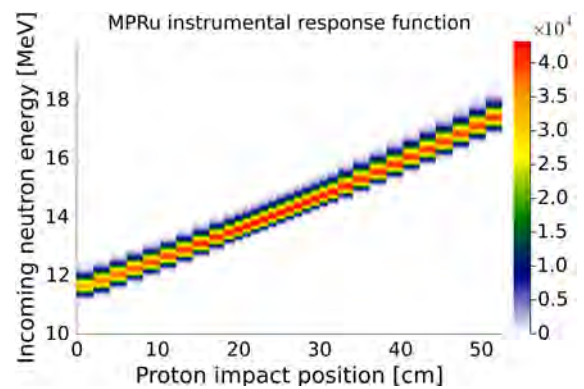


Figure 3. Instrumental response function for the MPRu diagnostic [9] at JET, for detecting neutrons in the range of 14 MeV.

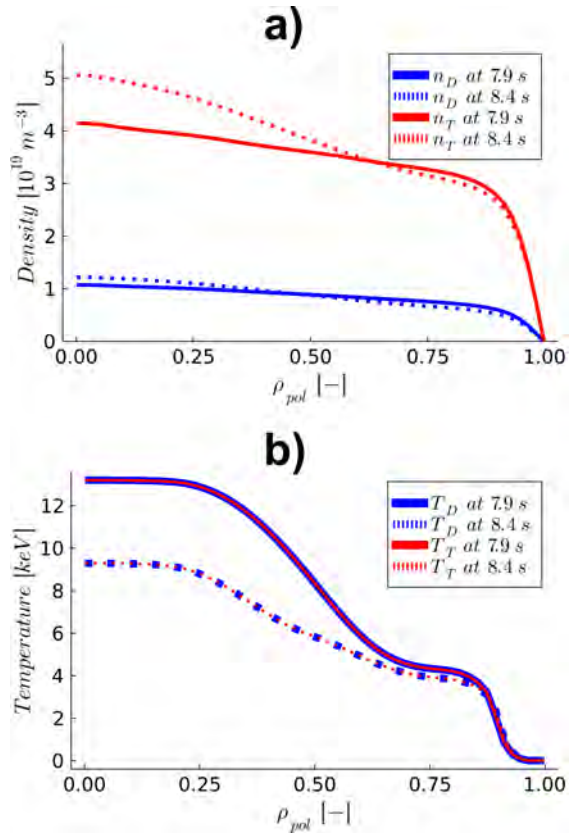


Figure 4. The a) density and b) temperature profiles for the bulk plasma of JET discharge 99965 at 7.9 and 8.4 seconds. The temperature profiles were assumed to be the same for deuterium and tritium at both timepoints.

in terms of fast-ion orbit types (co-passing, counter-passing, trapped etc). Using the OWCF, we can also split the fast-ion distribution itself into its orbit-type constituents, thereby enabling further analysis. This is done in the following section.

3. ICRH On/Off Effects

When ICRH is switched off, the density and temperature profiles for the thermal plasma changes (Figure 4). Since the phase-space sensitivity [6, 7, 13, 17, 18, 27–29] of a fast-ion diagnostic depends on the thermal plasma profiles, one might expect the so-called *fast-ion orbit sensitivity* [19, 20, 29–31] to change as well. However, as we can observe in Figure 6, in this case the change is only marginal. We can therefore conclude that most of the decrease in the diagnostic signals as ICRH is switched off (Figure 5) is likely due to the retraction of the high-energy tail of the fast-ion deuterium distribution (Figure 1b). But as the high-energy tail disappears when ICRH is switched off, how do the individual populations of orbit types change?

To answer these questions, we can split the fast-

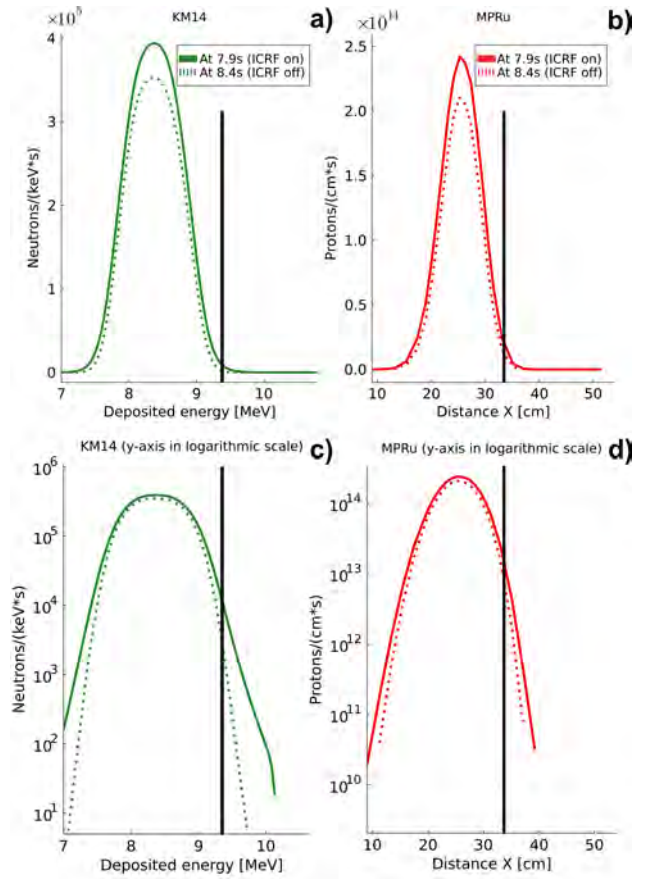


Figure 5. The synthetic diagnostic signals for the a) KM14 and b) MPRu diagnostics, computed using the DRESS [25] code with models of the sightlines, instrumental response functions and TRANSP [22] data for JET shot 99965 at 7.9 and 8.4 seconds. In c) and d), the same signals have been plotted with logarithmic scaling for the y-axis. The black lines mark the diagnostic measurement bins of interest, $E_{dep} = 9.3$ MeV and $X_{cm} = 33$ cm, for analysis in section 3 and 4.

ion distribution into its orbit-type constituents. As can be observed in Figure 7, as ICRH is switched off, regardless of orbit type, the orbit distributions retract downwards in fast-ion energy. For some higher energies that are still populated (e.g. $E \approx 250$ keV), the populations are approximately two orders of magnitude smaller. For $E = 300$ keV, when ICRH is switched off there are more populated trapped than counter-passing orbits ($f_{trapped} > f_{counter-passing}$), compared to when ICRH was on when the opposite was true ($f_{trapped} < f_{counter-passing}$).

In Figure 7, we can also observe how the peak of the trapped orbit population is the highest of all orbit types. One might therefore expect an e.g. diagnostic neutron signal s to be a result of 14 MeV-neutrons originating from mostly trapped orbits. However, as discussed earlier, a diagnostic signal s can be written as the result of a multiplication between the fast-

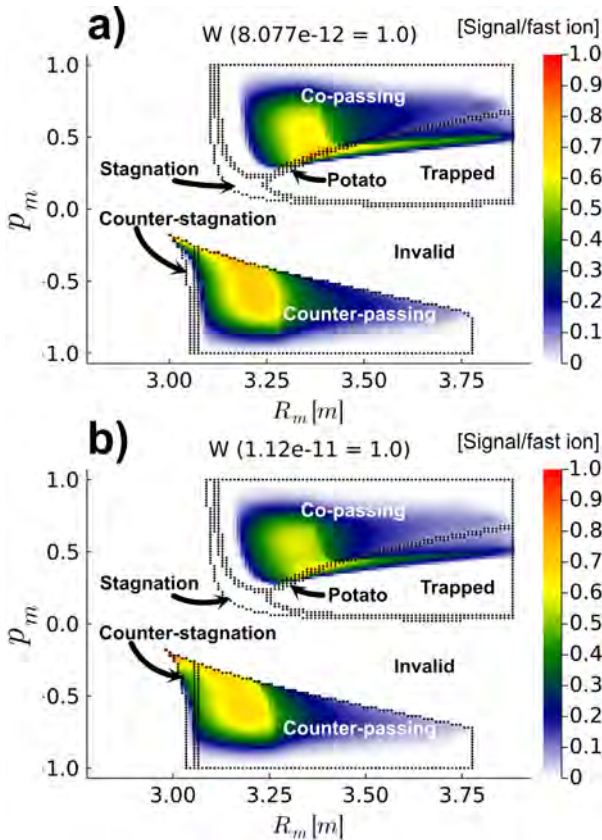


Figure 6. A 2D slice of constant fast-ion energy $E = 250$ keV of the full 3D orbit weight function for the $E_{dep} = 9.3$ MeV measurement bin of the KM14 neutron diamond matrix diagnostic at a) 7.9 and b) 8.4 seconds of JET DT shot 99965, respectively. The marginal change between timepoints is representative for other 2D slices of constant fast-ion energy and the MPRu diagnostic as well.

ion distribution f and the weight function w of the diagnostic, i.e. in its discretized form $s = wf$. Similarly to f , we can split w into its orbit-type constituents to examine how sensitive a diagnostic is to different orbit types. However, here we need to average over the number of grid points for each orbit type, to take the orbit-space metric into account. This has been done for the KM14 and MPRu diagnostics in Figure 8 and 9, respectively. As we can observe, for the $E_{dep} = 9.3$ MeV measurement bin of the KM14 diagnostic, the orbit sensitivity is highest for counter-passing orbits, followed by co-passing orbits. The trapped sensitivity peak is about half the height of the co-passing peak, and about a third of the height of the counter-passing peak. We would therefore expect a corresponding reduction and increase in the signal contribution from trapped and passing orbits, respectively. For the MPRu and the $X = 33$ cm measurement bin, the co-passing sensitivity peak is almost 6 times higher than the trapped peak. Therefore, even if we had a fast-ion

distribution consisting of six times as many trapped as co-passing orbits, we could expect the measurement of a proton at $X = 33$ cm to be (roughly) just as likely to have originated from a trapped orbit as from a co-passing orbit.

In Figure 8 and 9, it is also interesting to note that the orbit sensitivity increases in general when ICRH is switched off (7.9 s \rightarrow 8.4 s timepoints). This is likely due to the general increase of the thermal tritium density profile (Figure 4a) as ICRH is switched off, which would affect the orbit sensitivity more directly than the thermal tritium temperature profile (Figure 4b). In addition, the relative increase of the thermal tritium density profile ($\approx 25\%$) is similar to the relative increase of the sensitivity peaks ($\approx 25\%$), further supporting the hypothesis. However, this only holds for the KM14 diagnostic (Figure 8), for which the increase in sensitivity is more pronounced. This is likely resolved by the fact that KM14 has a LOS observing a larger portion of the plasma center compared to the outer plasma. A change in the plasma center would thus be likely to result in a larger change in the orbit sensitivity, compared to e.g. the MPRu with a less poloidally localized LOS.

4. Orbit Origin of Signal Loss

Having discussed the change of the fast-ion distribution f and the (discretized) orbit sensitivity w as ICRH is switched off in section 3, we are now ready to investigate the diagnostic signal s in terms of orbit types. As we can observe in Figure 10, for the measurement bins of interest $E_{dep} = 9.3$ MeV and $X = 33$ cm, the signals from all orbit types decreases as ICRH is switched off. We can also observe how the KM14 and MPRu signals at $E_{dep} = 9.3$ MeV and $X = 33$ cm are dominated by contributions from co-passing orbits, even though the trapped fast-ion orbit population is the largest (Figure 7). As previously discussed, this is because of the relatively high co-passing sensitivity of the KM14 and MPRu diagnostics at $E_{dep} = 9.3$ MeV and $X = 33$ cm (Figure 8 and 9).

Furthermore, it is also interesting to note that the KM14 diagnostic signal at $E_{dep} = 9.3$ MeV is likely to have no contribution from stagnation orbits whatsoever. This is simply because, for JET discharge 99965 at 7.9 and 8.4 seconds, the LOS of the KM14 diagnostic (Figure 2) misses the region of the poloidal cross-section where the stagnation orbits 'live' (i.e. the low-field side area close to the magnetic axis). For JET discharge 99965 at 7.9 and 8.4 seconds, about 0.3% of the fast-ion population consists of stagnation orbits. Therefore, unless the orbit sensitivity is very concentrated to the stagnation region in orbit phase-space, such a small fraction would have made a

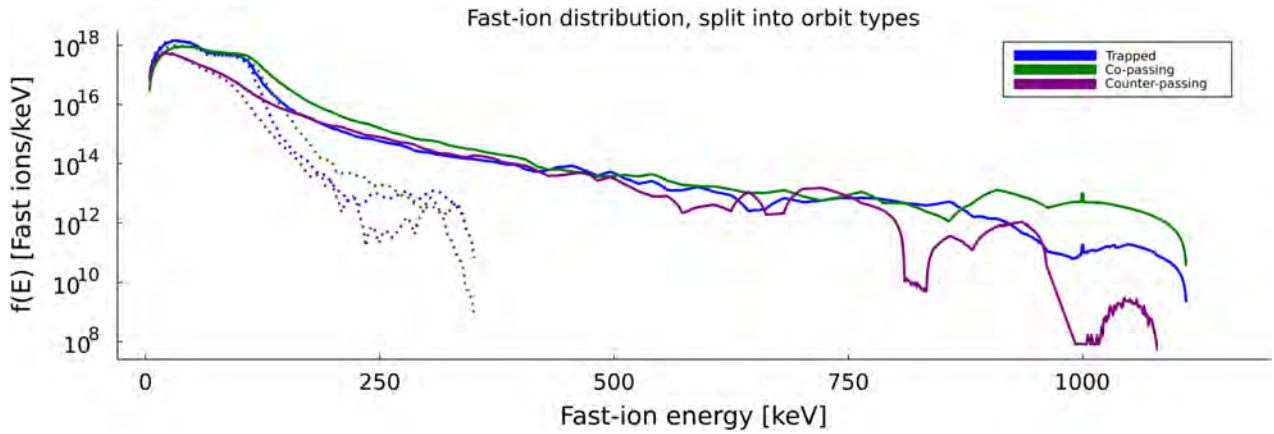


Figure 7. A plot showing the split of the energy dependence of the fast-ion distribution into its orbit-type constituents. The sum of the colored lines equals the black line in Figure 1 (minus the more 'exotic' potato, stagnation and counter-stagnation orbit types; omitted for clarity). The solid and dotted profiles correspond to the time windows at 7.9 and 8.4 seconds, respectively. The fast-ion distribution TRANSP ID is 99965K71.

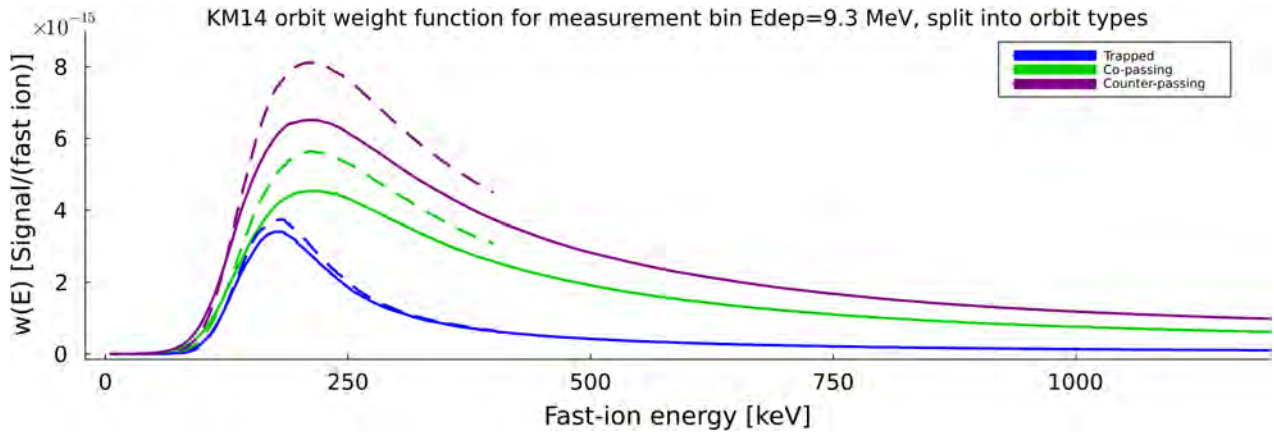


Figure 8. A plot showing the split of the energy dependence of the KM14 orbit weight function for the $E_{dep} = 9.3$ MeV measurement bin into its orbit-type constituents. The solid and dashed profiles correspond to the time windows at 7.9 and 8.4 seconds, respectively. For both timepoints, the orbit sensitivity was mapped only for the energy range of interest, i.e. where $f(E) > 0$. The profiles correspond to averages for each orbit type and energy.

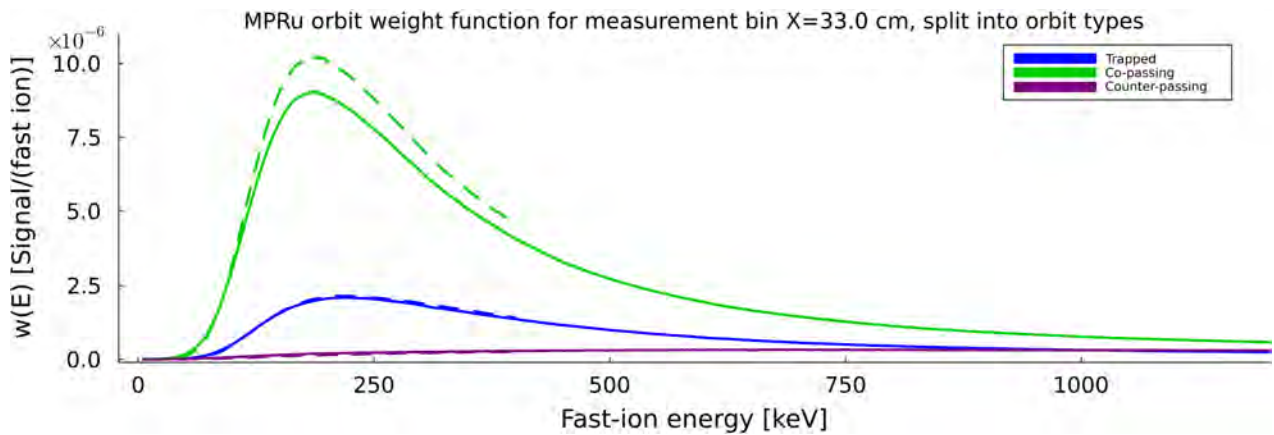


Figure 9. A plot showing the split of the energy dependence of the MPRu orbit weight function for the $X = 33$ cm measurement bin into its orbit-type constituents. The solid and dashed profiles correspond to the time windows at 7.9 and 8.4 seconds, respectively. For both timepoints, the orbit sensitivity was mapped only for the energy range of interest, i.e. where $f(E) > 0$. The profiles correspond to averages for each orbit type and energy.

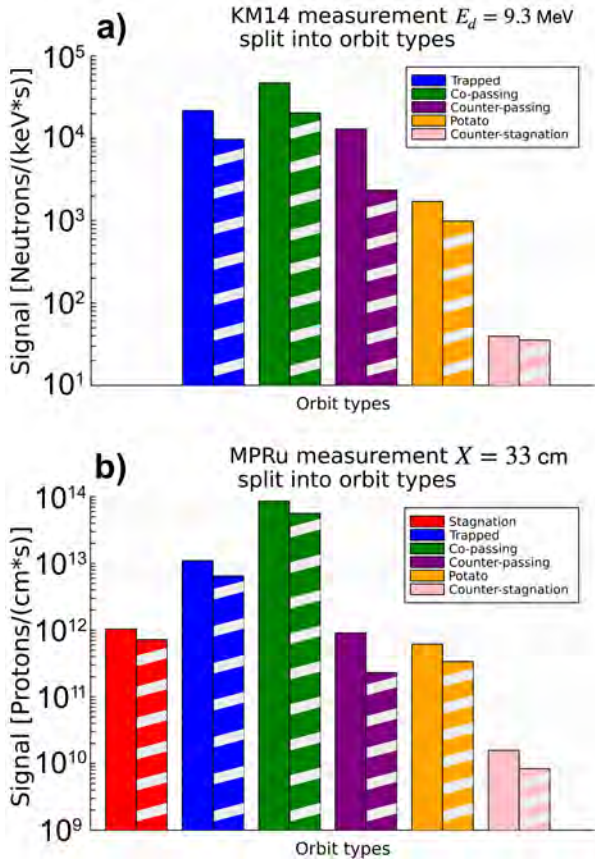


Figure 10. The (synthetic) diagnostic measurements at $E_{dep} = 9.3$ MeV and $X = 33$ cm for the a) KM14 and b) MPRu diagnostics, respectively, split into their most likely orbit-type constituents. The sum of the solid bars in a) and b) equals the value of the solid lines in Figure 5a/c and Figure 5b/d at $E_{dep} = 9.3$ MeV and $X = 33$ cm, respectively. The sum of the striped bars in a) and b) equals the value of the dotted lines in Figure 5a/c and Figure 5b/d at $E_{dep} = 9.3$ MeV and $X = 33$ cm, respectively.

negligible contribution to the diagnostic signal anyway (e.g. Figure 10b). However, as has been discussed in [19], the relative population of stagnation orbits is likely to be larger in future burning plasmas.

Continuing, we can perform a more detailed analysis via a so-called ‘split of the split’, where (for example) the energy dependence of the signal contributions in Figure 10 can be investigated. This has been performed for the KM14 and MPRu diagnostics in Figure 11 and 12, respectively. We can observe how most of the measurements at $E_{dep} = 9.3$ MeV and $X = 33$ cm are likely to have originated from fast ions with an energy of around $E = 100$ keV. This energy is approximately in the middle of the peak of the fast-ion distribution (Figure 7) and the orbit weight functions (Figure 8 and 9) where the wf product is maximized. We can also observe how, when ICRH is switched off, even though the signal densities for all

orbit types decrease, the peaks of the signal densities remain roughly at the same fast-ion energy $E \approx 100$ keV.

Finally, we can examine the difference between the solid and striped bars in Figure 10, color by color, to deduce the most likely orbit-type origin of the decrease of the diagnostic signals in Figure 5 at $E_{dep} = 9.3$ MeV (difference between the solid and dotted lines in Figure 5a/c) and $X = 33$ (difference between the solid and dotted lines in Figure 5b/d), respectively. This has been done in Figure 13. We can observe how most of the decrease in both the KM14 and MPRu signals is likely due to a loss in co-passing orbit contribution to the signals. This is because the orbit sensitivity is relatively high towards co-passing orbits for both diagnostics (Figure 8 and 9) for the measurement bins of interest ($E_{dep} = 9.3$ MeV and $X = 33$ cm, respectively). Combined with a substantial decrease in the co-passing distribution in the fast-ion energy range where the peak of the orbit sensitivities are located ($E \approx 250$ keV)(Figure 7), this results in a substantial decrease in the signal originating from co-passing fast-ion orbits.

Furthermore, we can also examine the relative decrease of the signal *per orbit type*. This has been done in Figure 14. We can observe how the relative decrease in signal contribution is greatest for counter-passing orbits. As we can observe in Figure 8 and 9 the great relative decrease in counter-passing signal contribution is due to the great decrease in the counter-passing distribution (Figure 8) as ICRH is switched off.

5. Conclusion

In this work, we have investigated the decrease in signal for the KM14 and MPRu fast-ion neutron diagnostics at JET as ICRH was switched off in DT-discharge 99965. It was found that, for the measurement bins of interest, the signal decrease was likely due to a decrease in contribution from co-passing deuterium orbits. This was likely due to the relatively high sensitivity towards co-passing orbits for both diagnostics for the measurement bins of interest. It was also likely due to the decrease in the high-energy co-passing population by several orders of magnitude as ICRH was switched off.

In JET DT-discharge 99965, the KM14 diamond matrix diagnostic is very likely completely unable to observe any signal originating from stagnation orbits. This is due to its sightline not observing the volume just on the low-field side of the magnetic axis, where

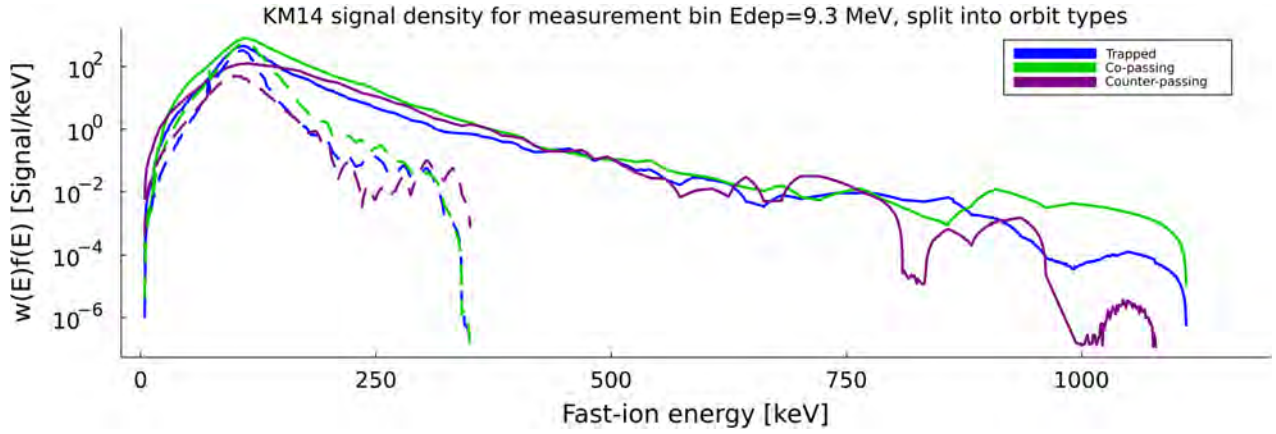


Figure 11. A plot showing the split of the energy dependence of the KM14 signal density for the $E_{dep} = 9.3$ MeV measurement bin into its orbit-type constituents. The solid and dashed profiles correspond to the time windows at 7.9 and 8.4 seconds, respectively. The integral of a solid (or dashed) profile with a specific color equals the height of the solid (or striped) bar with the same color in Figure 10a.

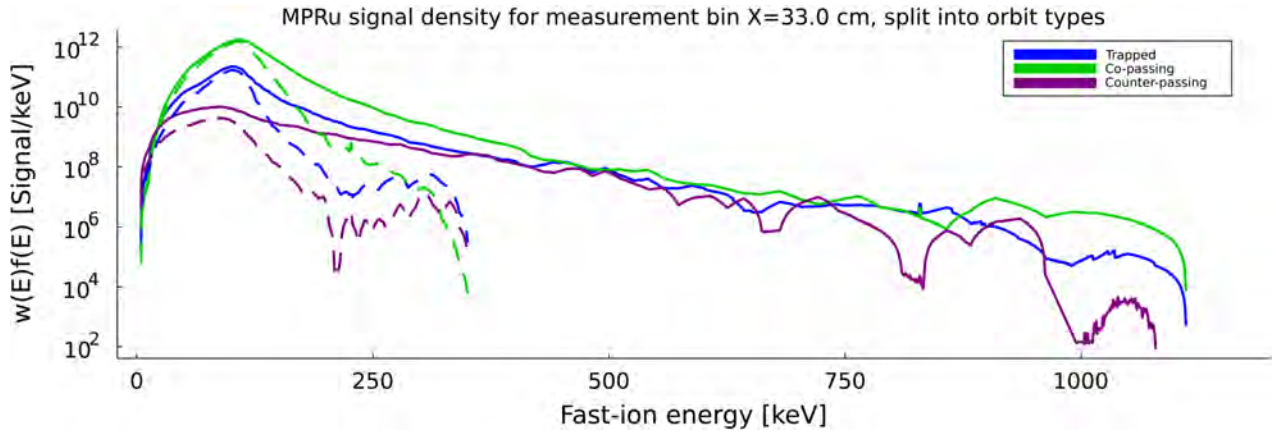


Figure 12. A plot showing the split of the energy dependence of the MPRu signal density for the $X = 33$ cm measurement bin into its orbit-type constituents. The solid and dashed profiles correspond to the time windows at 7.9 and 8.4 seconds, respectively. The integral of a solid (or dashed) profile with a specific color equals the height of the solid (or striped) bar with the same color in Figure 10b.

the stagnation orbits are localized. However, for the 7.9s and 8.4s timepoints, the stagnation orbits are unlikely to make up more than about 0.3 % of the fast-ion population, making their contribution likely to have been negligible anyway.

Furthermore, even though the fast-ion distribution is likely to be comprised of mostly trapped orbits for JET DT-discharge 99965 at 7.9s and 8.4s, the signals in the measurement bins of interest for the KM14 and MPRu diagnostics are likely to have originated mostly from co-passing orbits. This is due to the orbit sensitivity being greater towards co-passing orbits than trapped orbits for the KM14 and MPRu diagnostics, for the timepoints and measurement bins of interest.

In future work, this method of splitting the fast-ion distribution and diagnostic signals into their orbit-type constituents will have several areas of application.

This includes confirming the presence of high-energy co-passing orbits as a result of heating schemes such as the three-ion heating scheme. It can also be used to optimize the design of fast-ion diagnostics, to ensure that their sightlines are able to observe the full fast-ion distribution function. This is seen as vital for understanding how the behaviour of the fast-ion distribution function will affect the fusion plasma as a whole, in both present-day and future fusion experimental reactors such as JET and ITER.

Acknowledgements

This work has received support from the Niels Bohr Foundation which is a merger of The Niels Bohr Grant, The Emil Herborg Grantpart, The Grant of MA Marcus Lorenzen, The Ole Rømer Foundation and The

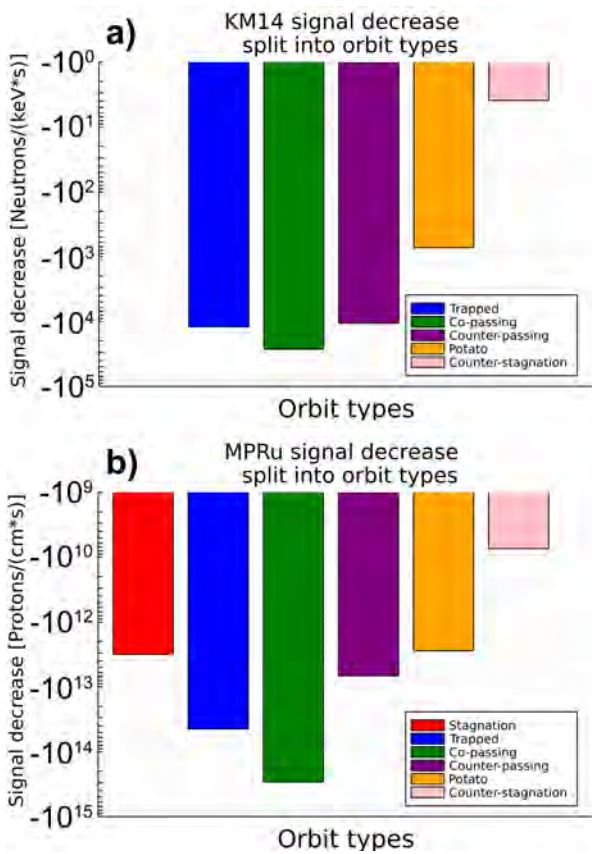


Figure 13. The signal decrease of the a) KM14 and b) MPRu diagnostics at $E_{dep} = 9.3$ MeV and $X = 33$, respectively, as ICRH is switched off, split into its most likely orbit-type constituents. For every color, it is the difference between the striped and solid bars in Figure 10.

Julie Marie Vinter Hansen Travel Grant. The views and opinions expressed herein do not necessarily reflect those of The Royal Danish Academy of Sciences and Letters.

This work has been carried out within the framework of the EUROfusion Consortium, funded by the European Union via the Euratom Research and Training Programme (Grant Agreement No 101052200 — EUROfusion). Views and opinions expressed are however those of the author(s) only and do not necessarily reflect those of the European Union or the European Commission. Neither the European Union nor the European Commission can be held responsible for them.

References

- [1] J Mailloux *et al* 2022 *Nucl. Fusion* in press
- [2] E Joffrin *et al* 2019 *Nucl. Fusion* **59** 112021
- [3] L Garzotti *et al* 2019 *Nucl. Fusion* **59** 076037
- [4] Hyun-Tae Kim *et al* 2019 *Nucl. Fusion* **60** 066003
- [5] J Eriksson *et al* 2019 *Plasma Phys. Control. Fusion* **61** 014027

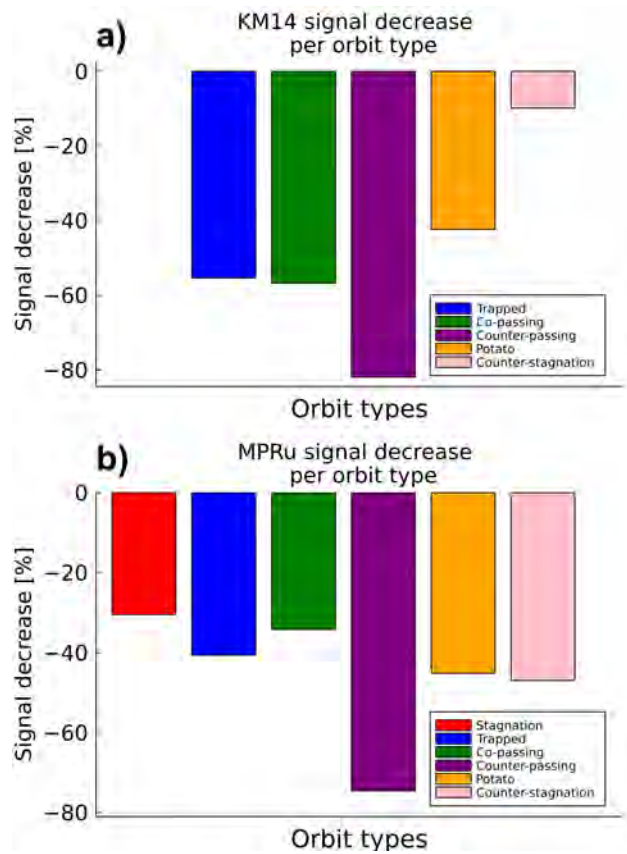


Figure 14. The relative signal decrease of the a) KM14 and b) MPRu diagnostics at $E_{dep} = 9.3$ MeV and $X = 33$, respectively, as ICRH is switched off, for each orbit type. For every color, it is the difference between the striped and solid bars in Figure 10, divided by the value of the solid bar.

- [6] A S Jacobsen *et al* 2017 *Rev. Sci. Instrum.* **88** 073506
- [7] A S Jacobsen *et al* 2015 *Nucl. Fusion* **55** 053013
- [8] M Gatun Johnson *et al* 2008 *Nucl. Instrum. Methods Phys. Res. A* **591** 417–430
- [9] E Andersson Sundén *et al* 2009 *Nucl. Instrum. Meth. Phys. Res. A* **610** 682–699
- [10] A Muraro *et al* 2016 *Rev. Sci. Instrum.* **87** 11D833
- [11] M Salewski March 2019 *Fast-ion diagnostic in fusion plasmas by velocity-space tomography* (Kongens Lyngby, Denmark: Technical University of Denmark)
- [12] M Salewski *et al* 2014 *Nucl. Fusion* **54** 023005
- [13] M Salewski *et al* 2014 *Plasma Phys. Control. Fusion* **56** 105005
- [14] M Salewski *et al* 2017 *Nucl. Fusion* **57** 056001
- [15] M Salewski *et al* 2018 *Nucl. Fusion* **58** 096019
- [16] B Madsen *et al* 2020 *Nucl. Fusion* **60** 066024
- [17] B S Schmidt *et al* 2021 *Rev. Sci. Instrum.* **92** 053528
- [18] WW Heidbrink *et al* 2021 *Plasma Phys. Control. Fusion* **63** 055008
- [19] H Järleblad *et al* 2022 *Nucl. Fusion* **62** 112005
- [20] L Stagner *et al* 2022 *Nucl. Fusion* **62** 026033
- [21] M Salewski *et al* 2013 *Nucl. Fusion* **53** 063019
- [22] Breslau J, Gorelenkova M, Poli F, Sachdev J, Pankin A and Perumpilly G 2018 TRANSP [Computer Software] <https://doi.org/10.11578/dc.20180627.4>
- [23] A Pankin, D McCune, R Andre *et al* 2004 *CPC* **159,3** 157–184

- [24] P Mantica, Scien Coord 2022 https://users.euro-fusion.org/tfwiki/index.php/M21-07:_Observation_of_alpha_heating_via_Ti_modulation_and_its_effect_on_Te_response
- [25] J Eriksson *et al* 2016 Comp. Phys. Comm. **199** 40–46
- [26] H Järleblad *et al* 2022 A framework for synthetic diagnostics using energetic-particle orbits in tokamaks submitted
- [27] M Salewski *et al* 2015 Nucl. Fusion **55** 093029
- [28] M Salewski *et al* 2016 Nucl. Fusion **56** 046009
- [29] Stagner L and Heidbrink W W 2017 Physics of Plasmas **24** 092505
- [30] Stagner L 2018 Inference of the Fast-ion Distribution Function Ph.D. thesis University of California, Irvine
- [31] H Järleblad *et al* 2021 Rev. Sci. Instrum. **92** 043526